AN INVESTIGATION OF THE MANTLE-CRUST TRANSITION BENEATH NORTH AMERICA & POISSON'S RATIO OF THE NORTH AMERICAN CRUST

Juan Pablo Ligorría, Ing. Geofísico. M.Sc.

A Dissertation Submitted to the Faculty of the Graduate School
of Saint Louis University in Partial Fulfillment of
the Requirements for the Degree of
Doctor of Philosophy

2000

COMMITTEE IN CHARGE OF CANDIDACY:

Associate Professor Charles J. Ammon,
Chairperson and Advisor

Professor Robert B. Herrmann

Assistant Professor John P. Encarnación

ACKNOWLEDGEMENTS

I am deeply grateful for the efforts of researchers and scientists in the development of IRIS (the Incorporated Research Institutions for Seismology), the U.S. Geological Survey's National Seismic Network, as well as operators of the Canadian National Seismic Network, the University of California at Berkeley, the California Institute of Technology. The data used throughout this study wouldn't have been collected without their unselfish contribution.

Before the presentation of this dissertation, I had the opportunity to share partial results of this study with many audiences. The final outcome documented here has benefited from such an enthusiastic exchange of scientific views about the Mantle-Crust Transition, and its surrounding environment. Unfortunately I cannot site each and every colleague who discussed parts of this study, but I must recognize the valuable comments and reviews by Dr. Robert B. Herrmann, and Dr. John P. Encarnación.

It wouldn't be fair to present this document without recognizing the great influence that Dr. Charles J. Ammon, my advisor, has in it. His contagious pursuit for scientific knowledge and professional excellence were enough motivation, not only to conduct this study, but also to enjoy my stay in Saint Louis University.

Finally, I express my gratitude to my wife Mercedes, and to our children José Antonio and Juan Manuel. While I was doing this, they did everything else.

Table of Contents

List of Tables

List of Figures

1 INTRODUCTION

The mapping of Earth's interior is among the most successful achievements in the geosciences. For much of the last century geoscientists and in particular, seismologists, have refined ideas and improved maps of the internal structure of our planet. From elementary observations of Earth's shape, mass, and inertial properties, it is widely accepted that the planet is highly differentiated (Poirier, 1991) with a light, thin crust, lying on a thick mantle, which in turn rests on a dense core. From work based primarily on seismic observations, this differentiated structure can be closely approximated by homogeneous shells of uniform or slowly varying properties of depth (*e.g.* Dziewonski and Anderson, 1981). Material properties change with depth as a result of composition changes, or pressure and temperature increases. Major changes in Earth structure generally represent chemical and/or thermal boundaries, while other global transitions signal the onset and the end of pressure induced changes in mineralogy (*e.g.* Brown and Mussett, 1993).

Earth's outermost "shell" is the crust, which accounts for only a fraction of a percent of Earth's mass and volume (Turcotte and Schubert, 1982). However, the crust is an important geochemical reservoir, enriched with more than 30% of Earth's potassium, uranium, and thorium (Taylor and McLennan, 1995). About 79% of the volume of Earth's crust is continent, 21% is ocean, and the remaining 1% is transitional between the two (Condie, 1993). The crust is about 40 km deep beneath the continents and is composed principally of SiO_2-rich igneous and metamorphic rocks overlain by sedimentary material (*e.g.* Meissner, 1986; Condie, 1993). The continents range in age from the earliest parts of Earth's history to the present; the oldest crustal rocks are about 4 Ga (*e.g.* MacDougall, 1996). The long history of the continents is reflected in their complexity; continental crust can be strongly heterogeneous, even its thickness ranges from about 15 to 70 km. Like the continents, the oceanic crust is a volcanic extract from the mantle but it is structurally and chemically different from the continents. For example, oceanic crust is much thinner, on the order of 7 km (ranges from 5 to 15 km), much younger (< 200 Ma), and chemically more uniform than its continental counterpart.

Beneath the crust is the mantle, the largest component of Earth by volume. The mantle is almost 3000 km thick and composed mainly of ultramafic silicates rich in olivine, pyroxene, garnet, or higher P equivalents (*e.g.* Condie, 1993). The mantle accounts for approximately 83% of Earth's volume, and just under 68% of its mass (Turcotte and Schubert, 1982). At the greatest depths is Earth's mostly iron core, composed of a liquid outer shell (the source of the geomagnetic field) and a solid inner (perhaps anisotropic) sphere. The core accounts for 16% of Earth's volume and 32% of its mass (Turcotte and Schubert, 1982).

1.1 Important Questions

Many questions regarding the details of Earth's structure remain unanswered, and are the focus of ongoing research. In this dissertation I focus on the nature of the continental crust underlying North America. Specifically, I explore the variations in bulk crustal chemistry by estimating Poisson's Ratio, a parameter sensitive to the amount of silica in rocks. The relationship between Poisson's ratio and composition is not unique, but generally provides more information on composition that either P or S velocity alone. I also map variations in the Mantle-to-Crust Transition (MCT) thickness beneath the continent. The MCT may hold clues to the answers to important questions regarding crustal evolution. Is the MCT frozen at the time of creation of the crust? Is it modified only during large-scale plate interactions (subduction, collision) or does it evolve as material is added to the base of the crust during underplating during rifting, plume or other volcanic processes? Can the character of the MCT be related to the recent or ancient geologic history of the region? The work described here does not provide answers to all these questions, but represents a step towards those answers.

1.2 Why North America?

Central to any scientific study are the observations. North America is an ideal field area for this work since it is a composite of tectonic provinces that vary in age and history, and it is the home of many seismic stations that provide a substantial data set for this survey (Figure 1.1). The western cordillera of North America includes the volcanic provinces in Mexico and the U.S. Pacific Northwest, a major strike-slip boundary along the coast of California, the elevated, wide continental rift in the Basin and Range, and the Rocky Mountains. The large, stable eastern portion of the continent hosts the Appalachian Mountains, as well as the shields and platforms that comprise the eastern conterminous U. S. and Canada. Figure 1.1 is a map of the

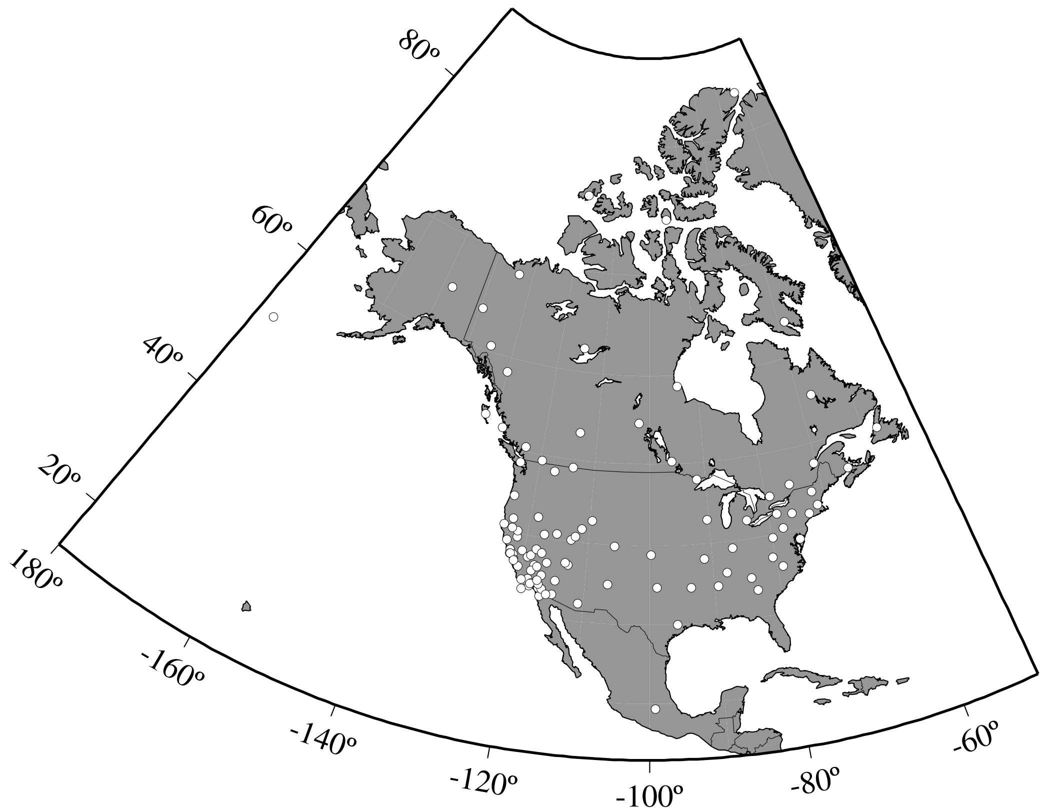

Figure 1.1 Broadband three-component seismic stations over the study area. Each symbol identifies the location of a station used in this work. Permanent and temporary stations are included. Regions of active earthquake activity are much better sampled than the more stable continental interior.

locations of the seismometers used in this study. The stations are concentrated in regions of active tectonics, particularly in the western conterminous United States. Coverage of Mexico is limited to a single station, but Canada has a nice distribution of stations sampling several geologic provinces. Although many of the “older” regions of the continent suffer from less coverage, the number of stations is sufficient to make a first -order investigation of crustal and MCT heterogeneity.

1.3 Methods and Techniques

To estimate Poisson's ratio I use receiver functions to examine the propagation times of P and S-waves traveling between Earth's surface and the MCT (Zandt and Ammon, 1995; Zandt *et al.*, 1995). I also use receiver functions to explore variations in the MCT thickness, but focus on the frequency-dependent amplitudes of waves converting from P-to-S waves at the MCT. The receiver function technique is ideal in regions of simple structure, but has some rather simple assumptions that often are inappropriate in regions of complex structure. Still, the method has proven to be a powerful tool, with relatively easy and inexpensive application, which provides a straightforward approach for imaging seismic velocity transitions in the lithosphere (*e.g.* Ammon *et al.*, 1990; Owens, 1984; Langston, 1979) and upper mantle transition zone (*e.g.* Gurrola *et al.* 1994). Further, recent advances in seismic data collection and storage provide an unprecedented opportunity to gather large amounts of high quality, broadband, data that comprise an ideal data set for this study.

1.4 An Outline

Before launching into the seismological aspects of these investigations, I begin with a review of properties of the MCT and ideas on the evolution of continental crust in Chapter 2. This literature search was written as much for myself as for the reader, but the material forms the background under which the seismological results described in later chapters must be viewed. Since receiver functions are the primary data used in both investigations of the North American crust, I provide an overview of receiver functions and receiver-function methods in Chapter 3. Again, much of this material is available in existing literature, but I also describe the method I developed and used to estimate the MCT thickness, which cannot be found elsewhere. In Chapter 4, an alternative method to calculate receiver functions is described and tested. This method, based on the iterative process introduced to seismology by Kikuchi and Kanamori (1982), results in simpler signals that ease interpretation. Much of Chapter 4 appeared in Ligorría and Ammon (1999). With the reviews complete, I describe the data used in Chapter 5, which includes maps and a tectonic classification used to interpret the results in later chapters. Finally, Chapter 6 is a description of the Poisson's ratio study, using the iterative deconvolution method outlined in Chapter 4. Chapter 7 is a report of the variations in MCT thickness beneath North America. Although some interpretation is included in Chapters 6 and 7, a summary of the results and implications of this work is provided in Chapter 8. Since the data set is large and the interpretation is focussed on medians, averages, and general trends in the observations, I provide many of the detailed numbers and measurements in appendices that follow the main body of the text.

2 The Continental Mantle-to-Crust Transition

In this chapter, I discuss the nature of the Mantle-to-Crust Transition (MCT), i.e. its composition, formation, and the processes that can affect those properties. This material is drawn from the published literature, and my goal is to provide adequate background for my investigations of crustal Poisson's ratio and thickness variations of the MCT beneath North America, which are described in later chapters. The study of the MCT has a direct relationship to the study of all thermomechanical processes that occur in the lithosphere (or tectosphere, if you like). The crust and uppermost mantle form the plates of plate tectonics, and they constitute a package whose interactions forge most of the large scale surface tectonics that are the focus of geologic investigation. The MCT is the structure across which the crust and mantle interact, couple, and sometimes decouple. An investigation of the MCT may provide valuable insights on lithosphere structure, evolution, and or the role of magmatic underplating in crustal growth, etc. (e.g. Clowes, 1993; Mengel and Kern, 1992; Nelson, 1991; Rudnick, 1990; Mooney and Braile, 1989; Furlong and Fountain, 1986). The MCT is a global boundary with global geologic importance.

From a seismologists' viewpoint, the MCT is in a class of geologic features that are perhaps most suitable for seismic investigation - major boundaries in elastic properties. Elastic boundaries are the source of specific seismic waves (reflections, refractions, diffractions) that affect seismograms, the central data in any seismic analysis. In Chapter 6 I use waves traveling between Earth's surface and the MCT to estimate the bulk elastic properties of the North American continental crust, in Chapter 7 I focus on the MCT, mapping thickness variations looking for systematic trends in the evolution of this compositional boundary between crust and mantle.

Because of proximity of the lower crust and upper mantle to the MCT, a literature review of these regions is relevent to my later investigations of the crust and MCT beneath North America. Since the mantle provides the basic material to assemble the crust and the heat to drive element redistribution in the crust via magmatic and fluid activity (e.g. Taylor and McLennan, 1995; O'Reilly et al., 1997), the composition and structure of the continental mantle are important in any discussion of the continents and the MCT. The lower crust is perhaps the most enigmatic part of the continents and certainly the composition of the lower crust is the largest unknown in estimates of the bulk composition of the crust (e.g. Taylor and McLennan, 1995; Rudnick and Fountain, 1995).

I begin with a definition of such common terms as mantle, crust, and MCT, which can be distinct from the "seismic Moho". Following a brief introduction to the transition, I review the nature of the upper mantle and lower crust. Next I describe previous investigations of the MCT after which I conclude with a review of tectonic processes that can affect the nature of the MCT. The subject is vast and this review is by necessity limited in scope. I hope to introduce the most relevant material on the subject, and I hope to provide a starting point for the interested readers.

2.1 Moho, Crust-Mantle Boundary, and MCT

The distinction between crust and mantle as petrological units is relevant for the interpretation of large-scale processes such as the nature of Earth's accretion, crust-mantle evolution, and the concept of crustal growth (O'Reilly, 1989). The difference between the seismic Moho and petrological crust-mantle boundary goes beyond semantics and is related to the very definition of the Earth's crust and mantle. I use the term crust to identify material that has been extracted from the mantle. It consists largely of silicate material formeed during Earth's early differentiation and extraction of the continental crust, with later additions through a variety of magmatic processes. The petrologic crust-mantle boundary is a compositional feature. The seismic-geophysical Moho is a boundary between materials with differing elastic properties (Mengel and Kern, 1992). Neither is necessarily a first-order (sharp) boundary.

Usually, it's acceptable to assume that the two features coincide, but that is not always the case. The continental lower-crust and the upper mantle materials may have similar seismic velocities. For example, mafic lower crust could have indistinguishable seismic properties from mantle rocks at 30 – 50 km depth, as long as the constituent minerals have attained thermodynamic equilibrium (Hynes and Snyder, 1995). An increase in lower-crustal velocity from "pure-crustal" to "pure-mantle" values may reflect the appearance of garnet, which depends on composition and thermomechanic environment where mineralogical changes occur (e.g. O'Reilly and Griffin, 1996; Anderson, 1989; Jordan, 1979). In other cases, hydrated upper-mantle rocks may be seismically indistinguishable from lower crustal rocks (Anderson, 1989). Under hydrous conditions at shallow mantle temperatures, peridotite can metamorphose to serpentinite resulting in a significant reduction in density and seismic velocity.

Two notable examples illustrate the potential differences between the MCT and the seismic Moho. First, beneath the relatively simple oceanic crust, the MCT and the seismic Moho are not coincident (e.g. Brown and Mussett, 1993). Thus our best example of the MCT shows a seismic-petrologic discrepancy. Second, at one well studied exposed section of continental MCT near Val Malenco in the Italian Alps, Hermann et al. (1997) inferred that mantle-like seismic velocities for a garnet-rich restitic granulite (crustal material). Although their inference is based on a density-velocity extrapolation, it is possible that in this one-kilometer thick MCT, the seismic Moho does not coincide with the petrologic crust-mantle boundary but is probably located in the lowermost continental crust (Hermann et al., 1997).

Two other examples of discordant MCT and seismic Moho's based on *in situ* observations on continents are:

- Hynes and Snyder (1995) observed anomalous strong seismic reflectors 20-30 km deeper than the presumed seismic Moho beneath the Scottish Caledonides. Hynes and Snyder (1995) hypothesized that the deep reflector is the petrologic crust-mantle boundary and the shallower structure is a result of rocks with crustal composition possessing a high-pressure mineralogy that produces mantle-like seismic characteristics.

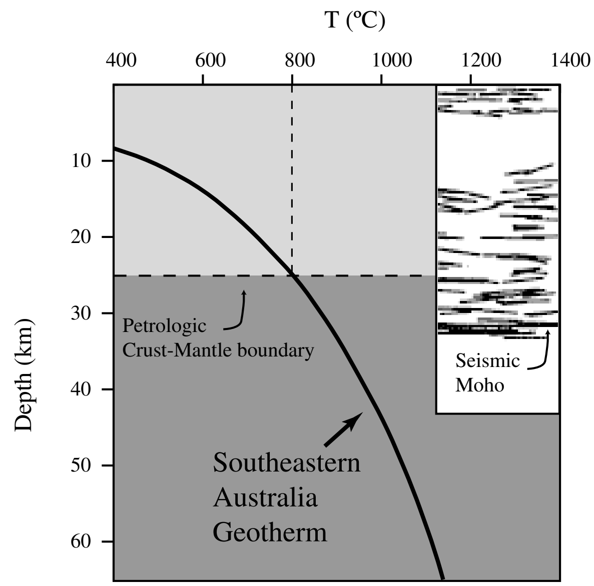

Figure 2.1 Example of discrepancy between estimations of the seismic Moho and the petrologic crust-mantle boundary (modified after O'Reilly and Griffin, 1996). The latter is determined by reference to a known geotherm (Southeastern Australia Geotherm), that points out the spinel-lherzolite stability field (~ 800 ºC). The cartoon of a seismic reflection section contains strong reflections near the base of the crust, which are interpreted as the seismic Moho.

- In southeastern Australia, a seismic-petrologic discrepancy is suggested by a difference between xenolith and seismic observations (Figure 2.1). Xenolith data place the MCT at the depth several kilometers above the seismic Moho (O' Reilly and Griffin, 1996). However, Clitheroe (1999) suggested that the what's observed is only an apparent discrepancy resulting from measurement and interpretation uncertainty in both seismic and petrologic observations.

To better understand these observations, and the nature of the MCT, we must integrate information regarding the composition and mineralogy of the lower crust and upper mantle with observations of the MCT and seismic Moho. In the next section I outline some of what we know about the upper mantle and lower crust.

2.2 General Trends in Continental Lithosphere Properties

Shields and platforms occupy by far the largest area of continents. Hence, although several authors have overemphasized the significance of crustal structure of Phanerozoic crust, Precambrian crust is more "typical" continental crust (Christensen and Mooney, 1995). As explained later, there seems to be a secular change in the nature of lithosphere genesis processes. Therefore, models of lithosphere formation based on modern processes may be inadequate, even for Proterozoic time, and are almost certainly not applicable to Archean time. Crustal volumes and the underlying lithosphere mantle have been formed together, and generally have remained coupled together thereafter (Griffin et al., 1998).

The Archean lithosphere may be the refractory residue of an ancient high-temperature differentiation process. Lithosphere under Archean cratons has been protected from outside influences by a combination of circumstances: it is cold, strong, it has high viscosity, it is probably refractory compared to lithosphere elsewhere, it is also buoyant and is isolated from active tectonics (Anderson, 1995). The stability and thickness of Archean mantle is directly related to its low density, which in turn reflects its high degree of depletion in basaltic components (Griffin et al., 1998).

The traditional idea of Archean crust of the shield-type is that it tends to be thick, with a dominant gabbro underplate, with Vp higher than 7 km/s (Durrheim and Mooney, 1994). There is an apparent correlation between tectonothermal age and MCT depth: crust thickens with age. This may be due to (a) magmatism associated with extension processes, (b) accretion to existing continents, and (c) long term chemical and volume changes of crust-forming, mantle-derived magmas (Jarchow and Thompson, 1989). As a rule of thumb, the velocity contrast around the MCT tends to be less drastic beneath young orogenic zones (0.5-1.5 km/s) than beneath cratons (1-2 km/s) (Anderson, 1989).

There are differences between the lowermost structure of Archean and Proterozoic crust (Durrheim and Mooney, 1994) that may reflect different modes of crustal formation. In addition, the bimodal distribution of P-velocities beneath shields and platforms suggests two crust-forming processes: 1) Low-velocity lower-crust implies an arc magmatism mechanism, and 2) High velocities, suggest underplating processes or the presence of high-grade metamorphic rocks of supracrustal origin (metapelites). During the Phanerozoic, magmatic underplating appears to supplement arc magmatism as a means of continental growth (Holbrook et al., 1992). The evidence of a Proterozoic crust thicker than Archean crust, suggests that Archean crust generally lacks the basal high velocity layer (and it appears taht way where it can be checked). Further, geochemical analyses of sediments and mantle xenoliths have been interpreted to show clear difference between Archean and Proterozoic lithosphere (Durrheim and Mooney, 1994). A further difference is in the velocity gradient of the MCT, which is estimated to be about $0.4 \pm 0.2\ s^{-1}$ at the base of Archean crust, while the gradient beneath Proterozoic crust is generally smaller (Durrheim and Mooney, 1994).

The latter observation is consistent with the information provided by xenolith studies, which indicate that Archean mantle contains significant amounts of depleted garnet lherzolites, concentrated in zones 150-180 km deep, and the dominance of depleted lherzolites at shallower depths. Phanerozoic samples from the same data set show a lithospheric mantle characterized by more fertile compositions, abundant evidence of multiple metasomatic events and rare harzburgites. Therefore, xenolith data suggests an increase in average clinopyroxene/garnet ratio from Archean through Proterozoic to Phanerozoic time (O'Reilly et al., 1997). This secular change can be due to a decline in mantle temperature, which plays a major role in the magmatic and rheologic processes of crustal evolution (Christensen and Mooney, 1995). A consequence of the depleted character of Archean lithosphere is that it may have become more refractory, less vulnerable to partial melting, stiffer and more stronger, thereby inhibiting convection and reducing heat flow (Durrheim and Mooney, 1994).

While there is a good correlation between Archean cratons and high velocities, little correlation exists for younger cratons and mobile belts. The high velocity region beneath cratons may be a static keel or a dynamic down-welling (Anderson, 1995). Common features for Proterozoic crust include (Mooney and Braile, 1989):

- Top of the middle crust (Vp ~ 6.6 km/s) is everywhere at 19 ± 4 km
- A mafic lower-crust (Vp ~ 7.0 - 7.6 km/s) is present with 7 to 15 km thickness
- Crust thickness is about 45 ± 5 km

- Lower-crustal layer often has high velocity gradient and sometimes grades smoothly into the upper-mantle. This layer most likely consists of high-grade intermediate-to-mafic composition metamorphic crust.

Average cratonic (or shield) geotherms are the lowest lithospheric geotherm. Indeed, geotherms constructed from xenoliths in kimberlites may suggest a lithosphere that is relatively thermally unperturbed (O'Reilly and Griffin, 1996).

After the marked change at the Archean-Proterozoic boundary, there has been a steady change in mantle melting and crustal generation process, to produce progressively less depleted subcontinental mantle through time (Griffin et al., 1998). Phanerozoic (Cambrian and younger) crust tends to be about 30 km thick, with relatively low average velocity, indicative of high degree of crustal differentiation (Durrheim and Mooney, 1994). Nearly all continental crust with thickness outside the 24 – 56 km range is late Cenozoic in age. This observation implies that thick crust will not remain thick but will evolve toward typical ~40 km crust (Christensen and Mooney, 1995). However, if underplating of mafic magma is a process taking place everywhere, it may suggest that the hypotheses of a constant crustal thickness is likely to be misleading, since the crustal thickness seems to change with time (age) (Nelson, 1991).

2.2.1 Physical Properties of The Continents

I conclude with a summary of important properties of the continental crust. The precise breakdown of global crustal geology depends on the reference. Condie (1993) lists area extents of shields, platforms, paleozoic, and younger orogens separately.

Christensen and Mooney combine orogens, but list extended crust separately. Zandt and Ammon (1995) used the classification of Condie in their analysis of global Poisson's Ratio variations. For global comparisons, I will later use the classifications of Christensen and Mooney (1995). Table 2-1 is a summary of several important physical properties of the continental crust. Surface area and mean thickness are taken directly from Christensen and Mooney (1995), Volume percentage is computed from the area and thickness, and average heat flow is from Condie (1993) with two exceptions. The average heat flow is from Pollack et al., (1993) and the continenal arcs heat flow corresponds to the Cenozoic igneous province in the same reference.

Table 2-1: Physical Properties of the Continents

Crustal Type	Surface Area (%)	Mean Thickness (km)	Volume (%)	Average Heat Flow (mW/m^2)
Shields (15%) & Platforms (44%)	69	41.5	73	46
Orogens	16	46.3	19	62
Extended Crust (Basin & Range)	9	30.5	7	77
Continental Arcs	1	38.7	1	97
Total	100	41.0	100	65

2.3 The Upper Mantle and Lower Crust

Observations of the *in situ* environment around the continental MCT are key to any understanding of the processes taking place near the MCT and how they relate to the lithosphere. The term lithosphere has different connotations within subdisciplines of the geosciences. Geochemists view the lithosphere as a reservoir that can remain isolated from convective mantle for more than 10^9 yrs and that can be remobilized or melted to provide continental flood basalts (Anderson, 1995). Other "lithospheres" in the literature include the crust and the seismic high-velocity layer (i.e. lid), the elastic shell, tectosphere, the mechanical boundary layer (MBL), the plate, and the thermal lithosphere (e.g. O'Reilly and Griffin, 1996; Anderson, 1995; Chapman and Furlong, 1992; Jordan, 1988). Usually the thermal definition is favored in geophysics. In this view, the base of the lithosphere is bounded by the 1300 °C isotherm, which also defines the boundary between strong, elastic, brittle, high velocity mantle and weak ductile, low-velocity mantle immediately below (Anderson, 1995).

2.3.1 The Upper-Mantle

Because it is inaccessible, the composition of the upper-mantle has been inferred through indirect evidence and theoretical models. The upper-mantle is assumed to be the residuum of crust formation (O'Reilly, 1989) and petrological models suggest that since basalts represent melts, and some peridotites residues of melting, some mixture of these rocks should approximate the composition of primitive upper-mantle. The source of mid-ocean ridge basalt (MORB) has been the logical choice for upper-mantle composition, since MORBs represent the most uniform and voluminous magma type (e.g. Anderson, 1995; Rudnick and Fountain, 1995; Anderson, 1989), although non-MORBs have been attributed to continental crustal contamination or to melting of "primitive" lower mantle plumes. Approximately four billion years of crustal extraction from the mantle have resulted in an upper mantle depleted in elements that are concentrated in the continents (Anderson, 1995). Since the extraction process was gradual, the mantle became more and more depleted as the continental reservoir grew. The evolution of these reservoirs may produce systematic variations in crustal composition with age, but any such trends have been difficult to identify with geophysical measures. The only well established differences are between Archean and younger crust (e.g. Durrheim and Mooney, 1994; Griffin et al., 1998).

Petrologic models also suggest that the extraction of crustal material from the mantle leaves behind ultramafic materials which are chiefly composed of ferro-magnesian minerals with relatively low silica content. Peridotite (lherzolite, dunite, harzburgite) is the general name applied to ultramafic rocks composed primarily of olivine, orthopyroxene, and clinopyroxene (Figure 2.4). A potential problem in confirming peridotite as the major upper mantle constituent is that it has similar compressional wave velocities as eclogite, a dense clinopyroxene-garnet-rich rock, i.e. a high-pressure form of MORB and picrite (Anderson, 1989). However, the V_P/V_S ratio of mafic rocks increases with garnet, clinopyroxene, or FeO content, enabling eclogitic rocks to be distinguished from peridotitic rocks (the anisotropic properties of these two rocks also differ).The integration of different sets of elastic constants (i.e. velocities) and consideration of possible rock types (from felsic to ultramafic), leads to the conclusion that velocities of ultramafic rocks most closely fit observed *Pn* velocities, supporting a dominant ultramafic composition of the upper-mantle (Jarchow and Thompson, 1989). Further support for the ultramafic nature of the mantle comes from ophiolite studies, which suggest that the upper

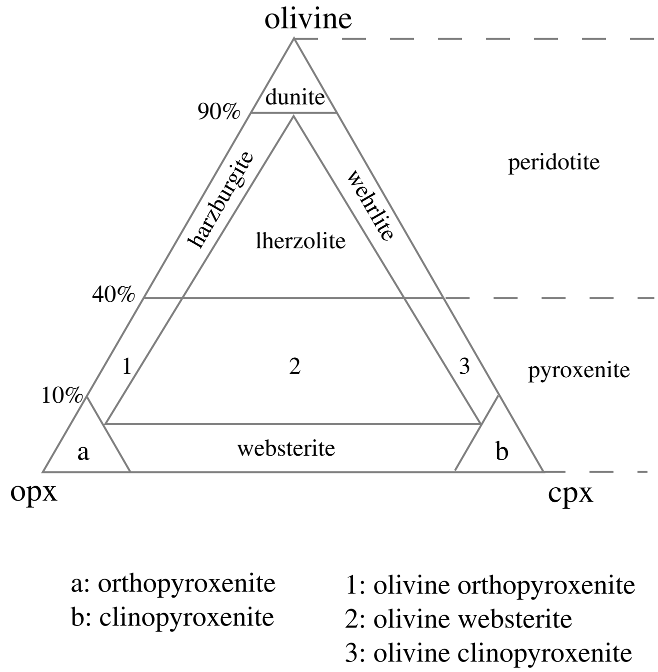

Figure 2.2 General classification of ultramafic rocks according to the relative content of the three main constituent minerals: olivine, orthopyroxene (opx) and clinopyroxene (cpx) (modified after Anderson, 1989).

mantle beneath oceanic crust is dominantly composed of plagioclase lherzolite beneath slow spreading ridges and harzburgite (with dunite) beneath fast spreading ridges.

Xenoliths, rocks brought to Earth's surface by volcanic activity, provide additional information on upper-mantle composition. Xenoliths observed in alkali basalts from continental rifts contain ultramafic spinel lherzolites, while garnet lherzolites (assumed to have originated from depths greater than about 100 km) are more common in kimberlite volcanics (Condie, 1993). Both samples suggest that the mantle rocks have had less than 10% basalt extracted from the original rock. Evidence from garnet lherzolites supports an upper-mantle under continents containing garnet (~6%), clinopyroxene (~3%), orthopyroxene (~27%) and olivine (~64%) (Jordan, 1979). Lastly, geochemical analyses indicate that the upper-mantle is heterogeneous. Although the configuration of distinct mantle geochemical reservoirs is poorly mapped, variations in the mineralogy and composition in the upper mantle should be kept in mind when interpreting observations and drawing conclusions from seismic observations.

2.3.2 The Lower-Crust

The composition of the lower-crust is the largest source of uncertainty in determining the continental crust's overall composition (e.g. Rudnick and Fountain, 1995; Taylor and McLennan, 1995). In general, the lower-crust is presumed to be lithologically heterogeneous, with an average mafic composition, but it may range to intermediate bulk composition in some regions (Rudnick and Fountain, 1995). Estimates of Poisson's ratio (e.g. Zandt and Ammon, 1995; Chapter 6) suggest that at times the lower crust may approach felsic compositions. The strong heterogeneity in the lower crust suggests that it can be composed of metamorphosed rocks (including sediments pushed deep during collisions) or igneous rocks. As reference for the following discussion, Figure 2.3 is a summary the main groups of crustal igneous rocks and their major mineral components.

Part of the conundrum in unraveling the average properties of the lower crust arises from one of the major paradoxes in crustal geochemistry - xenolith data suggest a mafic composition, while exposed sections of the lower crust favor a more intermediate composition. Both data sets are subject to problems of interpretation, includ-

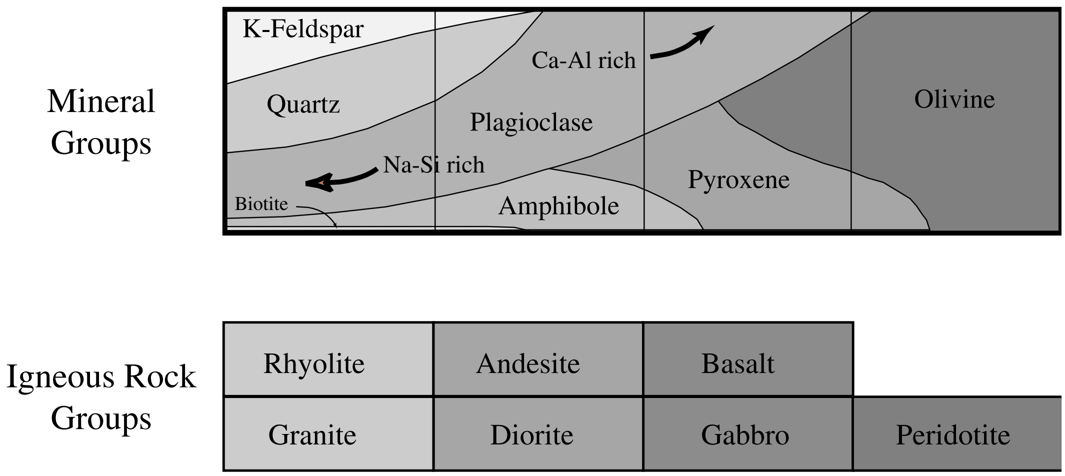

Figure 2.3 General classification of igneous rocks according to mineral content (modified after Hambling and Howard, 1995).

ing the simplest question, is either is representative of the true lower crust? Exposed geologic cross-sections of the lower crust may be grouped according to the mechanism that exposed the terrane. The four main groups, and some examples of continental locations are (Percival et al., 1992): a) Compressional uplifts (e.g. Kapuskasing uplift, Ontario, Canada; Ivrea Zone, Italy; Kohistan arc, Pakistan), b) Wide-oblique transitions (e.g. Pikwitonei granulite domain, Manitoba, Canada; Western gneiss terrane, Australia), c) Impactogenic uplifts (e.g. Levack gneiss complex, Superior Province, Canada; Vredefort dome, South Africa), and d) Transpressional uplifts (e.g. Tehachapi complex, Sierra Nevada, California; Fiordland, South Island, New Zealand).

Many of the exposed geologic sections are in fact segments of continental or arcs that were deeply buried during collisions but relatively quickly (they didn't equilibrate under lower crustal conditions) worked their way back to Earth's surface

(Taylor and McLennan, 1995; Rudnick and Fountain, 1995). Recent analysis of the pressure-temperature history of many of the more felsic high-grade terranes suggest that they experienced only a brief time in the deep crust, and thus follows the inference that they are not representative of “mature” continental lower crust (e.g. Rudnick and Fountain, 1995; Hermann et al., 1997). Isobarically cooled granulites, which are generally more mafic, are interpreted as more representative of the lower-crust (Hermann et al., 1997). Thus although many exposed high-grade terranes suggest a more felsic composition, xenoliths and isobarically cooled high grade exposures are believed to be more representative of typical continental lower crust, and they are more mafic (Taylor and McLennan, 1995; Rudnick and Fountain, 1995).

Other data are consistent with a mafic lower crust. Heat flow observations on the continents and estimates of the upper crustal composition indicate that the lower crust must be relatively depleted in heat-producing elements (Taylor and McLennan, 1995). If this is not the case, then the entire heat flowing out Earth’s surface above many low heat-flow provinces of the continents would be produced within the continental crust, leaving no input from the mantle. Seismic evidence also supports a lower crust of mafic composition. Holbrook et al., (1992) performed a world-wide compilation of seismic refraction studies and concluded that roughly half (53%) of the lower continental crust has “mafic” like velocities. Their average continental crustal thickness was 41 km, with an average V_P of 6.45 km/s overlying an upper-mantle of V_P ~ 8.09 km/s. These values and the work of (Christensen and Mooney, 1995) suggest that a lower continental crust lithology that is chemically equivalent to gabbro, but garnet granulite seems to be the dominant rock type

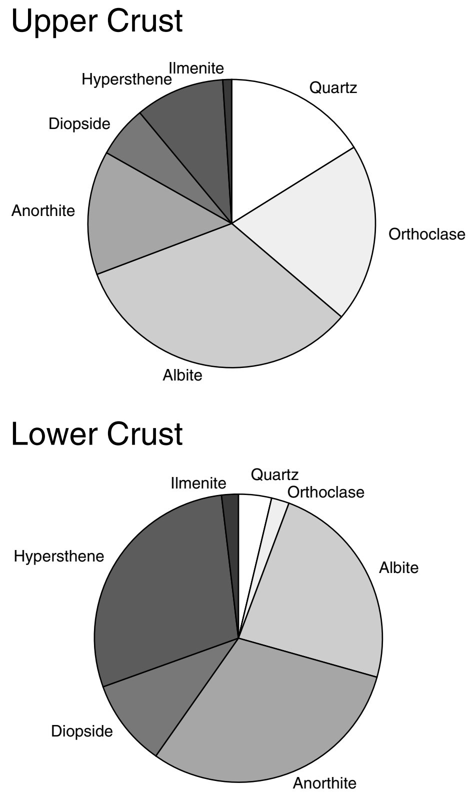

Figure 2.4 Estimated normative mineralogy of the upper and lower crust (Taylor and McLennan, 1995). The upper crust is enriched in quartz, orthoclase, and Na-rich plagioclase. The lower crust is enriched in Ca-rich plagioclse, and the orthopyroxene hypersthene.

immediately above the MCT. Using observations of V_P in combination with geochemical and heat flow information, the P-velocity measurements can be satisfied by a lower crust composed of mafic granulites (e.g. Rudnick and Fountain, 1995). An "average" lithology for the lower-crust would include at least as 65% mafic granulite with 5% metapelites and perhaps 30% intermediate felsic granulites. Estimated normative mineralogies for the upper and lower crust from Taylor and McLennan (1995) are shown in Figure 2.4.

These are of course, average properties of a complex geologic environment. Several properties of the lower crust are believed to vary with tectonic age and or geologic province. For example, the continental lower crust ranges from nearly transparent to highly reflective (Mooney and Meissner, 1992). Mooney and Meissner (1992) outline the variation for several tectonic environments:

- Precambrian crust has a structureless lower crust, which contrasts with structural features in upper and middle crust.
- In Proterozoic orogens there is sometimes evidence of suture zones extending throughout the lower-crust. Phanerozoic orogens, have apparently lost their roots and show sub-horizontal reflectivity although some suture zones remain. Paleozoic orogens tend to have a transparent lower-crust; e.g. most of the Appalachians, show a transparent lower-crust, with exception of the eastern section, where the lower-crust seems to be affected by collision and becomes highly reflective as it extends into the passive opening of the Atlantic platform.
- Young (post-Mesozoic) orogens show crustal roots that seem to be in isostatic equilibrium. The lower-crust reflects recent tectonics, and sub-horizontal patterns may be the result of multiple shear zones and delamination.
- Recently extended crust has a highly reflective lower-crust, in contrast to nearly transparent upper crust and upper-mantle.

The origin of extensive lower-crustal layering inferred from its high reflectivity, could be explained as a combination of (e.g. Mooney and Meissner, 1992; Rudnick and Fountain, 1995): high velocity intrusions (V_P ~ 6.6 km/s) within a lower velocity matrix (V_P ~ 6.0 km/s), fine scale layering typical of high-grade metamorphic terranes, faults that juxtapose contrasting rock types, significant anisotropy associated with metamorphic rocks, and or thin metamorphic layers together with high pore pressure or partial melt. Warner (1990) discussed the following hypotheses regarding the highly reflective character of the lowermost crust:

1. Shear zones due to strain fabrics, faults or ductile shearing. Shear zones are favored if we assume that different rheologies of lower-crust and upper-mantle might produce a different character on seismic data. Shearing of equi-dimensional pre-existing heterogeneities would produce laminar (or lenticular) bodies within shear zone. An objection to the shear zones model is the fact that no direct correlation exists between the present day position of the brittle-ductile transition and the top of the reflective layering. Further, unrealistically large strains are necessary to produce continuous shear structures to explain continuity of reflections throughout the whole lower-crust. Indeed, rheologic models of the crust predict weakening of strain with depth, which makes juxtaposition or shearing heterogeneity very unlikely.

2. Underplating processes at the base of the crust. Underplating is related to sills, layered intrusions, or cumulates, thought to be trapped around the MCT by a combination of density contrast and/or changing rheology. This hypothesis is supported by the reflective coefficient (> 0.1) of mafic intrusions into granitic or andesitic crust. Lower-crust xenoliths indicate mafic granulites as dominant components of the medium. Further, underplating may provide a heat source to drive high-grade metamorphism and produce crustal granulites, which would be difficult to explain without partial melting within the underlying upper-mantle.

3. Aqueous fluids within stratified porosity. This idea is supported by the fact that seismic velocity in rocks can be dramatically reduced by the presence of small amounts of fluids. The high electrical conductivity of the lower-crust is difficult to explain without saline fluids (although graphite has also been proposed to explain these observations). However, petrological observations are inconsistent with long-lasting free water at the MCT - observed small scale heterogeneity in oxygen isotopic ratioswould be homogenized in the presence of water. The latter objection is supported with the occurrence of anhydrous granulites within lower-crustal xenoliths and at the base of exposed geologic cross sections. In support of these ideas, experimental work by Markl and Bucher (1998) showed that salt and chlorine-rich minerals may form from an originally water-rich fluid through short-lived series of hydration reactions in granulites. Their work shows that fluid was present in the lower-crust in only small amounts and was not stable over geologically long periods of time, i.e. lower-crust is likely devoid of free fluid phase during most of its history.

2.3.3 The Upper Crust

The upper crust is generally much better exposed and sampled by geologic processes, and thus its composition is much better known. From the analysis of exposed rock types, the composition of sedimentary rocks and soils, a fairly stable estimate of the composition of the upper crust (Figure 2.4) has been established (Taylor and McLennan, 1995). In comparison with the lower crust, the upper crust is more enriched in felsic materials, including heat producing elements. Typically the upper crust has a lower seismic velocity, Poisson's ratio, and density than its lower counterpart (Christensen and Mooney, 1995).

The chemical differences between the upper and lower crust are thought to be the result of magmatic differentiation and enrichment of the upper crust by crustal melting (at least since the Proterozoic) (Taylor and McLennan, 1995). The depletion of Europium (Eu) in post-Archean sediments provides the evidence that much of the post-Archean upper crust has an intracrustal origin (crustal melting leaves Eu in plagioclase) (Taylor and McLennan, 1995). Exactly when differentiation occurs may vary, but likely events include arc volcanism, underplating, and collisional processes.

2.4 The Mantle-To-Crust Transition

Since we have two general classes of crust, oceanic and continental, it is reasonable to expect that there may be differences between the MCT that underlies each (Figure 2.5). My comparison of the properties of the oceanic and continental MCT structures closely follows the earlier work of Jarchow and Thompson (1989). Some of the inferences regarding the nature of the MCT are questioned later when more recent surveys are reviewed.

2.4.1 Continental and Oceanic MCTs

In general, differences between oceanic and continental MCT can be summarized as follows (Jarchow and Thompson, 1989):

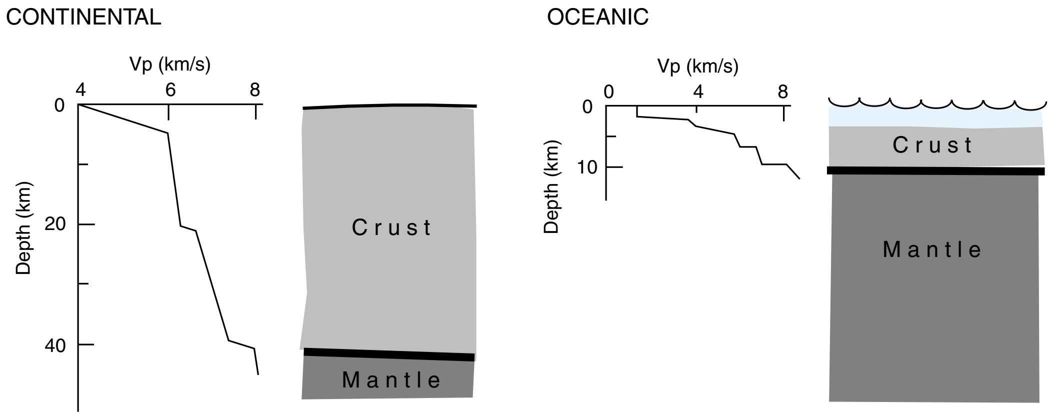

Figure 2.5 Simplified cartoons of "slice" sections of typical Continental and Oceanic crust and uppermost mantle. The global seismic velocity discontinuities are represented by the Vp vs. Depth plots to the left, of which the seismic Moho is the most prominent (modified after Jarchow and Thompson, 1989).

- The Oceanic MCT is a zone of almost constant thickness, containing mafic and ultramafic lithologies mostly made of discontinuous lenses with sharp contacts. It forms contemporaneously with the oceanic crust and is not significantly modified with time. The oceanic MCT seems to be continuous, about one-km thick, but may be thicker near hot-spots.

- The continental MCT has a heterogeneous nature, separating an upper-mantle composed of several varieties of peridotitefrom a lower-crust composed of eclogite, mafic granulite, some silicic granulites and gabbro-amphibolite. The continental MCT has a complex genesis. In old shields and cratons it tends to be deeper and a smooth gradational contrast, possibly due to relatively less melting and differentiation subsequent to its formation. Young orogenic zones, on the other hand, show substantial MCT topography, possibly associated with crustal thickening by means of low-angle thrust slivering. The Continental MCT under island arcs resembles the oceanic MCT, i.e. a mafic-ultramafic transition due to active igneous-metamorphic processes, but the mantle directly below the MCT may be actively deforming. A similar case occurs beneath regions of recent, continental extension.

In short, the main differences between typical continental and oceanic MCT's are that the transition beneath the continents can be much older and is more variable. Investigations of the boundary continue, and more insights into the MCT complexity have been uncovered in recent seismic surveys.

2.4.2 Seismic Images of the MCT

Although seismic methods are arguably the best geophysical tool for observing the MCT *in situ*, clearly the best constraints regarding the structural characteristics of the continental MCT come from coincident application of complementary methods, including seismic reflection/refraction studies, xenolith analysis, petrologic modeling, *etc.* Associated with any seismic study must be consideration of resolution. Vertical resolution of seismic reflection profiling is comparable to one quarter of the wavelength (λ) of seismic signal. For a V_P ~ 6.0 km/s and a frequency around 25 Hz, vertical resolution could be up to 60 m. Fresnel zone (horizontal resolution) is about 3 km at 30 km depth for such frequency range (Mooney and Meissner, 1992; Dobrin and Savit, 1988; Telford et al., 1985).

Normally, resolution is incorrectly assumed to increase with frequency. More correctly, resolution increases with signal band-width. In particular, one short-coming of reflection and to some extent refraction studies of the MCT are their lack of long-period signals, which would be more sensitive to smooth changes in velocity that produce no high-frequency response. The high-frequency signals in reflection data show sharp changes in structure but any discussion of broad variations must include other observations (such as diving waves, or longer-period body wave studies such as receiver functions). Other problems with reflection studies include the variability in signal quality from the deep crust caused by variations in signal amplitude resulting from differences in geometrical spreading, scattering, intrinsic attenuation, as well as near-surface complexity.

Comparison of synthetically derived seismic amplitude spectrum, amplitude variations with offset, waveform character, and travel time curves, suggest a structure that resembles a laminated arrangement with alternating lenses of high and low velocities as a plausible explanation for the MCT (e.g. Mooney and Meissner, 1992; Mooney and Braile, 1989; Hale and Thompson, 1982). Among the possible explanations for a laminated MCT are the presence of relatively undeformed metasediments in the lower-crust, cumulate layers after a mix of mantle-derived magma and lower-crustal rock, ductile deformation of rocks, lenses of partial melt and the respective crystallization products (Hale and Thompson, 1982). However, Larkin et al. (1997) pointed out that a rough MCT could generate a similar seismic reflection response as a velocity gradient which again complicates direct interpretation of high-frequency, narrow-band reflection and refraction observations.

Uniformity in data quality is also important for sound generalizations of seismic profiles. Hammer et al. (1997) re-examined trends in MCT structure inferred from previous seismic reflection/refraction studies using a modern, more uniform quality set of observations from the Canadian LITHOPROBE program. From these high quality data, Hammer et al. (1997) inferred a more complicated nature of the MCT than had previously been surmised from reflection and refraction profiling. Their conclusions suggest that the nature of the MCT is dependent on the tectonic history of the structure. They found that regions experiencing substantial crustal strain (extensional or compressional) were likely to have a sharp, strong signal to the MCT. However, their primary conclusion was that the variations in Moho reflectivity signatures are not simply correlated with tectonic age or geologic province.

2.4.3 Exposed MCT Cross-Sections

Metamorphic rocks from exposed sections assumed to equilibrate under pressure and temperature conditions comparable to those expected at the base of the continental crust may provide key information of the MCT environment. Seismic velocities and densities of samples from these complexes correlate with values determined for the lower-crust through geophysical observations (e.g. Percival et al., 1992; Fountain and Salisbury, 1981). Therefore, examination of exposed cross-sections of the continental crust can place valuable constraints on theories concerning the evolution of the MCT.

The dominant structural fabrics of exposed sections are sub horizontal, which probably result from a combination of processes including (Percival et al., 1992): 1) silt-like igneous transition; 2) compressional low-angle shear; and 3) extensional collapse or spreading. The idea of lower-crust growth through underplating is supported in places like the Ivrea zone, where nearly 17% of the crust section was

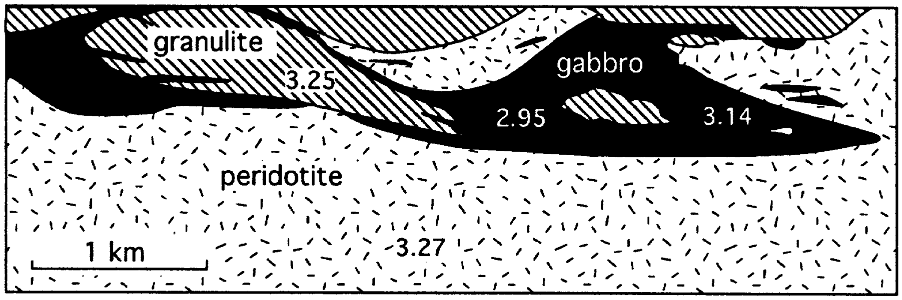

Figure 2.6 Sketch of the petrologic variations in the Val Malenco, Italy exposed section of the MCT. The boundary is complex and about one kilometer thick (From Herrmann *et al.*, 1997).

formed through underplating of magma derived from the mantle (Voshage et al., 1990). But alternative interpretations of exposed cross sections indicate that exposed cumulates may result from fractionation of mafic magmas ponded at the base of the crust, mafic and ultramafic cumulates would become part of the geophysically-defined mantle (Percival et al., 1992).

The most cited example of an exposed, continental paleo-MCT is the Ivrea Zone in the western Italian Alps, although recent work suggests that the feature is actually a fossil accretionary prism, not "typical" lower continental crust (Hermann *et al.*, 1997). Herrmann *et al.*, (1997) studied the Val Malenco exposure, also located in the Italian Alps, which they believe is more representative of a "typical" MCT. They observed a complex, at least one-kilometer thick transition from mafic lower crust to ultramafic, peridotite mantle. The Val Malenco transition (Figure 2.6) is composed of a mixture of dense pelitic granulite, gabbro, and peridotite (Hermann *et al.*, 1997).

In summary, the continental MCT is rarely exposed at Earth's surface and difficult to image in detail with indirect methods. The variability of the structure is significant and complicates our understanding its role in tectonics, history, and evolution of the continents. In view of the observed structural complexity, any effort at understanding the nature of the MCT must include consideration of the processes that are involved in the formation and modification of the transition.

2.5 Formation of the Continental MCT

The processes through which the continental MCT forms and evolves are a matter of current scientific debate. In continental arc regions, it seems obvious that these processes are very similar to those found in oceanic island arcs. However, fractionation processes are probably different beneath continental crust environments, because the chemical transition from mantle to crust environments will be strongly affected by the heterogeneity of the medium in anatectic processes.

After basalt fractionation at the critical pressure-temperature level, at the top of the mantle, the residual material cannot return to the deep mantle at the site of differentiation, because its density is lower and its resistance to deformation has increased by the elevation of its solidus through loss of volatiles. Therefore depleted mantle attaches to the lithosphere in the region surrounding the site of differentiation (Jordan, 1979). The fact that some ultramafic xenoliths and all mafic xenoliths recovered at some volcanic arcs (e.g. Adak region, Alaska) are undeformed, suggests that the deformation at these depths may be localized at the MCT (De Bari et al., 1987). Accordingly, hybridization is always likely to happen in strong compositional contrasts between crustal rocks and mafic magmas (McCarthy and Patiño-Douce, 1997). MCT formation in continental lithosphere could also be a process through which gabbroic rocks, at depths typical of the seismic Moho (~35 km), form garnet and sodic pyroxene at the expense of plagioclase and this process would lead to eclogitization (Hynes and Snyder, 1995).

Through the simulation of hybridization processes, a scale of about 10^3 m was assigned for the melt extraction and hybridization processes to take place at the MCT (McCarthy and Patiño-Douce, 1997). The crystallization sequence in gabbros at the Val Malenco region (Italian Alps) is consistent with crystallization at 1 – 1.2 GPa, which correspond to 35 – 42 km depth for the MCT at the time of gabbro intrusion (Hermann et al., 1997). Formation of the MCT by magmatic underplating and overplating will be accompanied by an elevated, strongly curved geotherm. This geotherm will decay when magmatic activity ceases and a conductive geotherm takes over, with a time constant around 10 Ma. (O'Reilly, 1989).

The thickness of the MCT is a function of the volume of emplaced material, since crustal addition is directly related to the volume of melt generated at the MCT, which depends on the amount that the temperature of the mantle surpasses the solidus and also the behavior of the involved material (Furlong and Fountain, 1986). Critical factors that affect crustal anatexis processes and MCT dimensions include temperature, enthalpy, rheological properties, and composition of rocks undergoing partial fusion (Raia and Spera, 1997).

2.6 Modification of the Continental MCT

The processes of modification of the continental MCT have a direct relationship with all those mechanisms of dynamic exchange between crust and mantle materials. The mapped structure of the MCT does not always reveal a direct correlation with surface geology structures, suggesting that the MCT can be a relatively young feature that may not be able to sustain deformation for long periods of time or is decoupled from upper crustal tectonics (Larkin et al., 1997). Although the MCT at accreted terranes can be structurally modified through terrane collision or slivering, the fundamental character of the transition seems to be ruled by igneous processes originated at the upper mantle (De Bari et al., 1987).

Some of the more relevant processes affecting the evolution of the MCT would include (Mengel and Kern, 1992; Arndt and Goldstein, 1989), (Figure 2.7):

- Influx of mafic magma from the mantle, accompanied with differentiation of this magma in the lower-crust and return to the mantle of ultramafic cumulates such as the intrusion of basaltic magmas at the base of the crust.
- Continent-continent collision, which induces lower-crustal mafic material to be transported deep enough to become eclogite-facies rocks. Former granulites and gabbros increase their velocities but still are not olivine dominated rocks; i.e. the petrologic crust-mantle boundary would be deeper than the mapped seismic Moho.

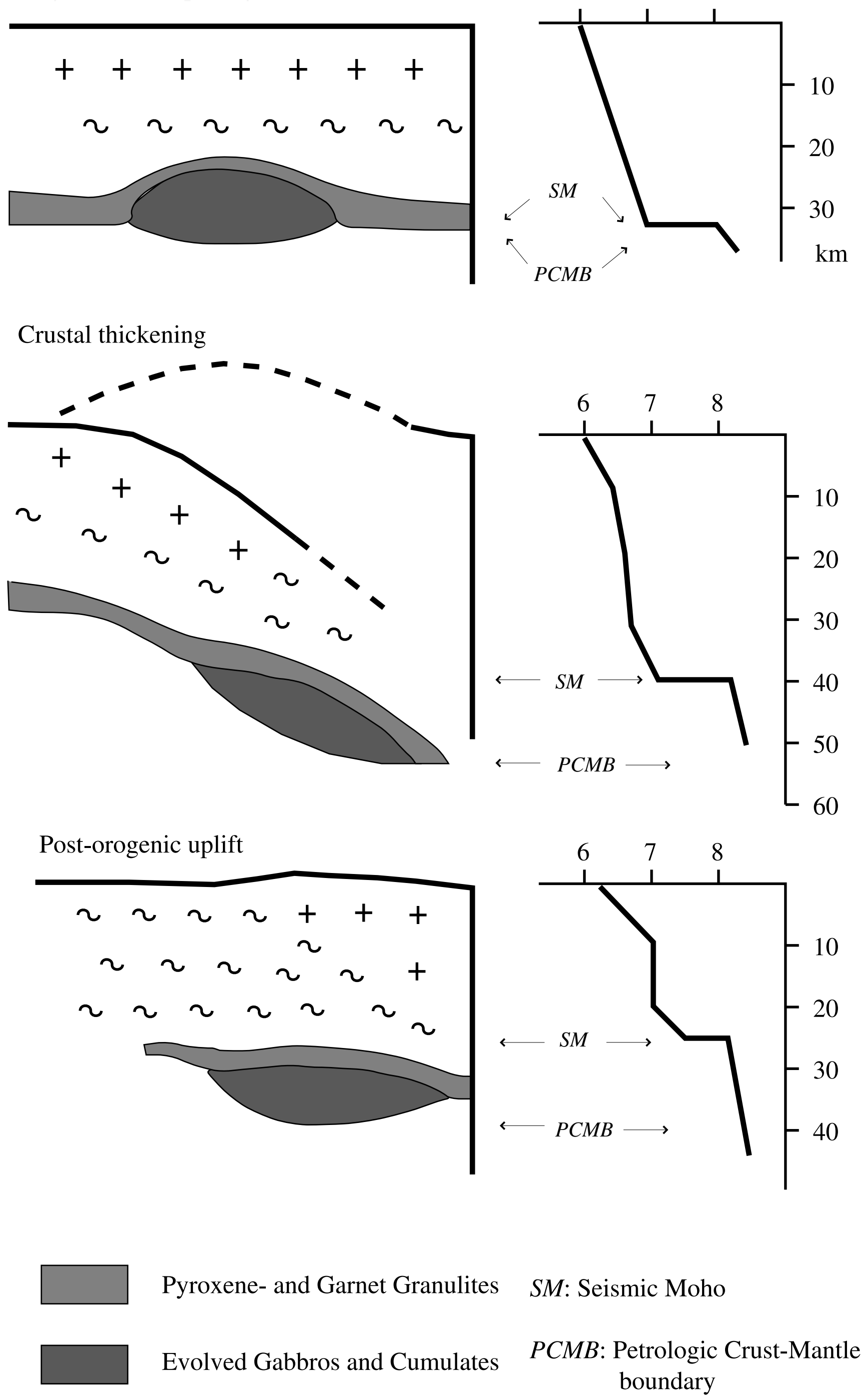

Figure 2.7 Schematic diagrams of the evolution of mafic lower crust during three main processes: Magmatic underplating, crustal thickening and post-orogenic uprise (modified after Mengel and Kern, 1992). At different stages the vertical transport of mafic granulites takes place together with gabbros and cumulates, creating and modifying the typical upper (+) and intermediate (~) crust materials. The correspondent *Vp* vs. depth sections change in response to different depths of mafic rocks of the lower crust, and show the different locations of the seismic Moho (SM) and the petrologic crust-mantle boundary (PCMB).

- Thermal and post-orogenic isostasy and thermal relaxation processes would induce the MCT to rise at “normal” depths but eclogite-facies assemblages are still preserved and the seismic Moho and petrologic crust-mantle boundary are at different depths. The former lower-crust mafic material transformed into eclogite may become detached and sink into the mantle.
- Generation of and/or return to the mantle of mafic restites left after the intracrustal melting that produces granitoid magmas; i.e. foundering.

In the following, I divide these processes in two major groups: 1) Mechanical processes, that take place as the product of mechanical interactions driven by tectonic and/or gravitational forces, and 2) Igneous processes, driven by interaction and/or generation of magma at the MCT environment.

2.6.1 Mechanical Processes

In general, three major mechanical processes can be identified: Collisional thickening, foundering and shearing. The first one, has a direct relationship to delamination mechanisms and is therefore discussed in the same context. Foundering is conceived as the product of transport of material through the MCT due to its negative buoyancy. Shearing at the base of the crust is a consequence of the stress regime throughout the lithosphere, but deserves a separate treatment because it may be induced either by tectonic or shearing motions in the upper-mantle, related to extension.

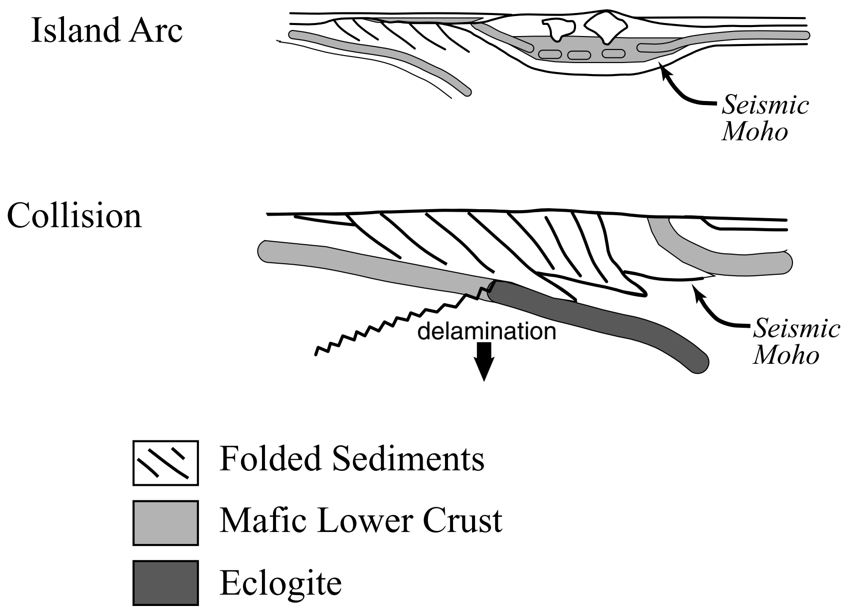

Figure 2.8 Illustration of the two main processes that drive collisional thickening and delamination and consequent modification of the MCT: Island Arcs and Collisions (modified after Nelson, 1991).

2.6.1.1 Collisional Thickening and Delamination

Collisional processes have severe implications for the evolution of continental lithosphere, such as (Nelson, 1991): a) Island arcs are amalgamated and form continents, in which case the MCT will separate ultramafic cumulate rocks and residual mantle; the seismic Moho would lie at a distance above the base of the crust, b) Lithospheric delamination removes mantle lithosphere and a portion of the lower-crust; the MCT will become topographic as well as compositionally complex, c) Over-thickened crustal welts become gravitationally unstable when tectonic forces relax and will collapse into the upper-mantle, the MCT would be a dubious feature before the crustal material is assimilated by the upper-mantle (Figure 2.8).

Delamination also denotes the separation of the mantle portion of the lithosphere beneath the collision zone and it may also involve a significant portion of the lower-crust, which may undergo eclogitization. This material becomes gravitationally unstable and tends to sink together with the mantle portion leaving a relatively silicic upper crust behind. Hence, delamination acts as a mechanical process that pushes the bulk composition of the continental crust toward intermediate composition (Nelson, 1991). Thus, delamination of lower continental crust may be an important process by which continental material is recycled into the convecting mantle, implying that the lower-crust must be mafic so it can transform into eclogite with a density exceeding that of underlying mantle (Rudnick and Fountain, 1995).

2.6.1.2 Foundering

Foundering is the differentiation of the crust caused by intracrustal melting and the separation of lighter, felsic magma from heavier, mafic cumulates (Arndt and Goldstein, 1989). Foundering may be a significant process for losing incompatible trace elements from continents due to interlayered evolved rock types within a mafic-dominated MCT (Rudnick and Fountain, 1995). Foundering takes place in a variety of environments, e.g. continental volcanism, orogenesis, island arc volcanism (Figure 2.9). The scale of crustal foundering through the MCT may be a significant contributor in growth process of crust. Indeed, crustal foundering is a plausible explanation for the reworking and refining of ascending mafic magmas in subduction and flood basaltic volcanism, where two stages may be identified: 1) Products of mafic differentiation segregate at the MCT and 2) Material left in the crust goes to partial melting and further crust-mantle segregation. The final end member of the process is felsic material, i.e. mature continental crust (Arndt and Goldstein, 1989).

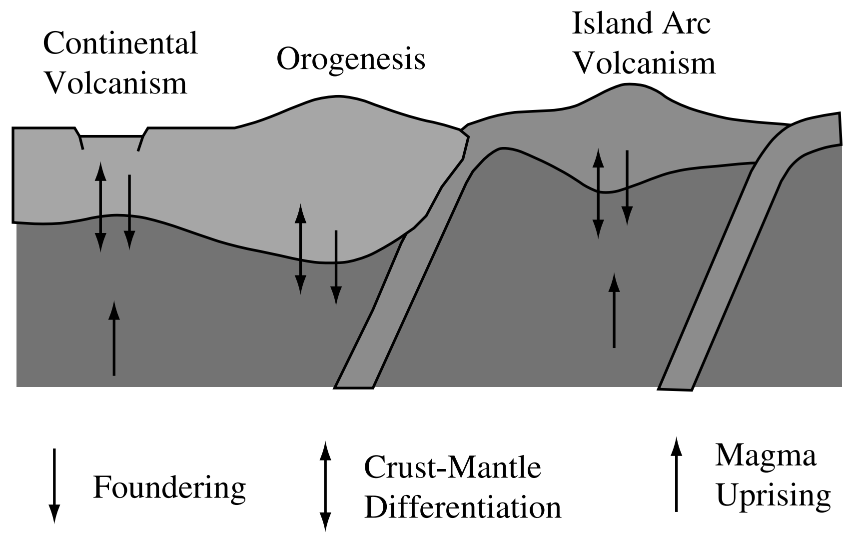

Figure 2.9 Cartoon illustrating where crustal foundering processes lead to formation and recycling of continental crust through the MCT (modified after Arndt and Goldstein, 1989).

Using the volumetric argument that the mass of granitoids seems to be less that the portion expected from their supposedly mafic source, it has been suggested that mafic restites left after intracrustal melting that produces granitoid magma founder and return to the mantle. A similar process may occur beneath magmatic arcs, where basaltic-picritic magmas interact with crustal rocks and, after relaxation of compression and erosion, the crust will return to normal thickness and residual mafic minerals with high densities will return to the mantle (Arndt and Goldstein, 1989).

2.6.1.3 Shear motions at the MCT

Deformation in the lower-crust and MCT cannot be separated from the deformation of the entire lithosphere. To assess the extent of strain within the lower-crust, whole lithosphere deformation must be considered and, in particular, the role of lower-

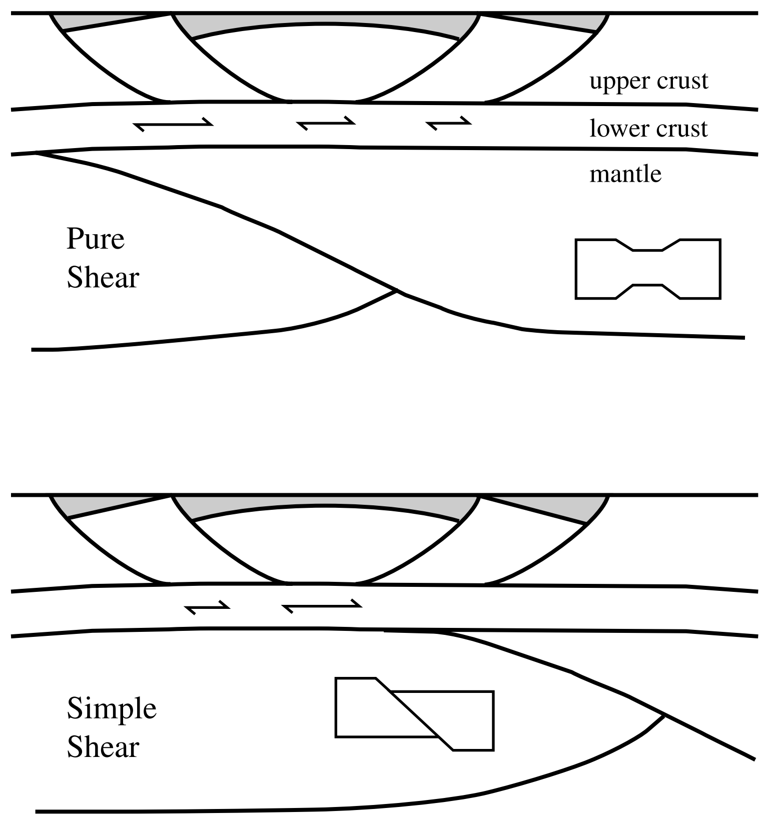

Figure 2.10 Simplified diagrams of lithosphere sections under extension. The upper sections is being deformed by bulk pure shear, whereas the lower sections is being accommodated by simple shear. The arrows show relative amount and sense of simple shear in the lower-crust which is also being stretched (modified after Reston, 1990).

crust in that deformation. Shear deformation in the lower-crust seems to be a combination of pure and simple shear, depending on the role of the lower-crust in the extension regime. However, both pure and simple shear seem to accommodate along localized zones of simple shear, which in places are a likely explanation for the seismic reflectivity of the lower-crust (Reston, 1990), (Figure 2.10).

Shear process at the base of the crust have been associated to extensional terranes, as well as collision zones. In both environments, processes other than shear motions have been demonstrated to have more relevance in the modification of the MCT, such as magmatic underplating and collisional related mechanisms (Warner, 1990). However, crucial questions about the relative contribution shear motions, size and shape of underplating, melt fractions, and instantaneous pervasiveness remain unanswered (Jarchow et al., 1993).

2.6.2 Igneous Processes

Extensive magmatic and metamorphic events in continental interiors occur when sub-lithospheric heat sources are focused for long periods of time in the same location. This effect, rather than being a continent-wide phenomena, suggests a localized source and in some cases uplift and fracturing precede volcanism (Anderson, 1989). For instance, frequent association of magmatism and continental extension, and the high elevation of some appreciably extended terrains (e.g. Basin and Range province) suggest that hot, less dense mantle and magma play and important role in the mechanics that rule temperature and strength regimes, and the most obvious indicator of massive magmatism may be its effect on buoyancy and elevation (Lachenbruch and Morgan, 1990).

The amount of melt generated around the MCT will depend on (Warner, 1990):

- Coincidence of lithospheric extension with high temperatures, which is not uncommon since nearly one-third of the globe's area has an asthenospheric temperature anomalously high.

- Small amounts of lithospheric extension would produce moderate amounts of melt with low viscosity, which could be rapidly emplaced in the continental crust.
- Thermal boundary layer at the base of the lithosphere may delaminate and founder immediately prior to any stretching episode.

The two major magma-related processes that change the configuration of the MCT are: underplating and metasomatism. The former has been recently presented as a major mechanism in continental growth and a feasible explanation for MCT structure. Metasomatism, is a very important dynamic process, related to migration of fluids, that may change the bulk composition of the region where it occurs, e.g. mantle enrichment.

2.6.2.1 Mafic Underplating

The process of underplating, i.e. the emplacement of mafic magma to the base of the crust, may be a factor in the growth and modification of continental crust (Furlong and Fountain, 1986). Geochronological studies have established that episodes of basaltic underplating correlate with major regional geological events, but also imply that significant underplating occurs without manifestation at Earth's surface (Rudnick and Fountain, 1995).

Underplating could take place in many environments, such as continental margin (calc-alkaline suites), localities of continental flood basalts, or near basalt-rhyolite volcanic suites (Furlong and Fountain, 1986). Simply put, basaltic underplating may occur anywhere that mantle upwelling is likely to generate mafic magmas; e.g.

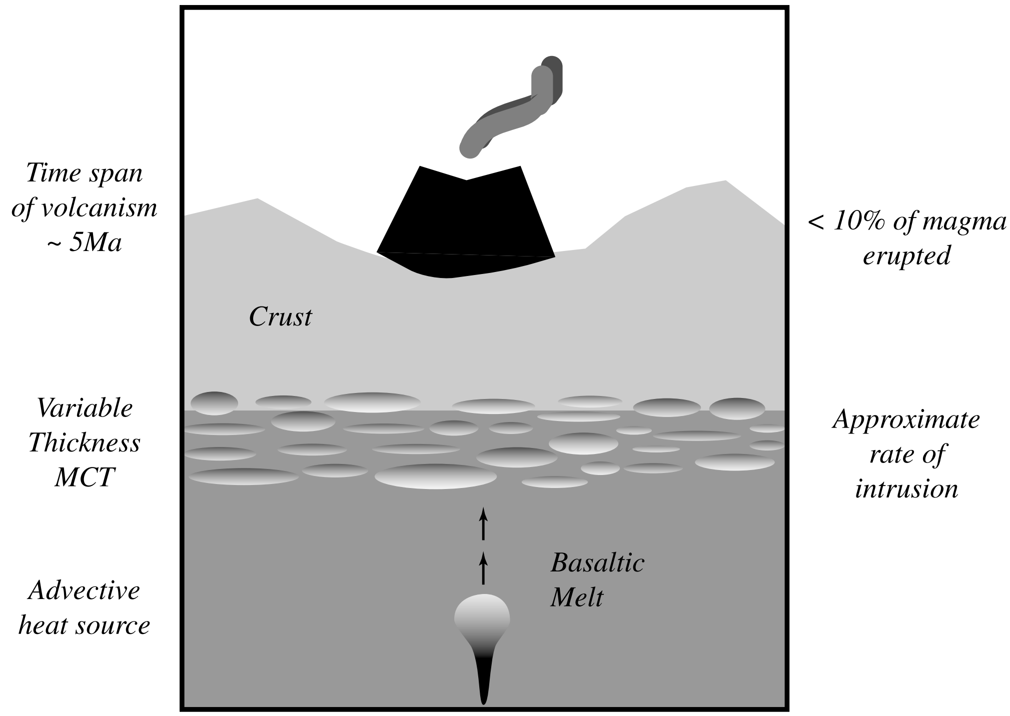

Figure 2.11 Cartoon showing the constraints provided by geological, xenolith and seismic evidence (right) that lead to infer the structures (left) that suggest the configuration of underplating at the MCT.

above subduction zones, continental rifts and/or intraplate settings (Rudnick, 1990), (Figure 2.11).

The most viable mechanisms that could cause magmatism leading to underplating are (Warner, 1990):

- Arc magmatism
- Rising mantle plumes
- Melting by adiabatic decompression following lithospheric extension.
- Delamination of an over-thickened and unstable thermal-boundary layer

Shallow (30 km) underplating can produce thick layers with mantle-like velocities. A deeper emplacement, on the other hand, will produce either mantle or intermediate lower-crust-upper-mantle velocities (Furlong and Fountain, 1986). The maximum MCT depth attainable through mafic underplating process may be limited by the gabbro/eclogite phase transition (~50 km). However, any subsequent magmatic addition would result in thickening of the MCT, but not deepening of the seismic Moho (Nelson, 1991).

2.6.2.2 Metasomatism

Metasomatism is the enrichment of magma by migrating fluids. Metasomatism can occur in magma chambers at or near the MCT and includes injection of mantle-derived magmas, which may occur in combination with melting and assimilation of lower-crust material (Voshage et al., 1990). The widespread presence of melt intrusions in ultramafic xenoliths, from several locations worldwide, indicates that mantle metasomatism is a general mechanism, related to the worldwide occurrence of acidic melts in the lithosphere (Schiano and Clocchiatti, 1994). Further, derivation from metasomatized mantle is an appealing concept to explain the chemical signature of continental flood basalts. The isotopic characteristics of some xenoliths from lithospheric mantle resemble lower continental crust, suggesting that material from the lower-crust finds its way into the mantle (Arndt and Goldstein, 1989), through the MCT.

2.7 Conclusion

In conclusion, the nature of the MCT is likely to be complex, varying from one tectonic province to another and within tectonic provinces. We have learned much from the few available exposed sections, and much from high-frequency seismic imaging. However, to date no one has performed a more systematic investigation of the boundary with longer seismic periods that will be more sensitive to the broad variations in structure and velocity changes. That is one of the goals of the work in this dissertation.

3 RECEIVER FUNCTIONS

Receiver function analysis is a straightforward approach to estimate the shear-velocity structure of the upper-mantle and crust beneath a three-component seismic station (Langston, 1979;1989). Although receiver functions can be defined for any wave, the most commonly used arrivals are teleseismic P-waves, which approach a seismic station with a relatively steep (< 25°) angle of incidence, and are well approximated with a simple plane-wave. Under these conditions, the vertical component of motion is much less sensitive to P-to-S conversions from sub-horizontal velocity contrasts in the underlying medium and contains predominantly near-source and lower-mantle propagation effects. The essence of receiver function analysis is to use the vertical component of motion to isolate the nearby receiver effects from the horizontal components of motion. The idea was first used by Phinney (1964) who modeled frequency-domain spectral amplitude ratios of teleseismic P-waves recorded at stations located in Albuquerque, New Mexico and Bermuda. Langston (1979) created the modern view of a receiver function when he used deconvolution and a time-domain analysis to study converted phases generated from structures beneath Mount Rainier, Washington. He called the process of isolating the receiver response from the observed seismograms “source equalization”. Several methods have been proposed for source equalization (*e.g.* Burdick and

Langston, 1977; Langston, 1979; Gurrola *et al.*, 1995; Sheehan *et al.*, 1995; Ligorría and Ammon, 1999).

In this chapter, I introduce the frequency-domain deconvolution method used by Langston (1979) and which has been widely applied to broadband data for determination of average crustal structure (*e.g.* Owens *et al.*, 1987; Mangino *et al.*, 1993; Randall and Owens, 1994; Langston, 1994; Cassidy, 1995). Also, I illustrate the application of receiver functions to the description of the mantle-crust transition, as it is the focus of a later chapter in this dissertation.

3.1 What Is A Receiver Function?

A receiver function is a time series consisting of the response of the velocity structure beneath the receiver station to an incident plane P-wave. Mathematically, it is the result of deconvolving the vertical component of the P-wavetrain from a horizontal component. In simple (plane-layered) media, the shape of a receiver function is similar to the radial component of displacement without the P-wave multiple (Langston, 1979; Ammon, 1991), and are characterized by signals of the direct P arrival, the P-to-S conversion at an interface m and the multiples of these (Figure 3.1). The amplitude and arrival times of phases in a given receiver function provide information about both the travel time from the interface to the surface (essentially the depth divided by the average velocity above the interface) and the character of the velocity contrast (its thickness and velocity change). A significant trade-off exists between the depth of an interface and the average wave velocity above it (Langston, 1979; Ammon *et al.*, 1990).

3.2 Receiver Function Estimation

3.2.1 Water-Level Deconvolution

Water-level deconvolution was introduced to seismology by Clayton and Wiggins (1976) and is a common approach used in seismic deconvolution problems, including receiver function analyses, empirical Green's function studies, and instrument deconvolution. Several descriptions of the application of water-level deconvolution to receiver functions are available in the literature (*e.g.* Mangino *et al.*, 1993; Cassidy, 1992; Ammon *et al.*, 1990; Owens, 1984; Langston, 1979). A thorough study and comparison of deconvolution methods, including the water-level method can be found in Oldenburg (1981). In this section, I briefly outline of the method.

The water-level method is a pragmatic solution to the often troublesome problem of deconvolution. In an ideal situation we could simply perform a complex division of Fourier spectra to compute a receiver function. However, noise in the observed

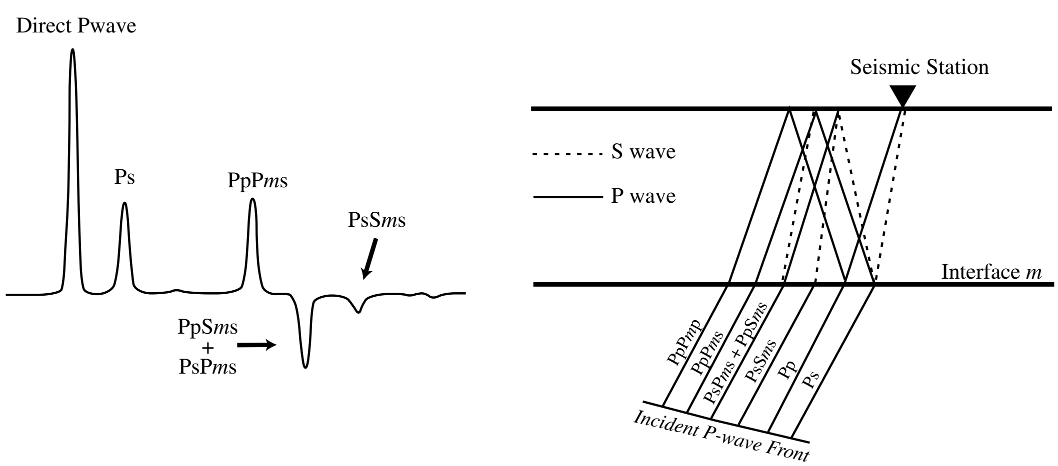

Figure 3.1 (Left) Radial receiver function generated by a simple layer over a half space. The nomenclature used to identify the arrivals is from Berteussen (1977). (Right) The paths for the converted (Ps) and multiples in the a simple model. Each interface in a model produces a set of similar arrivals that sum to create the complete receiver function.

signals or missing spectral content in the signal produce low-spectral amplitudes in the spectrum of the vertical seismogram. Dividing by small-amplitude values is numerically unstable. The essence of successful deconvolution is the stabilization of the quotient for values with small values in the denominator.

Water-level stabilization is simple. Never divide by small values. The response at frequencies where the vertical spectrum has a low amplitude is artificially attenuated by increasing the amplitude in the denominator. Specifically, in the frequency domain, the receiver function spectrum, $H(\omega)$, is obtained from the deconvolution of the vertical component, $Z(\omega)$, from the radial component, $R(\omega)$:

$$H(\omega) = \frac{R(\omega)Z^{\dagger}(\omega)}{\varphi(\omega)}G(\omega) \tag{3–1}$$

where

$$\varphi(\omega) = max\{Z^{\dagger}(\omega)Z(\omega), c \cdot max\{Z^{\dagger}(\omega)Z(\omega)\}\}, \tag{3–2}$$

and c is the water-level parameter. $G(\omega)$ is a Gaussian filter applied to reduce high-frequency noise amplified by the deconvolution.

$$G(\omega) = \exp\left\{\frac{-\omega^2}{4a^2}\right\} \tag{3–3}$$

where a, the Gaussian width parameter, controls the filter width. A useful rule of thumb would be that the Gaussian filter gain is 0.1 at a frequency about one half the value of the maximimum value of ω equal to three times the Gaussian width factor.

Clayton and Wiggins (1976) discuss the relationship between the water-level parameter and the trade off between amplitude resolution and arrival time resolution. If $c = 0$, the deconvolution is the best estimate of the true impulse response and provides the best arrival time resolution, but the amplitudes can have substantial variance. If $c = 1$, on the other hand, the deconvolution is the scaled cross-correlation of $r(t)$ and $z(t)$, and thus is a least-squares estimate of the true arrival amplitude at the sacrifice of arrival time resolution (Clayton and Wiggins, 1976; Owens, 1984). For most applications the value of c is chosen using visual inspection of the deconvolution stability. The choice is made to reduce the value of c and minimize the effects of the water-level on the solution.

3.2.2 Stacking

An optional process that has become standard practice in receiver functions analyses is the stacking of signals approaching the seismometer with a common back azimuth and slowness. The purposes of stacking are improving signal-to-noise ratio, smoothing differences in arrival amplitude due to slight changes in slowness, and reducing the contribution from local scattering. The imposed bounds for stacking data depend on the particular study, but one must consider (Owens *et al.*, 1983) that for a given change in epicentral distance the change in travel-time is least at larger distances, and that deep interfaces are least likely to be enhanced by stacking unless the events used are closely clustered in distance. To avoid the distortion of multiple arrivals by stacking, the selected clusters should be confined within a distance range of 15º for events with epicentral distance larger than 70º and this range should be kept to < 10º for closer groups of events (Owens, 1984). Cassidy (1992) recommended a back-azimuth bracket of ±10º.

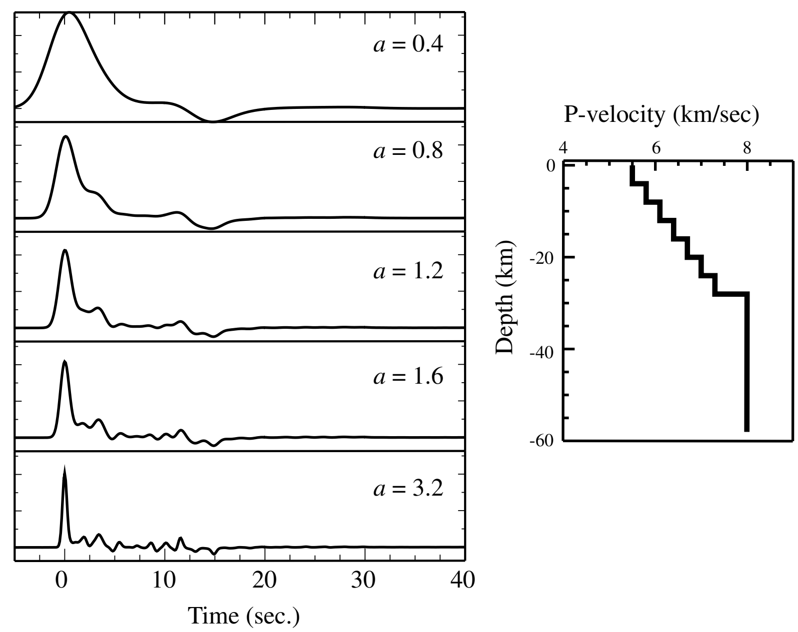

Figure 3.2 Variation of the radial receiver function as a function of Gaussian width parameter for a simple model consisting only of a gradient. See text for description.

3.3 Receiver-Function Interpretation

3.3.1 Receiver Function Frequency Analyses

By varying the pass band of the Gaussian filter used in the source equalization procedure, the receiver response at different frequency bands can be analyzed (*e.g.* Owens and Zandt, 1985). If the focus of interest is on broad velocity structure, scattering effects may be avoided by reducing the width parameter, a, in the Gaussian filter (Equation 3-3 on page 50) and looking at longer periods (Mangino *et al.*, 1993). This idea is illustrated in Figure 3.2 using a simple gradient velocity structure. As illustrated in the figure, while narrow-band receiver functions (*i.e.* $a \sim 0.5$) show only gross features, the broader bandwidths (*i.e.* $a \sim 1.0$) provide better resolution of the details of the structure. The interpretation of a broad-band receiver function is usually more complicated, but that's the price for estimating more details of the receiver structure. In general, the chosen Gaussian width parameter is a compromise between the signal-to-noise ratio and the extent of detail sought in the analysis. Later I use the Gaussian filter to explore the frequency dependence of the crust-mantle transition response while exploring for variations in the nature of the boundary between crust and mantle.

3.3.2 Receiver Function Inversion

I will use the method of Ammon *et al.* (1990) to estimate earth models needed to account for the effects of the near-surface on the arrivals generated at the crust mantle-transition. This inversion scheme incorporates an efficient calculation of differential seismograms developed by Randall (1989), and based on the reflection-matrix theory of Kennett (1983). The main limitation of the inversion algorithm is the assumption of flat-lying interfaces, and substantial non-uniqueness is likely using observations from a single station.

The relationship between the observed receiver function and the earth model is nonlinear, so the inversion is handled using a first-order linearization and iterative inversion (*e.g.* Jackson, 1972; Wiggins, 1972; Ammon *et al.*, 1990). The nonlinear relationship between the receiver function, d, and the velocity model, m, can be represented as

$$d = F[m] \tag{3–4}$$

where F is a nonlinear functional representing the computation of a receiver function. To estimate m, an initial model, m_0, is constructed and a first-order Taylor expansion about m_0, allows us to approximate (3-4) as

$$(D, \delta m)_j = F_j[m] - F_j[m_0] \tag{3–5}$$

where $(D, \delta m)$ is the inner product between D, the partial derivative matrix of $F_j[m_0]$, and the model correction vector δm. If we define $m = m_0 + \delta m$, then we can use

$$(D, m)_j = d_j - F_j[m_0] + (D, m_0)_j \tag{3–6}$$

to invert directly for m. The partial derivatives for the matrix D are estimated using a finite-difference approximation, implemented by Randall (1990), based on the propagator-matrix method of Kennett (1983). To stabilize the inversion I appended a smoothness constraint to the equations and minimize model roughness (Ammon *et al.*, 1990). The inversion is performed using a singular-value decomposition.

The residual vector, r (the observed receiver function less the predicted receiver function), is related to a vector of shear-velocities, m, by

$$\begin{bmatrix} D \\ \sigma\Delta \end{bmatrix} m \approx \begin{bmatrix} r \\ 0 \end{bmatrix} + \begin{bmatrix} Dm_0 \\ 0 \end{bmatrix}. \tag{3–7}$$

The matrix D contains partial derivatives of the receiver function with respect to the layer shear velocities, and the matrix Δ constructs the model roughness (second-difference). The parameter σ balances the fit to the data and the minimization of model roughness. The second term on the right is added to allow a direct solution for the shear velocities as opposed to a correction vector - the jumping algorithm of Parker (*e.g.* Constable *et al.*, 1987; Ammon *et al.*, 1990).

Shear-wave velocity is used because all the arrivals following the direct P-wave on the radial receiver function are shear waves or P-to-S converted multiples. Owens (1984) showed that the radial receiver function waveform is more sensitive to the shear-velocity than the P-velocity. While subsequent work has shown that this is a good, but not perfect observation (*e.g.* Zandt and Ammon, 1995), we retained the approach in this analysis because our primary interest in our inversions is in analyzing the frequency dependence of the MCT-generated waves, not estimating the detailed geology beneath the site.

Convergence of the algorithm is usually good, and assessing the large number of candidate models is usually much more trouble than finding an adequate fit of most reasonable-amplitude receiver functions. For examples and more details regarding the algorithm I refer the reader to Ammon *et al.* (1990). As used in this work, the inversion is a tool to help reduce the affects of the near-surface structure on conclusions drawn regarding the MCT. I conclude this chapter with an illustration of the receiver function analyses that form the basis of future chapters.

3.3.3 Receiver Function Lateral Sampling Range

Related to the simplicity of the structure is the range of structure sampled by a receiver function. The lateral distance sampled by a receiver function is roughly equal to the horizontal distance traveled by the deepest multiple arrival and is illustrated in Figure 3.3. This lateral distance is of course a function of how far back into the signal we look, but for typical crustal depths (~40 km), this multiple is recorded within approximately the first 20 seconds after the onset of the P arrival. In other

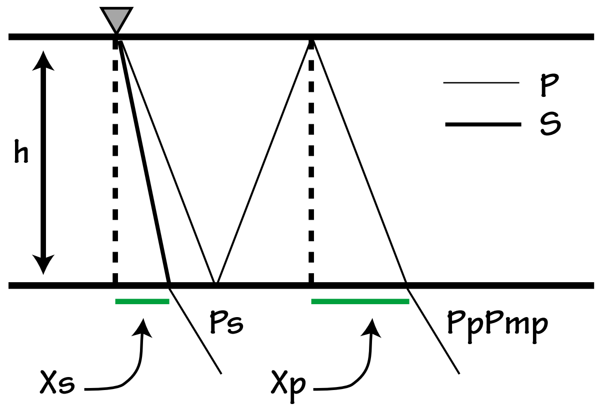

Figure 3.3 The lateral sampling of a receiver function can be estimated using Snell's Law to compute the path of the deepest sample interface. When multiples are included in the analysis the result is that the lateral sampling is roughly one to two times the depth to the interface.

words, the "multiples" portion of the radial receiver function sample an area of radius approximately one to two times the depth of the reflecting interface; for example, for deep crustal boundaries (~ 35 – 50 km) the total lateral extent is about 70-120 km (Cassidy, 1992).

Since the assumption of a laterally-homogeneous, horizontally-layered, velocity structure is an obvious idealization of a more complicated reality, both radial and transverse receiver functions are computed, although the interpretation process is focused on the radial receiver function. For simple, sub-horizontal structures, the transverse receiver function amplitudes are small (*e.g.* Langston, 1979; Ammon and Zandt, 1993). The effect of lateral complexities (*e.g.* major structures, dipping interfaces) is moderate on the vertical component of motion which is dominated by the steeply incident P-wave. In most instances, variations with back azimuth are observed in the radial component, but the most dramatic effect of heterogeneity is the production of a distinct and complicated transverse signal (*e.g.* Mangino *et al.*, 1993; Cassidy, 1992; Langston, 1977) which often varies strongly with incident angle and P-wave back azimuth.

3.3.4 Limitations of Receiver Function Analysis

The usual problem faced in receiver function studies is the contamination of radial receiver functions by scattered signals. Fortunately the transverse receiver function amplitude is a direct and easy-to-compute measure of the scattering (*e.g.* Cassidy, 1995; Ammon and Zandt, 1993; Cassidy, 1992). Complications in the interpretation caused by scattered waves can be reduced by stacking different receiver functions arriving from slightly different azimuths and epicentral distances (Ammon, 1991). With observations from a single station, there is little you can do to constrain lateral variations in structure. For the simplest heterogeneity like dipping layers some systematic variations with azimuth provide some constraints on the dip and velocity contrast of the interface (Langston, 1979). When heterogeneity is large, stacking observations from all azimuths may enhance the part of the signal generated from sub-horizontal interfaces (Hebert and Langston, 1981).

Large velocity variations are usually well constrained by receiver function analyses, but broad velocity transitions are not easy to resolve (Cassidy, 1992). Further, even with well-resolved features, a significant compromise exists between the velocity above the discontinuity and the depth to the interface (Ammon *et al.*, 1990). This limitation is a consequence of relative travel time constraints combined with a limited range of seismic arrivals suitable for the technique.

3.4 Receiver Functions and the MCT

3.4.1 A Numerical Example

In relatively simple areas, the receiver function is dominated by wave interactions near Earth's surface and at the crust-mantle transition. In a later chapter I use observed receiver functions for stations throughout North America to explore for systematic variations in the thickness of the crust mantle transition. Obviously important then is how a change in mantle-crust transition thickness affects a receiver function. The key to the resolution of velocity transition thickness is band-width (Owens and Zandt, 1985).

To illustrate the ideas, consider the receiver functions shown in Figure 3.4. For a sharp contrast, the converted waves are broad-band and visible even at high frequencies. The broad transition is visually indistinguishable from the sharp contrasts at long-periods, but produces little high-frequency response. Careful study of the figure also reveals that the Ps converted wave pulse width and amplitude is also sensitive to the change. In fact, because the multiple arrivals sample the MCT twice, they are more strongly affects by a transition feature than the converted Ps wave. For example, if you study the response at periods below 0.25 hertz, you see that the ratio of amplitudes of the multiple and converted phases differ for the different thickness transitions. The effect is subtle, but allows us to use both the broadband aspects and the amplitude ratios and longer periods to estimate the velocity transition thickness. Using the amplitude ratio is important because it allows us to use longer-period

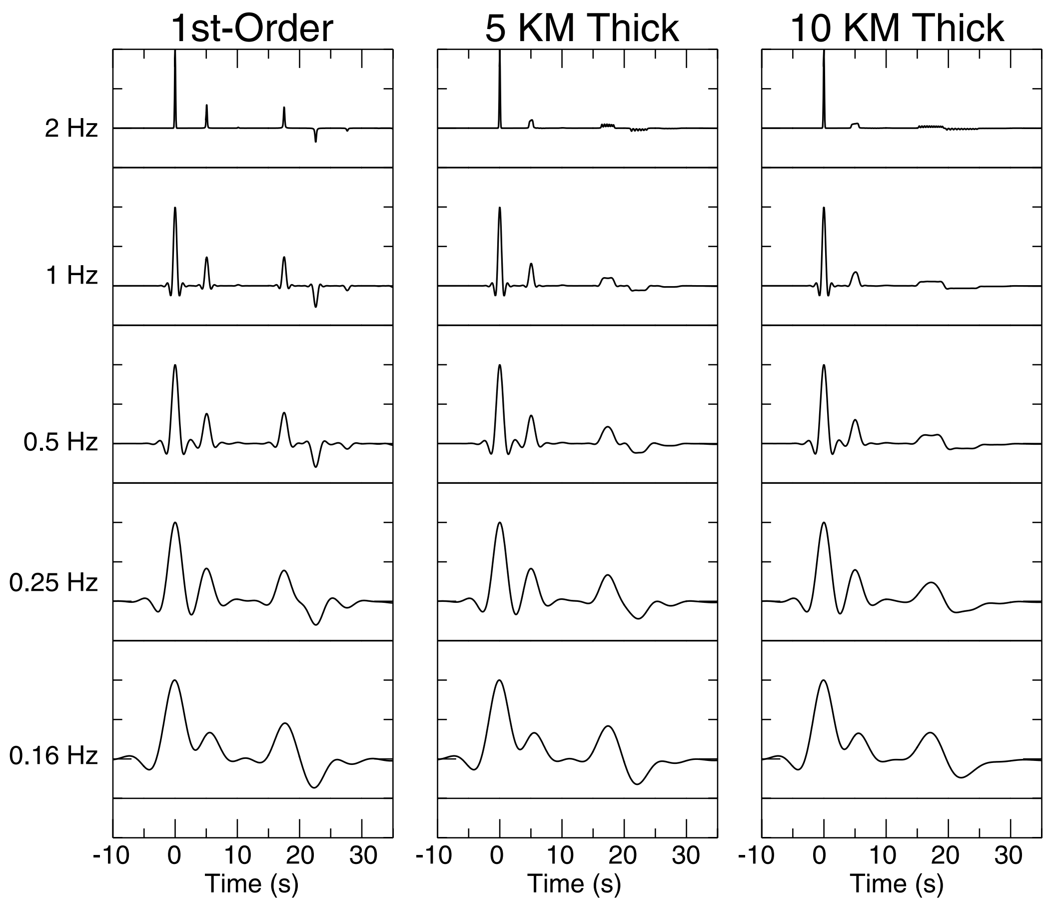

Figure 3.4 Receiver function response as a function of velocity transition thickness and frequency. Each panel shows the radial and tangential receiver functions in five band-widths - the low-pass filter corner frequency is indicated to the left of each pair of traces. The upper trace is the radial, the zero trace is the tangential. First-order indicates a velocity step. The sharper the interface the broader band are the converted waves. For the broad transition, the high-frequency receiver functions show little evidence of the feature.

receiver responses, which may be less affected by scattering than those at short-periods.

To investigate the potential of amplitude ratios more thoroughly, I simulated a set of receiver functions using a Gaussian factor of 1.0, for a set of different thickness MCT's. The Gaussian factor of 1.0 produces longer period receiver functions than are usually used in analyses, but which are likely to be less contaminated by scat-

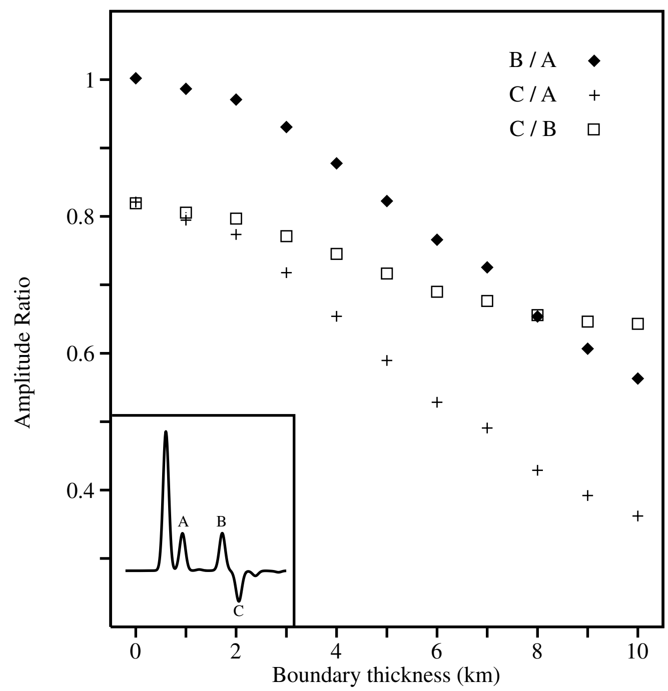

Figure 3.5 Three amplitude ratio estimates of the more prominent signals of a synthetic receiver function (inset), for different thicknesses of an MCT-like boundary. A Gaussian width factor of 1.0 is used for all signals. The test shows the sensitivity of the technique to changes in the discontinuity thickness larger than 2 km.

tering from small-scale heterogeneity. Amplitude ratios for each of the arrivals commonly observed in receiver functions were computed for the synthetic seismograms and are shown in Figure 3.5. The results of this test illustrate that the ratio of the amplitude of the PpPms arrival to the amplitude of the Ps (B/A in Figure Figure 3.5), as is the ratio of the amplitude of PpSms+PsPms to the amplitude of Ps (C/A in Figure 3.5, see Figure 3.1 for ray definitions). The ratio varies by up to 40-50% for a range in thickness of 10 kilometers. Generally the two easiest to identify arrivals in a receiver function are the Ps and PpPms waves, so we selected those for use in our analyses.

Although the example is oversimplified by using a single-layer over a half-space velocity structure, it illustrates the sensitivity of receiver functions to variations in MCT thickness. Variations in MCT width less than 2 km are difficult to assess, but changes of more than 2 km show 30% to 60% amplitude-ratio variations which should often be resolvable. Before continuing with an example using actual observations, we point out that the resolution from this method is likely to be on the order of two kilometers. Although we desire a better resolution, measurements with this lower resolution are likely to be more reliable since we use lower-frequency observations which are less contaminated by scattering. In some instances we, or others, may achieve higher resolution, but for the survey study discussed later, we focus on the resolution that we can achieve with routine processing.

The heterogeneous nature of the environment surrounding the MCT and that near Earth's surface precludes the analysis at high frequencies (> 1.5-2 Hz). For this reason, a qualitative comparison with synthetic data would provide the best estimate of MCT thickness. To do so, after the selection of best signals for a particular site, the data are inverted to estimate a gross model from an overall stacked receiver function. This gross model is then used as a reference for the correspondent MCT amplitude-ratios plot, which is constructed for different frequency content (*i.e.* values of a), as well as slowness values. The velocity model is also used for the further estimation of synthetic receiver functions that are visually compared with the observed receiver function stacks.

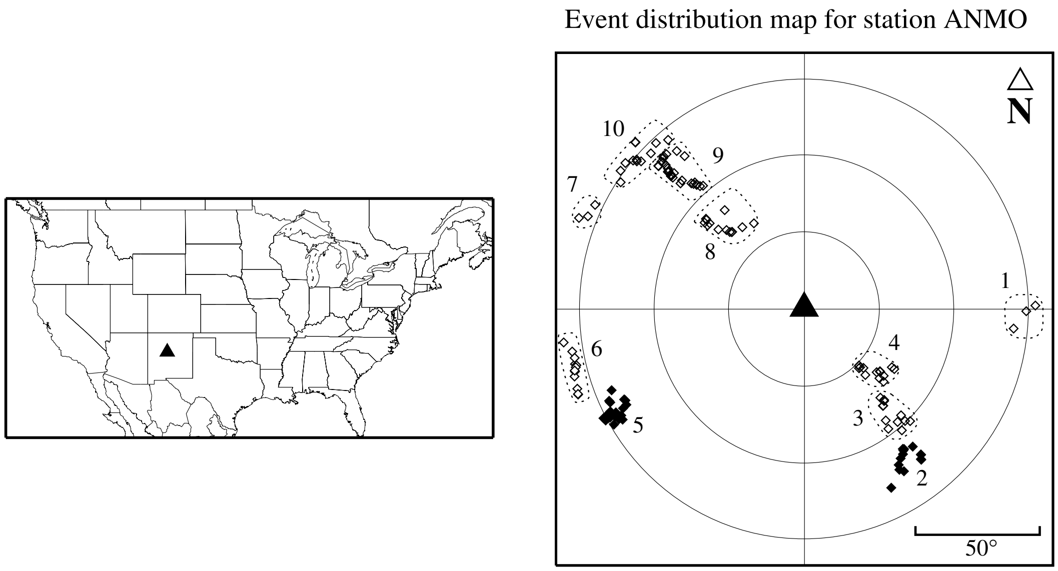

Figure 3.6 (Left) Location of station ANMO, Albuquerque, New Mexico. (Right) Distribution of P-wave used in receiver function analysis of ANMO. Each point represents a receiver function estimate. The location of the point shows the azimuth from the station to the event (back azimuth) and the epicentral distance. The events are grouped into azimuth and distance clusters for analysis.

3.4.2 An Application - Station ANMO, Albuquerque, NM

To demonstrate the suitability of the receiver functions technique for this study, I present an example of the receiver functions calculated for station ANMO, Albuquerque, New Mexico (Figure 3.6). Station ANMO is situated on Pennsylvanian and later sediments overlying a Pre-Cambrian basement (Padovani and Carter, 1977). The main regional tectonic feature is the Rio Grande Rift which is associated with a broad region of negative gravimetric anomalies in the western United States (Hanna *et al.*, 1989). To the east of the Rift is the southernmost part of the Great Plains and, to the west, the Colorado Plateau (Bally *et al.*, 1989). Seismic events with magnitudes greater than 6, with epicentral distances from ANMO between 30° and 95°, and recorded between 1990 to 1997, were collected and receiver functions were computed. The data consist on P-wave arrivals from 119 events, including sources located to different azimuths of the station: southeast (37 events, clusters 1-4), southwest (27 events, clusters 5-6) and northwest (55 events, clusters 7-10) (Figure 3.6).

To reduce interference from the shallow structure on the MCT thickness estimate, a time-domain inversion was performed to estimate the “average” structure appropriate for station ANMO. All the receiver functions were stacked, regardless of their azimuth and distance. The resulting average receiver function is shown in Figure 3.7. An initial model based on the average structure of the rift was used to start the inversion and the resulting shear-wave structure is shown in Figure 3.7. It contains a shallow low velocity zone (between about 2-10 km) and a crust-to-mantle velocity contrast approximately six kilometers thick (Figure 3.7). No interpretation the structure is made because we only seek a model suitable for partially accounting for near-surface affects on the MCT thickness measurements (I’ll be doing a similar analysis for more than one hundred sites across North America).

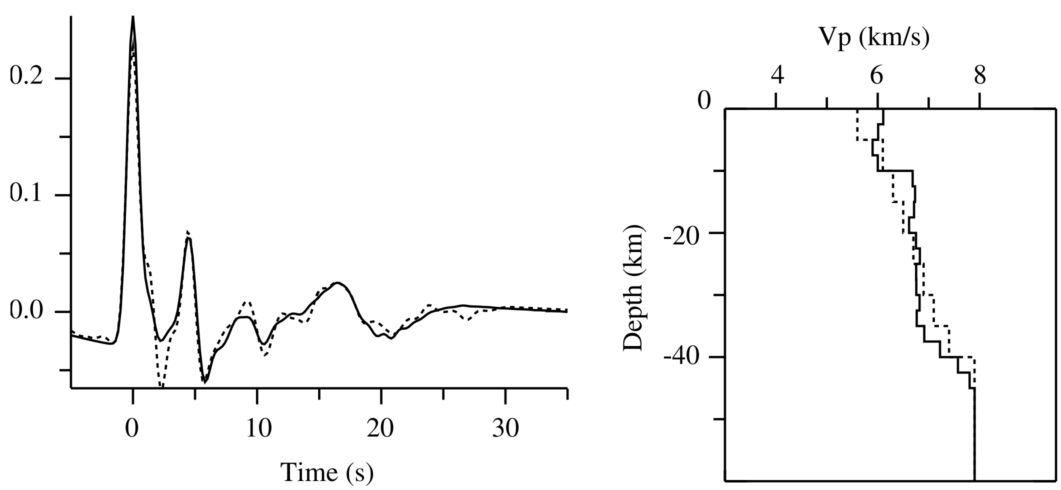

Figure 3.7 (Left) Receiver function stack of all observations (dashed line), regardless of azimuth and distance compared with the prediction (solid line) resulting from a linearized time-domain inversion. (Right) The initial (dashed) and final model from the inversion.

At this stage the receiver functions were grouped into clusters that have similar back-azimuths and incidence angles, or horizontal slownesses (Figure 3.6). The observations from different directions and horizontal slownesses were analyzed separately to produce an estimate of the thickness for each incident wave direction. We explored the MCT thickness by appending different MCT thicknesses beneath the upper-crustal model to prepare MCT amplitude-ratio curves appropriate for each distance for which we had observations. Then the observed amplitude-ratios of the PpPms to Ps phases were measured and plotted on the MCT amplitude-ratio diagrams. We performed calculation for three bandwidths corresponding to Gaussian width factors of 1.0, 1.5, and 2.5, and P-wave horizontal slowness values of 0.04, 0.05, 0.06 and 0.07 s/km. Horizontal slowness, or ray parameter is related to the incidence angle of the wave by Snell's Law ($p = \sin i / \alpha$, where α is the P-velocity and i is the wave incidence angle). Values of the ray parameter for teleseismic P-waves are available from standard travel time tables, once the earthquake location is known.

Individual receiver function stacks were computed for the 10 clusters and PpPms / Ps amplitude-ratios were calculated for each cluster's stack. Each amplitude ratio was compared with a theoretical amplitude ratios computed using the shear-velocity structure from the inversion and using the appropriate horizontal slowness. In practice, we found it helpful to visually compare a synthetic receiver function calculated using the estimated MCT thickness with the observed (stacked) receiver function. Visual comparison is subjective but can often identify the quality of the estimate by considering many factors such as the overall complexity of the receiver

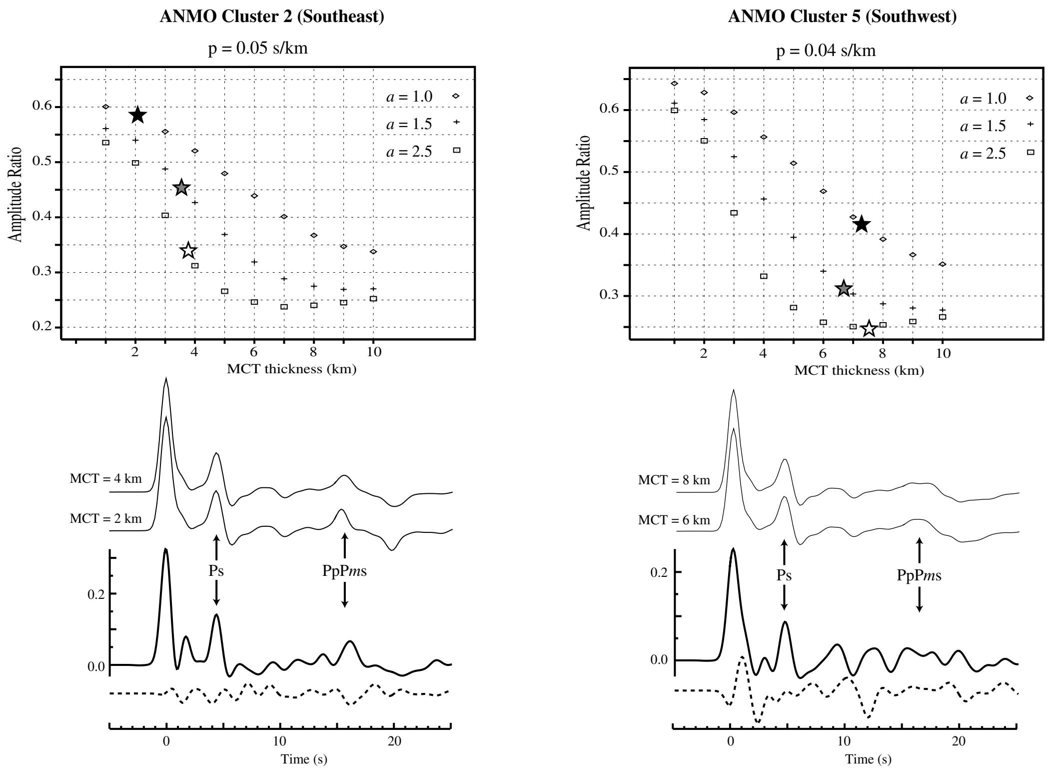

Figure 3.8 MCT receiver function analysis for clusters 2 (left) and 5(right), station ANMO (solid diamonds in events map of Fig. III.8). The MCT amplitude-ratio diagrams (upper plots) are obtained from the velocity structure inverted from a stack of all receiver functions (see text for explanation). The observed ratios of the amplitudes of the Ps and PpPms phases are also plotted as stars for three different values of Gaussian filters width a (black star =1.0, grey star=1.5 and white star =2.5). Synthetic radial receiver functions (thin traces in the middle) for the estimated MCT thickness range (2-4 km for cluster 2 and 6-8 km for cluster 5) are compared with the observed signals (solid curves in the bottom) for confirmation of the MCT thickness assessment. The waveforms were computed using a Gaussian width factor of 2.5. The transverse receiver functions (dashed curves) are also displayed as a qualitative measure of the level of scattering in the structure beneath the station.

function and the size of the tangential receive function, which is a direct measure of complexity.

Figure 3.8 is a summary of the results obtained for clusters 2 (southeast) and 5 (southwest) at station ANMO. The MCT amplitude-ratio plots for slowness values of 0.05 and 0.04 are presented at the top. The stars identify the observed measures, the diamonds, crosses and squares identify the theoretical values. Each diagram shows the measured ratios using Gaussian widths factors of 1.0, 1.5 and 2.5. The thickness of the transition can be read off the chart. Beneath the amplitude ratio diagram are predicted receiver functions computed using transition thickness values that bracket the measured ratios. Below that diagram are the stacked radial and tangential receiver functions, calculated using a Gaussian width factor of 1.5. The synthetic/observed match is never perfect - the idea here is to focus only on the MCT arrivals since the velocity structure used to calculate the predicted waveforms is an average of a laterally varying structure.

The results on the left suggest that the MCT to the southeast of ANMO is relatively sharp, on the order of 2-4 km thick. Support for this conclusion is available in the observed receiver function, which has a large, strong Ps conversion and an easily observable PpPms arrival. Although the timing of these waves on the predicted waveforms for 2 and 4 kilometer transition thickness is not perfect, the main character of the arrivals is reproduced well. One might suggest that an even sharper MCT may be present based on the narrowness of the Ps converted phase (compared with the predictions) on the observed radial receiver function. Finally, note the small amplitude of the scattered wavefield as illuminated by the modest-amplitude tangential receiver function. This is a high-quality measurement.

The implications for the southwest are more complicated because the observed signal is more complicated. First, note the tangential receiver function contains two relatively large, but distinct arrivals. The first appears to be associated with near-surface structure to the southwest of ANMO, the latter shows up later and ascertaining its source is impossible with data from a single station. Still, the MCT associated waves on the radial component arrive at different times than these scattered waves, so we proceed with the analysis. In this case, the PpPms arrival is difficult to identify - we only really know that no larger arrival exists. Our measurements of the amplitude ratio in the region therefore represent maximum values. The results suggest a value of MCT thickness between 6 and 8 kilometers. The comparison of the observed and predicted receiver functions is not bad, but a detailed assessment is difficult. Again, the width of the observed Ps is narrower than the predicted, suggesting that the measurement may be over-estimating the true thickness. One possibility is that lateral variation of the MCT is causing a sharp Ps and a broad PpPms arrival. If this is the case, our estimate of MCT thickness will lie between the two extremes, perhaps closer to the thicker transition, since the PpPms multiple amplitude is more sensitive to the transition than is the converted Ps phase.

Considering the surrounding tectonics, these observations suggests that igneous activity in the Rio Grande rift may have left it with a thicker MCT structure compared with structures immediately east of the rift (southeast of ANMO). The example also illustrates potential problems with our approach. For example, the amplitude ratios are susceptible to noise and at time can be difficult to make. Clearly the method will not work at every station and every azimuth. However, only a substantial survey will indicate the potential of the approach. My application of this analysis method to waveforms recorded at more than one-hundred seismic stations distributed across North America is described later in Chapter 7. As work progressed on this project it became clear that an additional tool in receiver function analysis, a broad-band iterative deconvolution method applied to receiver function analysis would help make more accurate measurements. In the next chapter, I describe this iterative, time-domain approach to receiver function estimation.

4 ITERATIVE DECONVOLUTION APPLIED TO RECEIVER FUNCTION ANALYSIS

Receiver-function analysis (*e.g*. Langston, 1979) is a straightforward, simple method of extracting constraints on crust and upper-mantle structure from teleseismic waveforms recorded at three-component seismic stations. A receiver function is the time series that when convolved with the vertical-component seismogram reproduces the horizontal-component seismogram and the timing an amplitude of the arrivals in the receiver function are sensitive to the local earth structure (Langston, 1979). Langston (1979) pointed out that the basic characteristics of receiver functions, perhaps most impressive is the clean, causal, seismogram-like signal that results from the deconvolution of the vertical from the radial response of a plane-layered structure. The simplicity of the method assures it is a routine component of analyzing observations from permanent network stations and portable stations deployed as part of passive-source temporary networks. The wide application of the technique has produced several complete descriptions of the receiver-function methodology (*e.g*. Langston, 1979; Owens, 1984; Ammon *et al.*, 1990; Ammon, 1991; Cassidy, 1992; Mangino *et al.*, 1993).

Computing a receiver function is a deconvolution problem, the reader may refer to Oldenburg (1980) for a comprehensive discussion of deconvolution methods. The most commonly employed method in receiver-function studies is a water-level stabilized, frequency-domain division (*e.g*. Clayton and Wiggins, 1976), described in the previous chapter, although others have used time-domain approaches (*e.g*. Gurrola, 1995; Sheehan *et al.*, 1995) based on linear inverse theory. When the data are wide-band with good signal-to-noise levels, most deconvolution methods work well and the advantages of one technique over the other are insignificant. Thus, often the best approach to compute receiver functions for permanent stations with years of data available is simply to exploit signals from large events. However, for select azimuths at most permanent stations and in the case of most temporary deployments, we never have enough observations from all azimuths and we must incorporate signals from smaller events, which leads to difficult deconvolutions and noisy receiver functions. Then the choice of a deconvolution technique may make a difference.

In this chapter, another tool in the receiver-function toolbox is investigated, an iterative time-domain deconvolution commonly used to estimate large-earthquake source time functions (Kikuchi and Kanamori, 1982). The iterative time-domain approach has several desirable qualities such as a constraint on the spectral shape at long periods that can be advantageous in receiver-function analyses and an intuitive stripping of information from the original signal, garnering the largest, most important features first, and then extracting the details. The mathematical basis of the approach is clearly described in Kikuchi and Kanamori (1982) and is summarized in the following section.

4.1 Receiver-Function Iterative Deconvolution

In receiver-function estimation, the foundation of the iterative deconvolution approach is a least-squares minimization of the difference between the observed horizontal seismogram and a predicted signal generated by the convolution of an iteratively-updated spike train with the vertical component seismogram. This discussion is conducted in terms of the radial receiver function but the approach is equally applicable to the transverse motion and can be easily generalized to accommodate simultaneous deconvolution of any number of signals.

The basis of the approach is to minimize the difference between an observed signal and the synthetic signal generated by the iterative convolution of a spike wavelet train with the unperturbed response of the propagating medium. For our case of interest, the spike wavelet train seek is the receiver function, *h(t)*, which is convolved with the vertical component of motion, *v(t)*, to obtain the radial component of motion, *r(t)*,

$$r(t) = h(t) * v(t), \tag{4–1}$$

where * represents the convolution operator. In the iterative deconvolution process, we obtain an iterative receiver function, $h_i(t)$, that will be equivalent to *h(t)* if the misfit between *r(t)* and the convolution of $h_i(t)$ with *v(t)* is below a preset tolerance level.

First, the vertical component is cross-correlated with the radial component to estimate the lag of the first and largest spike in the receiver function (the optimal time is the largest peak in the absolute sense in the cross-correlation signal). To construct $h_i(t)$, we add a series of time lagged Gaussian pulses with form in the frequency domain,

$$G(\omega) = \exp\left(\frac{-\omega^2}{4a^2}\right) \tag{4–2}$$

Then the convolution of the current estimate of the receiver function with the vertical component seismogram is subtracted from the radial component seismogram, and the procedure is repeated to estimate other spikes lags and amplitudes. With each additional spike in the receiver function the misfit between the vertical-and-receiver-function convolution and the radial-component seismogram is reduced and the iteration halts when the reduction in misfit with additional spikes becomes insignificant.

To estimate the misfit, a weighted norm is applied, using the sum of the square values of r for the scaling of a residual vector between and $\hat{r}(t)$. Hence, the scaled error (ε) of the j-th iteration of the process is

$$\varepsilon_j = \frac{\sum_i (r_i - \hat{r}_i)}{\sum_i (r_i)^2} \tag{4–3}$$

where

$$\hat{r}(t) = h_i(t) * v(t) \ . \tag{4–4}$$

The misfit is defined as

$$100 \times (\varepsilon_{j-1} - \varepsilon_j) \tag{4–5}$$

where

$$\varepsilon_1 \equiv 1.0 \ . \tag{4–6}$$

The approach is introduced in the following sections using several numerical examples followed by examples that include short-period and broad-band observations.

4.2 Numerical Experiments

The synthetic tests begin with two simple layer-over-a-half-space models – one with a sharp boundary and one with a smooth transition from a crust-like layer to a mantle-like half space. The third example is constructed using a more complex velocity model based on the refraction wide-angle reflection results of Benz *et al.*, (1990). In each case, the synthetic seismograms were computed using the method of Randall (1989), that is based on the propagating-matrix technique of Kennett (1983). The seismograms were computed to correspond to a P-wave arriving with a horizontal slowness of 0.06 s/km, equivalent to a shallow source about 60° distant. The results shown in Figures 4.1 and 4.2 include a comparison of the iterative time-domain with a water-level receiver function estimate. In each case the receiver functions computed using Gaussian width factors of 1.5 and 2.5 are shown. The Gaussian width factor controls the bandwidth of the signal, the larger the value, the larger the bandwidth (2.5 is a value commonly used in receiver-function analyses). Also in each case we allowed iteration to continue until the change in fit resulting from the addition of a spike was 0.01%.

For the sharp contrast model (Figure 4.1), each significant arrival is accurately recovered by the iterative method, for the smooth-transition model, the response is recov-

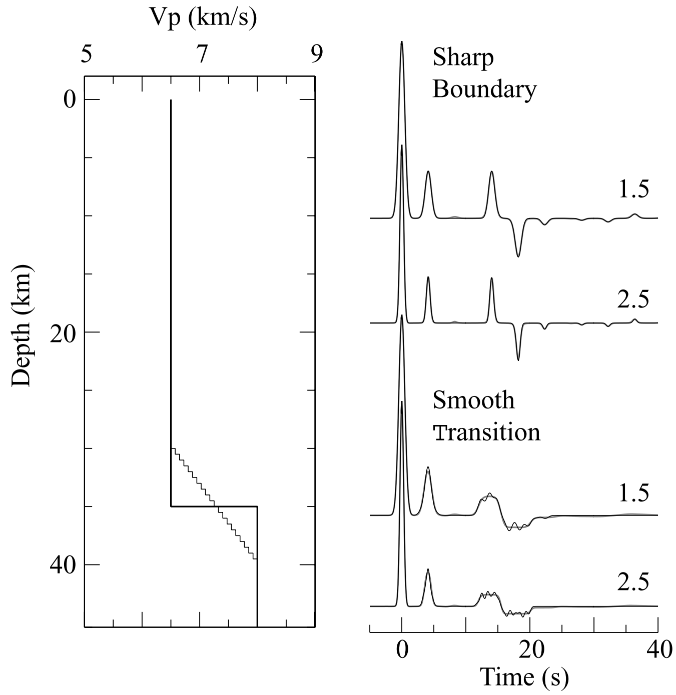

Figure 4.1 Comparison of frequency-domain (water-level) and iterative time-domain deconvolution results for two receiver responses with contrasting frequency characteristics. The estimated receiver functions are plotted on top of each other for two Gaussian pulse widths (shown above the right edge of the signals) for each model.

ered well, but not perfectly. Although noticeable in the time-domain signals, the differences in the receiver function estimates are limited to the frequencies above approximately one Hertz, and are a result of the Gaussian filter width selected for the process. Such details are inaccessible with even a modest amount seismic noise ubiquitous in observed seismograms, so these minor differences pose no problem for analysis.

In Figure 4.2 the iterative time-domain and frequency-domain approaches for a more complex velocity structure are compared. The variation of velocity with depth is shown on the left, and the iterative construction of the radial receiver function esti-

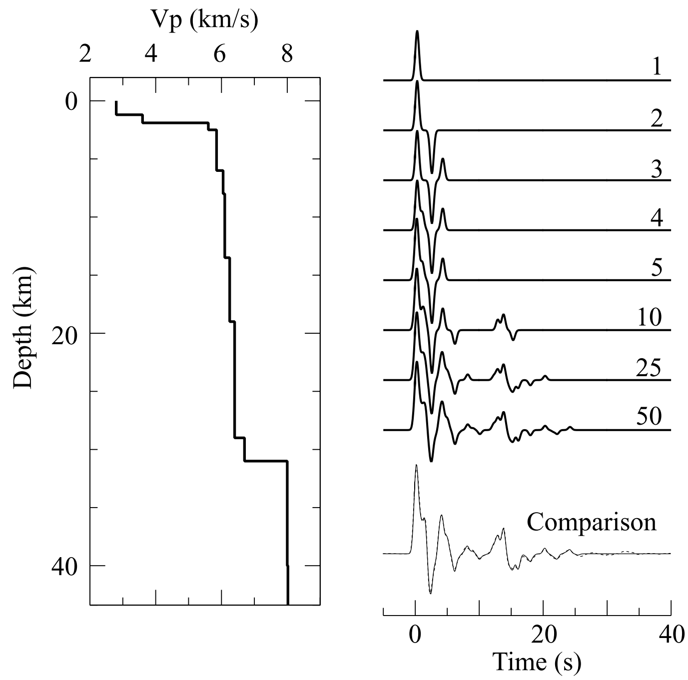

Figure 4.2 Comparison of the frequency-domain and time-domain receiver-function estimates for a more complicated velocity model. The intermediate estimates of the receiver function for select iterations are shown in the upper right. The receiver function which explains 99.5% of the original signal power in the radial response is compared with the frequency-domain solution in the lower right.

mate is shown on the right (the numbers to the right of each signal refer to the number of spikes in the receiver function estimate). Receiver functions estimated from iterative time- and frequency-domain approaches are overlaid on the lower right. The iterative time-domain receiver function shown satisfies the convolution definition of a receiver function (convolve the radial receiver function and the vertical seismogram to match the radial seismogram) to within 0.5% of the signal power. The comparison is excellent, although the match late (greater than 30 seconds) in the receiver function is less accurate because the number of spikes recovered by the iterative process was limited. The frequency-domain results at later lag times were matched, but only enough spikes to match all the important arrivals were chosen.

4.3 Applications to Recorded Observations

The advantages of the iterative time-domain technique with observed seismograms are now illustrated, beginning with an example using signals recorded during the 1988 PASSCAL Basin and Range Passive Source experiment. These data include intermediate and short-period signals, and like all deployments have their share of noisy data. Several authors have used these data to investigate the velocity structure beneath the region (*e.g*. McNamara and Owens, 1993; Randall and Owens, 1994; Peng and Humphreys, 1997) and the reader may refer to their works for detailed locations, instrument descriptions, and interpretation of the receiver functions. Figure 4.3 summarizes the results of a receiver function estimation using a short-period station located near the center of the PASSCAL temporary network. The teleseismic P-wave was generated by an mb 5.2, 500 km deep earthquake, located about 82° to the southwest of the seismometers. In Figure 4.3, the recorded seismograms are shown in the upper left, and the radial and transverse receiver functions estimated using a water-level and iterative time-domain approaches are overlaid in the lower panel. Also, the predicted radial and transverse seismograms (the match from the water-level deconvolutions is similar) are presented on the upper right.

The predictions are quite good, fitting about 95% of the observed power in the horizontal seismograms. The agreement in receiver function estimates is also good, most arrivals are visible on each receiver function. However, the long-period stability of the iterative time-domain results is evident in the amplitude of the early arriv-

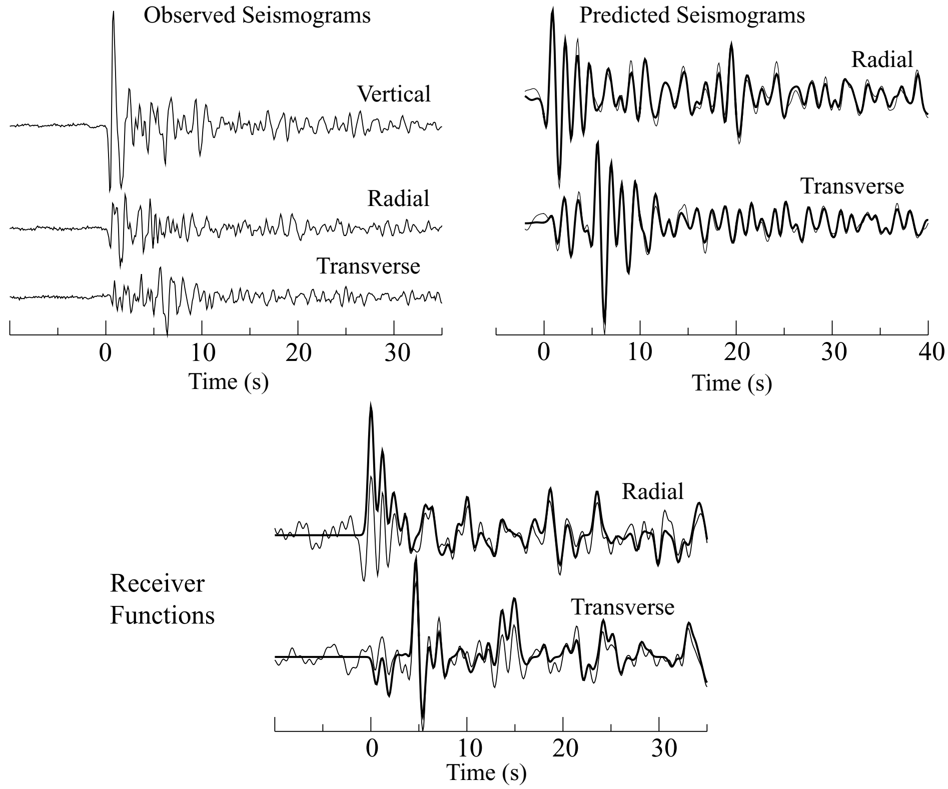

Figure 4.3 Receiver function estimation using a short-period signal from the 1988-89 PASSCAL Basin and Range experiment. The original signals from a 500 km deep, mb 5.2 earthquake are shown in the upper left, the receiver functions estimated using a water-level frequency-domain approach (thin line) are compared with those of the iterative time-domain approach (thick line) on the lower left. The predicted horizontal signals (the iterative deconvolution convolved with the observed vertical) are compared with the observed horizontal signals in the upper-right panel.

als. Unlike the water-level deconvolution, the time-domain signals have flat spectral levels at long periods (by design since the results are a sum of Gaussian pulses and all reasonable receiver responses are relatively flat at long periods). Also, the estimated receiver function does not suffer the acausal trough surrounding the P arrival that decreases the amplitude of the first few arrivals on the water-level radial receiver function. Also, the noise running throughout both the radial and transverse frequency-domain receiver functions is absent in the time-domain results.

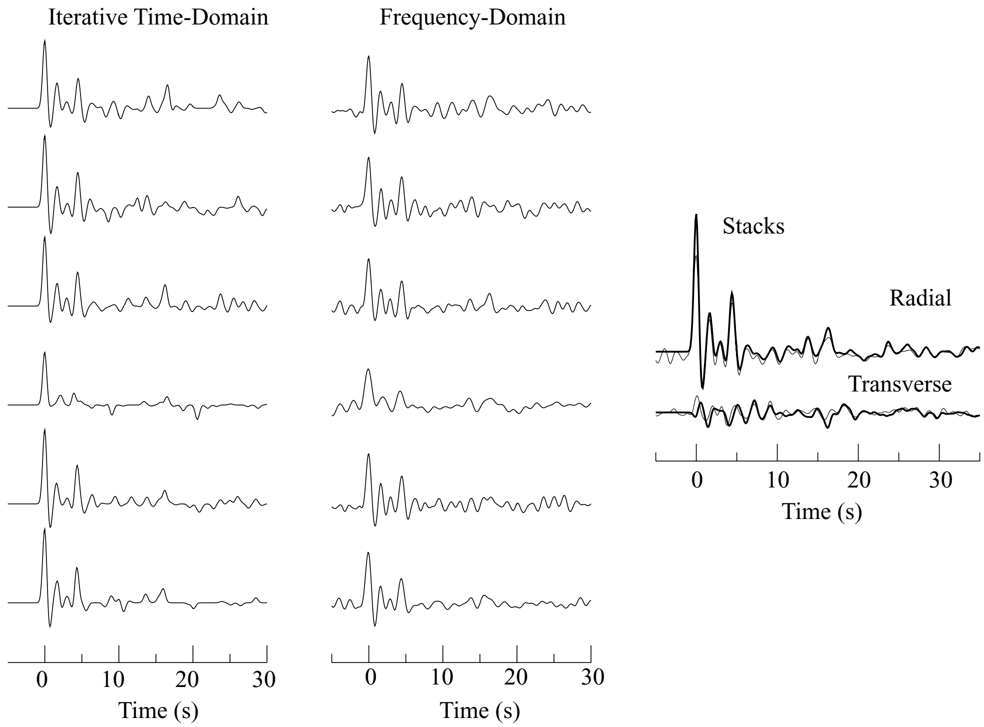

Figure 4.4 Comparison of receiver function deconvolutions for events approaching station ANMO, Albuquerque, NM, from the southeast. On the left are the time-domain estimates of the radial receiver function, in the middle are the corresponding water-level frequency-domain receiver functions. On the right are the average radial and transverse receiver functions from these six events (the thick line identifies the time-domain estimate).

Next, the iterative approach is illustrated on relatively simple and relatively complex receiver functions from two broad-band seismic stations, ANMO, located near Albuquerque, New Mexico, and MLA, located near Mammoth Lakes, California. Based on an examination of the observed receiver functions, the crustal structure to the southeast of ANMO is relatively simple, and a comparison of time- and frequency-domain receiver-function estimates is presented in Figure 4.4. On the left and center are individual receiver functions estimated using the two approaches. For these well-behaved signals the results are similar, but the sometimes-inescapable limitations of deconvolution are evident for both methods on the fourth deconvolution from the top. Neither technique produces a satisfactory result on this waveform. On the right the averages of the frequency-domain and iterative time-domain receiver functions are shown (excluding the problematic signal). The results compare very well and differ primarily in the amplitude of the P arrival, which is related to increased bandwidth in the iterative time-domain deconvolution. Examination of the spectra of the individual estimates indicates that the iterative time-domain approach produces more coherent amplitude spectra than the water-level approach, but the average time-domain variability between the two methods is small.

The receiver responses at MLA are much more complex as a result of its location in the Long Valley Caldera, a structure with a shallow low-velocity layer with a large velocity contrast at its base. The results are presented in Figure 4.5 using the same format as Figure 4.4. The complexity of the receiver response is apparent in the receiver functions estimated with either approach and the results from both techniques vary from waveform to waveform. Each signal begins with a small arrival (that's the P wave) and is followed by a large P-to-S converted phase from the bottom of the surface-layer. That P-arrival actually has an amplitude similar to that observed at ANMO but it is overwhelmed by the converted phase and reverberations in the caldera fill. Note how consistent the P arrival is on the iterative time-domain estimates but indistinguishable from the acausal noise on the individual frequency-domain responses. Again the results are consistent when all the observations are averaged, although the reliability of the P-arrival might be questioned after

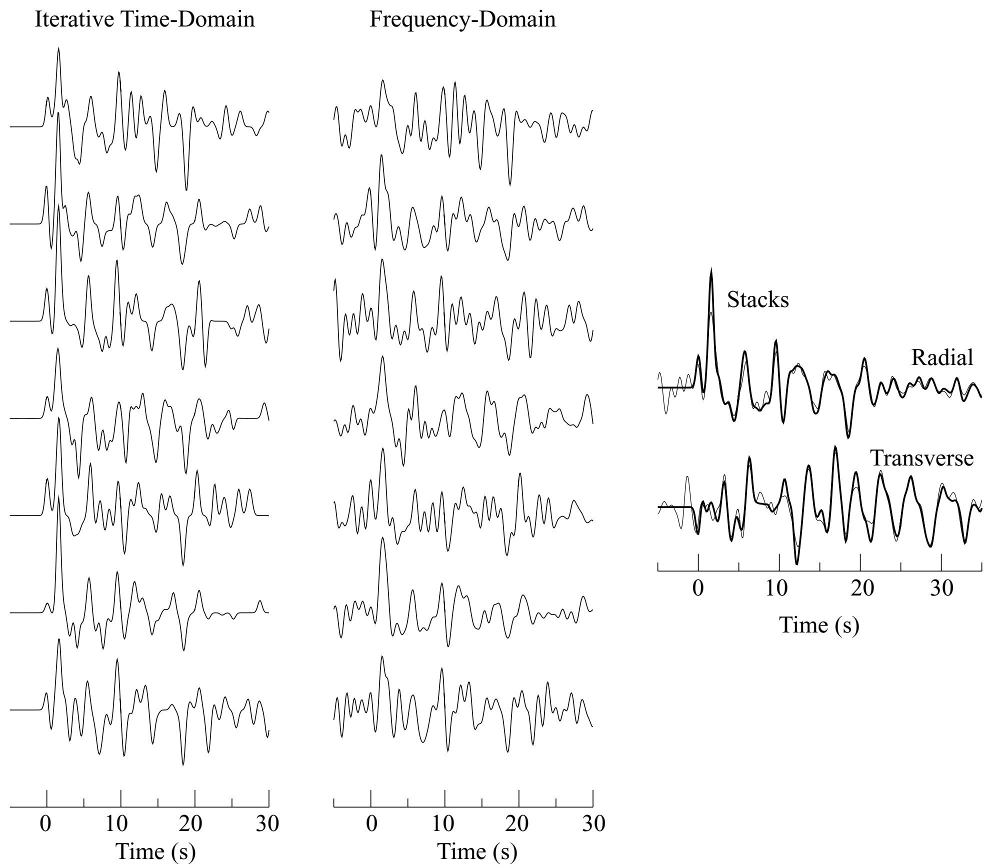

Figure 4.5 Comparison of receiver function deconvolutions for events approaching station MLA, located near Long Valley Caldera in eastern California, from the northwest. On the left are the time-domain estimates of the radial receiver function, in the middle are the corresponding water-level frequency-domain receiver functions. On the right are the average radial and transverse receiver functions from these six events (the thick line identifies the time-domain estimate).

examining the noise in the frequency-domain estimates. Once again the average time-domain variability between the two methods is small but the amplitude spectra of the iterative time-domain approach are more coherent.

Since the iterative approach constructs a receiver function in a way that allows truncation to include only the main arrivals, a potential application includes receiver-function estimation using secondary arrivals (*e.g*. PP, sPdiff, etc.). The iterative

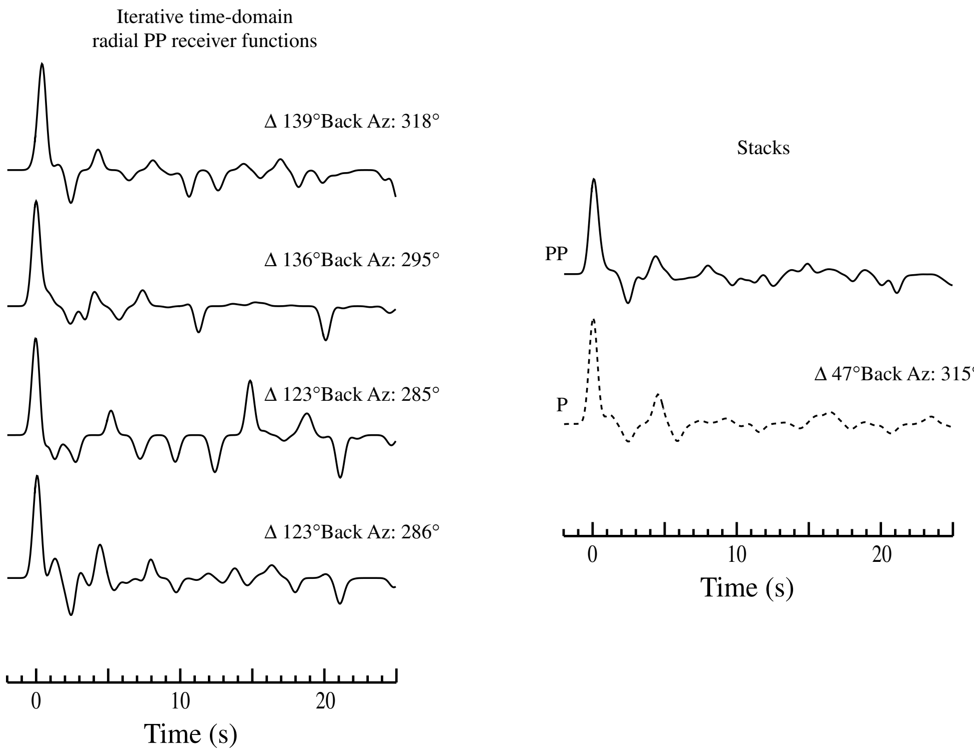

Figure 4.6 Resulting receiver functions using secondary PP signals. On the left panel, the iterative time-domain receiver functions from four events approaching station ANMO from similar teleseismic distances (Δ above the right edge of the signal) and back azimuths. The amplitude of the signals are normalized to unity, for comparison. On the right, comparison between the average radial receiver functions from the four signals on the left (PP, solid line) and a cluster of 13 P arrivals from a much shorter distance and approximately the same back azimuth (P, dashed line).

method was therefore tested using PP arrivals. Figure 4.6 shows receiver functions calculated using recorded signals at station ANMO. To the left receiver functions from four distant events using the PP arrivals are shown. In the right panel, the stack of those four signals is matched with a cluster stack of receiver functions estimated using P arrivals coming from approximately the same backazimuth. Although the results of the PP signals are not as clean as the P derived receiver functions, the major characteristics of the receiver structure can be recognized, *i.e.* the major phases are unequivocally reproduced. This test demonstrates the potential of the use of secondary arrivals to extend the amount of data available for receiver studies and expand the azimuthal coverage at most stations.

4.4 Discussion

The iterative time-domain deconvolution is equally effective for estimating receiver functions using high-quality signals, although less efficient than simpler methods such as water-level deconvolution. However, for a modest increase in computation costs, we have a simple, intuitive way of estimating receiver functions that is free of complex relationships between water-level values, time-domain smoothing and damping parameters, and the resulting receiver function. Additionally, the iterative approach has the advantage of requiring a level long-period spectrum *a priori* , which helps alleviate acausal troughs in the resulting receiver function. Like other time-domain inversion approaches, the iterative approach easily generalizes to a multi-waveform receiver-function estimation. Initial experiments with PP arrivals have been encouraging, but as expected the problem is not nearly as simple as that for the direct P wave and a greater number of secondary-phase observations are necessary to attain the confidence level in receiver functions estimated from direct P waveforms.

5 OBSERVATIONS

Observations are central to any scientific study. In this chapter, I describe the data collected, processed, and interpreted in Chapters 6 and 7. I begin with a brief overview of the different tectonic environments that make up North America, and which are used to classify the observations. I conclude this brief chapter with details regarding the compilation and organization of the data.

5.1 Tectonic Provinces of North America

The North American plate is home to a rich variety of tectonic environments. Many descriptions of the major tectonic and geomorphic elements present in North America are available in the literature (*e.g.* see the volume edited by Bally and Palmer, 1989). A comprehensive review of the many interpretations and tectonic divisions of the region is out of the scope of this study. In my description of the MCT beneath the continental crust of North America, I use a simplified tectonic classification based in the division proposed by Bally *et al.* (1989), and sketched in Figure 5.1. The main tectonic provinces included are:

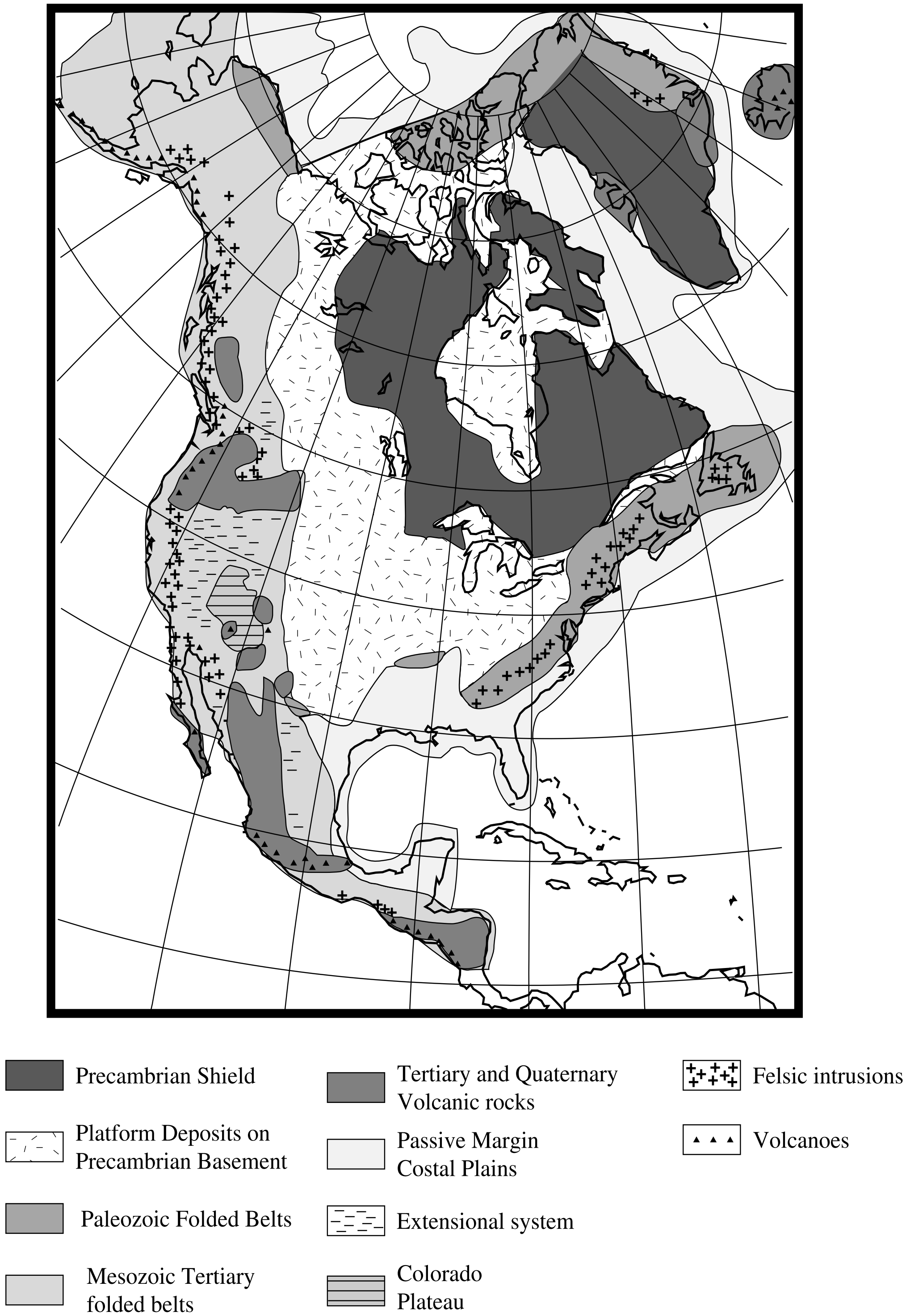

Figure 5.1 Tectonic setting distribution in North America (modified after Bally *et al.*, 1989).

- *Precambrian shields* are stable regions of the craton that include precambrian outcrops of the Canadian and Greenland shields. The exposed shield is mostly Archean in age (about 84%), although only about 55% of the whole craton has this age (Hoffman, 1989).

- *Platforms* are subsurface extension of the precambrian shield basement unit, overlaid by various sedimentary basin deposits (Bally, 1989). In North America, the platform regions include the Great Plains, the southern and eastern Coastal Plains and passive Margins, and the Central and Arctic lowlands. The North American passive margins extend throughout the Atlantic ocean coast of North America, including the Yucatan peninsula and the Gulf of Mexico. These sedimentary basins usually exhibit rifting events that preceded the deposition of a thick sedimentary wedge. The subsidence of the sedimentary cover has been attributed to a combination of thermal cooling and sediment loading (Bally, 1989).

- *Paleozoic folded belts* include the Innuitian folded belt region, the Northeast Greenland Mountains, and the Appalachian Mountains. Basement rocks underlying these regions are believed to be precambrian, but the folding events took place during the Paleozoic (Rast, 1989).

- *Mesozoic-Tertiary folded belts* extend throughout all the western part of North America, including: the Pacific (California) Coast-ranges, the Rocky Mountains, the Sierra Madre systems in Mexico (*i.e.* Occidental, Oriental and Del

Sur). The mountainous regions surround the Basin and Range extensional regime, the Colorado Plateau, the Columbia Plateau, and contain numerous Tertiary and Quaternary volcanics.

Seismic study of the structure of North America has a long history. For the purpose of this study, it is useful to have a summary of the seismic structure “typical” of each tectonic environment. Frontally the recent literature contains quality summaries of these aspects of the continent. Mooney and Braile (1989) summarized the seismic properties of North America, focussing on crustal thickness and velocity structure, using information primarily from refraction and reflection seismic profiles. More recently, Christensen and Mooney (1995) re-visited the subject using an extended data base of seismic refraction profiles. Both of these summaries point out the complex composition of continental crust, acknowledging the involvement of “multiple episodes of accretion, deformation, metamorphism, plutonism, and volcanism” in crustal evolution (Christensen and Mooney, 1995). For comparison with the present work, six velocity structures were adapted from the results presented by Christensen and Mooney (1995) and Mooney and Braile (1989). These velocity models are summarized in Table 5-1.

5.2 Broadband Seismic Stations in the Study Area

With the increased deployment of broadband seismic stations over the last 15 years, the number of stations suitable for receiver function analysis has continued to increase. In fact, one of the reasons for pursuing the study of North America is the ideal combination of broad regions of distinct tectonics and the quantity of

Table 5-1: Average Continental Crust and Upper Mantle Seismic Velocity Models[a]

	P-wave velocity (km/s)					
Depth to Top of Layer (km)	**Orogens**	**Shields and Platforms**	**Continenta l Arcs**	**Extended Crust**	**California Coast ranges**	**Rifts**
0	5.69 ± 0.67	5.68 ± 0.81	5.80 ± 0.34	5.59 ± 0.88	5.30 ± 0.40	5.64 ± 0.64
5	6.06 ± 0.39	6.10 ± 0.40	6.17 ± 0.34	6.02 ± 0.45	5.60 ± 0.42	6.05 ± 0.18
10	6.22 ± 0.32	6.32 ± 0.26	6.38 ± 0.33	6.31 ± 0.32	5.90 ± 0.31	6.29 ± 0.19
15	6.38 ± 0.34	6.48 ± 0.26	6.55 ± 0.28	6.53 ± 0.34	6.60 ± 0.32	6.51 ± 0.23
20	6.53 ± 0.39	6.65 ± 0.27	6.69 ± 0.28	6.69 ± 0.30	6.60 ± 0.30	6.72 ± 0.35
25	6.68 ± 0.43	6.80 ± 0.27	6.84 ± 0.30	6.89 ± 0.40	6.80 ± 0.41	6.94 ± 0.37
30	6.81 ± 0.40	6.96 ± 0.30	6.99 ± 0.29	6.93 ± 0.46	-	7.12 ± 0.33
35	6.92 ± 0.44	7.11 ± 0.33	7.14 ± 0.25	-	-	7.12 ± 0.30
40	6.96 ± 0.43	7.22 ± 0.39	-	-	-	-
45	6.99 ± 0.52	-	-	-	-	-
Crustal Average	6.39 ± 0.25	6.42 ± 0.20	6.44 ± 0.25	6.21 ± 0.22	6.05 ± 0.21	6.36 ± 0.23
Pn **velocity**	8.01 ± 0.22	8.13 ± 0.19	7.95 ± 0.23	8.02 ± 0.19	8.00 ± 0.17	7.93 ± 0.15

a. From Christensen and Mooney (1995) and Mooney and Braile (1989)

quality seismic stations deployed across the continent. Efforts by seismologists during the same time have provided a wonderful computer-based facilities for accessing data recorded on these stations. I am deeply grateful for the efforts of researchers and scientists in the development of IRIS (the Incorporated Research Institutions for Seismology), the U.S. Geological Survey's National Seismic Network, as well as operators of the Canadian National Seismic Network, the University of California at Berkeley, the California Institute of Technology. The main resources of data for this study are the following institutions:

- The Northern California Earthquake Data Center (NCEDC) that provided data recorded by the UC Berkeley Digital Seismic Network (BK).
- The Incorporated Research Institutions for Seismology Data Management Center (IRIS-DMC), that provided data recorded by the Canadian National Seismic Network (CNSN), Geoscope (G), IRIS – IDA (II), IRIS – USGS (IU) and Terrascope (TS) seismic networks.
- United States Geological Survey (USGS), that provided data recorded by the United States National Seismic Network (USNSN)
- The Canadian government's CNSN network.

Table 5-2 is a list of each network's stations and their correspondent tectonic setting, as based on the tectonic division of North America shown in Figure 5.1. The character codes used to identify the tectonic environment of each station are listed in Table 5-3. Station locations are shown on topographic maps in Figure 5-2.

5.3 Data compilation and organization

For the interest of student readers, I review the basic steps in the collection, organization, and pre-processing of seismic signals to be used in this study. When dealing with a large, heterogeneous data set, organization is a critical aspect of insuring quality results, easing analysis, and investigating trends or patterns in the measurements. The routine processing at the heart of this study consisted of requesting,

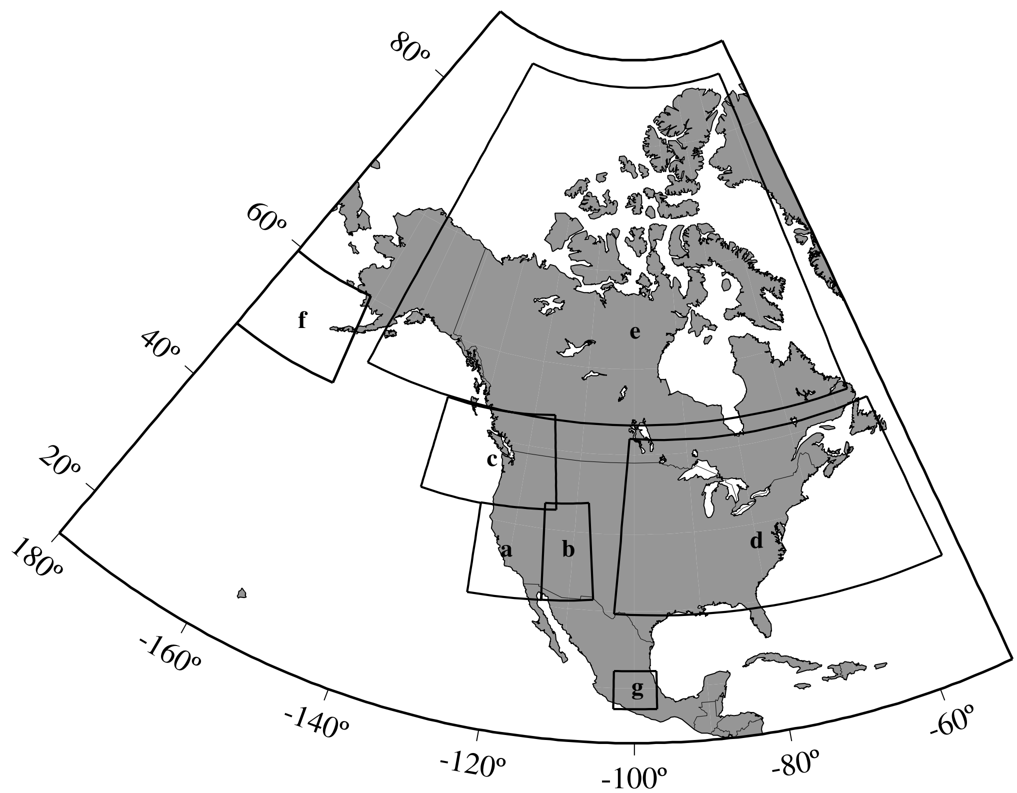

Figure 5.2 Broadband seismic stations available for this study. For convenience the location of the different sites, the stations are grouped in different maps (a to g).

retrieving and preparing the observations, and integrating and organizing the data. I describe each step in more detail in the following sections.

5.3.1 Data request, retrieval, and preparation

The first step is acquiring the waveforms. Data requests to individual networks can be constructed in a variety of ways, the easiest is to create an electronic-mail request for the waveforms. Each request requires a station information and time windows that are computed using the earthquake origin time and estimates of the P-wave travel time computed using standard travel time tables such as those of Jeffreys and Bullen (which can be found in Simon (1981)). The data are usually supplied in SEED format which can be unpacked and converted to separate files for each wave-

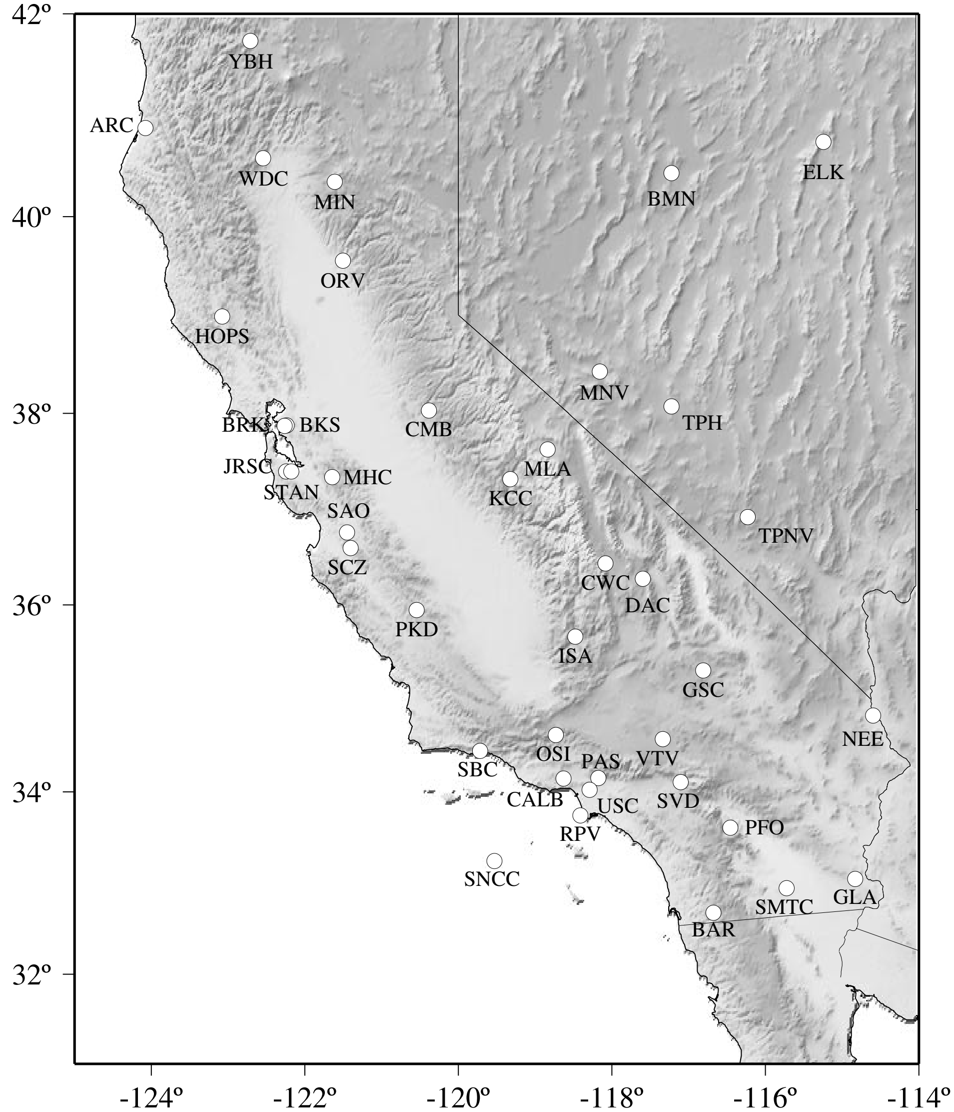

Figure 5-2a. Broadband seismic station locations in the Pacific southwest.

form along with information on the instrument response and history. Harley Benz generously provided data from USNSN stations in SAC format for the events that occurred between 1994 to the first trimester of 1998.

To perform a P-wave receiver function study, we required three-component (vertical, north-south and east-west) broadband signals. The event selection varies from study-to-study, in this effort I used signals from events with magnitude M ≥ 6, and

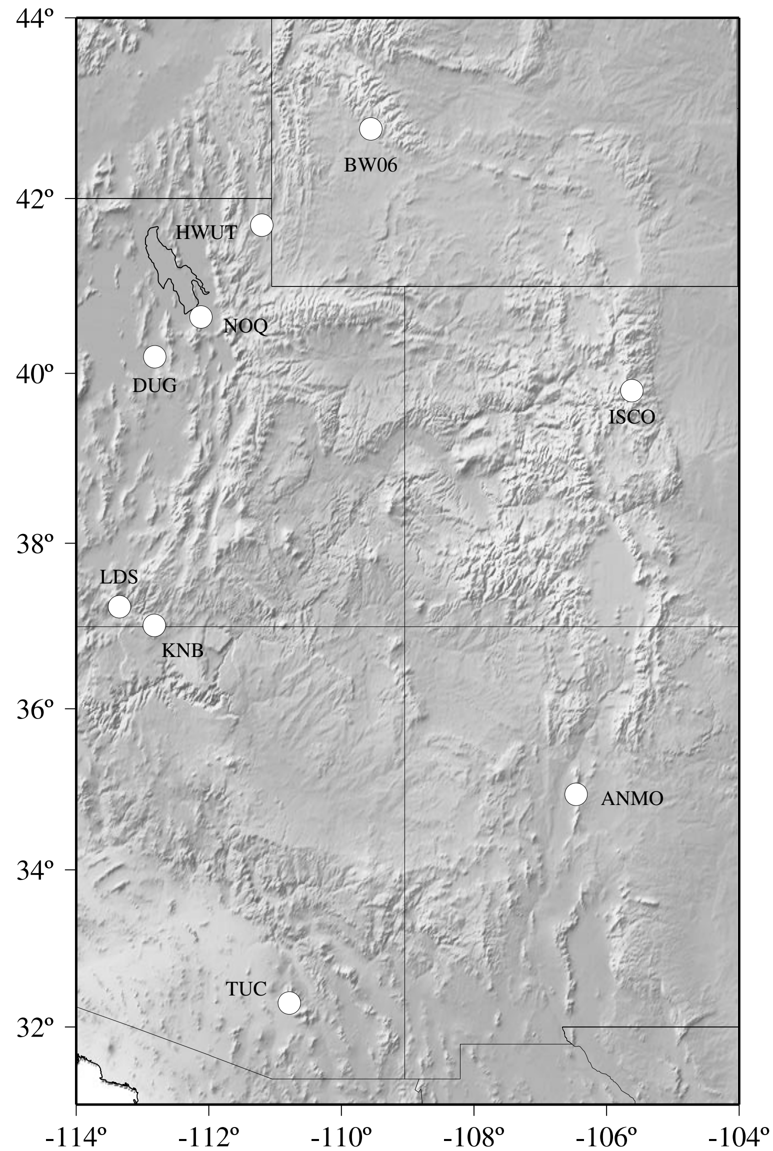

Figure 5-2b. Broadband seismic station locations in the Intermountain region.

with source-to-receiver epicentral distances between 30° and 95°, recorded between 1990 to 1997. Station locations are listed in Table 5-2.

Once the data were retrieved and organized into groups by recording station, information on each event location, component angles and component incidence angle were stored in each signal's SAC header fields. Because of the nature of receiver

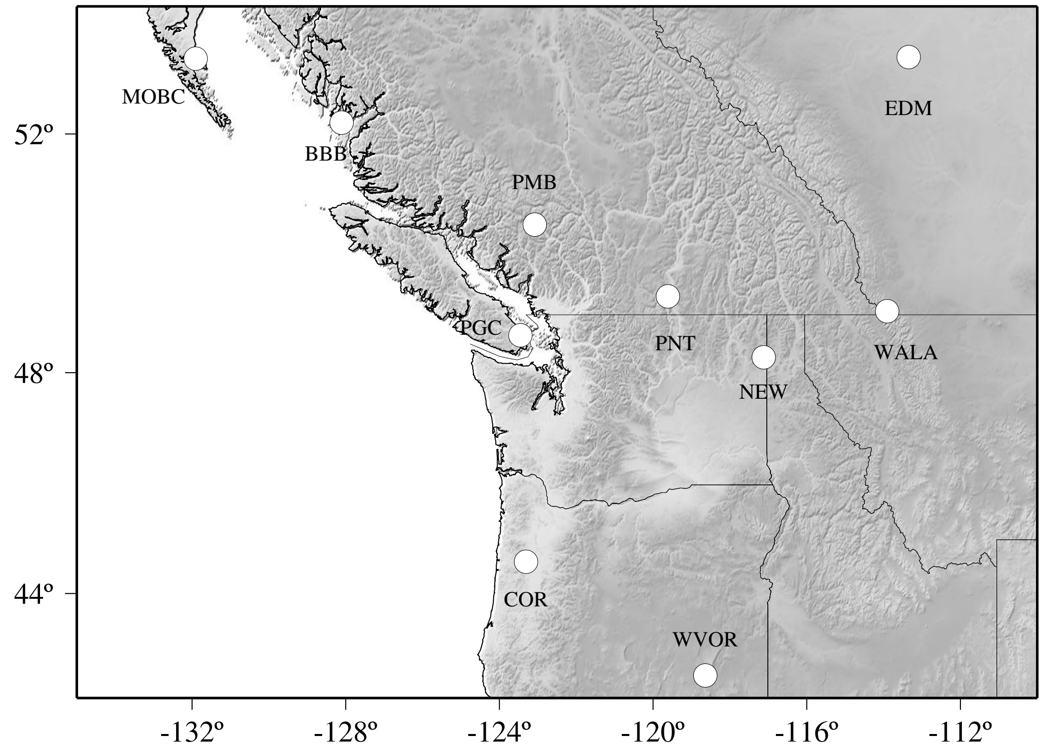

Figure 5-2c. Broadband seismic station locations in the Pacific northwest region.

function analysis, we do not necessarily need information on the instruments as long as the instrument responses of the three components are matched. This is invariably the case with modern instruments, but for instances where the gain is different for the each component, it was correct before computing the receiver functions. Also, before computing the receiver functions it is necessary to window the P-waveform from the signal. For this study, a 90 second-long window (30 seconds before and 60 seconds after) relative the onset of the P-wave arrival was used. To reduce the influence low-frequency noise on the receiver functions, all the signals were high-pass filtered with a two-pass Butterworth 0.02 Hz corner frequency filter.

Finally, each three-component signal was reviewed to remove signals that contained low signal-to-noise ratios and/or when any of the three components were not

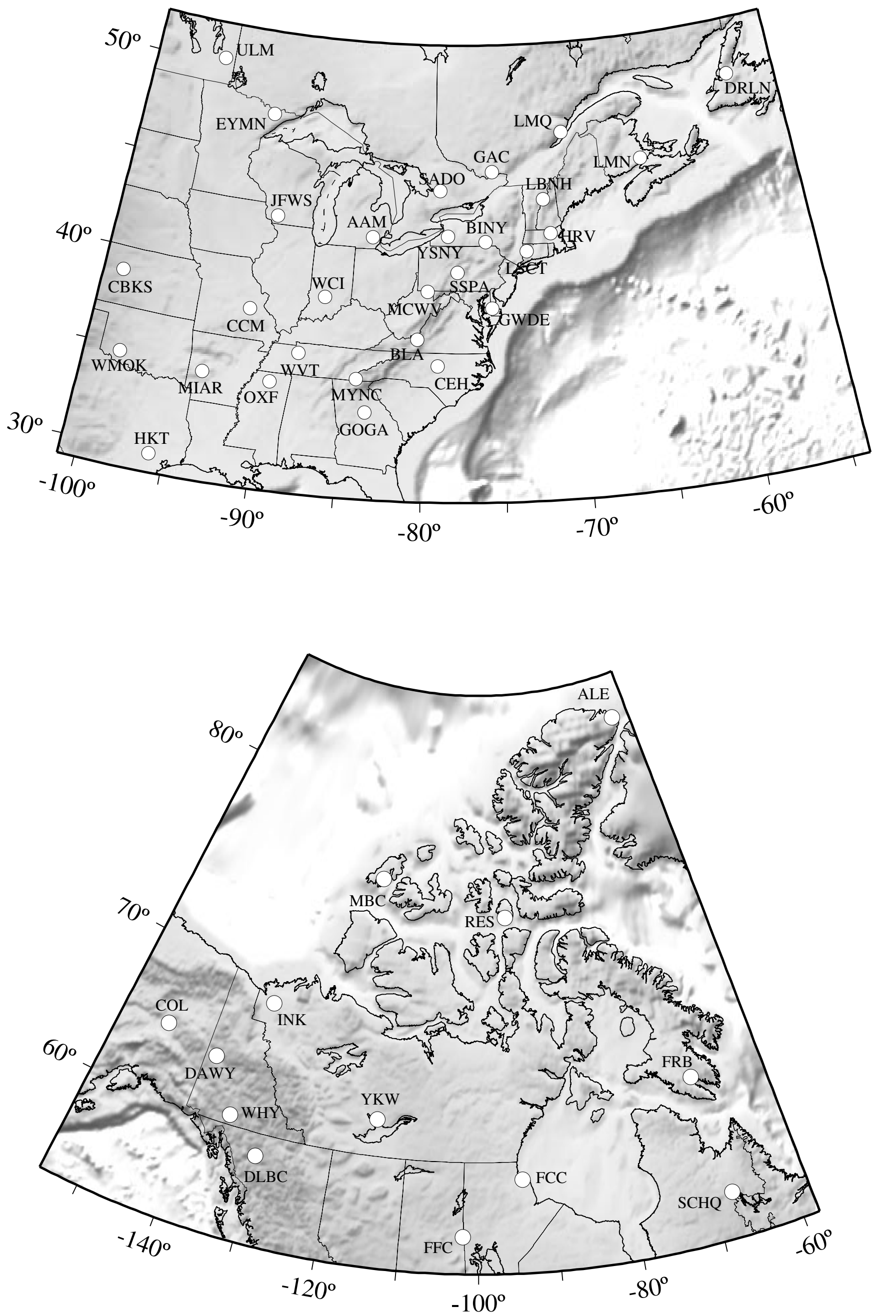

Figure 5-2d. Broadband seismic station locations in the eastern United States (top) and Canada (bottom).

recorded properly due to obvious instrument malfunction. After the removal of noisy and incomplete signals, receiver functions were calculated using a frequency-domain deconvolution, using a Gaussian filter width factor of 1.0. Following this

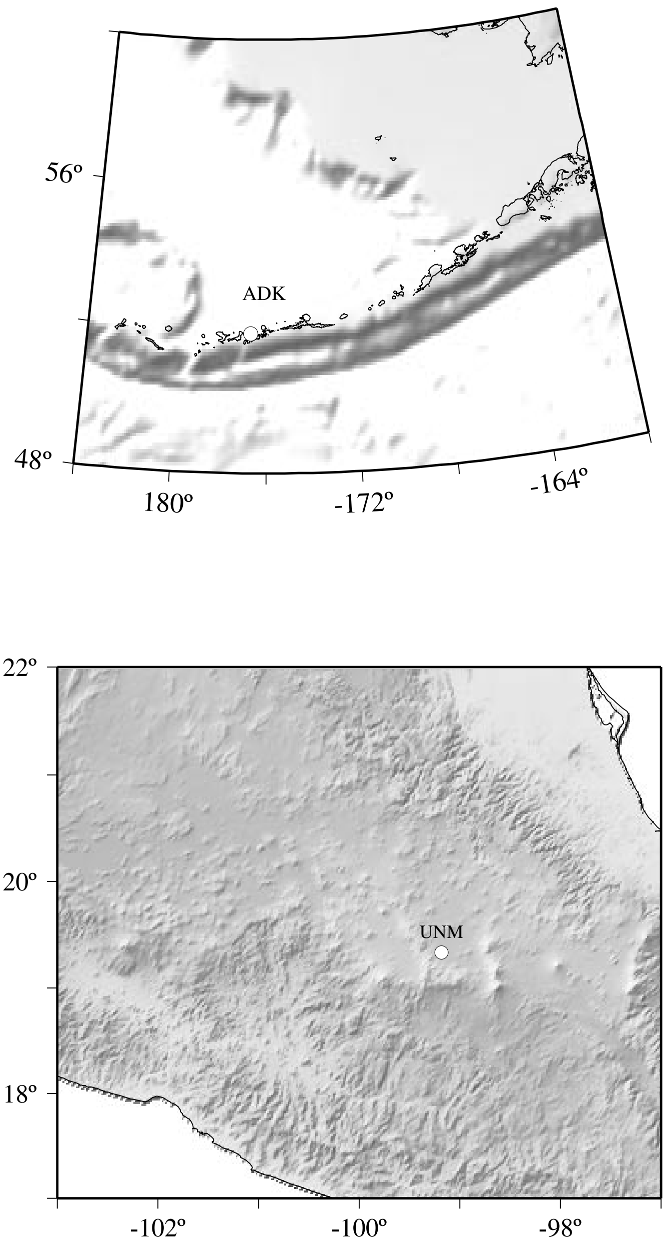

Figure 5-2e. Broadband seismic station locations in the Aleutian Islands (top) and Mexico (bottom).

suite of deconvolutions, each receiver function was reviewed and noisy receiver functions were discarded.

Table 5-2: Seismic Stations Used in This Study

Station	Latitude	Longitude	Region	Station	Latitude	Longitude	Region
BERKELEY DIGITAL SEISMOGRAPHIC NETWORK (BK)							
ARC	40.877	-124.075	F	BKS	37.877	-122.235	F
BRK	37.873	-122.260	F	CMB	38.035	-120.383	D
HOPS	38.994	-123.072	F	JRSC	37.404	-122.238	F
KCC	37.324	-119.318	D	MHC	37.342	-121.642	F
MIN	40.345	-121.605	D	ORV	39.556	-121.500	D
PKD	35.945	-120.541	F	SAO	36.765	-121.445	F
STAN	37.404	-122.174	F	WDC	40.580	-122.540	D
YBH	41.732	-122.709	D	-			
CANADIAN NATIONAL SEISMIC NETWORK (cnsn)							
BBB	52.185	-128.113	G	DAWY	64.066	-139.391	D
DLBC	58.437	-130.030	D	DRLN	49.256	-57.504	C
EDM	53.222	-113.350	B	FCC	58.762	-94.087	A
FRB	63.747	-68.547	A	GAC	45.703	-75.478	A
INK	68.307	-133.520	D	LMN	45.852	-64.806	C
LMQ	47.548	-70.327	B	MBC	76.242	-119.360	C
MOBC	53.197	-131.900	G	PGC	48.650	-123.45	G
PMB	50.519	-123.077	G	PNT	49.317	-119.617	D
RES	74.687	-94.900	B	SADO	44.769	-79.142	B
SCHQ	54.832	-66.834	A	ULM	50.249	-95.875	B
WALA	49.059	-113.911	D	WHY	60.660	-134.881	D
YKW	62.562	-114.605	A	-			
NETWORK: Geoscope (G)							
SCZ	36.600	-121.400	F	UNM	19.332	-99.183	G
NETWORK: IRIS – IDA (II)							
ALE	82.503	-62.350	C	FFC	54.725	-101.978	B
PFO	33.609	-116.455	D	-			
NETWORK: IRIS – USGS (IU)							
ADK	51.884	-176.684	G	ANMO	34.946	-106.457	D
CCM	38.056	-91.245	B	COL	64.900	-147.793	D
COR	44.586	-123.303	G	HKT	29.962	-95.838	B
HRV	42.506	-71.558	C	SSPA	40.640	-77.891	C
TUC	32.309	-110.785	E	-			
NETWORK: Terrascope (TS)							
BAR	32.680	-116.672	F	CALB	34.143	-118.627	F
CWC	36.439	-118.080	D	GLA	33.052	-114.827	E
GSC	35.303	-116.808	D	ISA	35.663	-118.473	D
MLA	37.631	-118.834	G	NEE	34.823	-114.596	E
PAS	34.148	-118.172	F	RPV	33.744	-118.404	F
SBC	34.442	-119.713	F	SMTC	32.949	-115.720	E
SNCC	33.248	-119.524	F	SVD	34.105	-117.097	D
USC	34.021	-118.287	F	VTV	34.567	-117.333	D
NETWORK: U.S. National Seismic Network (USNSN)							

Table 5-2: Seismic Stations Used in This Study (Continued)

Station	Latitude	Longitude	Region	Station	Latitude	Longitude	Region
AAM	42.300	-83.656	B	BINY	42.199	-75.986	C
BLA	37.211	-80.421	C	BMN	40.431	-117.222	E
BW06	42.778	-109.556	D	CBKS	38.814	-99.737	B
CEH	35.891	-79.093	C	DAC	36.277	-117.590	E
DUG	40.195	-112.813	E	ELK	40.745	-115.239	E
EYMN	47.946	-91.495	A	GOGA	33.411	-83.467	C
GWDE	38.826	-75.617	C	HWUT	41.700	-111.200	D
ISCO	39.800	-105.613	D	JFWS	42.915	-90.249	B
KNB	37.017	-112.822	D	LBNH	44.240	-71.926	C
LDS	37.243	-113.350	D	LSCT	41.678	-73.224	C
MCWV	39.658	-79.846	C	MIAR	34.546	-93.573	C
MNV	38.433	-118.153	E	MYNC	35.074	-84.128	C
NEW	48.263	-117.120	D	OXF	34.512	-89.409	B
TPH	38.075	-117.223	E	TPNV	36.929	-116.224	E
WCI	39.100	-86.500	B	WMOK	34.738	-98.781	B
WVOR	42.434	-118.637	D	WVT	36.130	-87.830	B
YSNY	42.476	-78.537	C	-			

Table 5-3: Tectonic Region Codes for Table 5-2

A: Shield	B: Continental Platform
C: Paleozoic Orogen	D: Mesozoic-Tertiary Orogen
E: Extended Crust	F: California Coast ranges
G: Continental Arc	

5.3.2 Data Integration and Organization

Once the useful signals has been identified, another round of deconvolutions were applied, this time with the iterative time-domain method describe in Chapter 4. Each pair of horizontal-component signals (*i.e.* north-south and east-west components) where rotated to their corresponding radial- and transverse-directions and receiver functions where calculated for each event using the iterative deconvolution method. Each receiver function was deconvolved using 100 iterations with a limiting error of 0.001 (*i.e.* up to 100 spikes make up the receiver function) and a Gaussian width factor of 2.5. All the resulting receiver functions were grouped in clusters of common source origin and final radial and transverse stacks where computed. The stacking constraints previously discussed in Chapter 3 were followed, that is, we averaged signals corresponding to events with back azimuth and epicentral distance variations ≤ 10º. For those stations with poor data distributions, stacking bins as wide as 15º were used.

The complete set of observations which form the foundation of this dissertation is documented in Appendix 2. I summarize the distribution of the data with respect to tectonic setting in Table 5-4 and Figure 5.3. As you might expect, the data set is

Table 5-4: Event Distribution Summary

Tectonic Setting	Stations	Clusters	Clust/Sta	# Obs.	Evn/ Clust
Shield	6	39	6.5	188	4.8
Continental Platform	15	74	4.9	281	3.8
Paleozoic Orogen	17	105	6.2	415	4.0
Mesozoic-Tertiary Orogen	27	234	8.7	1191	5.1
Extended Crust	11	73	6.6	278	3.8
San Andreas System	17	152	8.9	701	4.6
Continental Arc	8	54	6.8	266	4.9
TOTALS	**101**	**731**	**6.94**	**3320**	**4.43**

dominated by stations located in active tectonic settings (*e.g.* Mesozoic-Tertiary Orogens, California Coast Ranges, Paleozoic Orogens). We separated the California Coast Ranges out from the other regions simply because of the large number of stations in this region (Figure 5.2). Strictly speaking, they should be included in any

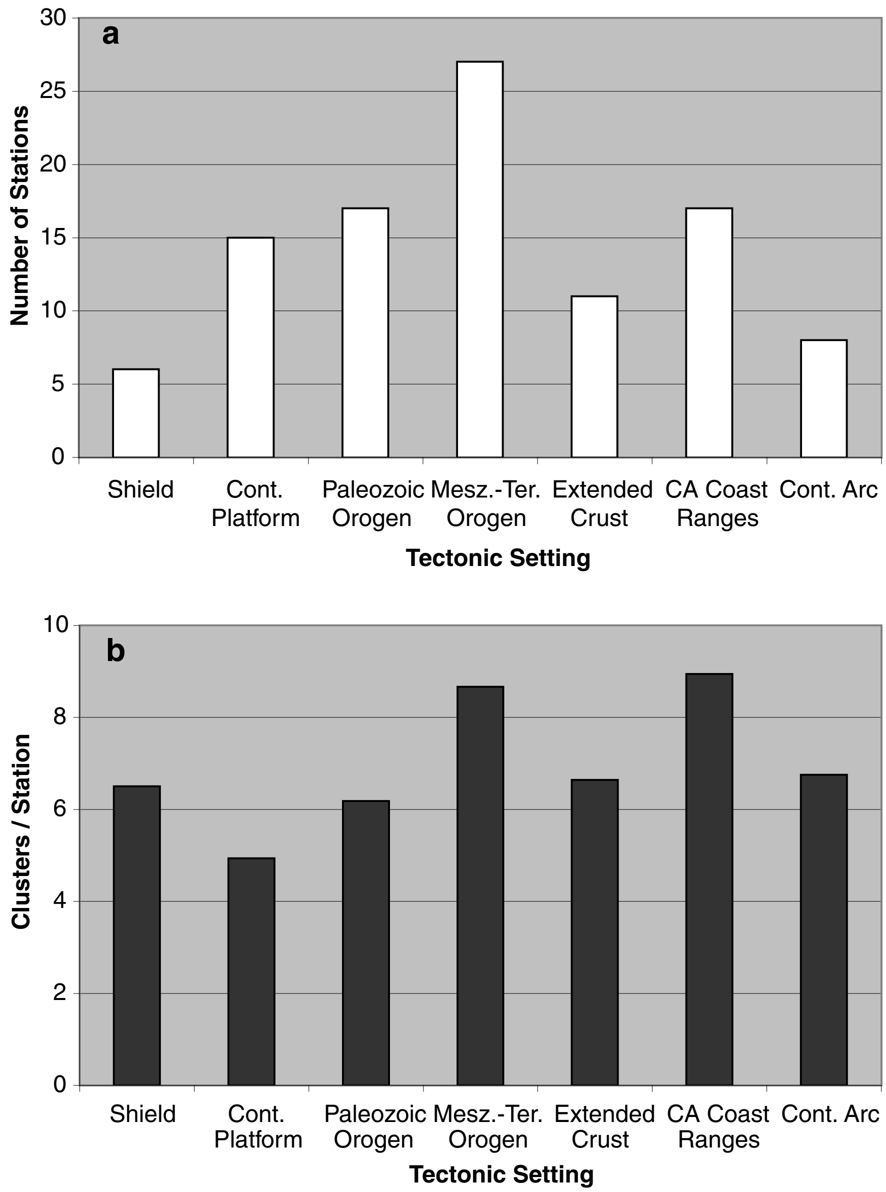

Figure 5.3 (a) Distribution of observations by tectonic province. Most of the stations are in regions of active tectonics (Mesozoic and Tertiary Orogens, and California Coast Ranges), and so most of the observations are also in this category. (b) Average number of azimuthal and/or distance clusters for stations in each tectonic province.

discussion of the Mesozoic-Tertiary Orogenic regions. The mean epicentral distance for the different settings is roughly similar (around 65º). The mean number of events included for each station is about 31 and the mean number of events per cluster is about 4. The back azimuth and epicentral distance bounds for cluster collection show consistent mean values of 3.5º and 3.9º respectively, which are well below the suggested limits for receiver function analysis (≤10º).

In the next two chapters I document my investigations of two aspects of lithospheric structure beneath these seismic stations. I begin with an investigation of the Poisson's Ratio variations and discuss their relationship to the bulk crustal composition of North America in Chapter 6 and I continue with an investigation of the MCT thickness in Chapter 7.

6 POISSON'S RATIO OF THE NORTH AMERICAN CRUST

Seismic studies have traditionally provided useful constraints regarding the physical and structural properties of Earth's crust. Usually the easiest parameters to constrain are the P *or* S velocities variations of the structure, and so these are the most commonly available parameters for tectonic and geologic interpretation. Although valuable, seismic velocity variations alone are limited in geologic applications because the correlation between lithology and such V_P (or V_S) is far from simple and the assignment of a lithologic equivalent to seismic velocities is far from straightforward. For instance, in typical lower crust rocks, an increase of mafic content or metamorphic grade both increase seismic velocities. Thus, using only seismic velocities there is no way to tell the difference between mafic rocks and metapelites (Holbrook *et al.*, 1992). The problems of interpretation of seismic velocities is an old one, and has no easy solution. However, the non-uniqueness of lithologic interpretation is reduced by combining P- *and* S-wave information, or equivalently using Poisson's ratio estimates (Holbrook *et al.*, 1992). The ratio of P to S velocities, or Poisson's ratio, which is a function of V_P/V_S, is sensitive to quartz and SiO_2 content in rocks. However, the relationship of decreasing V_P with the presence of SiO_2 is not simple; V_P is almost constant for granulite facies rocks between 65-75% SiO_2. Metapelites with high V_P exhibit strong anisotropy related to preferred phases orientation and this could help to distinguish them from granulite mafic rocks (Rudnick and Fountain, 1995).

Several studies have attempted to integrate crustal seismic velocities through Poisson's ratio (*e.g.* Christensen, 1995; Zandt and Ammon, 1995; Clarke and Silver, 1993; Holbrook *et al.*, 1992; Braile *et al.*, 1989; Gajewski *et al.*, 1987), but not all studies agree in their conclusions. For instance, Holbrook *et al.* (1992), interpreted relatively low Poisson's ratios (0.24-0.27) in shields and platforms to favor less mafic compositions. In contrast, Zandt and Ammon (1995), measured higher values (0.27-0.29) in similar environments, and concluded that an initial intermediate-to-mafic precambrian crust evolves to a refractory lithosphere. The apparent controversy seems to stem from the accuracy of Poisson's ratio estimations.

In this chapter, I estimate Poisson's ratio for the bulk crust beneath North America. I have two goals. First, to investigate observed Poisson's ratio variations obtained by Zandt and Ammon (1995). They found a complicated relationship between Poisson's ratio and crustal province, but they observed a systematically high Poisson's ratio for shield regions. Although they applied the same method used here, the number of observations in this study is much larger. Second, in addition to providing additional evidence regarding the nature of crust beneath stations, the estimated Poisson's ratios are used in the inversion of velocity structures beneath the stations in Chapter 7, when the nature of the MCT is investigated.

6.1 Poisson's Ratio and Crustal Composition

6.1.1 Poisson's Ratio

In an isotropic linear-elastic material, Poisson's ratio is the ratio of radial to axial strain when uniaxial stress is applied; *i.e.* the ratio of lateral contraction to longitudinal extension (Lay and Wallace, 1995). In terms of the Lamé elastic parameters (λ and μ), σ can be expressed as:

$$\sigma = \frac{\lambda}{2(\lambda + \mu)} \tag{6–1}$$

Poisson's ratio is a dimensionless elastic modulus that has a maximum value of 0.5 for a fluid (when $\mu = 0$). Using the definitions of V_P and V_S, also in terms of the Lamé parameters, and the material's density ρ:

$$V_P = \sqrt{\frac{\lambda + 2\mu}{\rho}} \qquad V_S = \sqrt{\frac{\mu}{\rho}} \tag{6–2}$$

σ may be written in terms of the V_P/V_S as

$$\sigma = \frac{\left(\frac{V_P}{V_S}\right)^2 - \frac{1}{2}}{2\left[\left(\frac{V_P}{V_S}\right)^2 - 1\right]} \tag{6–3}$$

For most rocks, the values of μ and λ are similar and σ varies from 0.20 to 0.35. The average Poisson's ratio for all rock types is 0.27 (Christensen, 1995). The relationship between Poisson's ratio and the V_P/V_S ratio is unique so we can use either in our discussion. The inverse relationship of 6-3 is

$$\frac{V_P}{V_S} = \sqrt{\frac{2(1 - \sigma)}{1 - 2\sigma}} \tag{6–4}$$

An increase in V_P/V_S corresponds to an increase in Poisson's ratio. A Poisson solid has a Poisson ratio of 0.25, and a V_P/V_S ratio equal to $\sqrt{3}$, (~ 1.732).

6.1.2 Poisson's Ratio and Rocks

Although the value σ is sensitive to mineral composition, both its pressure and temperature dependence is small for most rocks (*e.g.* Christensen, 1995; Tarkov and Vavakin, 1982). Christensen (1995) showed that the dependence of Poisson's ratio on temperature and pressure within the crust is minor for most common crustal rocks and environments. Of course extreme crustal temperatures that induce melt are likely to affect V_P and V_S differently, producing an increase in Poisson's ratio since V_S will decrease more rapidly with melt. Therefore, laboratory measurements of σ should be applicable throughout the crust.

In Figure 6.1, I show the laboratory high-pressure measurements of σ, corrected for temperature effects. The ranges of compressional velocity and Poisson's ratio for a range of rock types commonly assumed to comprise the mid and lower crustal lithology are shown on the left and right respectively. The boxes indicate the typical range of velocity and Poisson's ratio observed in laboratory measurements. As illustrated in this diagram, although Poisson's ratio can help distinguish between rock types, it alone cannot uniquely constrain the rock type. Clearly additional constraints on such diverse properties as seismic velocity, heat production, electrical properties, temperature and pressure conditions, fluid content, *etc.* are necessary to tightly identify crustal composition or mineralogy.

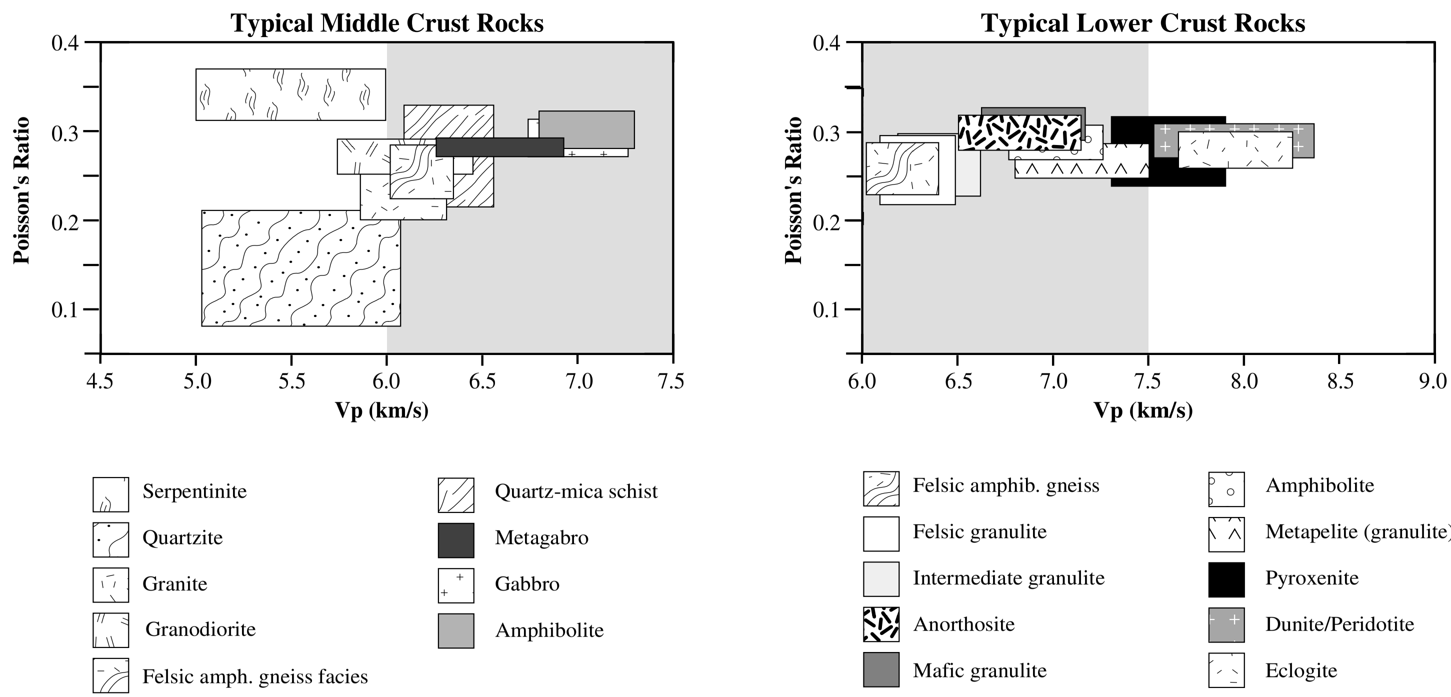

Figure 6.1 Laboratory measurements of Poisson's ratio and VP for mid-crustal (left) and lower-crustal (right) rock types. The width of the fields equals two standard deviations. The data are corrected for pressure and temperature effects. After Holbrook *et al.* (1992). The gray boxes on each diagram indicate the region with overlap in velocity and Poisson's ratio.

Of the typical mid-crustal lithologies, quartzite has the lowest value, near 0.20 while the largest values correspond to serpentine, which also has a relatively low P-wave velocity. Information on both P-velocity and Poisson's ratio would clearly distinguish these two rocks. The lithologies expected to comprise the lower crust, on the other hand, share common values of σ. However, the more mafic materials (*e.g.* granulites and pyroxenites) have higher velocities which provides and important means of favoring some lithologies when both velocity information is available.

6.2 Poisson's ratio estimation using receiver functions

In this study, I measured bulk crust Poisson's ratios, following the method initially proposed by Zandt *et al.* (1995) and later applied by Zandt and Ammon (1995). This simple method, based on the relationship of the ratio of the *Ps*-P time (t_{Ps}) and the *PpPms*-*Ps* time (t_{PpPms}) to the value of V_P/V_S, follows (Zandt *et al.*, 1995). Ray nomenclature is indicated in Figure 6.2, the explicit relationship is:

$$\frac{V_P}{V_S} = \left\{(1 - p^2 V_P^2)\left[\frac{2 \cdot t_{Ps}}{t_{PpPms}} + 1\right]^2 + p^2 V_P^2\right\}^{1/2} \qquad (6\text{–}5)$$

where p is the horizontal slowness or ray parameter. Equation (4) is independent of the crust thickness, but depends on an assumed value of V_P. The dependence, however, is second order in p, which is a relatively small number for teleseismic P-waves (typical values are 0.07 to 0.04 s/km). The small multiplicative coefficient in front of V_P reduces the sensitivity of the measurement to the assumed P-velocity,

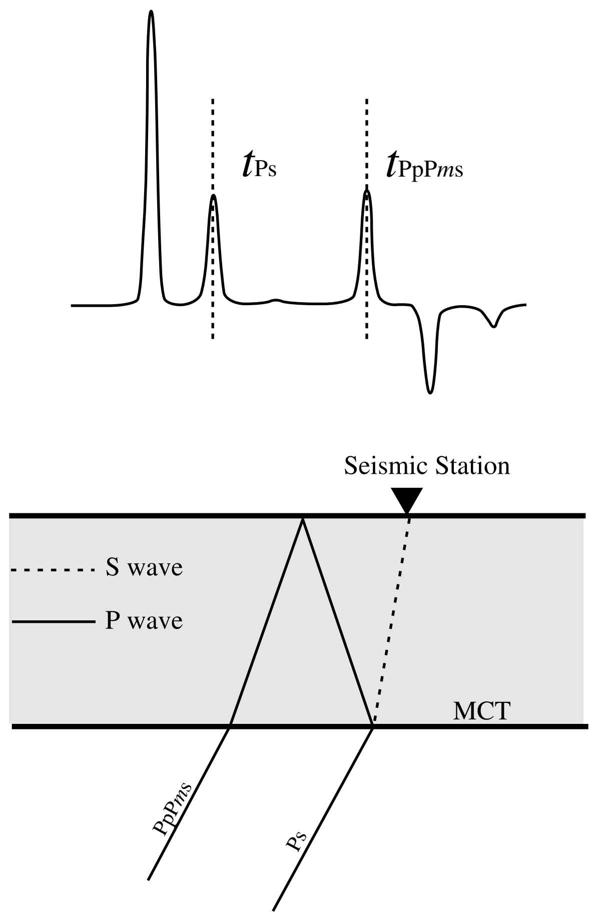

Figure 6.2 Simple cartoon showing *Ps* and *PpPms* phases used in the estimation of Poisson's ratio from radial receiver functions. The lower panel illustrates the correspondent traveling paths.

and the range in σ for a typical range in V_P is acceptably small (but not negligible). The point is that we can use (6-5) to estimate the V_P/V_S ratio, and then use (6-3) to estimate σ.

Of course implicit in the method is the fact that you must identify the two arrivals of interest. In practice, to enhance these arrivals and reduce the effects of scattering on the measurements, the receiver functions are low-pass filtered before the measurements are made. The resulting degradation in pick accuracy is worth the sacrifice for a more clear identification of the *Ps* and PpPmS arrivals. As expected, σ

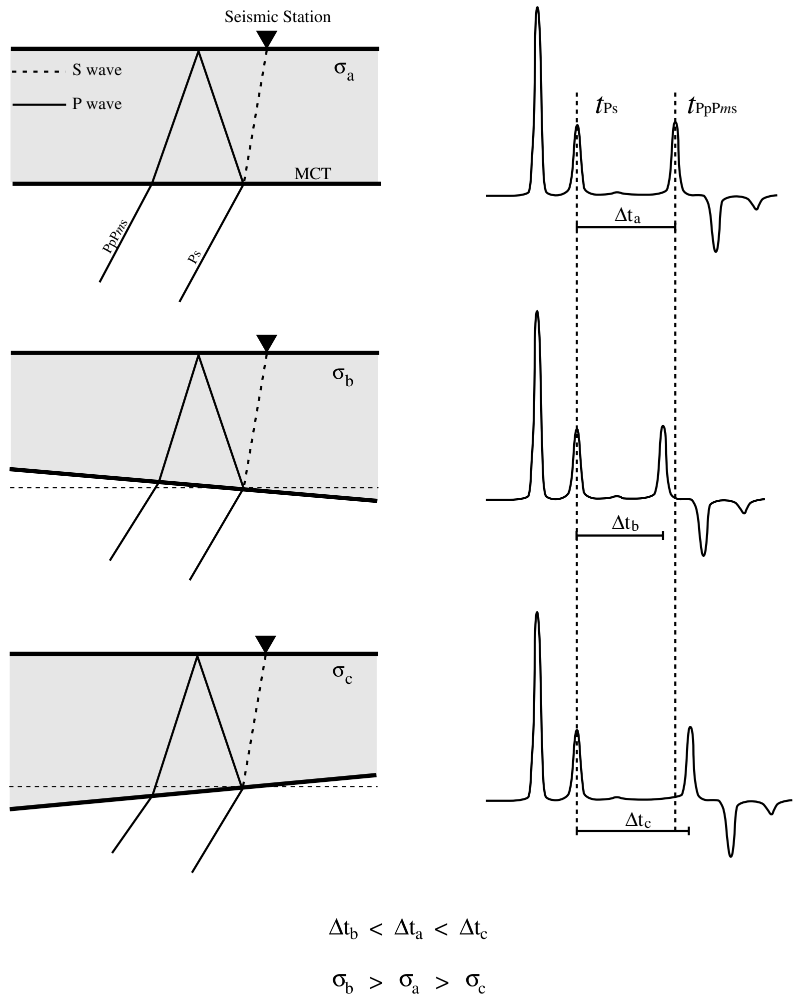

Figure 6.3 The effect of dipping MCT in Poisson's ratio (s) measurements is shown. The ray paths in three hypothetical models are shown to the left where the arrival to a horizontal (upper-left), down dip (middle-left) and up dip (lower-left) induce a moveout between the correspondent MCT phases (right). The resulting effect in σ is a larger estimate for down dip incidence of the wavefront in the transition and the contrary for an up dip incidence.

estimates obtained through receiver functions travel times are sensitive to factors that affect the travel times, t_{Ps} and t_{PpPms}. A change of 0.02 seconds in either time would induce a 0.001 change in σ, for a slowness of 0.05 s/km. Also, the derivation of equation (4) begins with the assumption that the MCT is horizontal. MCT dip will influence Poisson's ratio estimates (Figure 6.3). Waves traveling up-dip will result in an underestimate of σ, those traveling down-dip will produce an overestimate. Such factors can be important in regions of rapid crustal thickness variations such as coastal regions of California.

Before concluding, I note that we can also obtain an estimate of crust thickness, h, using the converted wave travel time, t_{Ps}, and the assumed values of V_P (also using the Poisson's ratio to compute the corresponding V_S) (Zandt *et al.*, 1995):

$$h = \frac{t_{Ps}}{\sqrt{V_S^{-2} - p^2} - \sqrt{V_P^{-2} - p^2}} . \quad (6\text{–}6)$$

Note that the dependence on the assumed V_P value is not second order in this equation, and the uncertainty on the thickness estimate can be large - on the order of 10 km. Still the values are obtained for virtually no extra effort, and worth some computation and thought. Zandt and Ammon (1995) used equation 6-6 to identify systematic variations in the mean estimates of crustal thickness with tectonic province.

Clearly, there are a number of problems that are likely to arise in an analysis of observations of this type. Earth's crust can be strongly heterogeneous and the simple assumptions that are used in this method are certainly going to be violated in more than one instance during a large reconnaissance study such as this. However, the large number of observations may allow the most important trends in crustal structure to rise above the scatter of individual observations. We draw no conclusions from single measurements and focus our attention on creating a large set of measurements suitable for exploring the major trends in the data - if any exist.

6.3 Observations - processing and organization

An obvious advantage in studying such an extensive region as North America is that various tectonic environments are investigated and therefore, different proposed crustal composition scenarios could be tested. In this case, the basic tectonic regions discussed in Chapter 5 are the subject of analysis. The Paleozoic folded belts, represented by recording sites in the Appalachian mountain system and the Innuitian Folded belt region, are treated here as a special group of orogens with the intention of investigating differences with the younger (*i.e.* Mesozoic and later) orogens. Also, the San Andreas Fault system has been treated as a separate group because of its involvement in recent tectonic activity.

Table 6-1 is a compilation of the average values of Poisson's Ratio for each station for which we had measurements. Average values for each station are listed, even though the measurements were made for each azimuth and distance clustered receiver function stack. Average V_P values listed in Table 6-1 were used as central values for the estimation of σ values in each tectonic setting group of stations. Radial receiver functions were computed using iterative deconvolution (Chapter 4) with a Gaussian-width parameter of 2.5. Receiver function stacks where low-pass filtered using a corner period of 3 seconds. The peak time of *Ps* and *PpPms* phases were manually picked in all signals. Once these times are measured we estimated values of V_P/V_S and crustal thickness using equations 6-5 and 6-6. Both equations equations require an assumption of a mean crustal P-wave velocity. In practice a range of P-velocities was investigated and the change in estimated Poisson's ratio is reflected in the uncertainty listed in the table. Still, the affect of this assumption on the results must be kept in mind when interpreting the results.

As discussed earlier, lateral heterogeneity can cause problems with receiver-function-based Poisson's ratio measurements. Therefore, after an initial suite of measurements, those signals which resulted in obviously extreme σ values (*i.e.* above 0.4 and/or below 0.1) were rejected. The exclusion of outliers resulted in a collection of observations from 82 stations distributed throughout the study region.

The complete set of measurements are provided in Appendix 3. The median value of Poisson's ratio for each station is shown on the map in Figure 6.4. Blue symbols identify sites with higher than the median Poisson ratios, red symbols identify sites with lower than the median ratios. No simple, overall pattern is discernible in the ratio map, which contains all the measurements without regard to quality. Undoubtedly some of the observation shown on the map are outliers. This should be expected in such a large survey of structures using a relatively simple assumption of simple structure.

To simplify our discussion of the results, we organized the measurements into groups, classifying stations by the tectonic province in which they are located. Of course some station are on the boundary of two provinces and some lateral variations are likely to be masked by the course grouping of measurements. The geologic classifications used to divide the observations are illustrated in Figure 5.1 on page 84. The results are displayed in Figure 6.6 through Figure 6.10. Each plot

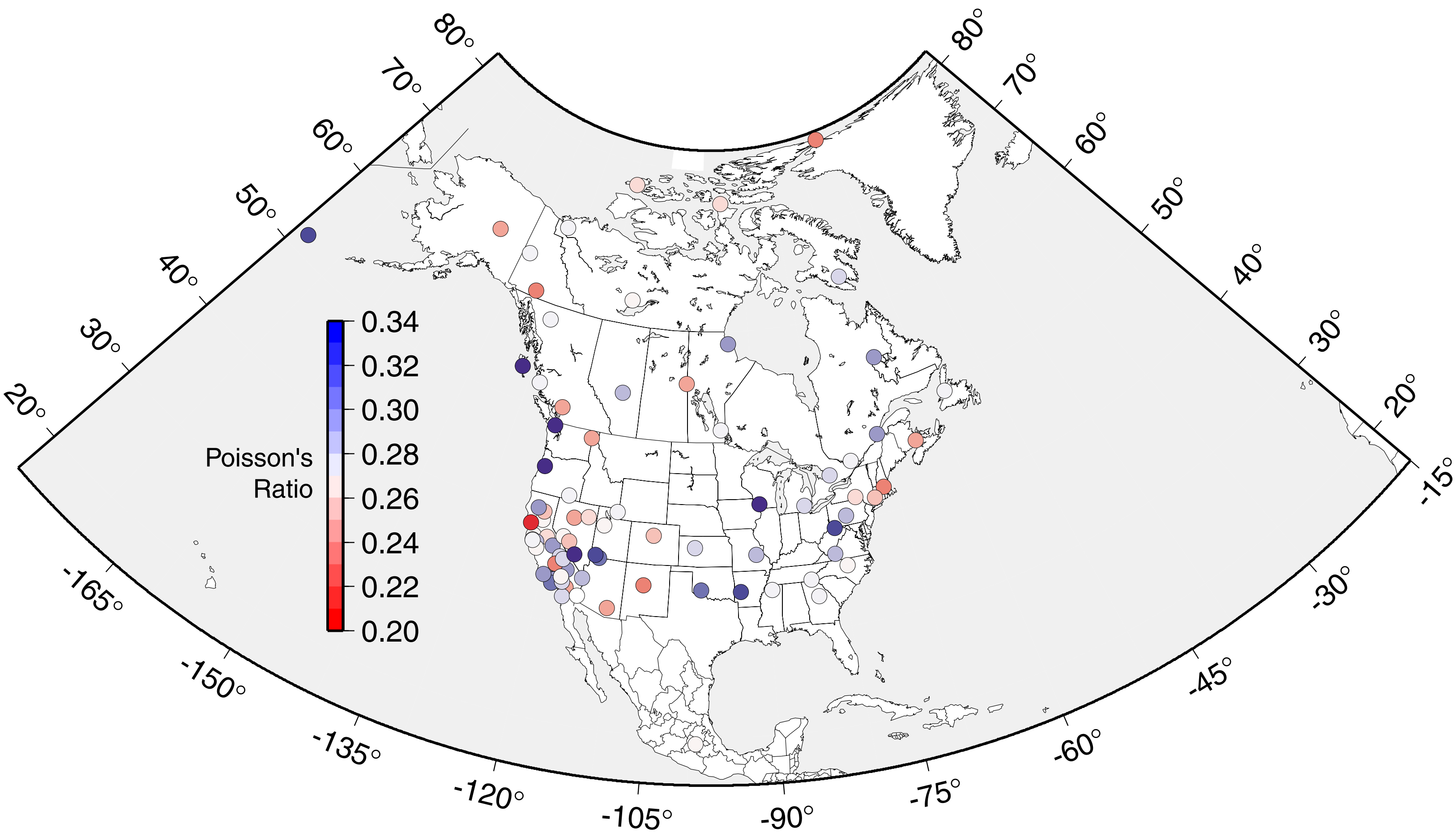

Figure 6.4 Poisson's Ratio observations for North America. Each symbol is the same size, red values are lower than the median, blue values are higher than mean (the average and median a very similar). See text for discussion.

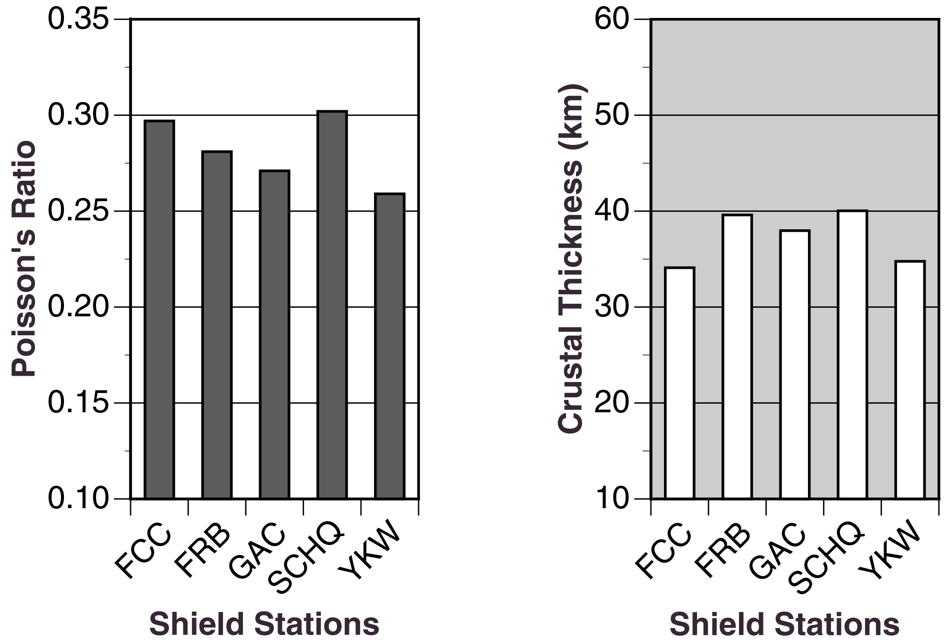

Figure 6.5 Poisson's ratio and crustal thickness estimates (median values from all azimuths and distance ranges) observed at seismic stations located on shields. Station locations are shown in Figure 5.2 on page 89.

shows the variations in the median values of Poisson's ratio and crustal thickness (estimated using equations 6-3 and 6-5, and 6-6 respectively). That is, the value shown is the median for all azimuths and distance clusters. Since some stations located near the boundary between disparate tectonic provinces, the median values may not be indicative of both provinces. For convenience in displaying the results, we split the California coastal measurements from the others (there are numerous stations in the state). Although this division was constructed only for convenience, as described in the next section, the observations from this transform boundary region show a systematic variation from other measurements. A numerical tabulation of the results is presented in Table 6-1 .

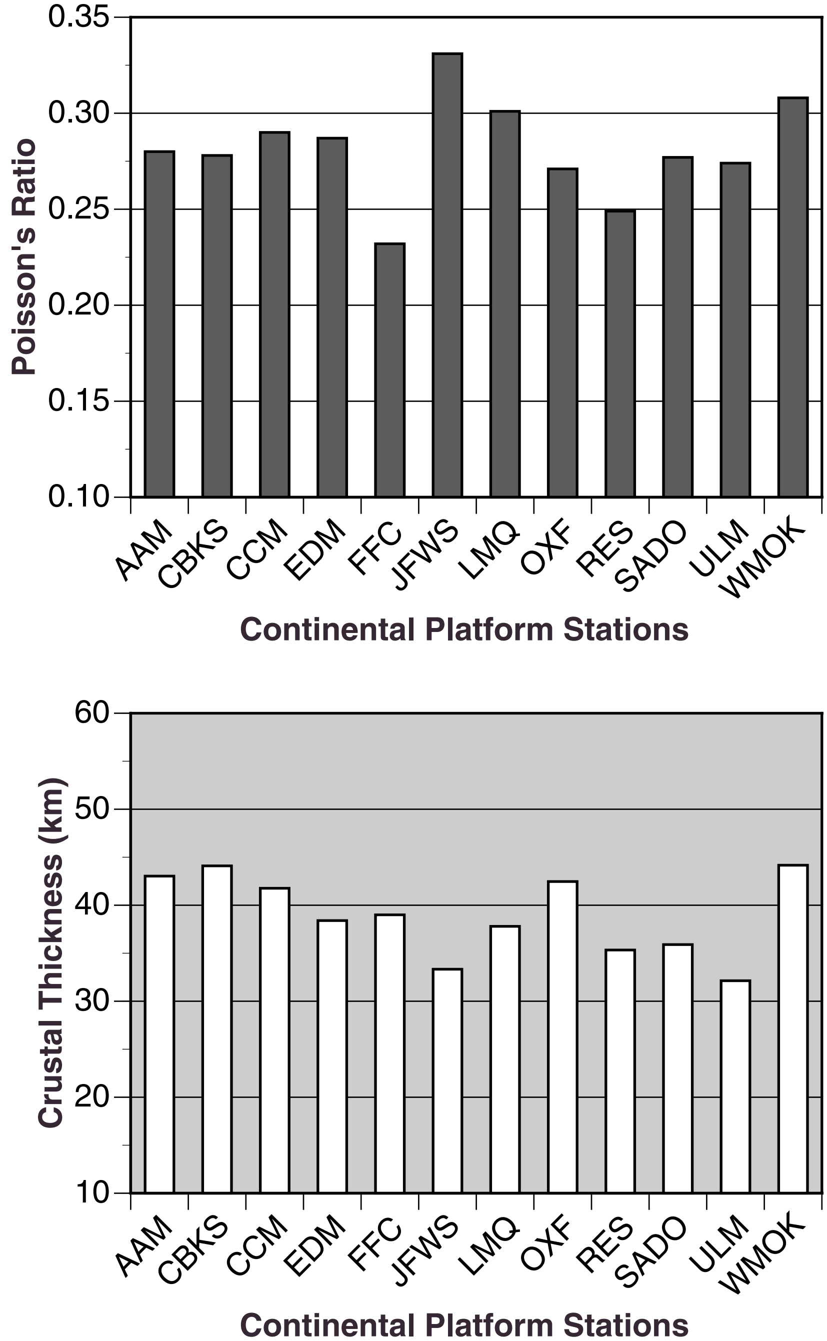

Figure 6.6 Poisson's ratio and crustal thickness estimates (median values from all azimuths and distance ranges) observed at seismic stations located on continental platforms. Station locations are shown in Figure 5.2 on page 89.

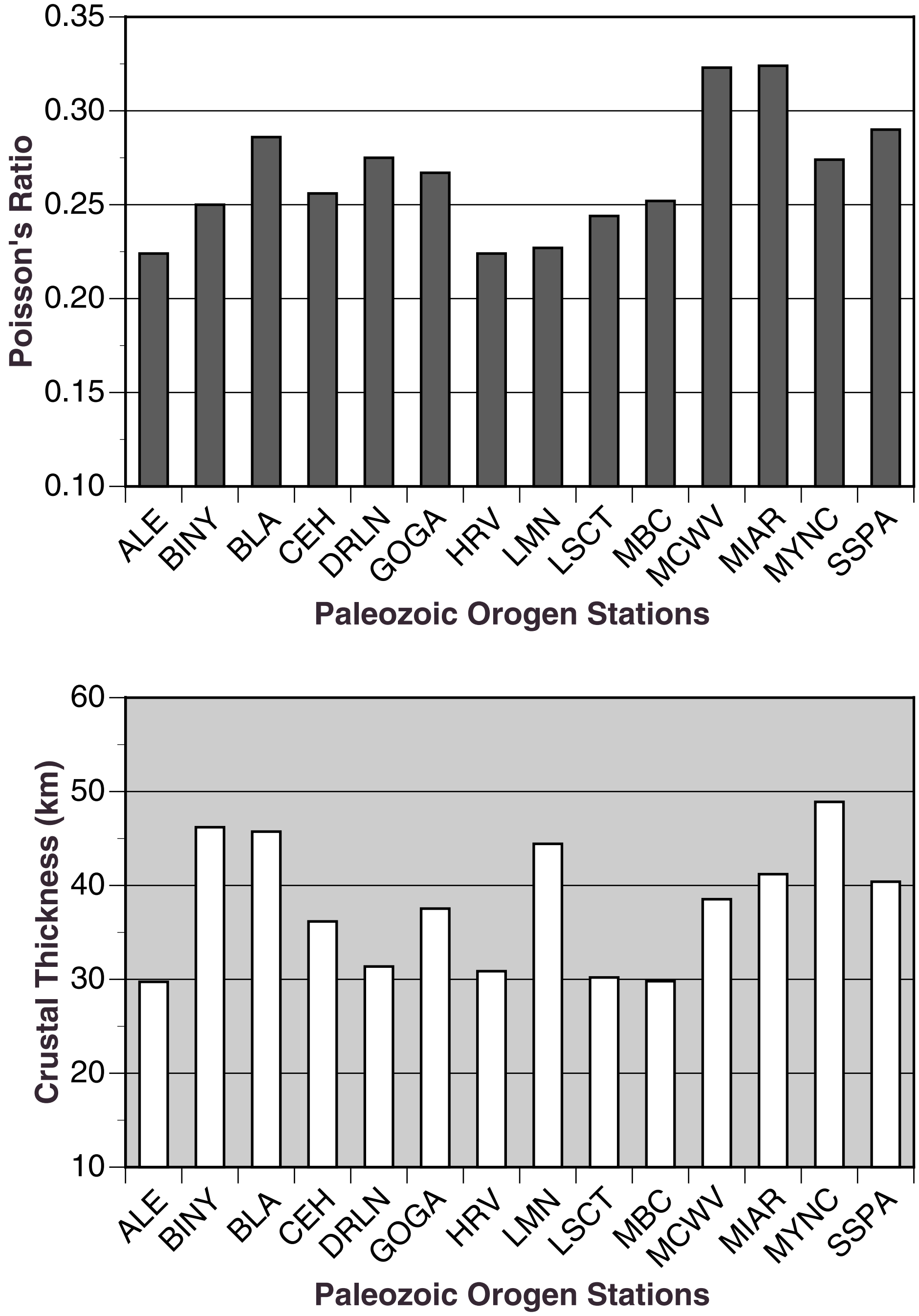

Figure 6.7 Poisson's ratio and crustal thickness estimates (median values from all azimuths and distance ranges) observed at seismic stations located on Paleozoic orogens. Station locations are shown in Figure 5.2 on page 89.

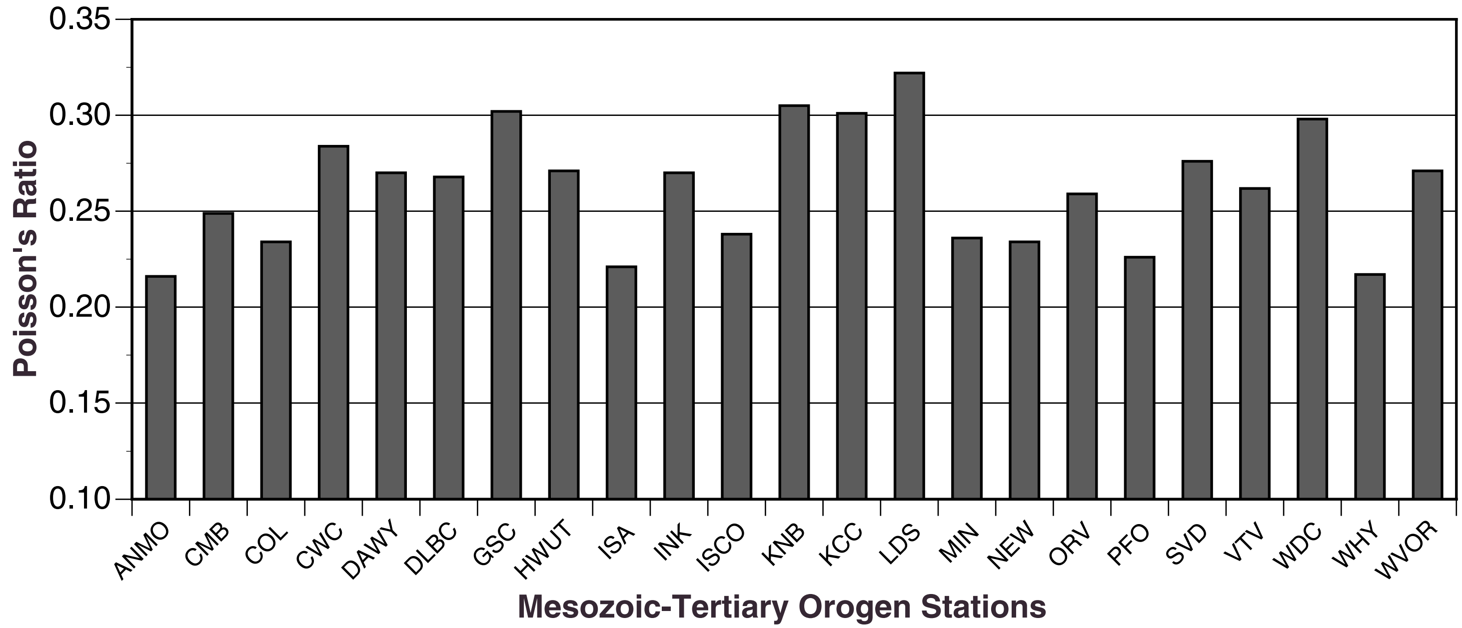

Figure 6-7a. Poisson's ratio and crustal thickness estimates (median values from all azimuths and distance ranges) observed at seismic stations located on Mesozoic-Tertiary orogens. Station locations are shown in Figure 5.2 on page 89.

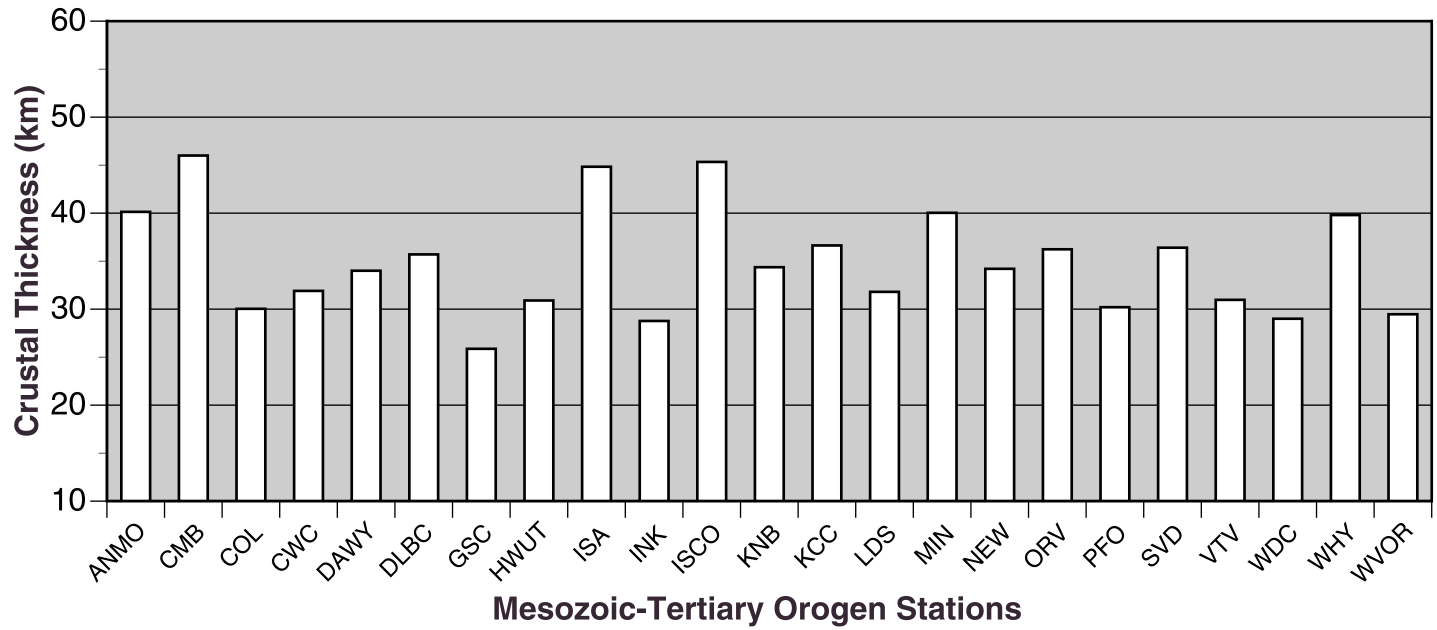

Figure 6-7b. Poisson's ratio and crustal thickness estimates (median values from all azimuths and distance ranges) observed at seismic stations located on Mesozoic-Tertiary orogens. Station locations are shown in Figure 5.2 on page 89.

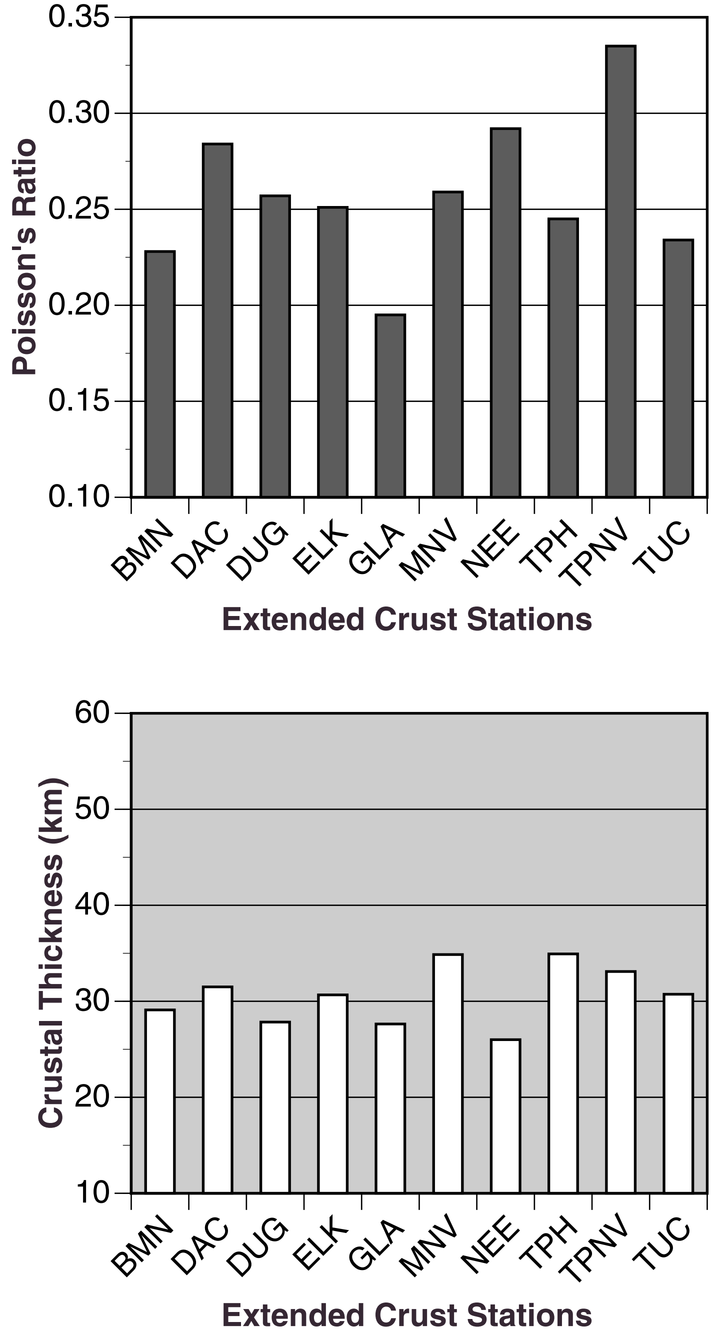

Figure 6.8 Poisson's ratio and crustal thickness estimates (median values from all azimuths and distance ranges) observed at seismic stations located on extended crust. Station locations are shown in Figure 5.2 on page 89.

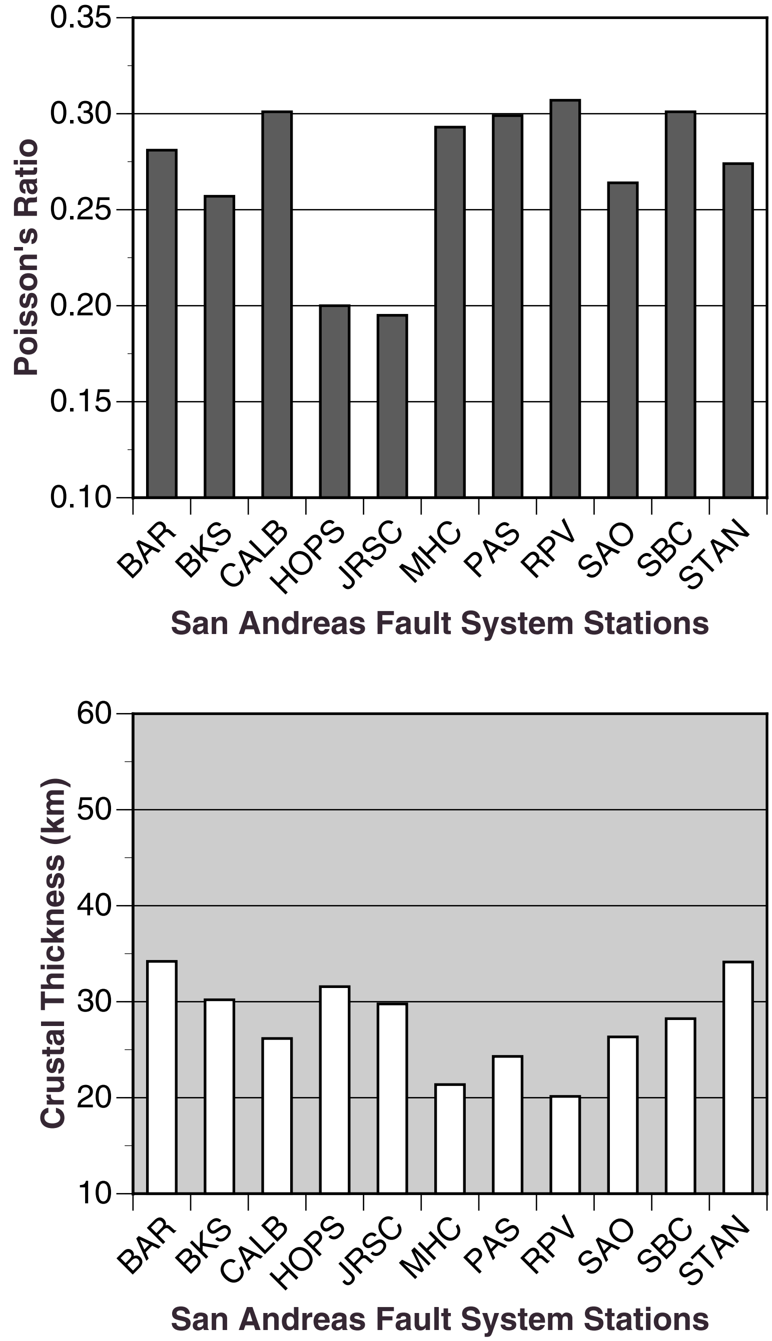

Figure 6.9 Poisson's ratio and crustal thickness estimates (median values from all azimuths and distance ranges) observed at seismic stations located in California's San Andreas Fault System. Station Locations are shown in Figure 5.2 on page 89.

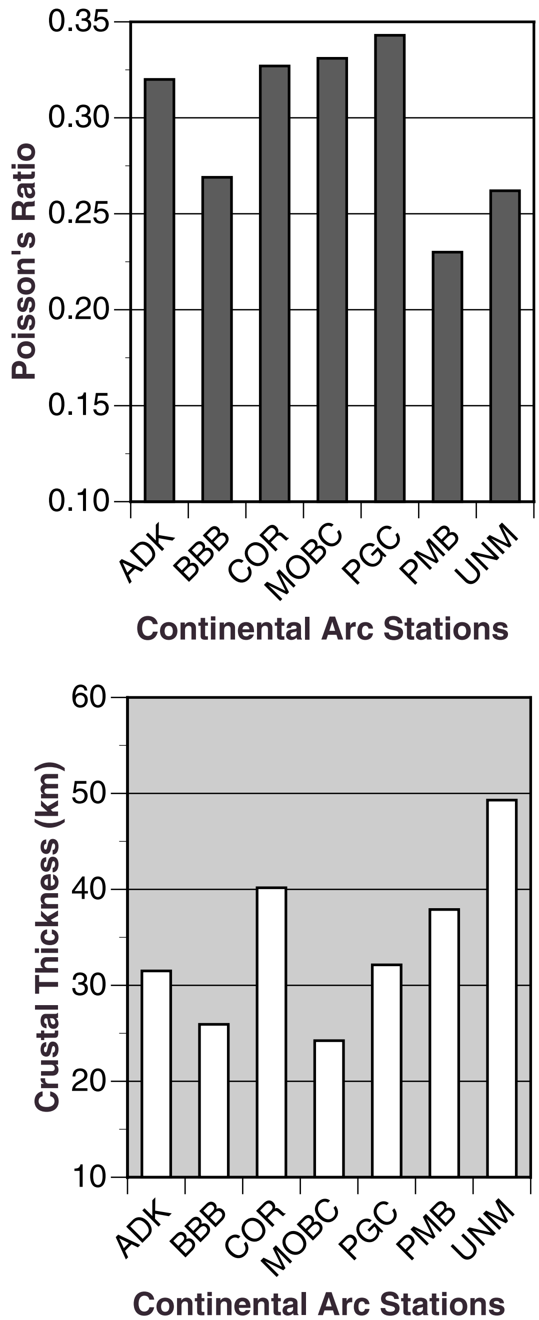

Figure 6.10 Poisson's ratio and crustal thickness estimates (median values from all azimuths and distance ranges) observed at seismic stations located on continental arcs. Station locations are shown in Figure 5.2 on page 89.

6.4 Poisson's Ratio Variations Beneath North America

It is important to consider that the methodology followed in this study is based in the assumption of two idealizations of a more complicated reality: Horizontal layer

Table 6-1: Poisson Ratio Estimates

Station	Cluster	V_P/V_S	±	Thickness (km)	±	σ	±
Shield (V_p 6.42 – 0.2 km/s)							
FCC	3	1.86	0.02	34.09	2.18	0.297	0.007
FRB	9	1.85	0.21	39.62	5.60	0.281	0.055
GAC	6	1.79	0.05	37.97	1.23	0.271	0.018
SCHQ	4	1.90	0.15	40.04	7.87	0.302	0.044
YKW	13	1.78	0.15	34.76	3.50	0.259	0.055
Average	7.00	1.84		37.29		0.282	
Median	6.00	1.85		37.97		0.281	
Standard D.	4.06	0.05		2.74		0.018	
Continental Platform (V_p 6.42 – 0.2 km/s)							
AAM	3	1.83	0.16	43.03	4.98	0.280	0.054
CBKS	6	1.81	0.09	44.10	2.64	0.278	0.031
CCM	9	1.86	0.16	41.77	5.65	0.290	0.046
EDM	3	1.84	0.12	38.39	6.21	0.287	0.042
FFC	8	1.70	0.09	38.99	4.56	0.232	0.042
JFWS	3	1.99	0.02	33.34	0.72	0.331	0.005
LMQ	2	1.88	0.07	37.81	4.14	0.301	0.022
OXF	2	1.79	0.04	42.46	1.83	0.271	0.017
RES	5	1.74	0.09	35.32	15.50	0.249	0.038
SADO	3	1.82	0.16	35.88	5.66	0.277	0.051
ULM	4	1.79	0.03	32.13	1.51	0.274	0.011
WMOK	3	1.90	0.06	44.17	3.75	0.308	0.018
Average	4.25	1.83		38.95		0.281	
Median	3.00	1.83		38.69		0.279	
Standard Deviation	2.30	0.07		4.19		0.026	
Paleozoic Orogen (V_p 6.39 – 0.25 km/s)							
ALE	12	1.69	0.08	29.72	2.18	0.224	0.042
BINY	4	1.74	0.10	46.20	3.93	0.250	0.038
BLA	5	1.83	0.07	45.72	3.36	0.286	0.026
CEH	5	1.75	0.07	36.16	2.01	0.256	0.028
DRLN	4	1.80	0.04	31.36	1.98	0.275	0.013
GOGA	6	1.80	0.14	37.52	4.86	0.267	0.051
HRV	12	1.68	0.07	30.84	1.30	0.224	0.036
LMN	2	1.68	0.01	44.42	5.25	0.227	0.007
LSCT	4	1.73	0.09	30.19	3.31	0.244	0.040
MBC	10	1.75	0.09	29.78	2.16	0.252	0.039
MCWV	3	1.96	0.12	38.53	5.62	0.323	0.029
MIAR	3	1.96	0.03	41.18	2.26	0.324	0.006
MYNC	2	1.79	0.04	48.88	1.32	0.274	0.014
SSPA	6	1.88	0.20	40.38	9.07	0.290	0.063
Average	5.57	1.79		37.92		0.265	
Median	4.50	1.77		38.03		0.262	

Table 6-1: Poisson Ratio Estimates (Continued)

Station	Cluster	V_P/V_S	±	Thickness (km)	±	σ	±
Standard D.	3.39	0.09		6.79		0.032	
Mesozoic-Tertiary Orogen (V_p 6.39 – 0.25 km/s)							
ANMO	10	1.66	0.05	40.13	1.92	0.216	0.026
CMB	5	1.74	0.11	46.00	8.30	0.249	0.044
COL	9	1.71	0.11	30.05	3.56	0.234	0.052
CWC	2	1.83	0.07	31.91	3.32	0.284	0.025
DAWY	3	1.79	0.09	34.00	1.61	0.270	0.036
DLBC	4	1.78	0.09	35.70	4.40	0.268	0.036
GSC	9	1.89	0.11	25.88	3.11	0.302	0.030
HWUT	2	1.79	0.08	30.89	1.15	0.271	0.030
ISA	13	1.68	0.10	44.83	5.21	0.221	0.050
INK	7	1.80	0.14	28.78	6.37	0.270	0.050
ISCO	5	1.73	0.13	45.35	6.09	0.238	0.068
KNB	4	1.98	0.32	34.36	3.40	0.305	0.096
KCC	5	1.92	0.21	36.63	4.82	0.301	0.064
LDS	3	1.96	0.10	31.79	6.21	0.322	0.024
MIN	6	1.71	0.06	40.04	1.72	0.236	0.029
NEW	7	1.71	0.10	34.19	4.34	0.234	0.050
ORV	5	1.76	0.08	36.24	4.01	0.259	0.033
PFO	9	1.68	0.04	30.19	0.74	0.226	0.018
SVD	8	1.80	0.07	36.40	3.23	0.276	0.023
VTV	9	1.78	0.14	30.98	4.32	0.262	0.048
WDC	4	1.87	0.10	29.01	10.19	0.298	0.029
WHY	8	1.67	0.08	39.79	4.95	0.217	0.048
WVOR	8	1.82	0.19	29.47	3.64	0.271	0.059
Average	6.30	1.79		34.90		0.262	
Median	6.00	1.78		34.19		0.268	
Standard D.	2.85	0.09		5.63		0.031	
Extended Crust (V_p 6.21 – 0.22 km/s)							
BMN	9	1.69	0.06	29.12	1.16	0.228	0.029
DAC	5	1.84	0.12	31.50	1.07	0.284	0.044
DUG	4	1.75	0.06	27.85	2.24	0.257	0.028
ELK	6	1.74	0.07	30.68	1.18	0.251	0.032
GLA	7	1.63	0.06	27.63	1.55	0.195	0.037
MNV	8	1.76	0.05	34.86	1.25	0.259	0.022
NEE	5	1.85	0.06	26.02	2.14	0.292	0.020
TPH	7	1.73	0.07	34.95	1.13	0.245	0.034
TPNV	6	2.01	0.08	33.10	1.10	0.335	0.017
TUC	8	1.70	0.07	30.73	1.71	0.234	0.032
Average	6.50	1.77		30.65		0.261	
Median	6.50	1.75		30.71		0.257	
Standard D.	1.58	0.11		3.05		0.040	
California Coast ranges (V_p 6.05 – 0.21 km/s)							

Table 6-1: Poisson Ratio Estimates (Continued)

Station	Cluster	V_P/V_S	±	Thickness (km)	±	σ	±
BAR	9	1.85	0.16	34.22	6.42	0.281	0.064
BKS	4	1.75	0.05	30.22	4.10	0.257	0.021
CALB	5	1.88	0.08	26.19	0.85	0.301	0.023
HOPS	4	1.64	0.06	31.57	1.04	0.200	0.034
JRSC	3	1.63	0.03	29.77	0.58	0.195	0.021
MHC	6	1.85	0.09	21.39	1.33	0.293	0.029
PAS	8	1.89	0.17	24.31	2.78	0.299	0.041
RPV	5	1.90	0.04	20.16	4.24	0.307	0.012
SAO	6	1.80	0.19	26.36	1.93	0.264	0.068
SBC	5	1.88	0.06	28.25	3.24	0.301	0.018
STAN	2	1.80	0.12	34.16	4.38	0.274	0.043
Average	5.18	1.81		27.87		0.270	
Median	5.00	1.85		28.25		0.281	
Standard D.	2.04	0.10		4.71		0.039	
Volcanic Arc (V_p 6.44 – 0.25 km/s)							
ADK	7	1.95	0.10	31.51	2.13	0.320	0.022
BBB	3	1.78	0.06	25.93	0.78	0.269	0.024
COR	13	1.98	0.09	40.17	4.05	0.327	0.019
MOBC	2	2.07	0.41	24.24	3.54	0.331	0.085
PGC	1	2.05	0.00	32.13	0.00	0.343	0.000
PMB	2	1.69	0.00	37.90	0.43	0.230	0.061
UNM	5	1.78	0.14	49.33	7.07	0.262	0.053
Average	4.71	1.90		34.46		0.297	
Median	3.00	1.95		32.13		0.320	
Standard D.	4.19	0.15		8.73		0.043	

distribution and lateral homogeneity in the crust. In other words, any generalities about continental crust composition cannot be drawn without overseeing specific cases, which most likely will deviate from any average. However, interesting trends can be identified in terms of the average (mean and median) V_P/V_S, thickness, and σ values obtained for different tectonic settings. Actually, we prefer the median values of the different distributions to discuss the observed results.

In any survey with a large number of observations, some measurements are bound to be outliers. There are two reasons to look carefully at outliers. First, if the measurement is correct, the structure is unusual and worthy of note. Second, if the measurement turns out to be misleading, through careful examination we may learn something important about our methodology that will help us in future applications of the method. Before proceeding to a general discussion of the results, I discuss those stations with unusually low or high Poisson's ratios.

6.4.1 Investigating Outliers

6.4.1.1 Yellowknife, Canada

Station YKW-CN has the lowest median Poisson's ratio among shield-type sites. YKW is at the border between the Slave province (shield), and the Western plains (Precambrian platform). The site has been investigated in detail by Cassidy (1995), who described "significant lateral variations in the earth structure" in the vicinity of YKW. Indeed, receiver functions that sample crust from the shield area tend to higher σ values (above 0.29) whereas low σ values (below 0.25) are calculated from signals that travel through the platform crust, which may to be affected by the sedimentary cover of the western plains (Figure 6.11).

6.4.1.2 Flin Flon and Resolute, Canada

FFC-II and RES-CNSN: Although not significant, these two stations tend to have low σ values among the Continental platform sites. Low σ values at FFC would support the influence of a quartz rich sedimentary cover, as suggested by Zandt and Ammon (1995). A tendency that may also be reflected in RES-CNSN site, although

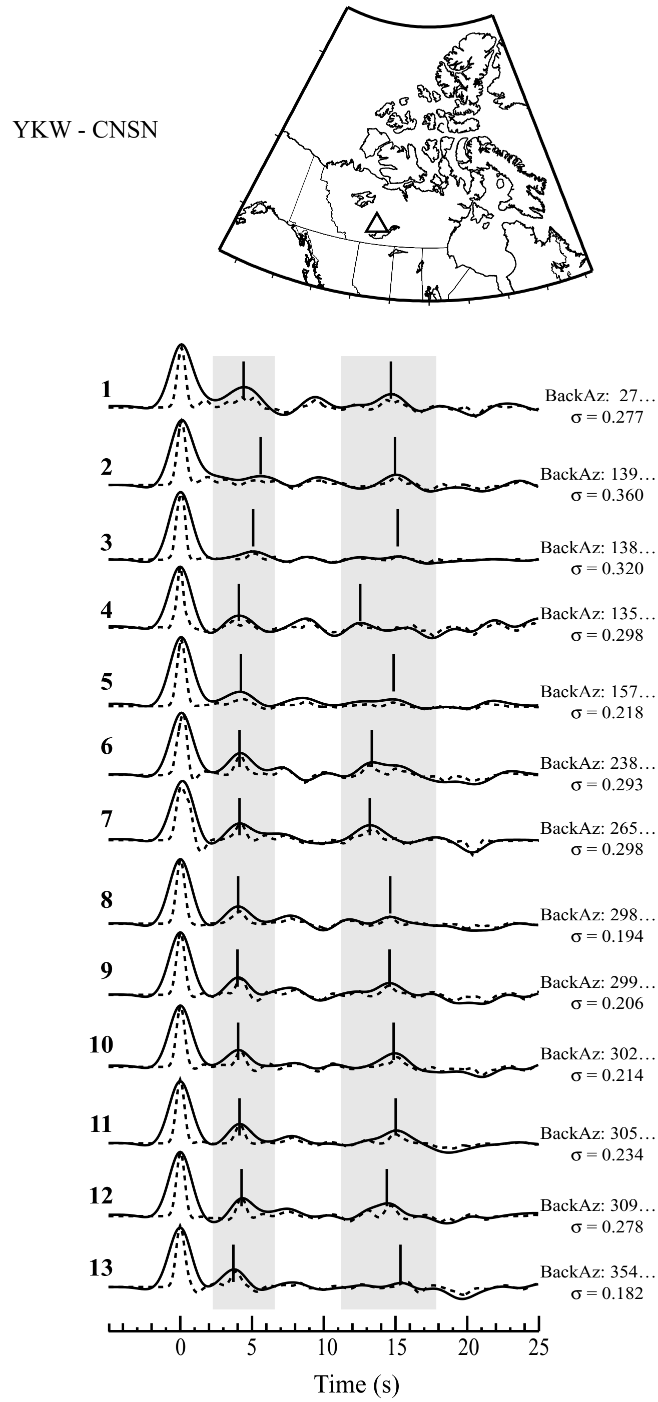

Figure 6.11 Radial receiver functions for station YKW-CNSN, located in Shield setting (onset map). The different back azimuth of arrival and estimated Poisson's ratio (σ) are indicated in the right edge of the signals. The gray boxes indicate the approximate time-window of the arrival of the *Ps* and *PpPms* phases. The number of identification of each cluster is shown to the left. (See text for discussion). The solid line is a filtered receiver function (used to make the time picks, which are indicated by the vertical lines) and the dashed line is a amplitude normalized version of the receiver functions (Gaussian width factor = 2.5), scaled to match the filtered signal amplitudes.

the proximity of this station to the Innuitian folded belts could also play a factor that bias the crust composition towards acid bulk composition.

6.4.1.3 Jewel Farm, WI, United States

JFWS-USNSN: This station's outstanding median (0.331) among platform sites could reflect a modest sedimentary cover (crustal thickness is around 33 km) combined with a strong Precambrian basement signature.

6.4.1.4 Mont Chateau, WV and Mount Ida, AK, United States

MCWV-USNSN and MIAR-USNSN: These two stations show the higher σ estimates among sites in Paleozoic orogens (Figure 6.12). MCWV is located in the western flank of the Appalachian thrust and signals coming from the south (clusters 1 and 2) are apparently being affected by structural complexities at the MCT, although transverse stacked signals do not show notorious higher amplitudes (Figure 6.12 (top)). The high σ value at station MIAR, on the other hand, may be an effect of conversions at a dipping structure, perhaps associated with the Ouachita mountains, as suggested by both the radial and transverse receiver functions stacks (Figure 6.12 (bottom)).

6.4.1.5 Goldstone, CA, Kanab, UT, Kaiser Creek, CA, and Leeds, UT, United States

GSC-TS, KNB-USNSN, KCC-BK and LDS-USNSN: Although it is not surprising to find high variability in Mesozoic-Tertiary orogenic crust, only four out of 23 stations show unusually high σ values ($\sigma \geq 0.30$). These four stations are all located in neighboring sites of the Basin and Range extended crust province. Station GSC has consistently high σ values (0.302 ± 0.03), perhaps due to its location on Pre-

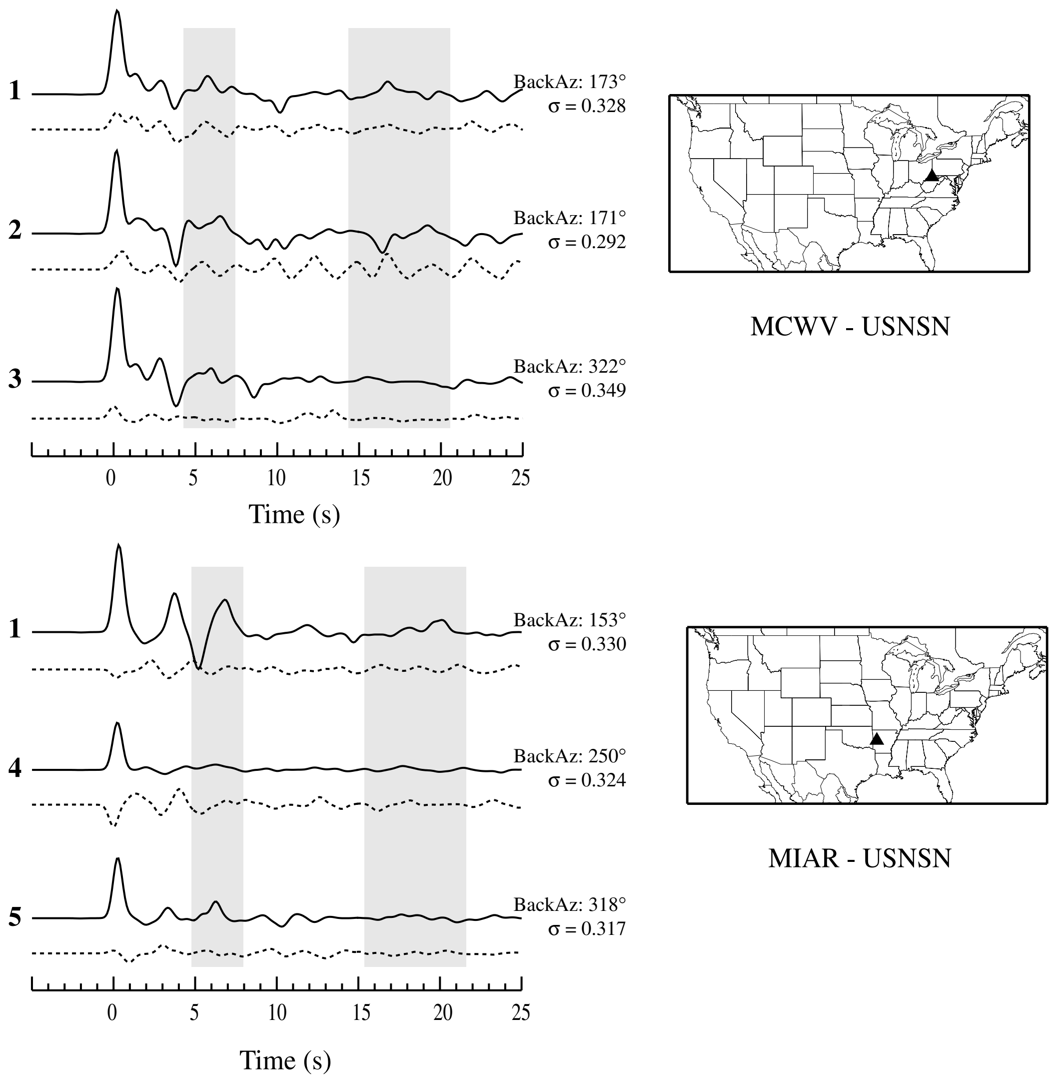

Figure 6.12 Time-domain receiver functions for stations MCWV (top) and MIAR-USNSN (bottom), located in Paleozoic Orogen settings. The transverse receiver functions are shown as dashed lines beneath the radial receiver functions. The gray regions identify the travel time windows for *Ps* conversions and multiples in typical crustal structures (See text for discussion).

cambrian metamorphic and plutonic rocks. KCC ($\sigma = 0.301 \pm 0.06$) is located nearby the active volcanic area surrounding Long Valley Caldera in eastern California, whose structural complexity is evident in moderate, yet consistent, transverse receiver signals. KNB ($\sigma = 0.305 \pm 0.09$) and LDS ($\sigma = 0.322 \pm 0.02$) are both located in the western border of the Colorado Plateau, a major physiographic province of Cenozoic age (Morgan and Swanberg, 1985) whose lower crust has been interpreted as a Garnet-bearing intermediate-to-mafic granulite and amphibolite (Padovani *et al.*, 1982). Thus, the high σ values at KNB and LDS are in good agreement with the influence of mafic partial melt systems interpreted by Benz and McCarthy (1994), at the Basin and Range-Colorado Plateau transition zone. The transverse receiver function stacks show notable amplitudes and low-velocity layer signatures in the radial receiver functions at KNB and LDS, suggest local structural complexity.

6.4.1.6 Tonopah, Nevada, United States

TPNV-USNSN: This is the only high σ value among the extended crust sites. All the receiver function stacks used for TPNV were calculated using signals arriving from the west-southwest or west-northwest, and the high measurement may be related to the influence of active volcanism present in that region. Although magmatic rocks in this area are mostly acidic, that would push Poisson's ratios towards lower values. The only way to increase the value would be with partial melt, but the data are not of the highest quality, and such a conclusion should be based on only the best data. Visual examination of the receiver-function stacks used for this station (Figure 6.13), indicates the complexity of the local structure (see notable amplitude of transverse signals).

6.4.1.7 HOPS-BK and JRSC-BK, United States

These two stations are the only sites where values are bellow 0.25 (0.200 and 0.195 respectively (Figure 6.14). The only four signals used for HOPS (all arriving from the southwest and northwest) show substantial local scattering, which could be due

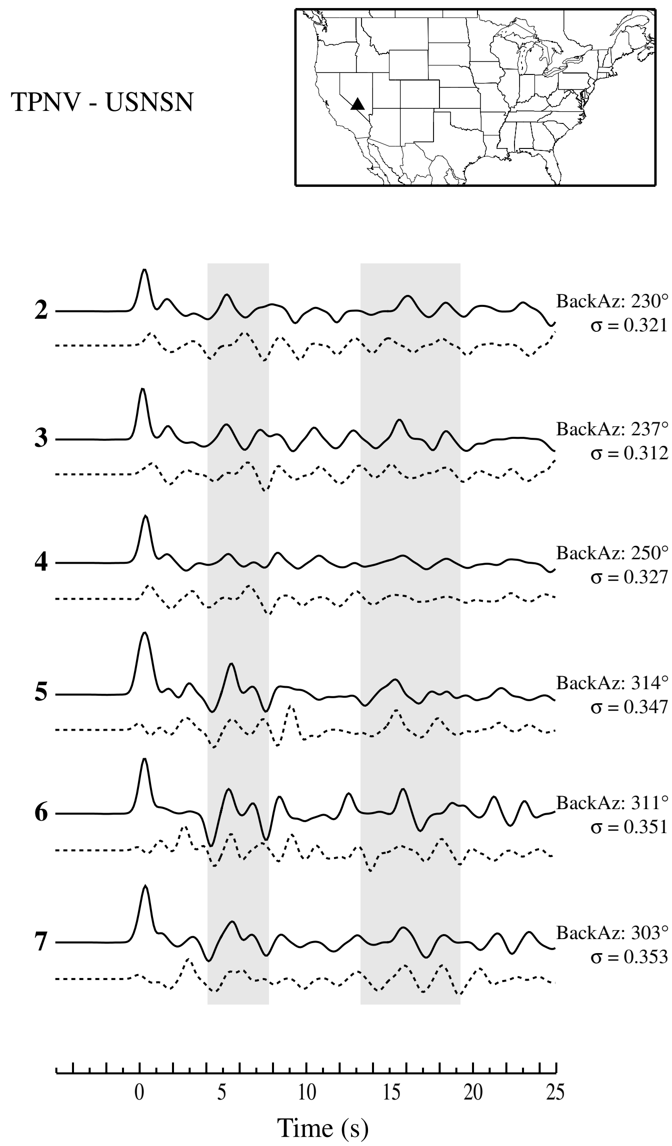

Figure 6.13 Receiver functions for station TPNV-USNSN located in an extended-crust setting. The transverse receiver functions are shown as dashed lines beneath the radial receiver functions (See text for discussion).

to structural complexities related to the San Andreas fault (Figure 6.14 (top)). A clear, but variable amplitude, *Ps* arrival is visible on all the stations, but no conclusions can be drawn from these signals, they violate the simple assumptions of the technique. JRSC receiver functions, on the other hand, show the presence of a sur-

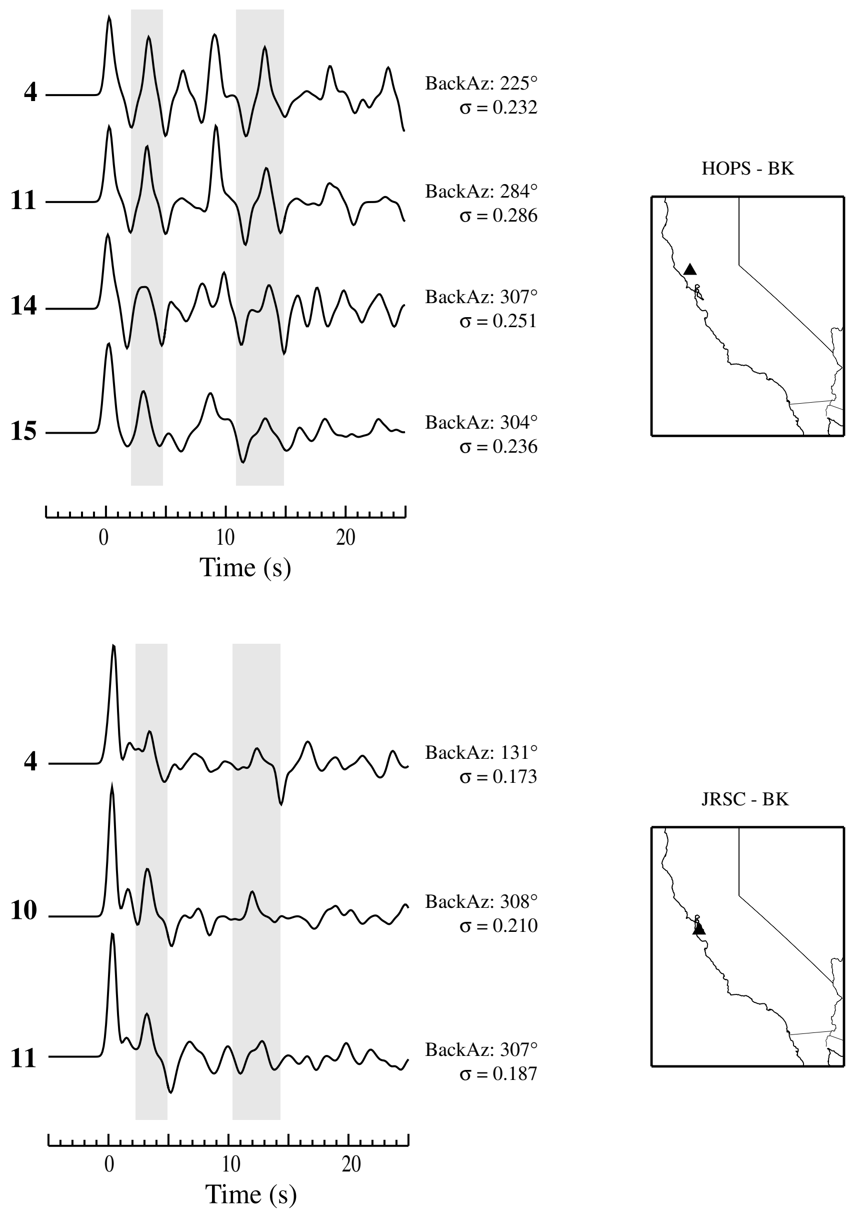

Figure 6.14 Radial receiver functions for stations HOPS-BK (top) and JRSC (bottom), located in California Coast-ranges. The notation is the same as in Figure VI.6 (See text for discussion).

face low velocity layer (Figure 6.14 (bottom)) but are not that complex. Clear candidates for the *Ps* and *PpPms* arrivals are visible in the shaded regions of 6.14 (bottom). The extreme low values for the southeast back azimuth may be biased by interference with scattered waves, but the low values from the northwest were measured from relatively simple receiver functions.

6.4.2 General Observations

The median value of V_P/V_S (1.794 ± 0.098) from all of our measurements is marginally higher than the average continental crust value (1.768), reported by Christensen and Mooney (1995) for a worldwide survey; with the V_P/V_S estimates at orogens (1.77 at Paleozoic and 1.78 for Mesozoic-Tertiary) approaching that global mean. The highest values obtained here, were those in volcanic arcs (1.95) and precambrian settings (1.85 and 1.83 for shields and platforms respectively). This observation would support the idea that V_P/V_S increases with temperature, pressure and partial melting (Anderson, 1989) and a refractory nature of Precambrian crust.

6.4.3 Poisson's Ratio

The overall Poisson's ratio average and median values coincide (0.270 and 0.271, respectively), in good agreement with average values for continental crust values reported by Christensen (1995) and Zandt and Ammon (1995). The highest median value corresponds to volcanic arcs (0.320 ± 0.043), which suggests these regions may have a dominant mafic composition, fluids (partial melt) or both. The story is more complicated however, since arc measurements actually split into two groups. Stations with low Poisson's ratio values are BBB, PMB, and UNM, which are all located on continental material. So are several of the other stations. The scatter could be a result of the difficulty of making the measurements in regions of complicated geology, or may indicate a variation within the arc province. With more observations we can do little more than note the variation.

The median values observed in shields (0.281± 0.018) and platforms (0.279 ± 0.026) overlap with the high σ estimates reported by Zandt and Ammon (1995) (0.29 ± 0.02 and 0.27 ± 0.03, respectively) which they interpreted as an indication of mafic lower crust composition. The California coast-ranges have notable high σ value with high variability (0.281 ± 0.039), which could reflect the influence of multiples signals from the south- and northwest Pacific ocean crust (*e.g.* CALB, RPV, SBC) and/or the moderate sedimentary cover in the Great Valley, underlain by the oceanic (Franciscan) basement (Irwin, 1990). Orogens show Poisson's ratio values below the 0.27 overall average (Paleozoic σ = 0.262 ± 0.031, Mesozoic-Tertiary σ = 0.268 ± 0.031), that would be expected from an upper crust material (sediments and dominantly felsic aggregates) recycling and/or thickening.

The relatively low values obtained in extended crust (0.257 ± 0.040) can be interpreted in several ways. One is to conclude that the Basin and Range crust includes a limited mafic contribution and is predominantly a thin felsic crust. Previous seismic refraction work in the Basin and Range region (Jarchow *et al.*,1993) favored mafic crust composition induced by active magmatic underplating, the presence of repeated metamorphic events in several locations could explain the involvement of upper crust material in the overall crustal composition. Investigating the variations in MCT structure, that is the subject in the following chapter, could test the latter hypothesis.

6.4.4 Crustal Thickness

Crustal thickness estimates are formally less reliable than V_P/V_S and σ values, due to their enhanced sensitivity to the assumed average crustal P-velocity values. Still, the patterns are in many ways simpler than those associated with Poisson's ratio. Our knowledge about the crustal thickness is much better than that of Poisson's ratio, so these results actually provide somewhat of a check on the identification of the *Ps* wave. Estimates of crustal thickness are summarized in Figure 6.15. Several trends are clear on the illustration. First, the crust is thin beneath the western conterminous United States - as expected from decades of other studies. A few stations with thicker than average crusts in the region are located along the spine of the Sierra Nevada (CMB, ISC). Coastal stations are also generally thinner than average. Stations in the U.S. Great Plains and along the spine of the Appalachian Mountains are thicker than average. The values for crustal thickness beneath the shield region of Canada are thinner than expected.

6.4.5 Do Poisson's Ratio and Crustal Thickness Correlate?

Since we've collected measurements of two fundamental parameters of the continental crust, it is natural that we would look for a correlation between the measures. In fact, if the evolution of the crust was a simple, step-by-step process evolving arc-like structures into shield like structures with thicker crusts while steadily modifying the composition of mafic to intermediate, we might expect a simple correlation. Such a simple view of continental crust, which is the product of billions of years of plate interaction and mantle convective processes is unlikely. The evidence is

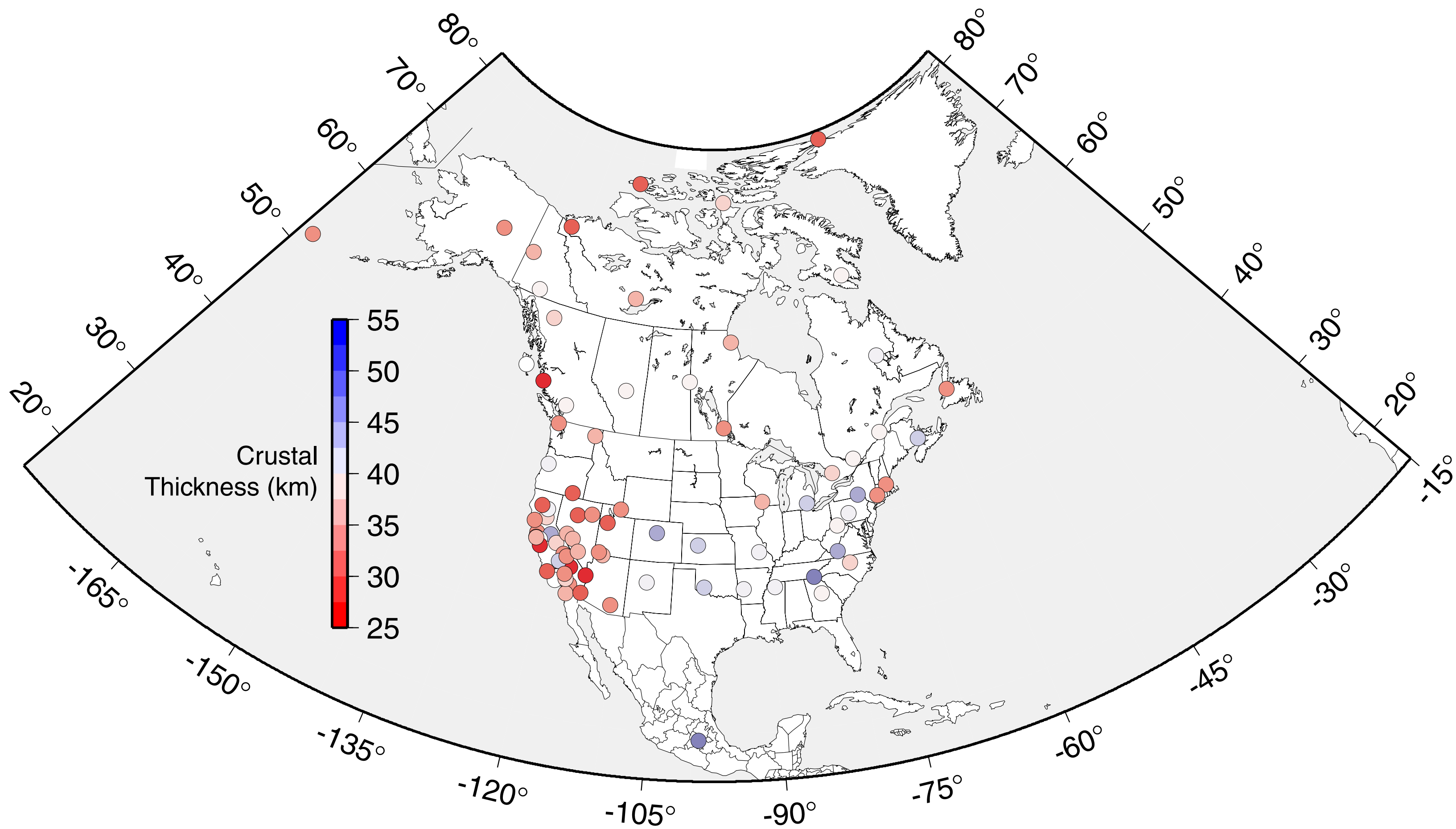

Figure 6.15 Crustal thickness estimates for each station. Values less than 40 km are shown with shades of red, those with crusts thicker than 40 km are shown in shades of blue. See text for discussion.

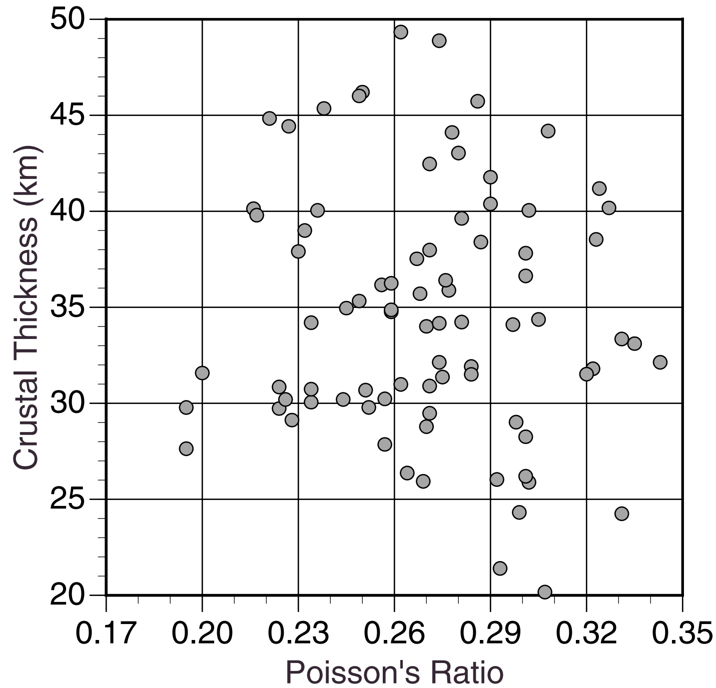

Figure 6.16 Variation of Poisson's Ratio with crustal thickness. The two properties do not correlate well.

shown in Figure 6.16. A breakdown of the measurements is presented in Figure 6.17. The only province which shows a visible correlation between the two values is the Mesozoic/Tertiary orogenic crust, which shows a tendency towards low Poisson's ratios in regions of thick crust. Even in this case, however, a thick crust is not a prerequisite of a low Poisson's ratio.

6.5 Discussion

A number of interesting trends in crustal parameters were uncovered in the study. The results are summarized in Figure 6.18 and Table 6-2. The "oldest" crust is shown on the left, the amount of "active deformation" is higher on the right. Poisson's ratio is shown on the top, crustal thickness on the bottom. The error bars represent plus or minus the absolute median deviation from the median. The stippled

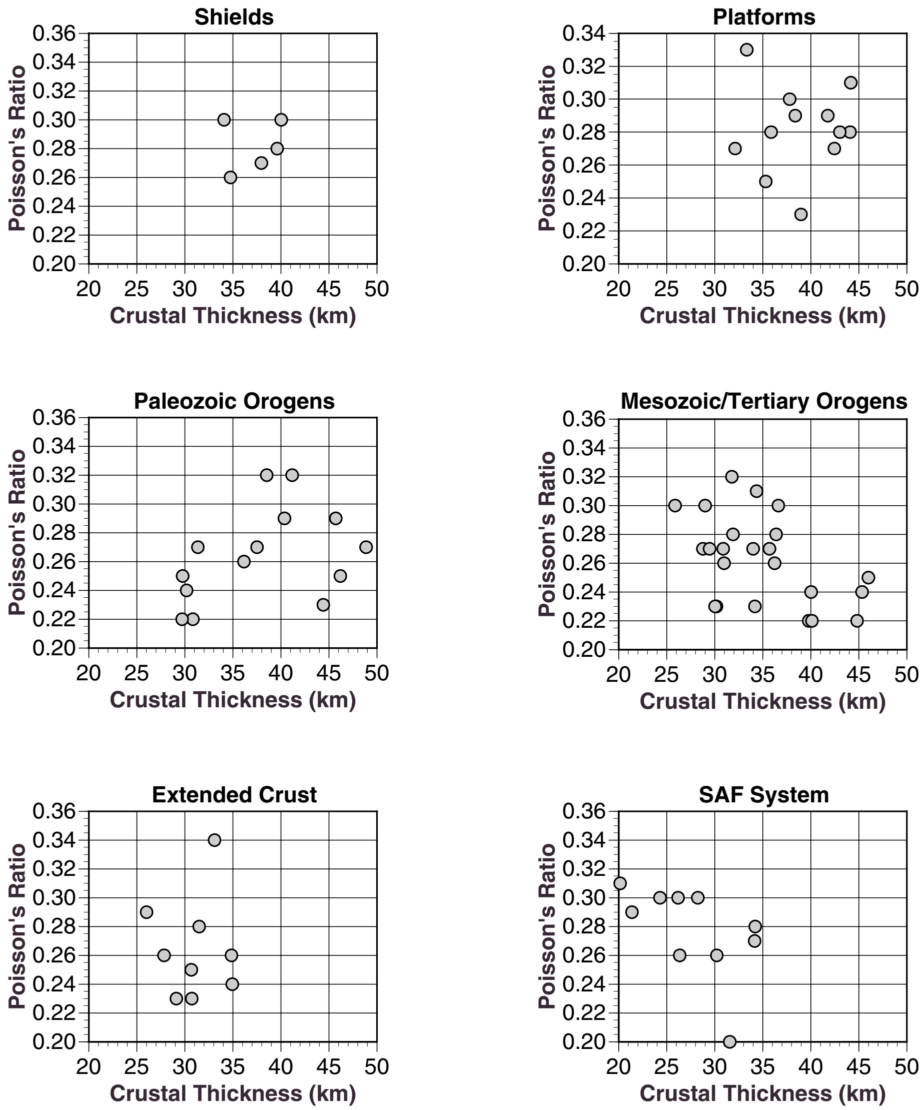

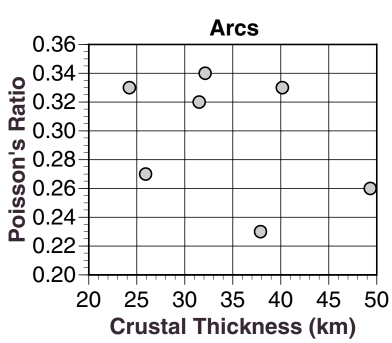

Figure 6.17 Variations of Poisson's ratio and crustal thickness for each tectonic province. The results show little correlation between the values, except for an apparent correlation between thick crust and low Poisson's ratios beneath Mesozoic and Tertiary orogens.

region on the Poisson's ratio plot indicates the region with lower-than-average values compared with the global survey of 114 stations by Zandt and Ammon (1995). The variation of Poisson's ratio from province to province is complex, and

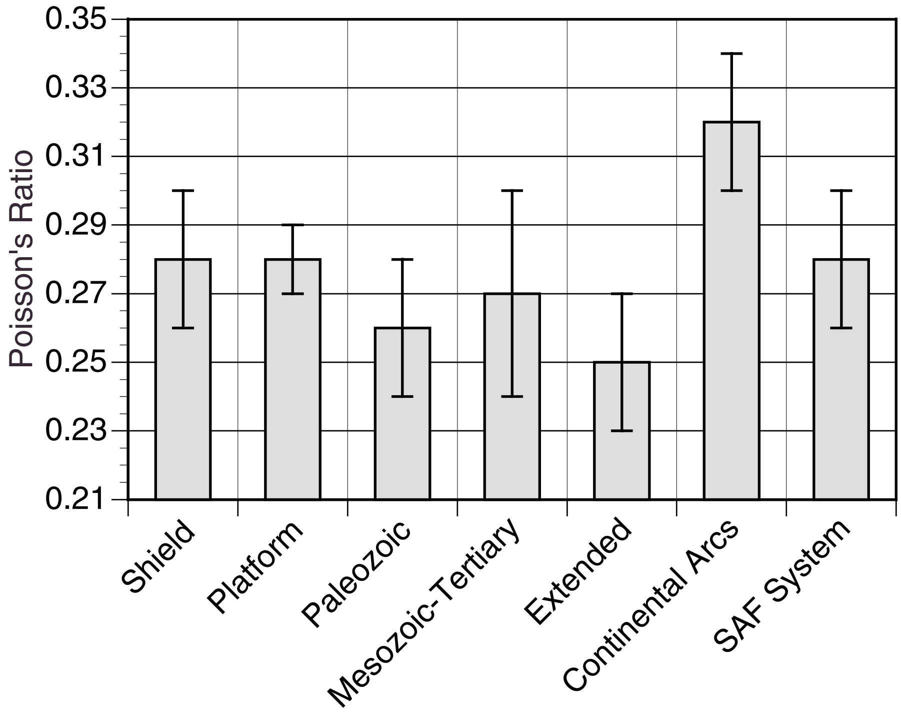

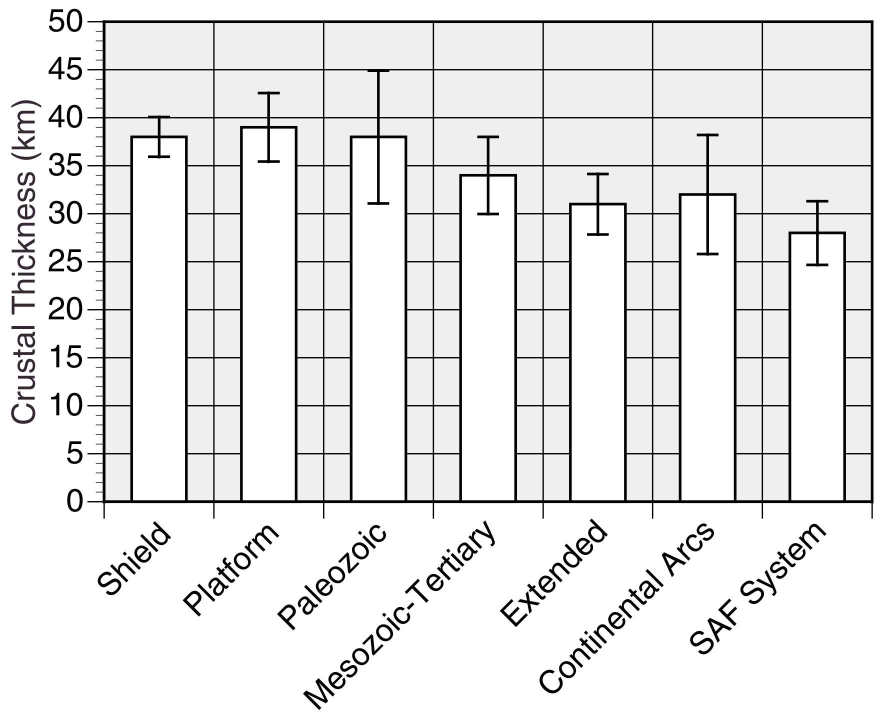

Figure 6.18 Summary of measurements. The median Poisson Ratio (top) and crustal thickness (bottom) values and median absolute deviations from the median for each tectonic province are shown. See text for discussion.

there appears to be no simple evolution of from a high value to a low value of Poisson's ratio with "tectonic age". However, the observations are intriguing.

The median shield and platform median values are above the global average, perhaps indicating a slightly more mafic composition as suggested in Zandt and Ammon (1995). Our results suggest that the picture may be more complicated. The Paleozoic mountain ranges (the Appalachian region) show a lower than average median value, indicative of a more silicic composition. The younger orogenic regions in the western part of the continent show the largest variability with a median value equal to the global average. Variations in these regions are large enough to be hiding some more intriguing geologic variations that may become more clear as more stations are installed and observations are collected.

Perhaps the most interesting observations in the collection are those for the extended regions of the crust. Poisson's ratio values are consistently low for these stations (mostly in the Basin and Range). The estimated crustal thickness for these stations is also internally consistent, the crust is uniformly thin beneath the sites, undoubtedly as a result of extension. The low Poisson's ratio values for these sta-

Table 6-2: Median Values for Each Tectonic Province

	Median Poisson's Ratio	Median Absolute Deviation	Median Crustal Thickness (km)	Median Absolute Deviation (km)
Shield	0.28	0.02	38	2.1
Platform	0.28	0.01	39	3.6
Paleozoic	0.26	0.02	38	6.9
Mesozoic-Tertiary	0.27	0.03	34	4.0
Extended	0.25	0.02	31	3.2
Continental Arcs	0.32	0.02	32	6.2
SAF System	0.28	0.02	28	3.3

tions are consistent with a silicic composition. And if this crust began as arc-like material, it has since that time evolved to a more felsic composition. We cannot say whether extension or earlier deformation episodes caused the change since the region has a long history of tectonic activity associated with subduction along the western margin of North America. Since the orogenic regions also seem to have more felsic compositions (than arcs), an argument could be made that at least part of the transition from mafic to felsic material in the extended crust probably occurred during earlier episodes of deformation. I point out however, that the path from arc-like to felsic composition need not be unique; many different tectonic histories could cause the transition in composition. However, felsic rocks are not the only materials that can have low Poisson's ratio and the crust beneath the Basin and Range could still be more mafic.

In the above discussion I dealt with median values of the parameters, which are less sensitive to the outliers in the data. For completeness, I conclude with a list the average and standard deviation values show similar trends. Crustal thickness values are thicker beneath shields (38 ± 3) and platforms (39 ± 4), which show notably low standard deviations. Orogenic crust, on the other hand, shows larger variability (± 7 in Paleozoic, ± 5 in California Coast-Ranges and ± 6 in Mesozoic-Tertiary), that reflects its structural complexity. Volcanic-arc crustal thickness has a large standard deviation (±9) that could be attributed to offshore stations (ADK, BBB and MOBC) although volcanic regions are structurally complex settings. Stations on extended crust have thinner crust (31 ± 3), a result that supports previous observations in the Basin and Range province (Mooney and Braile, 1989).

6.6 Conclusions

The observations suggest that transformation from arc-like crust to shield-like crust is more complicated than a simple smooth evolution. Measurements from continental arcs are consistent with a mafic composition, which is consistent with geochemical arguments for arc composition. If continental crust is born at arcs, it starts out with a mafic composition. Since on average the crust has a more intermediate composition, this means that crust must evolve to a more silicic composition. How does it evolve? The values measured for stations located in regions with recent orogenic events suggests a more silicic value. Together these observations suggest that orogenic processes lead to a relative increase in silica, perhaps by delamination processes that remove mafic material from the lower crust when increases in thickness push the lower crust deeper. Extended crust appears to be even more silicic than the orogens, which suggests that large-scale extensional processes may also mechanically favor a decrease in mafic content. It is not clear how this may proceed physically, but the extended region measurements are some of the most consistent in all the observations. The thicker and more intermediate structures of the shields and platforms suggest that later alterations to continental crust may include the underplating of more mafic material in the lower crust to bring the average composition.

These results are intriguing and raise many questions regarding the evolution of the continents, but perhaps most importantly we have identified trends in the characteristics of the crust upon which future research, benefitting from more dense seismic station coverage, may shed more light.

7 THE MANTLE-CRUST TRANSITION BENEATH NORTH AMERICA

Earth is unique in a number of ways, it's the only known planet to harbor life, the only planet in the solar system with large quantities of liquid water, and the only planet in the solar system that has a highly differentiated, enriched crust (*e.g.* Condie, 1993). Earth has two types of crust, continental (the focus of this study) and oceanic. The continents are much thicker and are comprised of lighter material, and their buoyancy results in the elevation well above the ocean floor. Although the continental crust accounts for a fraction of one percent of the planet's mass, it contains a large portion of the budget for several elements, including more than 30% of the heat producing elements, K, U, and Th (Taylor and McLennan, 1995). These facts, together with our obvious dependence on this region for survival, provide ample incentive for investigation of the continents.

Perhaps the most important scientific reason to study the continental crust is the fact that it houses most of our information on most of our planet's history. Packing all that information beneath about one-third of Earth's surface created complexity in geologic structure and composition. The relative simplicity of the "young" oceanic crust is a sharp contrast with the battered and weathered continents. Partially because of the availability of information from the simpler, younger oceanic litho-

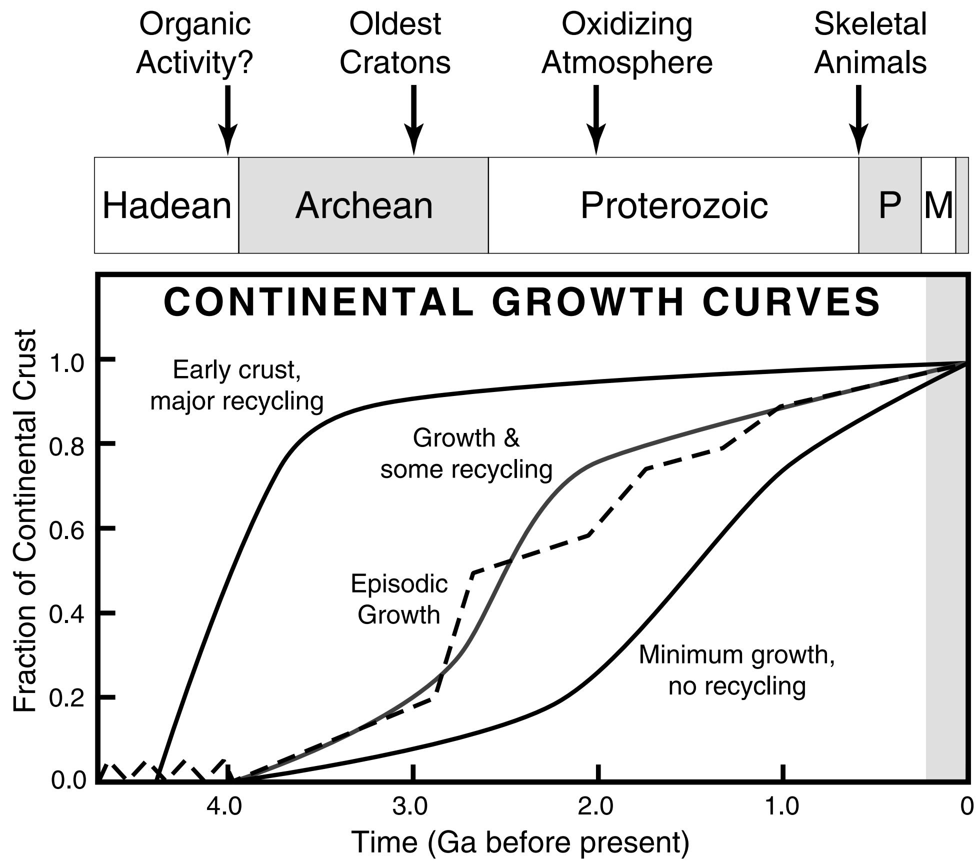

Figure 7.1 Viable growth curves for Earth's continents. The uncertainty is large, but the intermediate model with episodic growth is most favored. In general, models with about 50%-60% of the continents by about 2.5 Ga are common. In the time chart at the top, P indicates Paleozoic, and M Mesozoic. Illustration courtesy of C. J. Ammon, sources Brown and Musset (1993), Rogers (1993), Levin (1994), and McLennan (1992).

sphere, the history of the continents is reasonably well known for the last few hundred million years. But the farther back we probe, the more uncertain our reconstructions become. The prime example of our uncertainty is the fact that we remain unsure of the growth rate of the continents (Condie, 1993; Taylor and McLennan, 1995). The range of acceptable models for crustal growth is substantial (Figure 7.1) ranging from early, rapid growth with recycling to more moderate, steady growth, with alternatives for episodic surges in continent production. The favored model is intermediate in growth rate, with at least 50% of the continents in place by about 2.5 Ga, to satisfy freeboard constraints (Taylor and McLennan, 1995). Episodes of crustal growth are thought to occur at times of supercontinent assembly, when arc activity is near a maximum because the amount of subduction is great. Also continental collisions associated with super-continent formation would produce large scale crustal thickening and melting which would create more stable continental material suitable for long term survival (Taylor and McLennan, 1995).

Estimating the growth rate of the continents requires an understanding of the processes that produce continents, such as island or continental arc magmatism, and possibly, crustal underplating. Since the Archean, island arc accretion is thought to have dominated the production of new continental material, although large-scale volcanism which produces oceanic plateaus (*e.g.* Ontong Java) may have contributed significantly to the continents in the past (Abbott and Mooney, 1995). The level of their contribution depends on the subductibility of oceanic plateaus, which in turn depends on the nature of the lower crust beneath these structures (Neal *et al.*, 1997).

Lingering on the sidelines of any discussion of continental growth is the possibility of underplating material directly to the base of continental crust (*e.g.* Furlong and Fountain, 1986; Rudnick, 1990). Understanding the nature and amount of underplating is a challenge because few examples of the MCT are available for direct inspection (*e.g.* Hermann *et al.*, 1997). The most cited example of an exposed, paleo-MCT is the Ivrea Zone in the western Italian Alps, although recent work suggests that the feature is actually a fossil accretionary prism, not "typical" lower continental crust (Hermann *et al.*, 1997). Hermann *et al.*, (1997) studied the Val Malenco exposure, also located in the Italian Alps, which they believe is more representative of a "typical" MCT. They observed a complex, at least one-kilometer thick transition from mafic lower crust to ultramafic, peridotite mantle. The Val Malenco transition (Figure 2.6) is composed of a mixture of dense pelitic granulite, gabbro, and peridotite (Hermann *et al.*, 1997).

Understanding the growth and evolution of the continental crust remains one of the most encompassing and important problems in global geology. Its solution will require laboratory and numerical models, and field evidence constraining the composition, nature, and history of the crust and major crustal boundaries, such as the Mantle-Crust Transition (MCT). Many years of seismic studies of the continents have led to generalizations about the nature of the continental MCT and variations of the boundary with tectonic age or province. Older, stable regions are thought to host a more gradational transition, younger regions of active deformation are thought to be underlain by more variable, but often sharper transitions (Nelson, 1991, Hammer and Clowes, 1997).

In this chapter I summarize the results of my investigation of the thickness of the MCT beneath North America. I have two main goals in this work, to investigate the feasibility of using receiver functions to constrain MCT thickness, and to look for systematic variations in MCT thickness with tectonic age and/or history. I break my discussion into three sections: First, I report the estimated thickness of the MCT beneath those stations for which the measurements were possible. Then, I synthesize the thickness variations in a discussion of the geo-tectonic setting of the stations. And third, I discuss particular cases in light of observations that may provide further understanding of the nature of the MCT.

7.1 A Limit for Resolution

Two factors limit our ability to use receiver functions to estimate precise thicknesses of the MCT. First, since the incident P-waves travel great distances before sampling the receiver structure, they are inherently low-frequency (up to several hertz). In addition, receiver functions are commonly complicated by scattered waves, often generated in the shallow structures underlying seismic stations. Scattering generally decreases with increasing period, since longer period waves are less sensitive to small-scale heterogeneities. Velocity heterogeneity and its concomitant scattering restrict our resolution of the MCT thickness by limiting the bandwidth available for reliable observation of both the *Ps* and *PpPms* arrivals. For most practical purposes, experience suggests that useful receiver function information is available at periods from perhaps one second to a few tens of seconds (the long-period limit is imposed by Earth's background noise levels).

Since by definition, heterogeneity will vary from site to site, a precise limit on the resolution of the MCT thickness depends on the site. At times it may be possible to push the resolution smaller than a kilometer, if the high frequency signals are available. However, this is certainly not the case at every station. In most cases, the resolution of the MCT thickness will be on the order of one to two kilometers if we restrict our measurements to include periods longer than one to three seconds. For this initial survey of thicknesses, I accept the coarse resolution in order to obtain a broad sampling of the MCT thickness. I obviously will not resolve fine details in the structure or fine details in the variability of the MCT with tectonic age and/or history. Available resolution, while not high, should allow us to investigate the most important variations from “sharp” to “broad” and to explore any patterns that may arise during the mapping of the thickness across North America.

7.2 Estimating MCT Thickness

The entire set of observations was carefully reviewed and processed - details are provided in Appendix 2. The method used to estimate the MCT thickness was outlined in Section 3.4 on page 58. The procedure consists of several steps, which are reviewed in the following sections.

7.2.1 Receiver function cluster/stacks preparation

First, the iterative time-domain receiver functions (Chapter 4) were calculated for each event in each receiver-function distance-azimuth cluster. I used a Gaussian width factors of 2.5, 1.5, and 1.0, performed the deconvolution with a maximum of one hundred iterations and a misfit tolerance of 0.001. The resulting radial and transverse receiver functions were averaged to create signal “stacks” that were used to represent the response for each cluster. Only the radial receiver functions were kept for interpretations, transverse observations were used as a qualitative measure of the level of scattering influencing the radial measurements. An example is pre-

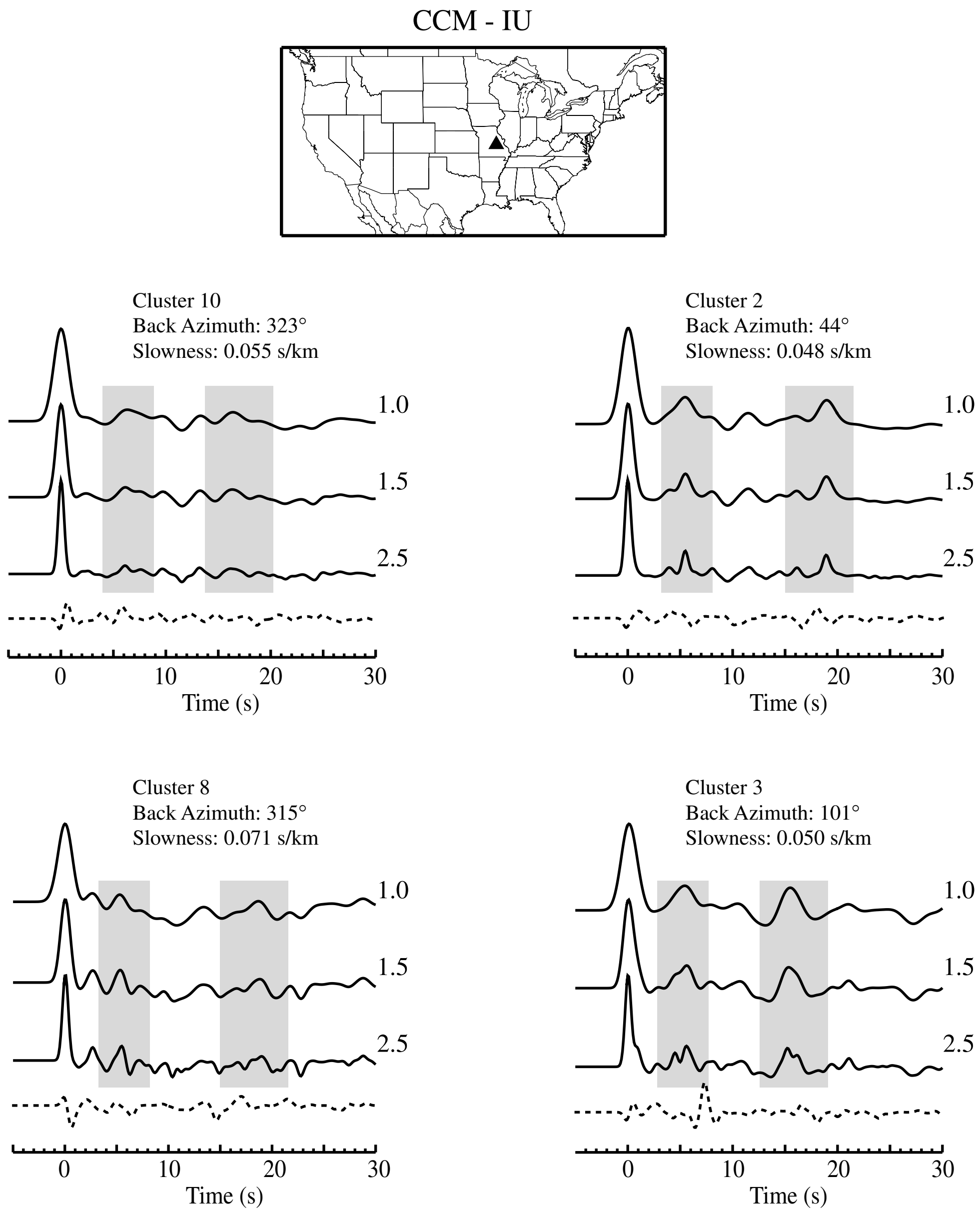

Figure 7.2 Example of observed receiver functions at station CCM-IU. Differences between the shape of Ps and PpPms phases (gray boxes) indicate changes in the configuration of the MCT. The four panels to the right are presented in clockwise azimuth order and the correspondent back azimuth and slowness for each cluster is indicated. The radial receiver function (solid curves) is shown for three different Gaussian widths a= 1.0, 1.5 and 2.5 (indicated in the right edge of the signals). The transverse receiver functions for a Gaussian width of 2.5 are shown as dashed lines beneath the radial receiver functions.

sented in Figure 7.2, but I only show the transverse signal for the Gaussian width of 2.5. In general, the relative amplitude of the transverse receiver functions decrease with decreasing width factor (lower frequencies).

The peak arrival times of the *Ps* and *PpPms* phases were picked for the three radial receiver function stacks (Gaussian width = 2.5, 1.5 and 1.0). This completes the preparation of the observations. The next step was to create the theoretical MCT amplitude-ratio thickness curves (Section 3.4 on page 58).

7.2.2 Inversion for receiver velocity crustal structure

To account for shallow structure influence on the MCT thickness measures, we constructed "average" shallow velocity structures for each station using a linearized, time-domain waveform inversion method (Ammon *et al.*, 1990). For each station I computed the average receiver function by computing the mean of all available distance-azimuth cluster stacks and inverted the "average" waveform for an "average" structure. For convenience, I used frequency-domain deconvolutions in this part of the analysis.

The nonlinear relationship between the receiver function, *d*, and the velocity model, *m*, can be represented as

$$d = F[m] \tag{7–1}$$

where *F* is a nonlinear functional representing the computation of a receiver function. To estimate *m*, an initial model, m_0, is constructed and a first-order Taylor expansion about m_0, allows us to approximate (7-1) as

$$(D, \delta m)_j = F_j[m] - F_j[m_0] \tag{7–2}$$

where $(D, \delta m)$ is the inner product between D, the partial derivative matrix of $F_j[m_0]$, and the model correction vector δm. If we define $m = m_0 + \delta m$, then we can use

$$(D, m)_j = d_j - F_j[m_0] + (D, m_0)_j \tag{7–3}$$

to invert directly for *m*. The partial derivatives for the matrix *D* are estimated using a finite-difference approximation, implemented by Randall (1990), based on the propagator-matrix method of Kennett (1983). To stabilize the inversion I appended a smoothness constraint to the equations and minimize model roughness (Ammon *et al.*, 1990). The inversion is performed using a singular-value decomposition. See Ammon *et al.*, (1990) for details.

I used a value of 0.1 for the smoothness parameter and a 0.001 singular-value decomposition truncation factor. Five iterations were found to be sufficient to obtain a reasonable model that fitted the data satisfactory. I used an inversion with one significant change to the method outlined by Ammon *et al.* (1990). Receiver functions do not usually have much energy at periods longer than about 30 seconds (C. J. Ammon, personal communication). The lack of long-period signal often produces acausal side-lobes on each arrival in the signal. Although experience suggests that the side-lobes are not a major factor in the inversions, I accounted for the lack of long-period energy in the observations by band-limiting our inversion to include periods longer than about 30 seconds (second-order, two-pass Butterworth filter with a corner at 0.03 hertz).

To construct the initial model for the inversions, I used structures available in the literature when available (*e.g.* CCM, COR, MNV, ANMO, PGC, YKW, INK, WHY, EDM). When existing models were not available, I used a modified version of the "standard" models for each province (Table 5-1 on page 87). In each case I fixed the crustal Poisson's Ratio to be consistent with that estimated in Chapter 6.

The purpose of this inversion was to obtain a velocity model of the upper and middle crust layers at each station and use these structures to compute the amplitude ratios for different MCT thicknesses. Therefore, the velocity model for each site should not be considered as definitive. The inherent non-uniqueness of seismic velocity inversions cannot be avoided (Ammon *et al.*, 1990), but the models are suitable for mapping MCT structure beneath the stations.

An example inversion is illustrated in Figure 7.3. The receiver functions are shown to the left and bottom of the models. Immediately the absence of a large converted wave and multiple suggests the need for a smooth transition from crust to mantle velocities. A possible *Ps* arrival with a peak at about 6 seconds lag suggests a relatively thick crust. The inversion starting model contains a relatively sharp MCT beneath a thick, simple crust. Inversion drives the model towards a smoother MCT and more crustal complexity including a faster near-surface velocity. The fit to the observations is acceptable for the three different bandwidths. Plots of each station-average receiver function and the estimated velocity structure used in this study are presented in Appendix C.

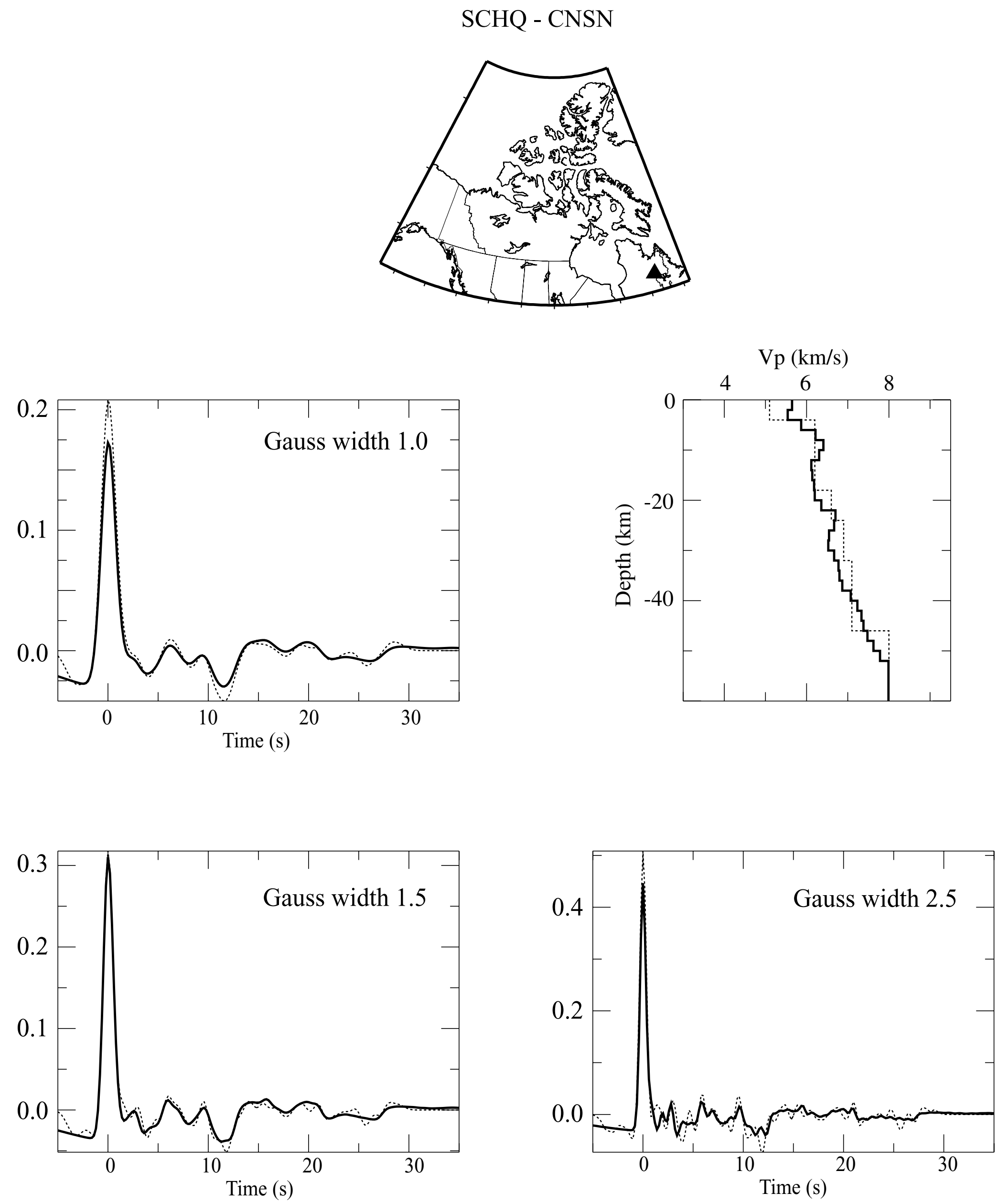

Figure 7.3 Inversion results for crustal velocity structure at station SCHQ-CNSN (onset map). The resulting velocity structure (solid line in upper-right panel) was obtained using the 1.5 Gaussian width receiver function stack (dotted line in lower-left panel) and a velocity model obtained by Cassidy (1995) (dotted line in upper-right panel). The solution was tested by matching the synthetics (solid curves) in three different Gaussian widths with their observed counterparts (dotted curves).

7.2.3 MCT Amplitude-Ratio Thickness Diagrams

Using the upper- and middle-crust layers from the station-average velocity-models, synthetic receiver functions were calculated using the method of Randall (1990),

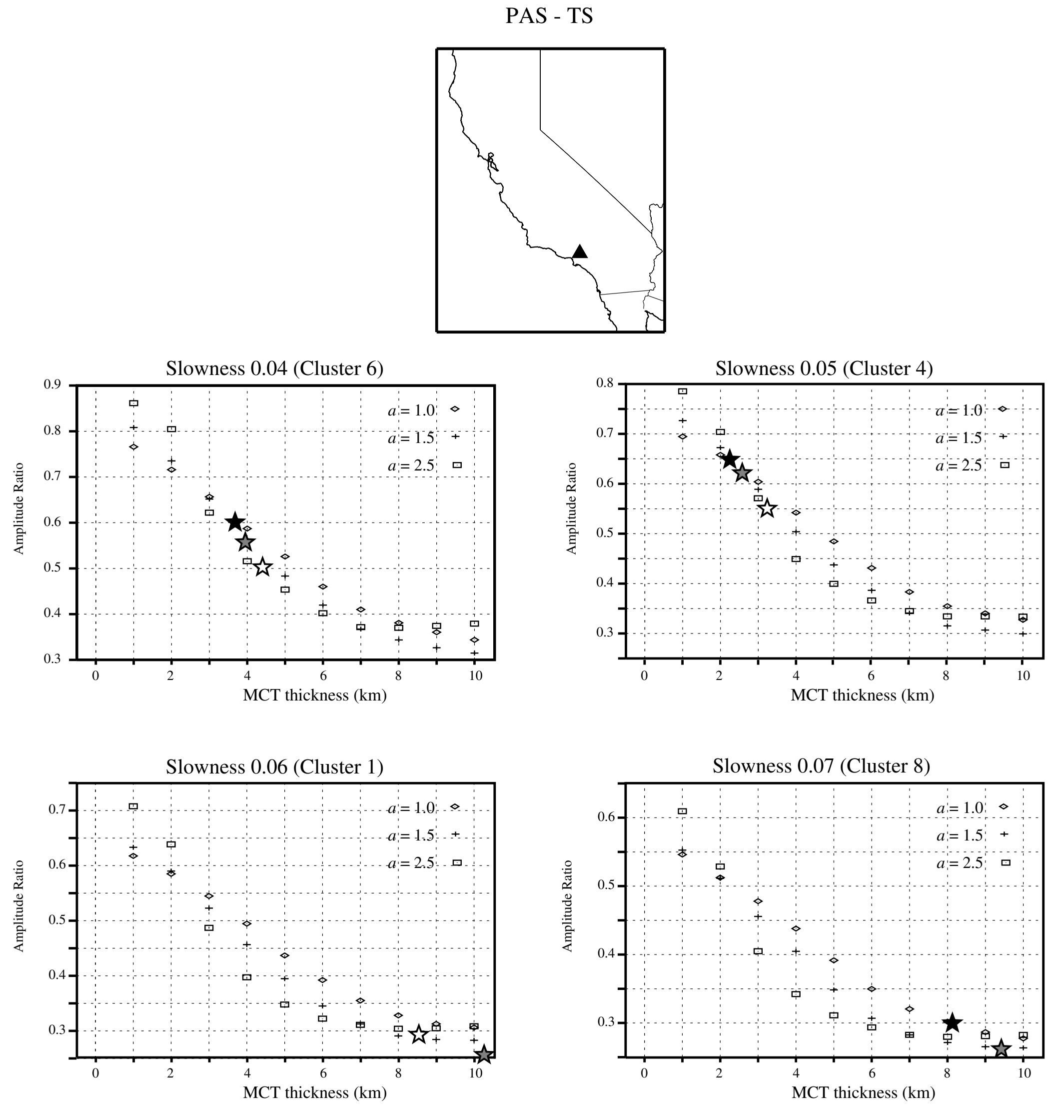

Figure 7.4 MCT amplitude-ratio diagrams for four different slowness values (0.04 - 0.07) used to estimate the MCT thickness at station PAS-TS (onset map). The corresponding observed Ps-PpPms phases amplitude ratio at clusters 6,4,1 and 8 are also plotted on top of the correspondent Gaussian width a curves (black star =1.0, gray star=1.5 and white star =2.5), suggesting the MCT thickness measured by the correspondent receiver functions. The results are checked with synthetic signals.

for ten MCT structures varying in thickness from 1 to 10 km thickness, and Gaussian widths of 1.0, 1.5 and 2.0. Then, the peak amplitude values of the *Ps* and *PpPms* arrivals were used to calculate an MCT amplitude-ratio diagram for each velocity structure. An example set of curves are shown in Figure 7.4 (an earlier example was

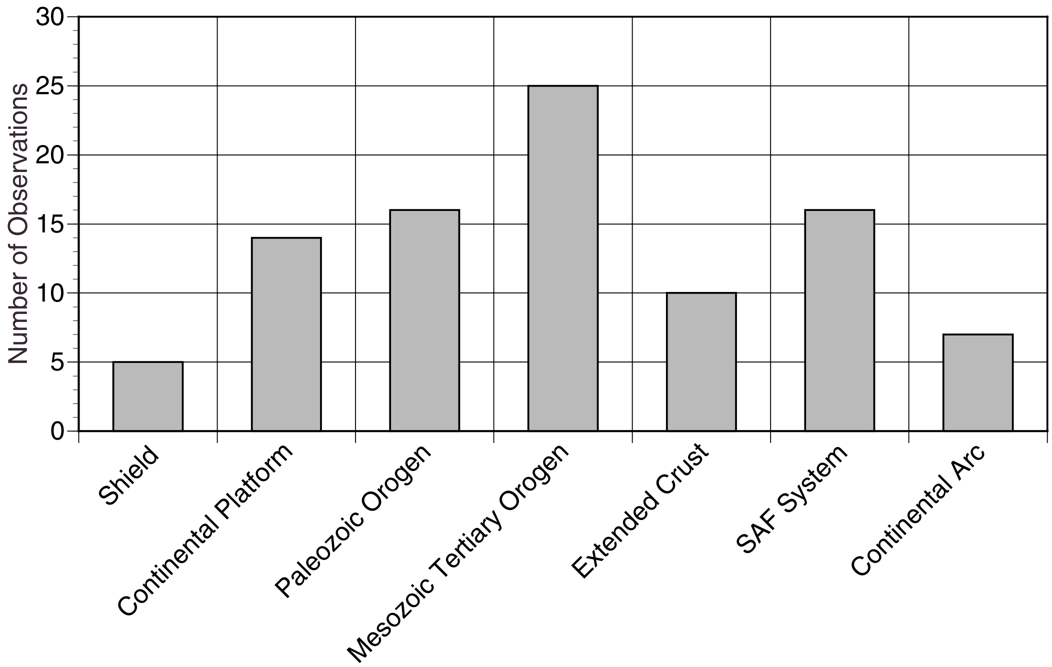

Figure 7.5 Summary of MCT structure beneath North America. The distribution of observations per tectonic setting indicates a major sampling in active tectonic regions (*e.g.* Orogens). SAF indicates San Andreas Fault.

shown in Figure 3.8 on page 66). Since the receiver function observations were available with a range of horizontal slownesses, the MCT amplitude-ratio diagrams were calculated for ray parameters of 0.04, 0.05, 0.06 and 0.07 s/km. Once the theoretical curves are computed, the observed amplitudes ratios were plotted on the amplitude-ratio diagram and an estimate of MCT thickness for each cluster's receiver function stack can be directly read from the curve.

7.3 Measured MCT Thickness Variations Beneath North America

Details of the results obtained after the analysis of 640 azimuth-distance-cluster signals, and a total of 93 stations, are reported in Appendix D. Figure 7.5 is a chart showing the distribution of observations with tectonic province. Most observations

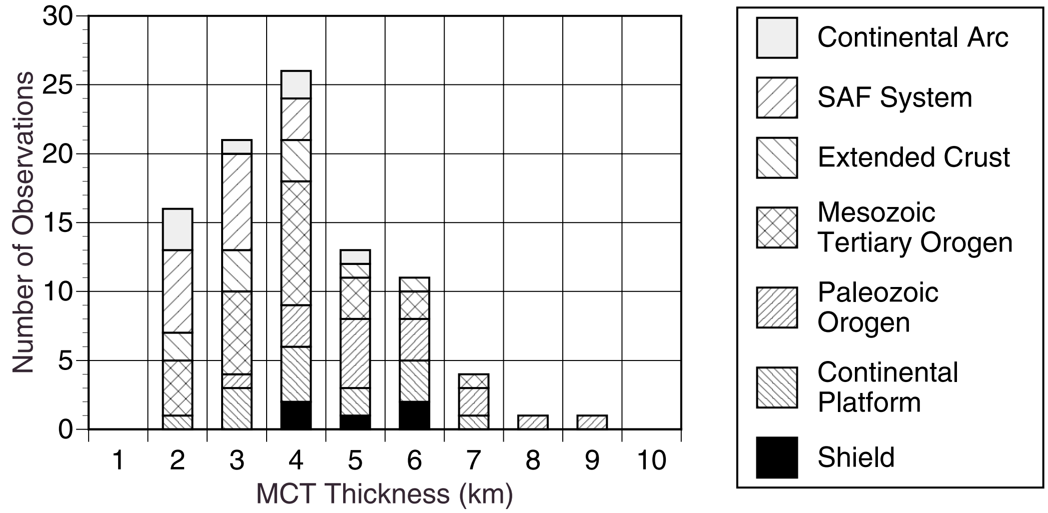

Figure 7.6 The distribution of MCT thickness estimates by tectonic setting (see text for discussion). The value for each station is the mean of all measurements at that stations. The median value of all measurements shown is 3.9 km, the mean is 4.1 km, the harmonic mean is 3.6 km, and the geometric mean is 3.8 km. All measures round to 4 km.

are from the western Cordillera of North America, where most of the continents seismic stations are located. We have few values from shield regions, but adequate numbers from platforms and Paleozoic orogens (mostly the Appalachian Mountains). We separate the large number of observations from within the San Andreas Fault System from the rest of the US for convenience. We have only a few measurements from arc regions, and these are generally areas of complex structure which make simple measurements a challenge.

Estimated values of MCT thickness are summarized in Table 7-1, Figure 7.6, and Figure 7.7. In the following section we discuss each tectonic grouping individually. First, the fact that we have no measurements below two kilometers is more a reflection of our data band width than a true statement regarding the thickness of the

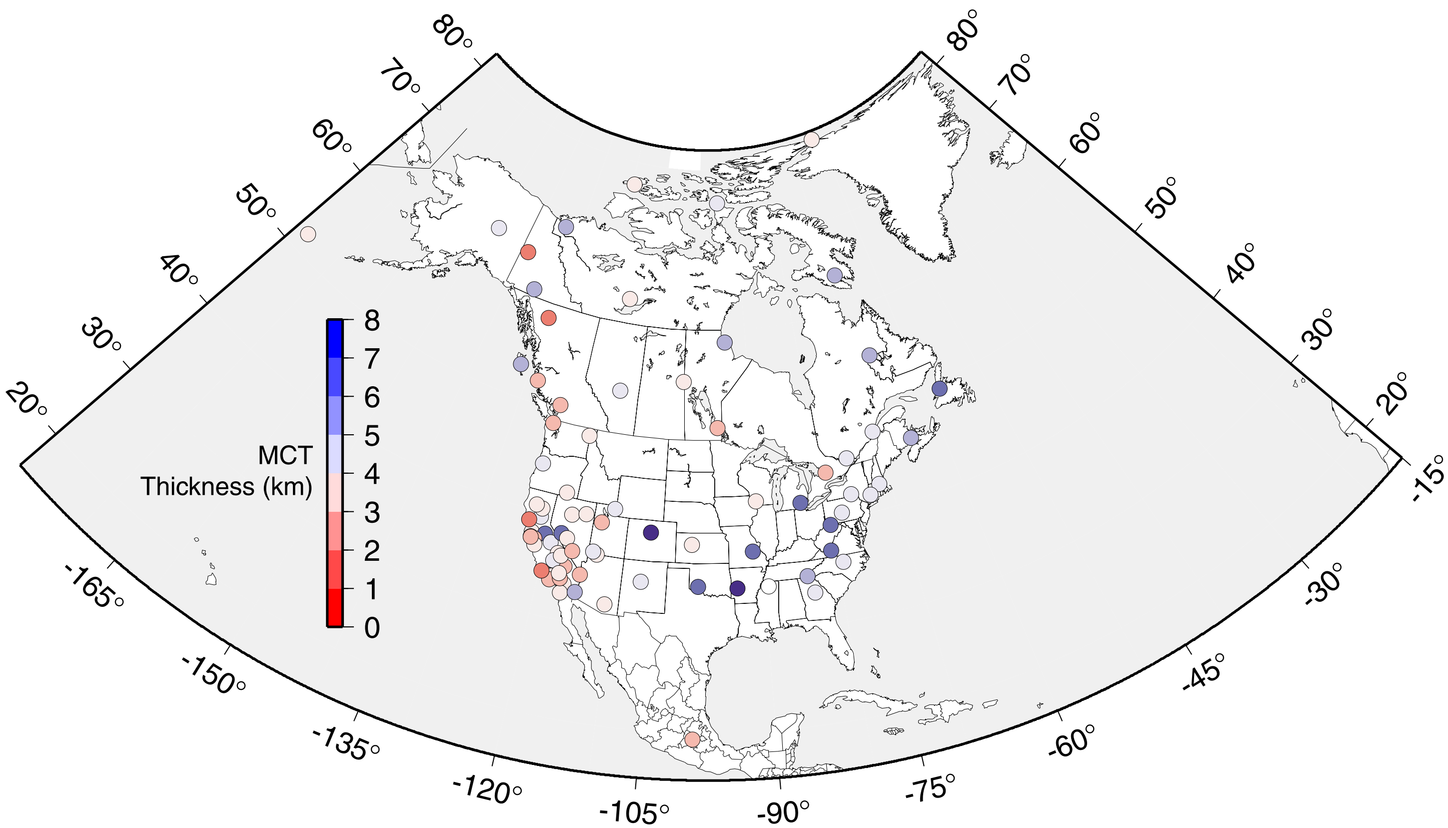

Figure 7.7 Estimated variations in MCT thickness. Blue symbols identify regions with a thicker than average MCT, red areas show regions with a relatively sharp MCT. Thin MCT values tend to be located in regions of active tectonics.

Table 7-1: Mean MCT Thickness Estimates

Station	Clusters	MCT	SD	Station	Clusters	MCT	SD
Shields							
FCC	3	5.83	1.61	FRB	10	5.95	1.36
GAC	6	4.08	2.01	SCHQ	5	5.30	2.39
YKW	13	3.81	2.62				
			Average	4.57			
			Median	4.08			
			SD	1.10			
Continental Platforms							
AAM	3	6.67	0.58	CBKS	6	3.50	1.05
CCM	11	6.45	2.11	EDM	3	4.00	1.73
FFC	10	3.95	1.42	HKT	5	5.80	2.28
JFWS	3	3.83	2.75	LMQ	2	4.50	3.54
RES	8	4.81	1.73	SADO	3	2.33	0.58
ULM	3	2.83	0.29	WCI	3	3.17	0.29
WMOK	3	6.50	1.50	WVT	4	5.38	1.38
			Average	5.01			
			Median	4.81			
			SD	1.55			
Paleozoic — Orogens							
ALE	17	3.97	1.14	BINY	5	4.40	1.67
BLA	5	6.60	1.67	CEH	5	4.60	2.22
DRLN	5	6.20	2.02	GOGA	6	4.58	1.91
HRV	12	4.21	1.21	LBNH	5	9.10	0.22
LMN	2	5.50	0.71	LSCT	4	4.88	2.59
MBC	14	3.00	0.98	MCWV	3	6.50	2.18
MIAR	5	7.00	2.83	MYNC	3	5.67	1.53
SSPA	7	4.64	1.31	YSNY	3	8.33	0.58
			Average	5.57			
			Median	5.19			
			SD	1.64			
Mesozoic-Tertiary Orogens							
ANMO	10	4.25	1.60	CMB	12	6.42	2.75
COL	11	4.23	2.92	CWC	2	3.00	1.41
DAWY	3	1.33	0.58	DLBC	3	1.83	0.29
GSC	10	2.95	1.04	HWUT	4	4.75	1.19
ISA	12	4.25	1.48	INK	11	5.68	2.44
ISCO	5	7.00	2.45	KNB	8	3.44	1.40
KCC	7	4.86	2.69	LDS	3	4.33	2.31
MIN	10	3.50	0.75	NEW	8	3.19	1.25
ORV	16	4.38	1.68	PFO	13	3.81	1.79
PNT	5	4.20	1.04	SVD	8	2.38	1.19
VTV	9	3.72	1.00	WDC	12	3.00	1.43
WALA	3	2.33	0.58	WNY	1	5.00	2.28

Table 7-1: Mean MCT Thickness Estimates (Continued)

Station	Clusters	MCT	SD	Station	Clusters	MCT	SD
WVOR	10	3.95	0.96				
			Average	3.92			
			Median	4.20			
			SD	1.33			
Extended Crust							
BMN	8	3.63	1.60	DAC	5	3.40	1.14
DUG	6	2.17	0.41	ELK	5	3.80	1.30
GLA	7	5.43	2.76	MNV	8	6.00	2.88
NEE	4	2.50	0.58	TPH	7	3.36	0.63
TPNV	6	2.83	0.93	TUC	8	3.88	1.62
			Average	3.70			
			Median	3.51			
			SD	1.21			
San Andreas Fault System							
ARC	6	3.00	0.89	BAR	9	3.50	1.39
BKS	15	3.33	1.75	BRK	1	2.00	0.00
CALB	6	4.42	2.69	HOPS	11	1.91	0.83
JRSC	11	2.50	0.50	MHC	13	2.58	1.12
PAS	9	3.61	1.82	PKD	8	2.31	0.84
RPV	6	2.83	1.47	SAO	16	3.34	1.61
SBC	8	1.94	0.18	SCZ	8	4.25	1.67
SNCC	6	2.75	1.25	STAN	4	2.25	0.50
			Average	2.91			
			Median	2.79			
			SD	0.78			
Continental Arc							
ADK	11	3.73	1.31	BBB	3	2.33	0.58
COR	13	4.27	1.88	MOBC	2	5.25	3.89
PGC	1	2.00	0.00	PMB	3	2.50	0.50
UNM	5	2.70	0.45				
			Average	3.17			
			Median	3.21			
			SD	1.02			

MCT. The resolution of the technique is at best one kilometer, so it would not be surprising for any individual measurement to jump from one column to another in the distribution, and it is certainly possible that measurement showing one or two kilometers thickness could in fact be sharper. The distribution as a whole is skewed towards thin MCT's with a median and mean values of 4 km. The harmonic mean of all measures, which weights smaller values more, is slightly lower, 3.6 km. Clearly, within the resolution of routine processed receiver functions, the average thickness of the MCT is about 4 kilometers. Including smaller values that we could not resolve would decrease all of the means, but is unlikely to change the median.

As illustrated in Figure 7.7, most of the thin MCT's are located beneath stations within recently deformed, or currently deforming crust. A few exceptions are located in the central and eastern portions of the continents and perhaps an equal number of outliers lie in the other direction and suggest thick transitions beneath the western Cordillera. We discuss these stations below. The overall pattern of sharp MCT's beneath regions of active or recent tectonics indicates that the lower crust and upper mantle are participants in tectonic activity, and change in response to lithospheric scale stresses. This in itself is not an expected result, but suggests that the main trends in the observations are reliable.

7.4 Variations in MCT Thickness With Tectonic Setting

The results reiterate the heterogeneous nature of the continental lower-crust (*e.g.* Rudnick and Fountain, 1995). Mesozoic-Tertiary orogens have more stations than any other province, followed by similar numbers for Continental Platform, Paleozoic orogen and San Andreas Fault System. MCT thicknesses for stations on shields are centered in the 4-6 MCT thickness range, but the measurements from Continental Platform, Paleozoic- and Mesozoic-Tertiary orogens are spread widely. Perhaps the only robust, systematic variation is a tendency for a thin MCT for younger tectonic settings (*e.g.* Extended Crust, SAF System, and Volcanic Arc).

In general, the MCT thickness mean around four km suggests stable MCT character, whose dependence on tectonic setting is limited. Conversely, the general overlap of standard deviation bounds among the different groups of data (SD in Table 7-1) hinders the formation of definite conclusions, and demands a close inspection of the observations. In the following seven sections I briefly describe the observations and discuss the major findings in the different tectonic-setting groups (*i.e.* Shield, Continental Platform, etc.). I emphasize median values of MCT thickness to avoid corruption of conclusions by outlier observations (which are interesting but a problem for generalization).

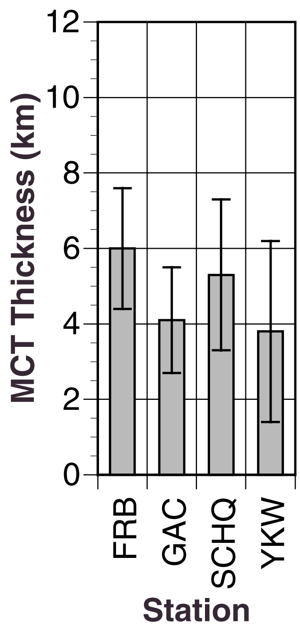

Figure 7.8 Only four measurements from shield stations were stable. The MCT thicknesses all differ from a first-order contrast, but are not too thick.

7.4.1 Shields

Shield observations are summarized in Figure 7.8. The median MCT thickness value of 4.08 km is robust (± 1.1km). Stations FCC and FRB fall above the median, and have the lowest azimuthal variation. SCHQ also has a thick MCT (5.3 ± 2.4) but more variable with the thicker values being observed to the south, southwest and northwest directions of the station. Two shield stations (GAC and YKW) have thinner MCT's. Both are located at the edge of the Canadian craton. GAC (4.1 ± 2.0) shows an eight-km MCT towards the south which contrasts with value observed in the other five measurements. Station YKW has the thinner MCT median that is a result of waves that approach the station from the southwest and northwest and show an MCT thickness between two and four kilometers. Arrivals from the east-southeast, on the other hand, show a much thicker MCT, between four and nine kilometers.

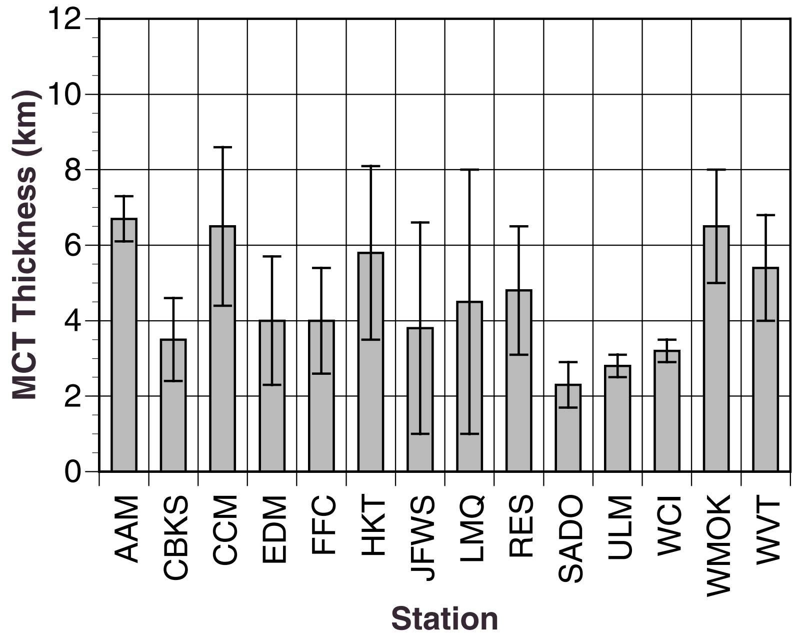

Figure 7.9 Platform measurements of MCT thickness are variable, ranging from thin to intermediate thickness. Small error bars does not necessarily indicate high-quality measurements - sparse measurements can produce small ranges in the observations.

7.4.2 Continental Platform

There is a tendency in Continental Platform stations towards thicker MCT values than shield stations, although more variable (4.81 ± 1.55 km). The histogram summary in Figure VII.6b points out stations AAM, CCM, HKT, WMOK and WVT with notably thicker MCT than the rest of their group, with station AAM being the more stable estimate (± 0.58). The results obtained in HKT are probably less reliable due to the difficulty of modeling the upper-crust layer. Clusters 3, 4 and 5 (southeast) in station CCM are probably being affected by local scattering inferred from notable transverse receiver signals; consistent thicker MCT values are observed towards the southwest and northwest of this site. Stations WMOK and WVT have few samples (three and four clusters respectively). At WMOK transverse receiver functions recovered from signals arriving from the southwest and northwest show significant amplitude, making those measurements less reliable. Station WVT, on the other hand, shows a contrasting difference between three signals from the southeast, with notable transverse receiver function amplitudes and clear Ps conversions in the radial receiver stacks, and the only signal from the northwest that has a modest transverse signal and subtle Ps and PpPms phases.

Among the stations whose MCT thickness is close to the median, JFWS and LMQ show the largest standard deviations. LMQ has only two observations that deviate from each other, despite common arrival azimuth. The transverse receiver signal from cluster 2 in LMQ has substantial amplitude. JFWS, on the other hand have clear MCT phases (*i.e.* Ps and PpPms); small transverse signals and the difference between southeast (2.0 ± 1.0 and 2.5 ± 1.0 MCT) and northwest (7.0 ± 2.0) signals may reflect a real change in MCT structure. Values observed at station RES are also close to the median (4.81 ± 1.73) and its proximity to the Innuitian folded belt may explain the variability of the observed MCT structure, although all transverse functions have small amplitudes suggesting limited scattering influence.

The Continental Platform stations that have thinner MCT thickness are CBKS, SADO, ULM and WCI. Despite the influence of a shallow low-velocity sedimentary cover in station CBKS, the observed Ps phases are very clear and the transverse receiver function signals are insignificant. Although stations SADO, ULM and WCI have only three clusters each one, the results obtained have small variability.

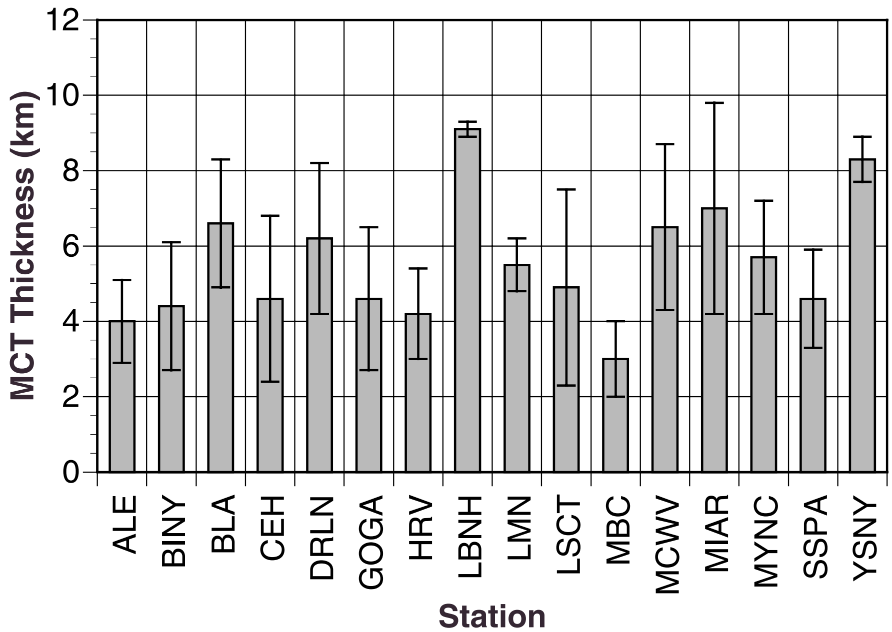

Figure 7.10 MCT thickness estimates for stations situated in Paleozoic Orogens. the range is again variable, but several large values (LBNH and YSNY) are located in New York - New Hampshire area.

Transverse signals in SADO and WCI have small, yet notable, amplitudes supporting the reliability of the estimated values.

7.4.3 Paleozoic Orogens

The median MCT thickness in Paleozoic Orogen stations (5.19 ± 1.64 km) is the largest value of all tectonic settings, although this estimate has also the largest standard deviation. The variety of the estimates is evident in the histogram distribution of Figure 7.10. However, the distribution is almost symmetric around the median, and the majority of the observations (11 out of 16) are one kilometer around the center of the distribution (Figure 7.6). The stability of the sample seems surprising if we consider the expected MCT topographic complexity in orogen settings, although some of the transverse receiver function signals show notable amplitudes, arguing for a structural complex crust (*e.g.* MBC, DRLN, MCWV, MIAR). The stations that fall closer to the median are CEH, GOGA, LMN, LSCT and SSPA. LMN has only two clusters, both sampling the south-southwest region; cluster number 2 is affected by a shallow low-velocity layer and show substantial transverse amplitudes. The four radial receiver functions from station LSCT have distinctive MCT phases and the only notable transverse receiver amplitudes are seen in the signal approaching the station from the south (184.4° back-azimuth). Stations CEH and GOGA, both located to the southeast of the Appalachian mountains show simple radial receiver functions and only the signals approaching GOGA from the northwest have large transverse amplitudes. Radial receiver functions recovered at station SSPA show a complex crustal structure and the MCT phases are difficult to identify, but only clusters 1,3 and 4 (arriving from different azimuths) show substantial transverse amplitudes.

Stations ALE, MBC and MIAR are the only three stations located in non-Appalachian sites. MIAR is in the Ouachita mountains (Figure 5-2d). ALE and MBC are both located in the Innuitian folded belt (Figure 5-2d). The resulting MCT thickness at MBC (3.00 ± 0.98 km) is notably stable, the radial receiver functions at this station have clear Ps conversions and the PpPms phase is consistently clear despite the complex overall characteristics of the signals, confirmed by steady large transverse receiver-signal amplitudes. Station ALE (3.97 ± 1.14 km), on the other hand, tends to thinner MCT values towards the northeast and southeast and the transverse receiver functions show small amplitudes in general with only one exception (cluster 4, back azimuth 84.1°). Station MIAR (already discussed in chapter 6), shows thinner MCT thickness towards the southeast, whereas the MCT thickens to the south-southwest and northwest.

The median MCT thickness values obtained at stations LBNH (9.10 ± 0.22) and YSNY (8.33 ± 0.58) are the only two notably thick estimates in the Paleozoic Orogen group. The observations at LBNH are reliable measurements, with the radial receiver function stacks showing clear Ps conversions and small amplitude PpPms multiples in all five cases; all transverse receiver functions have small-to-moderate amplitudes. Radial receiver functions at YSNY are all affected by a shallow low-velocity layer but Ps conversions are notably clear, although the thick MCT makes it hard to identify the PpPms phase; transverse receiver function amplitudes are small, yet notable.

7.4.4 Mesozoic-Tertiary Orogens

An apparently stable median MCT thickness (4.20 ± 1.33 km) could imply an indifferent-to-tectonics MCT nature (Figure 7.11). Conversely, the inherent structural complexity due to the extensive tectonic deformation in young (Mesozoic and younger) orogens could be associated to the scatter of the MCT thickness distribution shown in Figure 7.11. There does not seem to be any geographical preference for the estimates close to the median (*e.g.* ANMO, HWUT, ISA, KNB, LDS, MIN, PNT, VTV, WVOR) and the notable standard deviations argue for MCT structural complexity.

Stations COL, DAWY, DLBC, INK and WHY, located in the northern Cordillera (northwest Canada and Alaska), illustrate the variable character of the MCT in oro-

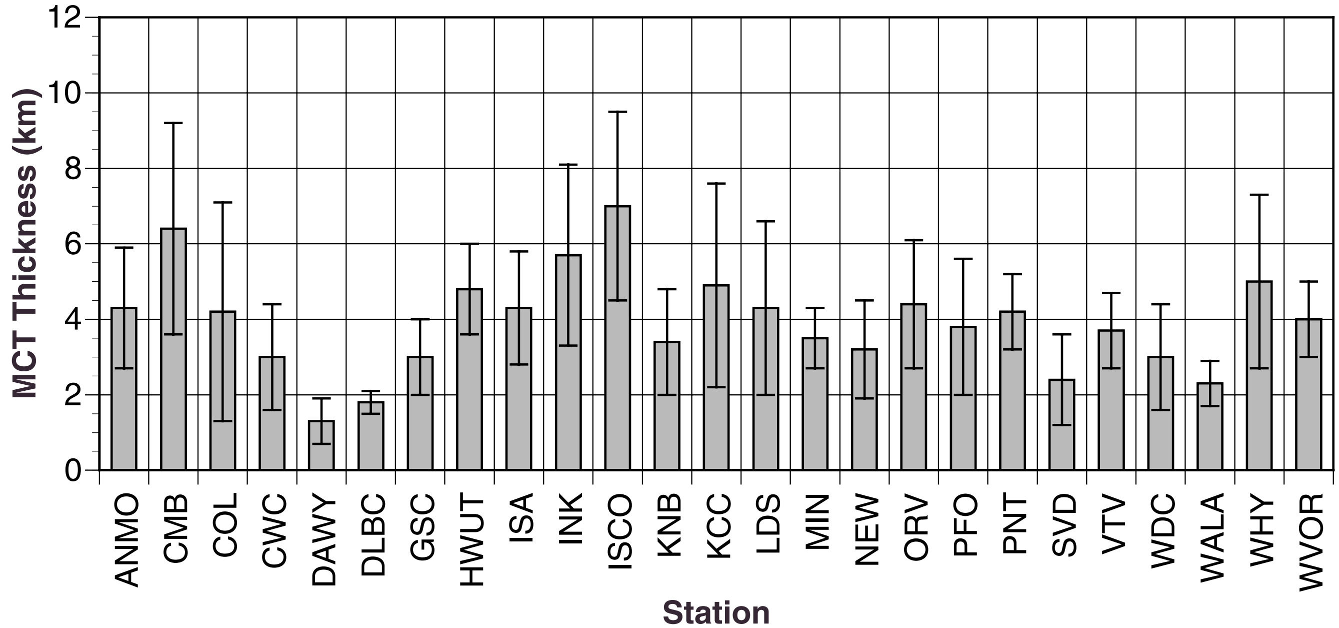

Figure 7.11 Estimated MCT thickness values for Mesozoic-Tertiary Orogenic regions. The range is large but most of the transitions are relatively sharp.

gens. The variable MCT thickness estimate at COL (4 ± 3 km) is the effect of a thick MCT structure to the northwest and a thinner MCT (lower than three km) seen by the rest of the clusters. The radial receiver functions of station WHY are all affected by a shallow low-velocity layer; transverse receiver functions from the southeast and southwest have notably larger amplitudes than the northwest signals. The west-northwest Ps signal is very clear at WHY, but the *PpPms* phase has a small and diffuse character supporting the interpretation of a thicker MCT structure. The *Ps* phases at station INK are clear, but the *PpPms* phases change abruptly around a 230º azimuth. The latter suggests a change of MCT structure at INK, from moderate thickness structure (around 4-5 km) to the southeast that becomes thick from the south-southwest to the northwest; transverse receiver signals are notable towards to the west-northwest of the station. The two thinner MCT estimates among the entire Mesozoic-Tertiary orogen sample are stations DAWY and DLBC (1.5 ± 1 km and 2 ± 0.5 km, respectively). The three cluster signals analyzed for station DAWY show simple receiver functions, with clear MCT phases in the radial stacks and small transverse amplitudes. The MCT at DLBC, on the other dips to the southeast, as evident from the large negative amplitude of the direct-P phase towards the southwest and northwest, and confirmed by the moveout of the PpPms phase.

The thick MCT at stations CMB (6.5 ± 3) and ISCO (7 ± 2.5) are notable in Figure 7.11. At CMB, the small transverse receiver-function amplitudes to the southwest contrast with large positive direct-P transverse phases to the northwest, suggesting a northeast dipping MCT. Both *Ps* and *PpPms* phases in most radial receiver functions are broad and have small amplitudes, with the notable exception

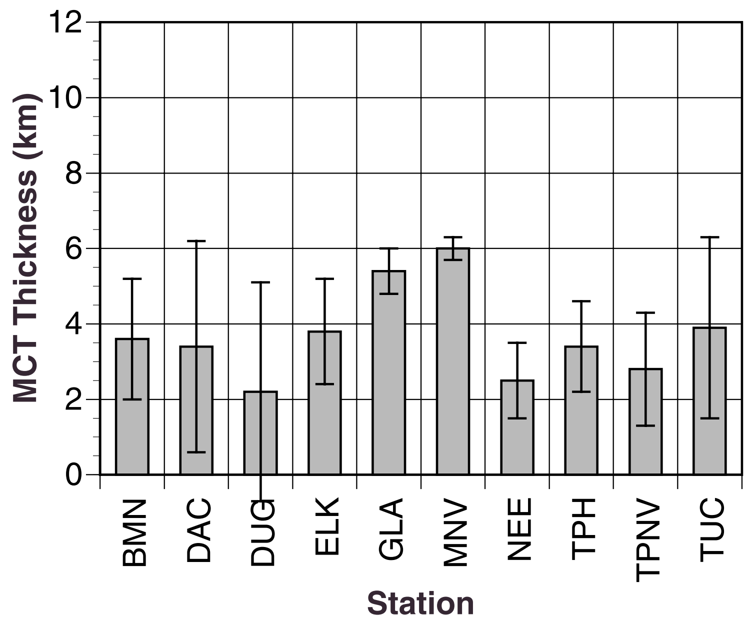

Figure 7.12 The MCT beneath the extended regions is thin for the most part. The two exceptions are GLA and MNV. MNV is located in a region of recent volcanic activity and complex structure. Several of the stations show large variations possibly complicated by shallow structure.

of clear Ps phases in signals approaching the station from the southeast. At station ISCO, the MCT shows a clear azimuthal change. To the northwest, despite the obvious influence of a shallow low-velocity layer, the MCT phases are clear and transverse amplitudes are moderate, meanwhile to the southwest and southeast the Ps phase in the radial receiver stacks is broad and has small amplitudes, with small amplitudes in the transverse stacks too.

7.4.5 Extended Crust

The Extended crust stations (Figure 7.12) are all located in the Basin and Range province. The relatively thin MCT median (3.51 km) agrees with the idea of a relatively young transition. Two stations with notably thicker MCT bias the variability estimate for this group (± 1.21 km): GLA and MNV. The MCT thickness to the west-southwest of GLA is consistently thick (> 7 km), in contrast with thinner estimates towards the southwest and southeast of the station. At MNV (6.00 ± 2.88) the MCT thickness is thinner (2-3 km) to the southwest and thicker to the southeast and northwest (7 km), where it also shows large transverse receiver-function amplitudes.

In general, the stations located in extended crust have a constant MCT thickness, although in some cases the large standard deviation estimates reflect the variability of the median. Station BMN (MCT ~ 3.63 ± 1.60 km), for instance, has a notable difference in the amplitude of transverse receiver stacks between the small signals from the east-southeast and the increasingly larger signals to the south, southwest and northwest. The MCT thickness estimates at BMN are notably thicker for the first group whereas the latter show a thinner transition structure. Another notably variable MCT thickness estimate is seen in station DAC (3.40 ± 1.14 km), where variation is influenced by the only five km thickness estimate in cluster 3 (back azimuth 236º). In general, the radial receiver signals in DAC show clear MCT phases, with the exception of cluster 3 where a diffuse PpPms phase and a broad Ps phase are observed. At station ELK, the resulting MCT thickness estimate (3.80 ± 1.30 km), is supported by clear Ps and PpPms phases. However, the MCT at ELK seems to have a southeast dip, suggested by the large direct-P phase in the transverse receiver stacks.

7.4.6 San Andreas Fault System

The median MCT thickness from the observations in the San Andreas Fault system stations is the thinnest value of the seven tectonic groups (2.79 ± 0.78 km), and the

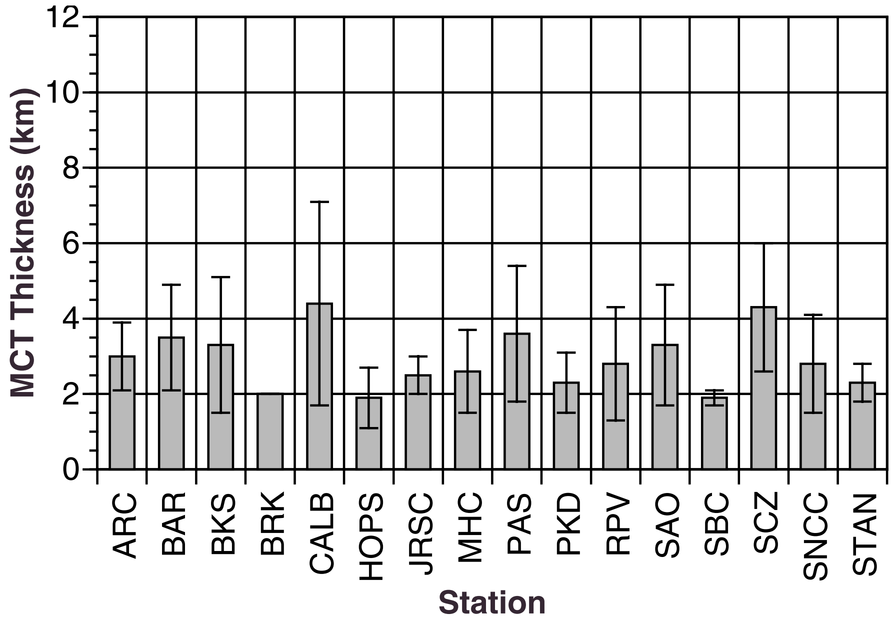

Figure 7.13 Stations within the San Andreas Fault System show relatively sharp MCT's with only a few measurements exceeding 4 km.

estimated MCT thickness values are all within the 2-4 km range (Figure 7.13). The influence of a recently deformed crust and the San Andreas fault system is evident in the variability of this group's estimates (Figure VII.6.f). Some stations show notably large standard deviations (*e.g.* BKS, CALB, PAS, SAO, SCZ), whereas others have very stable estimates (*e.g.* HOPS, JRSC, SBC, STAN), despite structural complexity in the local crust.

The radial receiver functions at BKS (MCT ~ 3.33 ± 1.75) show a complicated pattern, yet clear MCT phases (*i.e.* Ps and PpPms) are easy to identify. The outcome after the analysis of 14 clusters in BKS is a northwest-north very thin MCT (~ 2 km), with possible structural complexities suggested by large transverse receiver signals, contrasting with a thicker (3-6 km) southeast and southwest MCT. The results obtained at station CALB (MCT ~ 4.42 ± 2.69) are questionable. Transverse receiver function signals at CALB have notably large amplitudes, and the influence of a shallow low-velocity layer, may be reflected in some of the estimates at this station, like a dubious nine-km MCT thickness estimated to the south (back azimuth 184.1°). The MCT beneath SAO, on the other hand, show a clear pattern. The mean MCT thickness (3.34 ± 1.61) seem to be thicker to the southeast and southwest. Also, the MCT beneath SAO shows a clear northeast dip, suggested by clear negative-to-positive direct-P large amplitude in the transverse signals approaching from southeast to northwest back azimuth. At SCZ, the variable MCT thickness estimate (4.25 ± 1.67) does not seem to be the artifact of any azimuthal MCT change. However, the amplitudes in transverse signals from the northwest agree with the pattern seen in the neighboring site SAO. Radial receiver functions at SCZ show clear Ps conversions in signals approaching from the southeast and northwest, whereas radial Ps conversions from the southwest have smaller amplitudes, in agreement with a northeast dipping MCT.

7.4.7 Volcanic Arcs

The seven stations located in volcanic arc sites have a median MCT thickness (3.21 ± 1.02 km). Specific values are shown in Figure 7.14. The thickness distribution in volcanic arc settings is mostly constant, with the notable exceptions at stations ADK, COR and MOBC (Figure VII.6.g). Station ADK, located in the Aleutian Islands, shows a complex MCT structure and clear Ps conversions with notable moveout in the radial receiver stacks, which sometimes appear in the transverse stacks, arguing for dipping structure. The transverse receiver signals have generally large amplitudes but no azimuthal pattern seems obvious. The MCT thickness at

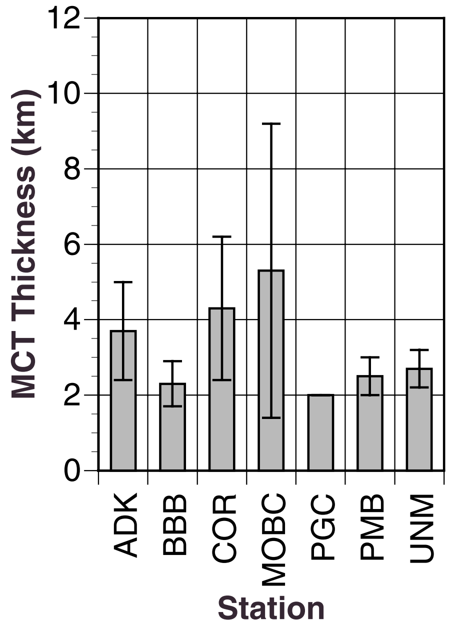

Figure 7.14 MCT thickness estimates for the seven stations located within regions of arc volcanism.

station COR is difficult to assess due to the presence of a thick low-velocity layer in the lower-crust. However, clear Ps conversions are consistent in the southeast and southwest quadrants, contrasting with a diffuse Ps signal in receiver signals approaching from the northwest. Further, the transverse receiver functions at COR have notable amplitudes in the southeast and southwest groups, but are smaller in the northwest group, which suggest a east dipping MCT structure. The two clusters analyzed for station MOBC approach the station from the southwest and northwest and clearly suggest a MCT dipping to the east. Another interesting MCT structure is seen in station UNM, whose transverse receiver functions have large amplitudes, as expected in a complex crustal structure. However, the MCT beneath UNM is thin (2.70 ± 0.45) and argues for a young but actively deforming lower-crust.

7.5 Discussion

Since the ideas and observations of estimating MCT thickness using single-station receiver functions are subject to some uncertainty, I have focussed only on broad scale trends in my interpretation to avoid reliance on any single measurements. Perhaps the most consistent measurements in the data are those from the extended crust and the California coastal regions, dominated tectonically by the San Andreas Fault System, but also strongly influenced by the association with subduction of the Farallon Plate for much of the late Mesozoic. Although there may be some variation within these measurements beyond the resolution of receiver functions, the fact that they show a more-or-less uniformly sharp transition is an indication that tectonic activity can modify the MCT.

The median values for each tectonic province is shown in Figure 7.15. Although we must be cautious when drawing conclusions for a large heterogeneous collection of measurements, the trends that we observe are interesting. The first-order trend is illustrated in the chart. Regions of current or recent tectonic activity have thin MCT's. Older regions tend to show an increase in thickness. In detail the observations suggest that any particular site may deviate from the general pattern, and indicate that the MCT is a complex feature.

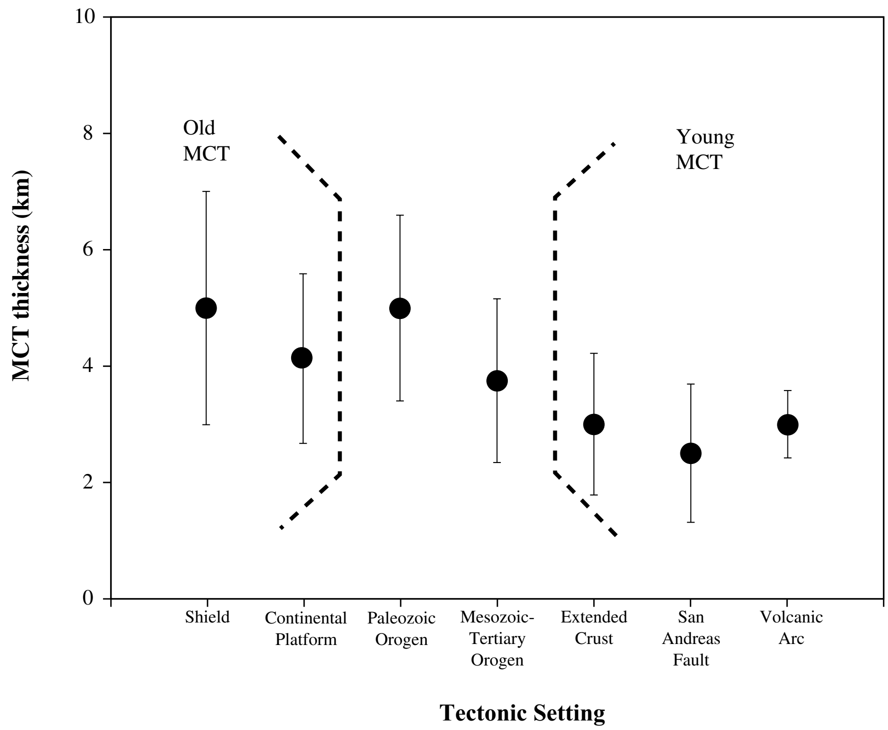

Figure 7.15 Median values of MCT thickness for each tectonic province. Mantle-Crust transition thickness estimates in the continental crust of North America for different tectonic settings. Error-bars equal two standard deviations from the median values (Table 7-1). A subtle indication that young MCT is thinner and old MCT maintains a "stable" thickness. Tectonic activity, in particular extension and active large scale faulting may rejuvenate the MCT, again creating a thin, sharp boundary.

8 CONCLUSIONS

Mapping the Earth's interior is an ultimate goal in Geoscience. Despite the extensive study of the continental lithosphere in the last century, there are still many questions regarding the composition and dynamic evolution of the middle- and lower-crust, as well as the upper-mantle. The continental Mantle-Crust Transition (MCT) is a key region, whose detailed study may provide relevant information regarding the different processes involved in the evolution of the lithosphere. The MCT reflects the different thermo-mechanical processes that affect the lithosphere. It is a geochemical transition zone that takes place in a 10^3 meter and larger scale (McCarthy and Patiño-Douce, 1997). The transition separates a lower-crust with dominant mafic composition from an ultramafic upper-mantle (Rudnick and Fountain, 1995). The main characteristics of the MCT, as suggested from a variety of evidence (e.g. seismic profiles, xenoliths, exposed cross sections) are: layered mafic and ultramafic composition, sub-horizontal structure and high thermal gradient.

In this study, I mapped thickness variations in the continental MCT beneath North America. The present availability of broadband seismic data made the goal of mapping the MCT structure beneath North America, an attractive approach to study the evolution of the continental lithosphere. I implemented a new method, based on techniques common in earthquake source analyses, to perform receiver-function source equalization. The method is stable and produces receiver functions with stable long-period spectral levels. That work has been published in Ligorría and Ammon (1999) and is in use in a number of receiver function studies.

Deconvolution is however, just a tool, the focus of this work has been the nature of the North American crust and variations in thickness of the MCT beneath the continent.

8.1 The Nature of the North American Crust and Mantle-Crust Transition

If the structure and the composition of the continental structure and the thickness of the MCT are related to simple evolutionary history of the crust we may see a correlation between values estimated in the previous chapter (Poisson's ratio and crustal thickness and MCT thickness). Comparisons between the three parameters are shown in Figure 8.1 and Figure 8.2. The values do not correlate well, consistent with preconceptions of complex continental structures and perhaps reflecting noise in the observations. Examination of trend for each tectonic province separately (Figure 8.3 and Figure 8.4) suggests that the crustal thickness and MCT thickness increase together beneath stations on platforms and in general, the MCT tend to be thicker than the median value of 4 km for stations on "mature" crust. The consistency of measurements from stations on extended crust and within SAF system is also clear. A few outliers complicate the issue but overall, the MCT is thin beneath

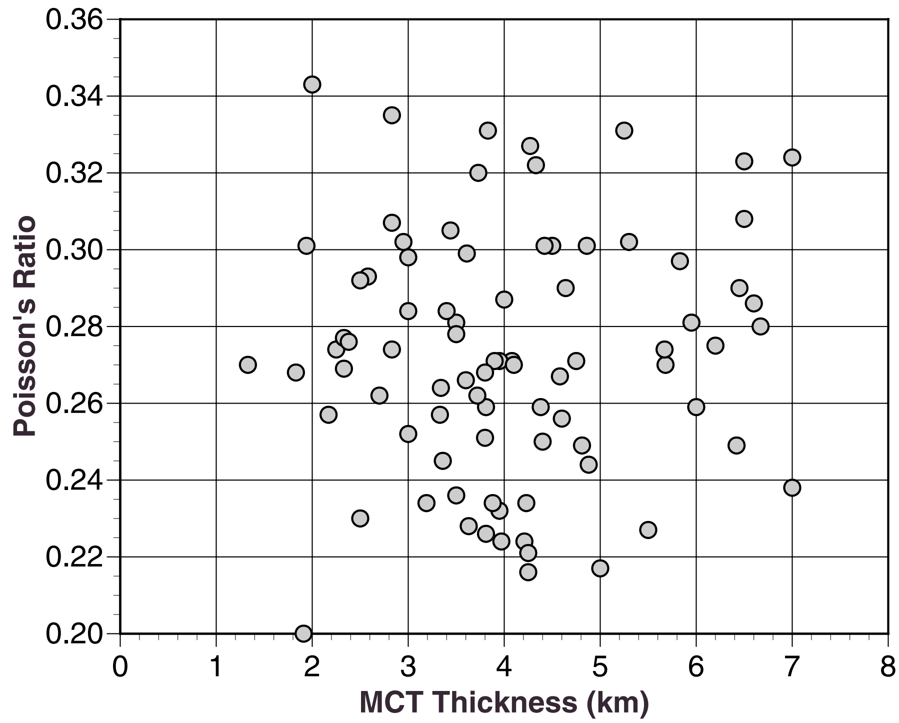

Figure 8.1 Comparison of all Poisson's ratio and MCT thicknesses estimated in this study. There is little correlation between the values when all measurements are combined.

regions of recent extension and recent shearing associated with the San Andreas system.

The comparisons between Poisson's ratio and MCT thickness are more interesting. The data are shown in Figure 8.5 and Figure 8.6. The mature crusts beneath shields, platforms, and Paleozoic orogens show consistently thicker MCT's and which correlates with Poisson's ratio. The correlation is intriguing, considering the uncertainties in measuring each of these quantities with receiver functions. The measurements beneath shields are too sparse to draw any conclusions, but together with the Platforms and Paleozoic orogens provinces, a pattern can be discerned. The cause of the trend is problematic. Adding a few kilometers of transitional material

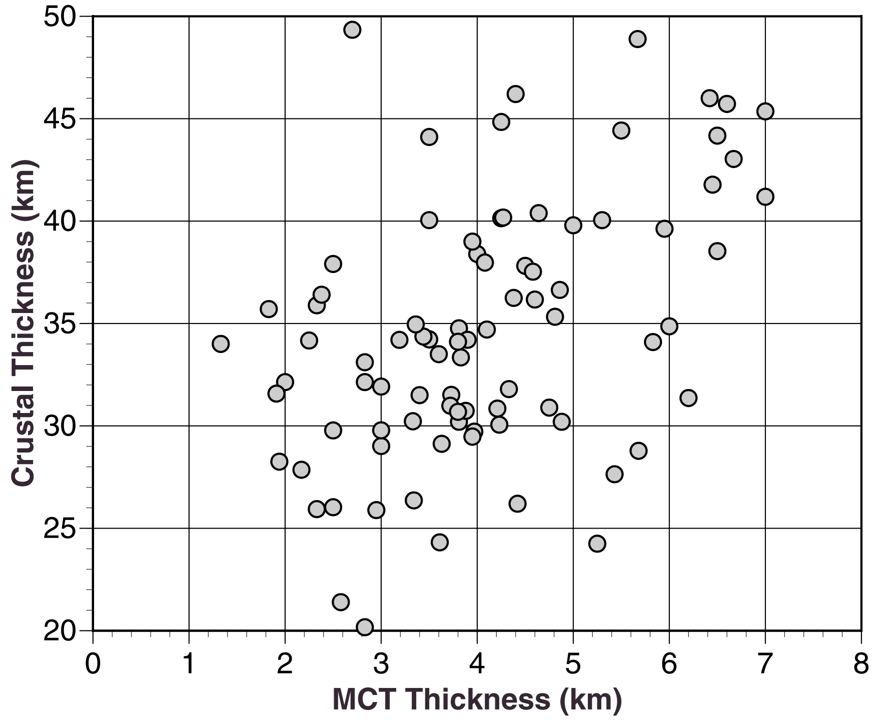

Figure 8.2 Comparison of all crustal thickness and MCT thickness values estimated in this study. The data show large variability but most of the thickest MCT are located beneath thick crusts.

at the base of the crust would not produce such a dramatic change in the receiver function travel times and hence would not strongly affect Poisson's ratio. Also, a transition comprised of a mix of crustal and mantle material could not produce the trend since the Poisson's ratio of ultramafic rocks is actually more similar to felsic rocks, *i.e.* it is not very high. Thus a correlation of higher Poisson ratio and more transitional MCT are indications of a differences in crustal composition. If we assume that the Poisson's ratio is indicative of a mafic composition, then the observations suggest that the lower crust of mature continental crust is mafic. A correlation of high Poisson's ratio and thick MCT does not necessarily indicate an increase in crustal thickness with age, they may simply indicate the level of crustal melting experienced in each region as these crusts experienced the transition from "imma-

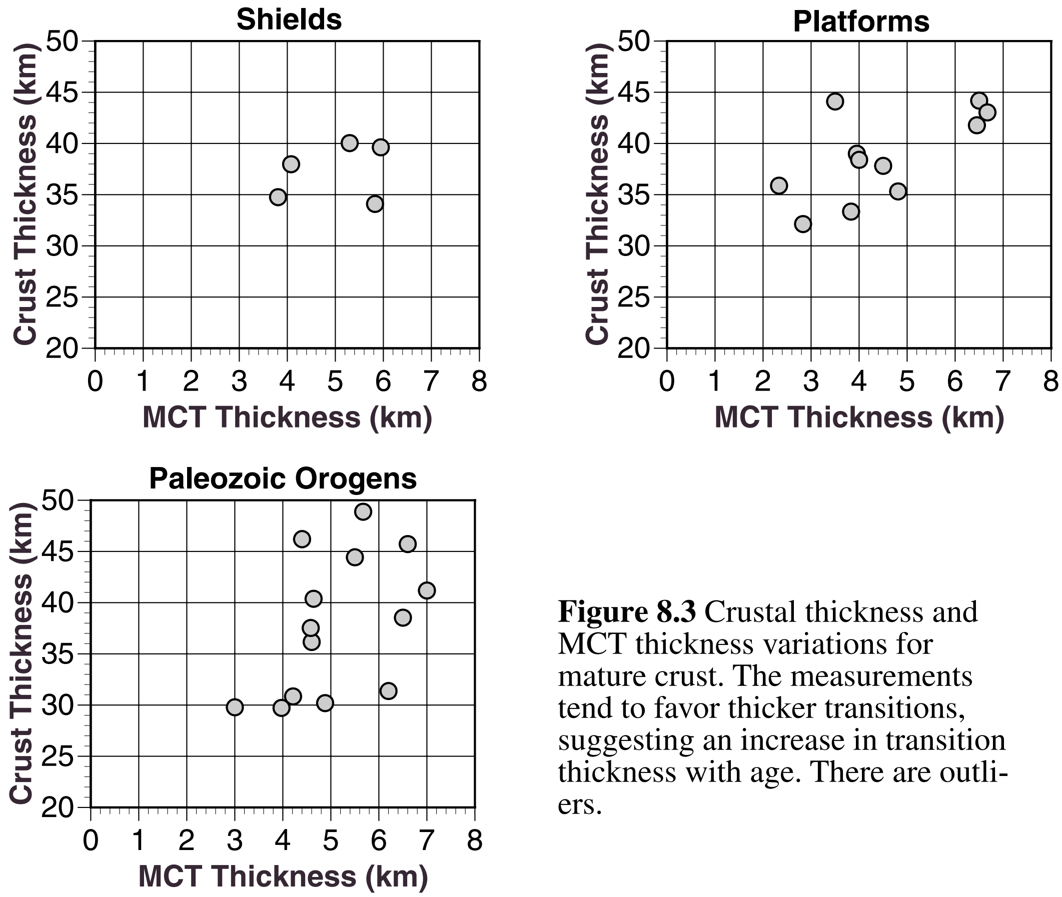

Figure 8.3 Crustal thickness and MCT thickness variations for mature crust. The measurements tend to favor thicker transitions, suggesting an increase in transition thickness with age. There are outliers.

ture" to "mature" or cratonic crust. The amount of differentiation to produce what is typical of continental crust may depend on the thickness of the crust (which influences the pressure-temperature regime experienced by the lower crust), but our results suggest that other factors must also be involved, since our observed relationships between MCT thickness and crustal thickness, or Poisson's ratio and crustal thickness are less clear as those for Poisson's ratio and MCT thickness.

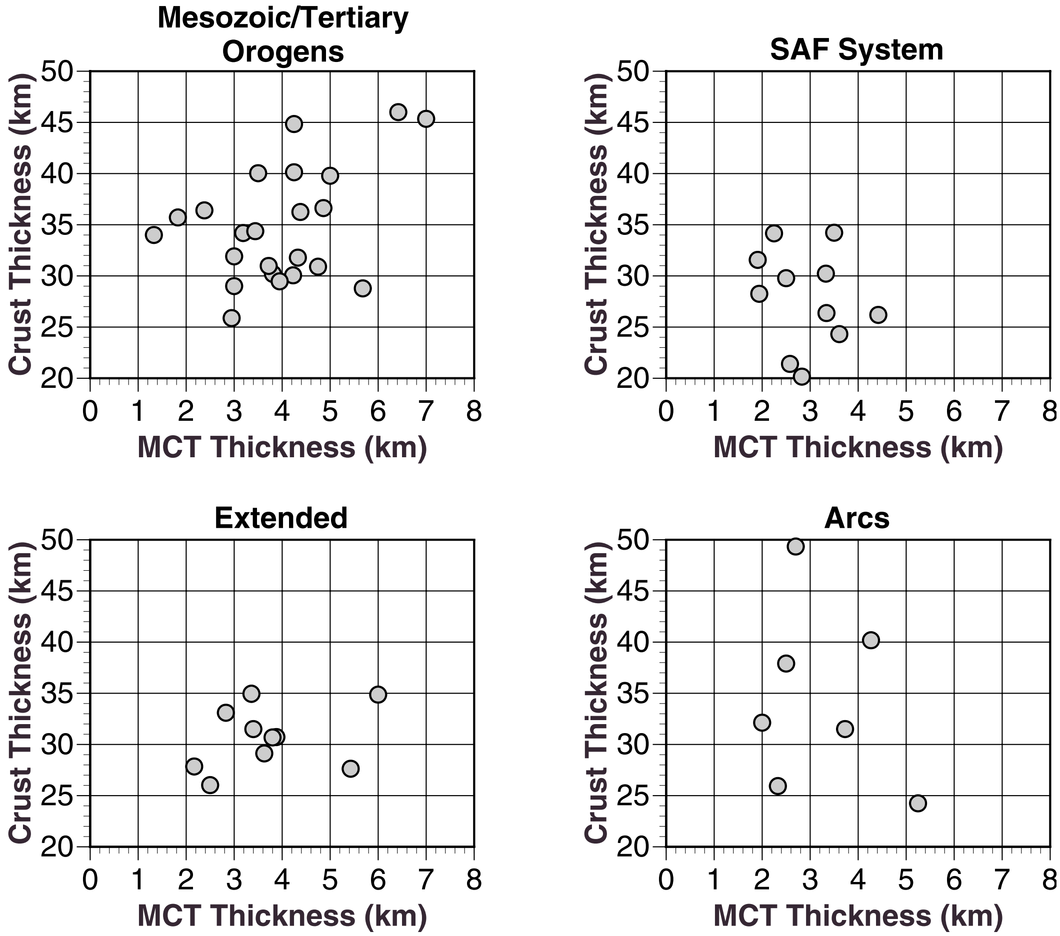

Figure 8.4 Crustal thickness and MCT thickness comparisons for active or recently actively deformed crust. The Mesozoic measurements show large scatter, but cluster near the median value of all measurements. The SAF System, Extended crust, and arc regions are predominantly thin.

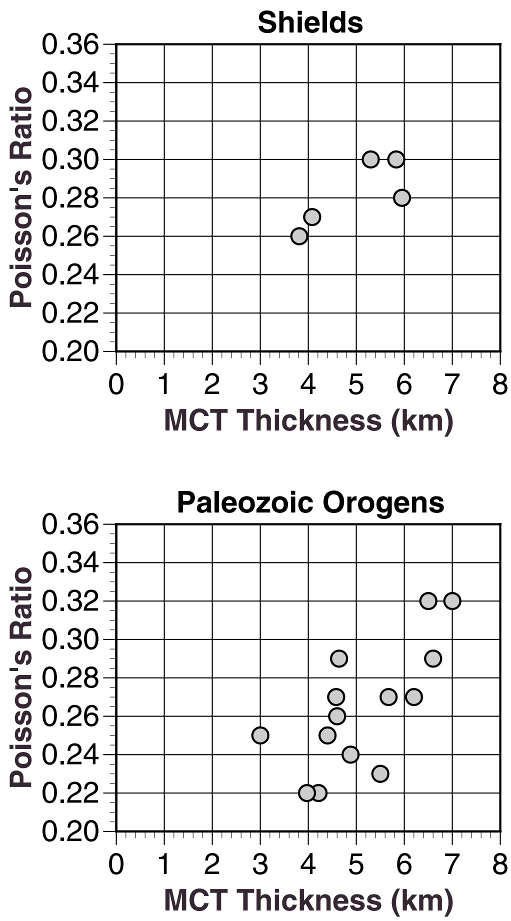

Figure 8.5 Poisson's ratio and MCT thickness variations for stations located in "mature" crustal provinces. With the exception of a couple of outliers, the data all show an increase in Poisson's ratio with MCT thickness.

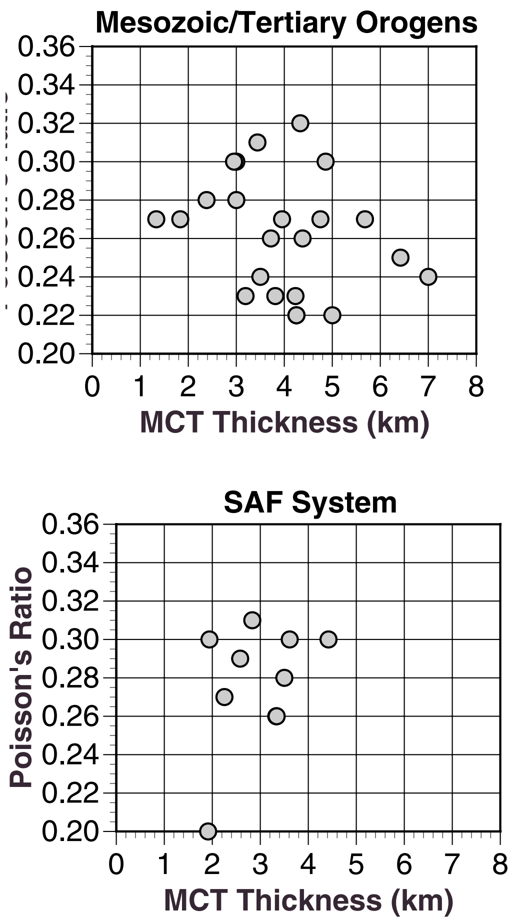

Figure 8.6 Variation of Poisson's ratio and MCT thickness for tectonically active, or recently active crust. The Mesozoic-Tertiary structures again show a large variability. Several outliers are noticeable on the extended and SAF system crusts, but for the most part the measurements in those provinces are consistent. The arc cluster into two groups with high Poisson's ratio and low Poisson's ratio.

A Station Distance and Azimuth Clusters

Table A-1: Observations Summary

ID	# Obs	Δ (°)	(±)	Back Az (°)	(±)	Depth (km)	(±)	p (s/km)	(±)
NETWORK: Berkeley (BK)									
ARC (Lat: 40.877 Lon: -124.075, Calif. Coast ranges)									
1	5	77	(4.9)	127.6	(3.7)	305.6	(290.9)	0.049	(0.003)
2	3	60.9	(0.8)	124.1	0.0	54.3	(42.3)	0.061	(0.001)
3	4	56.5	(1.9)	114.1	(2.2)	44.2	(53.9)	0.064	(0.001)
4	4	34.6	(2.6)	127	(3.7)	59.2	(68.1)	0.077	(0.002)
5	2	45.3	(10.6)	307.2	(3.1)	52	(26.9)	0.071	(0.006)
6	4	65.3	(2.6)	305.7	(1.7)	47.2	(43.7)	0.058	(0.002)
BKS (Lat: 37.877 Lon: -122.235, Calif. Coast ranges)									
1	5	31.9	(2.1)	126.5	(3.6)	50.4	(62.2)	0.079	(0.002)
2	7	53.2	(1.6)	116.1	(1.7)	38.4	(43.3)	0.067	(0.001)
3	3	58.6	(0.9)	124.1	(0.1)	75.7	(42.3)	0.062	(0.001)
4	2	70.5	(3.0)	127.4	(5.1)	332	(422.8)	0.053	(0.002)
5	3	80	(1.8)	134.6	(2.2)	32	(13.7)	0.048	(0.001)
6	2	54.5	(8.1)	179.6	(12.7)	12.5	(3.5)	0.065	(0.006)
7	6	73.9	(3.1)	233.2	(2.1)	201.7	(275.1)	0.052	(0.003)
8	6	86.3	(0.8)	241	(1.3)	95.5	(74.9)	0.044	0.000
9	8	84.5	(1.6)	250.3	(3.5)	39.6	(27.1)	0.045	(0.001)
10	7	89.4	(2.0)	262.3	(1.8)	56.1	(36.3)	0.043	(0.001)
11	2	82.5	(2.7)	284.3	(3.2)	327.5	(379.7)	0.046	(0.001)
12	6	37.9	(4.8)	310	(4.1)	28.3	(9.0)	0.076	(0.002)
13	4	55	(0.7)	312.1	(0.7)	41	(21.6)	0.065	(0.001)
14	16	66.8	(3.4)	307.4	(1.1)	43.2	(32.3)	0.057	(0.002)
15	8	81.4	(5.3)	304.8	(3.6)	179.8	(187.6)	0.047	(0.003)
16	2	96.7	(0.5)	303.3	(3.1)	91	(110.3)	0.041	(0.001)
BRK (Lat: 37.873 Lon: -122.260, Calif. Coast ranges)									
1	2	75.2	(1.8)	298.7	(5.4)	32	(32.5)	0.051	(0.001)
CMB (Lat: 38.035 Lon: -120.383, Orogen)									
1	4	31.4	(1.8)	128.6	(4.1)	57.8	(69.3)	0.079	(0.002)
2	10	54.1	(3.0)	120.9	(4.5)	50.8	(43.7)	0.066	(0.002)
3	3	69.6	(2.1)	128.1	(3.9)	420	(335.6)	0.053	(0.001)
4	11	80.8	(3.0)	133.6	(2.9)	230.1	(236.4)	0.047	(0.002)
5	14	79.4	(4.7)	233.2	(3.2)	219.5	(251.8)	0.048	(0.003)
6	9	87.1	(1.2)	243.9	(2.8)	71.3	(69.7)	0.044	(0.001)
7	7	90	(0.7)	263.1	(1.4)	103	(130.0)	0.042	0.000
8	3	83.5	(2.0)	285	(2.3)	223	(323.8)	0.045	(0.001)
9	9	38.3	(4.9)	310.1	(3.6)	26	(10.5)	0.075	(0.003)

Table A-1: Observations Summary (Continued)

ID	# Obs	Δ (°)	(±)	Back Az (°)	(±)	Depth (km)	(±)	p (s/km)	(±)
10	4	56.2	(0.4)	312.4	(0.6)	67.5	(56.0)	0.065	0.000
11	16	67.2	(3.2)	308.7	(2.6)	53.3	(35.7)	0.057	(0.002)
12	10	78.4	(4.3)	306.1	(3.4)	164.8	(181.6)	0.049	(0.003)
13	3	94.4	(3.4)	304.5	(1.9)	111.7	(87.5)	0.041	(0.001)
HOPS (Lat: 38.994 Lon: -123.072, Calif. Coast ranges)									
1	2	32.3	(2.3)	125.6	(4.9)	91	(99.0)	0.078	(0.002)
2	4	58.5	(2.8)	122	(4.1)	94.8	(46.3)	0.063	(0.002)
3	3	73.8	(4.9)	128.9	(4.1)	222	(315.3)	0.052	(0.003)
4	2	86.3	(2.1)	225.4	(0.3)	70.5	(53.0)	0.044	(0.001)
5	4	77.1	(3.9)	229.9	(1.4)	102.5	(55.4)	0.05	(0.003)
6	2	86.9	(1.4)	239.6	(2.1)	88.5	(78.5)	0.044	(0.001)
7	3	87.9	(0.1)	260.6	(0.6)	44.7	(29.0)	0.043	0.000
8	2	77.6	(3.0)	290	(5.9)	302.5	(415.1)	0.049	(0.003)
9	2	40	(0.8)	306.8	(0.2)	33	0.0	0.074	(0.001)
10	6	59.2	(5.4)	310.2	(4.4)	31.8	(7.4)	0.062	(0.004)
11	3	77.4	(6.3)	303.5	(3.0)	149	(187.6)	0.05	(0.005)
JRSC (Lat: 37.404 Lon: -122.238, Calif. Coast ranges)									
1	3	30.7	(1.7)	125.9	(4.2)	67.7	(80.8)	0.079	(0.002)
2	4	53	(2.0)	115.1	(1.6)	56.5	(52.1)	0.066	(0.002)
3	2	58	(1.0)	124	0.0	65	(53.7)	0.063	(0.001)
4	4	76.4	(5.8)	133.1	(2.5)	37.5	(13.8)	0.05	(0.004)
5	5	78.1	(4.7)	230.2	(2.6)	165.4	(218.2)	0.049	(0.003)
6	3	86.1	(1.3)	241.8	(3.1)	70	(64.1)	0.043	(0.001)
7	2	84.1	(2.4)	251.7	(2.1)	53	(28.3)	0.045	(0.001)
8	4	88.1	(0.4)	261.6	(1.1)	130	(172.3)	0.043	0.000
9	2	78.7	(2.9)	290.8	(6.0)	302.5	(415.1)	0.049	(0.003)
10	2	41.8	(1.2)	308.3	(0.1)	24.5	(12.0)	0.074	0.000
11	13	67.6	(5.1)	307.4	(2.1)	99.8	(145.2)	0.056	(0.004)
KCC (Lat: 37.324 Lon: -119.318, Orogen)									
1	2	71.4	(7.3)	133.9	(0.9)	41.5	(12.0)	0.054	(0.004)
2	4	77.3	(4.3)	233.1	(1.7)	183.8	(246.7)	0.049	(0.003)
3	2	87.6	(4.1)	257.2	(7.2)	58.5	(20.5)	0.044	(0.002)
4	3	61.8	(9.7)	313	(1.7)	100.7	(110.8)	0.061	(0.007)
5	5	71.2	(4.7)	307.6	(3.0)	84	(80.2)	0.054	(0.003)
6	2	81.2	(3.4)	291.8	(6.8)	79	(99.0)	0.047	(0.003)
7	3	85	(0.6)	306	(0.5)	27	(20.0)	0.045	0.000
MHC (Lat: 37.342 Lon: -121.642, Calif. Coast ranges)									
1	3	30.7	(1.6)	126.7	(4.3)	65.7	(82.6)	0.079	(0.002)
2	10	50.9	(3.7)	116.2	(3.0)	30.6	(37.6)	0.068	(0.002)
3	3	57.4	(0.8)	124.5	0.0	54.3	(42.3)	0.064	(0.002)
4	4	69.4	(2.1)	126.3	(3.4)	464.8	(288.3)	0.054	(0.001)
5	4	79.3	(1.5)	133.7	(3.1)	79.2	(95.2)	0.049	(0.001)
6	2	88.6	(5.9)	225	(2.5)	46	(18.4)	0.043	(0.003)
7	10	75.9	(3.0)	232.8	(2.5)	218.2	(240.7)	0.05	(0.002)
8	11	85.9	(1.0)	243.3	(2.7)	97.1	(70.5)	0.044	(0.001)
9	3	85.8	(2.0)	253.4	(2.4)	20.7	(11.6)	0.044	(0.001)

Table A-1: Observations Summary (Continued)

ID	# Obs	Δ (°)	(±)	Back Az (°)	(±)	Depth (km)	(±)	p (s/km)	(±)
10	7	89	(0.9)	262.4	(1.4)	110.6	(133.0)	0.043	0.000
11	3	86.1	(5.4)	284.5	(2.3)	221.7	(325.1)	0.043	(0.002)
12	2	31.5	(0.3)	320.8	(5.6)	121.5	(126.6)	0.079	(0.001)
13	4	43.9	(3.4)	309.3	(2.0)	30.8	(3.9)	0.072	(0.002)
14	3	56	(0.5)	312.2	(0.3)	41.7	(26.4)	0.065	0.000
15	14	67.3	(3.2)	308.9	(3.4)	82.4	(154.3)	0.056	(0.002)
16	5	81.8	(5.1)	302.9	(1.2)	97.2	(142.4)	0.047	(0.003)
17	2	97.4	(0.5)	303.6	(3.1)	91	(110.3)	0.04	0.000
MIN (Lat: 40.345 Lon: -121.605, Orogen)									
1	3	31.1	(0.6)	133.1	(0.1)	21	0.0	0.079	0.000
2	3	56.3	(2.2)	119.5	(6.6)	38.7	(26.5)	0.064	(0.001)
3	3	74.2	(4.9)	130.1	(4.5)	237	(341.3)	0.051	(0.003)
4	4	76.5	(3.9)	233	(1.0)	318	(327.0)	0.049	(0.003)
5	6	86.6	(2.0)	246.2	(5.2)	64.8	(72.0)	0.044	(0.001)
6	5	90.8	(2.7)	263.5	(2.4)	52	(43.5)	0.042	0.000
7	3	37.5	(5.3)	307.3	(2.9)	32	(1.7)	0.076	(0.003)
8	3	85.4	(5.5)	284.3	(2.2)	221.7	(325.1)	0.044	(0.003)
9	8	60.6	(4.3)	309	(3.8)	44.4	(41.2)	0.061	(0.003)
10	8	74.7	(6.0)	305.3	(3.7)	128.4	(178.0)	0.051	(0.004)
ORV (Lat: 39.556 Lon: -121.500, Orogen)									
1	6	32.1	(2.0)	130.1	(3.5)	45.5	(56.9)	0.078	(0.001)
2	7	54.2	(1.7)	116.2	(3.0)	38.6	(43.2)	0.066	(0.001)
3	3	58.6	(0.8)	125.7	0.0	54.3	(42.3)	0.063	(0.001)
4	2	67.5	(2.2)	131.4	(1.0)	69.5	(51.6)	0.056	(0.002)
5	10	82.8	(3.0)	133.9	(3.4)	195.6	(221.0)	0.046	(0.002)
6	15	77.7	(3.5)	232.2	(2.2)	256.5	(270.5)	0.049	(0.003)
7	11	86.3	(1.7)	245.8	(4.9)	68.7	(65.1)	0.044	(0.001)
8	8	90.1	(2.3)	263	(2.1)	93.2	(123.4)	0.042	0.000
9	4	84.6	(4.9)	284.1	(1.8)	169.8	(285.0)	0.045	(0.003)
10	3	32.2	(2.1)	311.1	(3.3)	24.3	(11.6)	0.078	(0.001)
11	4	40.8	(0.8)	305.9	(1.0)	29.2	(6.8)	0.074	0.000
12	5	54.5	(0.3)	311.3	(0.5)	60.6	(50.9)	0.066	(0.001)
13	19	65	(2.8)	307	(0.9)	39.2	(25.6)	0.058	(0.002)
14	2	68.6	(8.0)	314.5	(3.4)	252	(309.7)	0.054	(0.006)
15	4	77.8	(3.4)	303.4	(1.7)	111	(160.9)	0.049	(0.002)
16	9	84.4	(7.5)	303.3	(1.5)	93	(113.8)	0.046	(0.004)
PKD (Lat: 35.945 Lon: -120.541, Calif. Coast ranges)									
1	4	52.9	(3.7)	120.6	(4.9)	53.2	(40.6)	0.066	(0.002)
2	2	68.2	(3.0)	128.2	(5.0)	332	(422.8)	0.054	(0.002)
3	4	78.7	(3.5)	131.2	(1.8)	286.2	(231.4)	0.049	(0.003)
4	7	77.4	(4.1)	233.3	(3.6)	200	(246.4)	0.049	(0.003)
5	2	86.1	(0.4)	244.1	(2.9)	33	0.0	0.043	(0.001)
6	2	85.8	(1.4)	253.5	(1.3)	26.5	(9.2)	0.045	(0.001)
7	2	39.2	(5.5)	312.6	(3.9)	31.5	(2.1)	0.075	(0.003)
8	9	69	(3.7)	307.9	(1.7)	49.1	(30.0)	0.056	(0.002)
9	3	86.8	(1.9)	304.1	(1.3)	26.7	(4.5)	0.044	(0.001)

Table A-1: Observations Summary (Continued)

ID	# Obs	Δ (°)	(±)	Back Az (°)	(±)	Depth (km)	(±)	p (s/km)	(±)
10	2	71.8	(7.9)	315.9	(3.7)	252	(309.7)	0.052	(0.005)
SAO (Lat: 36.765 Lon: -121.445, Calif. Coast ranges)									
1	3	36	(5.8)	121.2	(1.7)	72.3	(77.0)	0.076	(0.002)
2	2	58.9	(1.4)	95.9	(4.3)	10	(7.1)	0.063	(0.001)
3	9	52.7	(1.6)	114.7	(2.7)	56.9	(76.2)	0.067	(0.001)
4	5	57.7	(1.2)	124.7	(0.9)	56.8	(39.6)	0.063	(0.001)
5	4	69.7	(1.8)	124.7	(0.4)	603	(19.5)	0.053	(0.001)
6	4	79.5	(3.7)	131.7	(1.4)	229.8	(260.5)	0.048	(0.003)
7	3	89.1	(2.9)	225.4	(1.8)	166.7	(146.1)	0.042	(0.001)
8	7	74.3	(3.3)	233.8	(2.0)	204.3	(246.9)	0.051	(0.003)
9	8	86	(1.1)	243.3	(2.9)	71.4	(51.0)	0.044	(0.001)
10	3	85.5	(2.4)	253.4	(2.5)	38.7	(31.9)	0.044	(0.001)
11	5	89.1	(1.1)	262.9	(1.4)	146.4	(144.6)	0.042	(0.001)
12	2	83.4	(2.7)	284.9	(3.2)	327.5	(379.7)	0.045	(0.001)
13	2	32	(0.3)	321.3	(5.5)	121.5	(126.6)	0.078	0.000
14	4	42	(1.4)	308.5	(0.8)	22.8	(11.5)	0.074	0.000
15	5	54.5	(3.2)	313.3	(1.5)	58.8	(52.2)	0.066	(0.002)
16	12	67.6	(3.1)	307.8	(1.2)	44.2	(34.8)	0.056	(0.002)
17	3	79.6	(4.8)	303.1	(1.2)	138.7	(185.3)	0.048	(0.003)
STAN (Lat: 37.404 Lon: -122.174, Calif. Coast ranges)									
1	2	31.9	(3.8)	125.7	(4.0)	27.5	(9.2)	0.079	(0.003)
2	3	51.5	(0.7)	115.7	(1.6)	15	(5.6)	0.068	(0.001)
3	3	76.8	(5.3)	129.8	(5.0)	282	(288.4)	0.05	(0.003)
4	2	78.3	(9.7)	228.5	(3.6)	18	(4.2)	0.049	(0.006)
5	5	62.7	(7.0)	309.9	(2.2)	51.8	(39.5)	0.06	(0.005)
WDC (Lat: 40.580 Lon: -122.540, Orogen)									
1	6	54.8	(1.8)	116.8	(2.4)	68.8	(91.5)	0.066	(0.002)
2	4	71.9	(2.0)	128.2	(3.9)	323.2	(335.5)	0.051	(0.001)
3	6	83.4	(2.4)	133.5	(3.4)	154.7	(214.0)	0.045	(0.002)
4	2	77.8	(0.8)	165.8	(3.2)	10	0.0	0.049	0.000
5	2	88	(2.6)	225.9	(0.1)	183	(212.1)	0.043	(0.001)
6	10	76.9	(4.1)	231.7	(2.0)	196.6	(243.3)	0.05	(0.003)
7	5	87.6	(0.9)	240.6	(1.4)	90.6	(76.1)	0.043	0.000
8	4	84.9	(1.2)	247.9	(2.9)	37.8	(24.1)	0.045	(0.001)
9	7	38.5	(3.5)	306	(2.0)	30	(6.3)	0.075	(0.002)
10	5	52.2	(1.5)	311.3	(1.5)	38.2	(19.2)	0.067	(0.001)
11	11	64.9	(3.2)	306.5	(1.4)	64.5	(64.3)	0.058	(0.002)
12	3	74.1	(1.0)	308.8	(2.3)	428	(55.8)	0.051	(0.001)
13	4	77.1	(1.9)	295.7	(4.8)	268	(175.3)	0.049	(0.002)
14	2	84	(0.1)	301.8	(0.1)	29	(2.8)	0.045	(0.001)
YBH (Lat: 41.732 Lon: -122.709, Orogen)									
1	2	65.2	(12.5)	122	(4.4)	409	(250.3)	0.057	(0.010)
2	3	81.1	(2.8)	231.9	(1.3)	545.3	(20.4)	0.046	(0.002)
3	4	87.9	(1.3)	241	(2.5)	59.5	(56.4)	0.043	(0.001)
4	6	89.7	(2.6)	262.7	(2.2)	104.7	(143.6)	0.043	(0.001)
5	3	84.2	(5.5)	283.4	(2.1)	221.7	(325.1)	0.045	(0.003)

Table A-1: Observations Summary (Continued)

ID	# Obs	Δ (°)	(±)	Back Az (°)	(±)	Depth (km)	(±)	p (s/km)	(±)
6	3	36.8	(3.9)	304.5	(0.5)	20	(11.5)	0.076	(0.002)
7	6	63.9	(2.8)	305.1	(0.5)	32.2	(14.0)	0.059	(0.002)
8	2	66.4	(8.1)	313.4	(3.3)	252	(309.7)	0.056	(0.005)
9	2	79.6	(5.3)	300.9	(1.0)	189	(229.1)	0.048	(0.003)
10	3	92.9	(1.7)	304.4	(1.2)	14.7	(4.7)	0.041	0.000
NETWORK: Canadian National Seismic Network (CN)									
BBB (Lat: 52.185 Lon: -128.113, Continental arc)									
1	3	84.7	(2.4)	226.2	(2.5)	400	(250.3)	0.044	(0.001)
2	2	87.1	0.0	248.3	(10.5)	83.5	(55.9)	0.043	0.000
3	2	40.4	(0.5)	302	(0.9)	33	0.0	0.074	0.000
DAWY (Lat: 64.066 Lon: -139.391, Orogen)									
1	2	67.4	(11.1)	118	(7.9)	146.5	(120.9)	0.056	(0.008)
2	3	89.7	(2.9)	215.9	(1.9)	400	(250.3)	0.042	(0.001)
3	2	87.1	(2.4)	238	(10.2)	83.5	(55.9)	0.043	(0.001)
4	2	30.5	(0.6)	279.8	(0.8)	33	0.0	0.079	0.000
DLBC (Lat: 58.437 Lon: -130.030, Orogen)									
1	3	56.9	(10.4)	128.4	(7.9)	108.7	(107.7)	0.064	(0.008)
2	2	89.7	(1.9)	223.2	(1.7)	330.5	(310.4)	0.042	0.000
3	2	88.5	(1.1)	246.4	(10.4)	83.5	(55.9)	0.043	(0.001)
4	2	36.5	(0.6)	294.1	(0.9)	33	0.0	0.076	0.000
DRLN (Lat: 49.256 Lon: -57.504, Paleozoic orogen)									
1	4	74.7	(4.0)	190.9	(1.9)	104.2	(114.5)	0.051	(0.003)
2	3	62.7	(3.5)	197	(4.1)	261	(289.0)	0.059	(0.002)
3	3	50.1	(4.0)	205	(0.2)	136.3	(103.2)	0.069	(0.002)
4	5	46.1	(1.9)	239.7	(7.3)	65	(55.8)	0.071	0.000
5	4	77.9	(6.0)	339.3	(2.4)	55	(47.0)	0.049	(0.004)
EDM (Lat: 53.222 Lon: -113.350,Continental platform)									
1	4	82.9	(9.3)	141.1	(2.6)	76.2	(58.6)	0.046	(0.006)
2	2	91.3	(1.6)	239.4	(1.8)	544.5	(7.8)	0.041	0.000
3	2	95.9	(0.3)	260	(10.5)	83.5	(55.9)	0.041	(0.001)
4	3	47	(0.6)	307.6	(0.5)	33	0.0	0.071	(0.001)
FCC (Lat: 58.762 Lon: -94.087, Shield)									
1	3	86.8	(3.8)	158.7	(1.4)	47	(3.0)	0.044	(0.002)
2	3	66.7	(9.3)	157.1	(2.3)	300	(247.8)	0.056	(0.007)
3	3	51.6	(0.6)	313.9	(0.3)	33	0.0	0.067	(0.001)
FRB (Lat: 63.747 Lon: -68.547, Shield)									
1	2	67.1	(4.3)	64.8	(0.5)	21.5	(16.3)	0.057	(0.003)
2	4	88	(2.0)	178.9	(3.0)	234.5	(244.3)	0.043	(0.001)
3	5	76	(2.6)	184.2	(4.0)	306	(284.8)	0.05	(0.002)
4	4	58.5	(2.3)	187.9	(2.7)	67.5	(109.7)	0.063	(0.002)
5	10	51.2	(0.8)	218	(5.1)	48.5	(42.8)	0.068	0.000
6	3	40.8	(1.5)	254.8	(6.7)	11.7	(5.7)	0.074	(0.001)
7	5	46.9	(4.0)	306.3	(3.7)	28.4	(10.1)	0.071	(0.002)
8	2	59.5	(0.4)	327.8	(0.5)	45.5	(36.1)	0.062	0.000
9	20	70.9	(4.8)	333.7	(3.2)	69.9	(108.0)	0.054	(0.003)
10	3	93.3	(2.5)	350	(0.4)	65.3	(89.8)	0.041	0.000

Table A-1: Observations Summary (Continued)

ID	# Obs	Δ (°)	(±)	Back Az (°)	(±)	Depth (km)	(±)	p (s/km)	(±)
GAC (Lat: 45.703 Lon: -75.478, Shield)									
1	2	45	(4.7)	181.8	(2.0)	129.5	(145.0)	0.071	(0.003)
2	2	58.8	(2.3)	180.7	(0.7)	69.5	(51.6)	0.062	(0.001)
3	10	34.7	(1.0)	220.5	(6.8)	47	(43.1)	0.077	0.000
4	2	74.8	(1.4)	225.6	(13.5)	12.5	(3.5)	0.052	(0.001)
5	2	57.3	(7.9)	315	(2.4)	32	0.0	0.064	(0.006)
6	2	70.8	(3.2)	328.4	(0.3)	52	(26.9)	0.054	(0.003)
INK (Lat: 68.307 Lon: -133.520, Orogen)									
1	2	79.8	(4.2)	11.2	(1.3)	21.5	(16.3)	0.049	(0.003)
2	5	78.8	(6.0)	121.3	(2.0)	94	(98.2)	0.049	(0.004)
3	5	55.6	(2.3)	138.9	(4.7)	59.4	(57.7)	0.065	(0.002)
4	4	92.9	(4.0)	220.5	(2.3)	310.2	(272.0)	0.041	(0.001)
5	4	90.8	(1.8)	242.1	(6.2)	68.2	(40.2)	0.042	(0.001)
6	4	32.9	(1.8)	277.3	(0.6)	29.8	(6.5)	0.078	(0.001)
7	5	44.9	(1.1)	279.3	(1.0)	57.4	(38.2)	0.072	(0.001)
8	4	53.1	(2.5)	282.9	(3.0)	83.2	(97.7)	0.066	(0.002)
9	3	65.2	(2.3)	286.8	(0.4)	26.7	(4.5)	0.058	(0.001)
10	3	76.9	(5.0)	291.5	(0.8)	27.7	(6.8)	0.05	(0.003)
11	5	90.9	(5.8)	284.4	(1.9)	26.6	(10.1)	0.043	(0.002)
LMN (Lat: 45.852 Lon: -64.806, Paleozoic orogen)									
1	4	75.4	(8.0)	185.8	(1.1)	43.5	(7.4)	0.051	(0.005)
2	3	46.7	(6.7)	194.6	(2.7)	182	(43.9)	0.071	(0.004)
LMQ (Lat: 47.548 Lon: -70.327, Continental Platform)									
1	2	79.3	(11.6)	181.5	(2.4)	41.5	(12.0)	0.048	(0.007)
2	2	49.7	(8.4)	186.2	(2.2)	157	(9.9)	0.069	(0.006)
3	2	37.8	(0.3)	219	(5.3)	47	(19.8)	0.075	(0.001)
MBC (Lat: 76.242 Lon: -119.360, Paleozoic orogen)									
1	3	70	(5.5)	2.1	(3.5)	19.0	(19.2)	0.054	(0.004)
2	2	94.9	(0.2)	134.0	(5.6)	332.0	(422.8)	0.040	(0.000)
3	5	77.6	(4.7)	135.6	(3.1)	19.6	(9.8)	0.050	(0.003)
4	9	60.6	(1.6)	156.5	(3.6)	45.4	(45.4)	0.061	(0.002)
5	3	39.1	(3.0)	181.7	(5.6)	11.7	(5.7)	0.075	(0.001)
6	4	95.5	(1.7)	263.0	(4.1)	38.0	(10.4)	0.041	(0.000)
7	3	79.3	(3.8)	280.3	(3.6)	27.7	(27.2)	0.049	(0.003)
8	2	39.0	(0.4)	279.5	(0.7)	45.5	(36.1)	0.075	(0.001)
9	14	49.8	(3.8)	286.9	(4.2)	90.6	(124.1)	0.069	(0.003)
10	3	64.2	(0.7)	296.3	(0.1)	27.0	(20.0)	0.058	(0.001)
11	6	73.8	(1.2)	303.4	(1.2)	19.3	(7.5)	0.052	(0.001)
12	4	86.0	(2.7)	297.3	(4.0)	33.8	(20.2)	0.044	(0.001)
13	3	95.7	(0.4)	297.9	(3.3)	27.0	(10.4)	0.041	(0.000)
14	2	75.4	(2.3)	325.9	(3.0)	66.5	(78.5)	0.051	(0.002)
15	3	67.5	(0.5)	350.0	(4.9)	89.0	(109.3)	0.056	(0.001)
MOBC (Lat: 53.197 Lon: -131.900, Continental Arc)									
1	2	85.1	(1.8)	221.7	(1.8)	330.5	(310.4)	0.044	(0.000)
2	2	37.9	(0.5)	299.4	(1.0)	33	0.0	0.073	(0.000)
PGC (Lat: 48.650 Lon: -123.45, Continental Arc)									

Table A-1: Observations Summary (Continued)

ID	# Obs	Δ (°)	(±)	Back Az (°)	(±)	Depth (km)	(±)	p (s/km)	(±)
1	2	65.8	(7.7)	124.7	(4.1)	198	(48.1)	0.057	(0.005)
2	4	85.5	(2.5)	233.8	(7.5)	330.8	(246.9)	0.044	(0.001)
3	2	44.9	(0.5)	307	(0.9)	33	0.0	0.07	(0.001)
PMB (Lat: 50.519 Lon: -123.077, Continental Arc)									
1	2	66.6	(7.8)	125.8	(3.8)	198	(48.1)	0.057	(0.005)
2	2	87.5	(0.2)	132.8	(0.3)	47	(4.2)	0.043	0.000
3	2	85.9	(3.2)	230.3	(3.7)	325	(302.6)	0.044	(0.002)
4	3	54.3	(17.9)	304.3	(2.2)	29.3	(6.4)	0.066	(0.012)
PNT (Lat: 49.317 Lon: -119.617, Orogen)									
1	2	40.1	(2.4)	139.4	(3.5)	47	(19.8)	0.037	(0.053)
2	3	68.4	(9.2)	128.8	(2.7)	327.3	(226.6)	0.055	(0.007)
3	3	87	(3.2)	136.9	(2.5)	47	(3.0)	0.044	(0.001)
4	3	87	(2.2)	233.1	(2.7)	400	(250.3)	0.043	(0.001)
5	2	91.3	(0.8)	254.9	(10.5)	83.5	(55.9)	0.042	(0.001)
6	2	46.5	(0.5)	307.8	(0.8)	33	0.0	0.071	0.000
RES (Lat: 74.687 Lon: -94.900, Continental Platform)									
1	4	82.5	(5.8)	161.5	(1.5)	64.2	(66.6)	0.046	(0.004)
2	4	57.2	(1.3)	185.4	(5.6)	66	(64.4)	0.064	(0.001)
3	4	42.4	(1.8)	301.4	(0.4)	29.8	(6.5)	0.074	0.000
4	6	53.7	(0.9)	307.1	(0.9)	53.3	(35.6)	0.066	(0.001)
5	3	65.7	(4.6)	309.7	(2.3)	35	(23.6)	0.058	(0.003)
6	3	70.8	(2.2)	319	(0.1)	34	(13.7)	0.054	(0.002)
7	2	79.7	(1.6)	325.9	(0.2)	25	(7.1)	0.049	(0.001)
8	2	89.3	(1.3)	323.5	(4.1)	33	0.0	0.042	(0.001)
SADO (Lat: 44.769 Lon: -79.142, Continental Platform)									
1	3	74	(9.3)	172.8	(3.2)	42.3	(8.6)	0.052	(0.006)
2	4	48.3	(9.0)	172.9	(3.2)	283	(205.2)	0.069	(0.007)
3	2	32.1	0.0	207.5	(6.2)	47	(19.8)	0.078	(0.001)
SCHQ (Lat: 54.832 Lon: -66.834, Shield)									
1	2	70.3	(4.2)	63	(1.2)	21.5	(16.3)	0.054	(0.003)
2	3	80.1	(4.6)	181.9	(2.6)	124.3	(131.4)	0.048	(0.003)
3	3	67	(3.5)	186.4	(3.8)	261	(289.0)	0.056	(0.002)
4	4	54	(5.0)	192.9	(1.1)	76.5	(104.0)	0.065	(0.003)
5	6	44.9	(1.0)	224.1	(7.1)	59.7	(51.6)	0.072	(0.001)
6	4	67.8	(5.6)	331.9	(2.1)	52.5	(48.1)	0.056	(0.004)
ULM (Lat: 50.249 Lon: -95.875, Continental platform)									
1	2	35.1	(1.3)	176.7	(5.3)	47	(19.8)	0.038	(0.055)
2	2	55.2	(8.5)	154.2	(1.7)	157	(9.9)	0.065	(0.006)
3	4	82.5	(7.1)	158.5	(3.8)	43.5	(7.4)	0.047	(0.004)
4	3	57	(0.6)	317.3	(0.4)	33	0.0	0.064	(0.001)
WALA (Lat: 49.059 Lon: -113.911, Orogen)									
1	2	47.4	(11.6)	138	(9.0)	146.5	(120.9)	0.069	(0.008)
2	4	76.4	(7.5)	137.7	(2.9)	211	(256.0)	0.05	(0.005)
3	2	91.8	(5.2)	147.5	(4.7)	40	(9.9)	0.042	(0.002)
4	3	89.9	(2.1)	237.5	(2.8)	400	(250.3)	0.042	(0.001)
5	2	94.9	(1.0)	259.1	(10.5)	83.5	(55.9)	0.041	(0.001)

Table A-1: Observations Summary (Continued)

ID	# Obs	Δ (°)	(±)	Back Az (°)	(±)	Depth (km)	(±)	p (s/km)	(±)
6	2	49.6	(0.5)	310.2	(0.7)	33	0.0	0.069	0.000
WHY (Lat: 60.660 Lon: -134.881, Orogen)									
1	5	51.1	(3.6)	132.5	(5.5)	65	(55.8)	0.068	(0.002)
2	2	72.5	(6.2)	118.2	(3.6)	20.5	(9.2)	0.053	(0.004)
3	4	86.7	(4.0)	219.3	(2.2)	310.2	(272.0)	0.043	(0.002)
4	2	86	(1.3)	239.8	(2.9)	53	(28.3)	0.044	(0.001)
5	2	87.8	(2.5)	253.3	(5.4)	51.5	(10.6)	0.043	(0.001)
6	2	90.1	(0.3)	268.3	(0.4)	32.5	(0.7)	0.042	(0.001)
7	5	44.2	(4.5)	285.7	(0.6)	36.6	(12.7)	0.072	(0.002)
8	4	54.6	(2.1)	287.2	(3.4)	83.2	(97.7)	0.065	(0.002)
9	2	66.4	(2.6)	289.2	(0.9)	26.5	(6.4)	0.057	(0.002)
10	4	79.7	(4.1)	291.7	(1.3)	38.5	(22.4)	0.048	(0.003)
11	4	91.1	(6.3)	282.8	(1.7)	25	(10.9)	0.042	(0.002)
YKW (Lat: 62.562 Lon: -114.605, Shield)									
1	2	82.7	(4.3)	27	(0.6)	21.5	(16.3)	0.047	(0.003)
2	6	93.7	(2.0)	139.1	(1.9)	132.7	(211.3)	0.041	0.000
3	3	81.5	(4.0)	138.5	(3.9)	276	(314.3)	0.046	(0.004)
4	5	64.9	(1.1)	135.5	(2.4)	144	(120.5)	0.058	(0.001)
5	11	47.8	(2.2)	157	(4.8)	51.8	(39.4)	0.07	(0.002)
6	9	95.2	(2.3)	238.2	(1.5)	489.8	(168.4)	0.041	(0.001)
7	3	96.2	(0.4)	264.8	(4.4)	40.3	(6.4)	0.041	(0.001)
8	6	42.1	(1.3)	298.5	(0.6)	30.8	(5.3)	0.074	0.000
9	9	54	(0.6)	298.9	(0.6)	49.3	(42.8)	0.066	(0.001)
10	7	61.8	(2.1)	302.4	(3.7)	120.6	(171.9)	0.06	(0.002)
11	8	73.2	(1.8)	305	(0.4)	27.1	(9.4)	0.053	(0.001)
12	6	87.3	(4.6)	309	(1.9)	29.3	(22.5)	0.044	(0.002)
13	2	81.4	(0.7)	354	(6.4)	26	(9.9)	0.047	(0.001)
NETWORK: Geoscope (G)									
SCZ (Lat: 36.600 Lon: -121.400, Calif. Coast ranges)									
1	3	42.5	(8.9)	119.7	(2.7)	44.7	(30.4)	0.073	(0.005)
2	5	75.1	(4.8)	233	(4.0)	131	(256.1)	0.051	(0.003)
3	4	84.6	(2.0)	252.4	(3.2)	38.2	(35.2)	0.045	(0.001)
4	2	91.7	(3.8)	264.6	(1.6)	53.5	(6.4)	0.042	(0.001)
5	2	83.8	(2.2)	283.3	(0.9)	36.5	(31.8)	0.045	(0.002)
6	3	36.4	(5.5)	313.7	(4.3)	33	(3.6)	0.076	(0.002)
7	2	56.8	(0.5)	312.7	(0.4)	52.5	(26.2)	0.064	(0.001)
8	5	74.3	(3.4)	306.8	(3.4)	84.4	(149.2)	0.052	(0.003)
UNM (Lat: 19.332 Lon: -99.183, Continental Arc)									
1	6	43	(6.3)	138.7	(4.2)	249.3	(272.4)	0.072	(0.004)
2	6	87.2	(5.8)	249.1	(3.2)	212.8	(218.8)	0.044	(0.002)
3	4	32.9	(4.7)	322.3	(4.7)	15.2	(3.4)	0.078	(0.002)
4	2	53.9	(5.8)	327.2	(5.1)	23	(12.7)	0.066	(0.004)
5	4	84	(3.7)	321.5	(2.0)	42.2	(20.0)	0.045	(0.002)
NETWORK: IRIS – IDA (II)									
ALE (Lat: 82.503 Lon: -62.350, Paleozoic orogen)									
1	5	71.2	(6.0)	18.8	(3.0)	38	(48.3)	0.054	(0.004)

Table A-1: Observations Summary (Continued)

ID	# Obs	Δ (°)	(±)	Back Az (°)	(±)	Depth (km)	(±)	p (s/km)	(±)
2	4	60.8	(3.0)	41.6	(3.4)	145	(96.2)	0.06	(0.002)
3	4	55.6	(7.3)	64.4	(4.1)	14	(4.8)	0.065	(0.005)
4	2	57	(7.8)	84.1	(7.5)	12	(2.8)	0.064	(0.006)
5	2	95.9	(0.5)	187.4	(3.2)	368	(371.9)	0.04	0.000
6	3	86.6	(1.8)	195.3	(0.5)	26.7	(6.5)	0.044	(0.001)
7	5	77.5	(1.6)	193.6	(2.8)	42.2	(46.9)	0.05	(0.001)
8	2	73.3	(0.1)	202.3	(1.3)	16	(8.5)	0.052	0.000
9	8	67.1	(1.4)	218.1	(4.5)	52	(46.2)	0.056	(0.001)
10	3	47.9	(3.7)	246.8	(5.1)	13	(4.4)	0.07	(0.002)
11	6	37.8	(3.8)	295.1	(7.9)	57.2	(75.8)	0.075	(0.001)
12	4	43.7	(1.4)	322.3	(5.0)	68.8	(54.6)	0.073	(0.001)
13	10	51.6	(0.5)	331	(0.9)	45.2	(40.9)	0.068	0.000
14	12	59.7	(5.1)	339	(2.2)	124.4	(185.6)	0.062	(0.004)
15	3	80.9	(2.9)	332.9	(0.9)	223	(323.8)	0.047	(0.001)
16	6	73	(1.8)	354.3	(2.4)	43.5	(55.2)	0.052	(0.001)
17	4	84.1	(3.0)	355.3	(2.3)	34.2	(24.7)	0.045	(0.002)
FFC (Lat: 54.725 Lon: -101.978, Continental platform)									
1	2	91.3	(3.1)	10.3	(6.6)	116.5	(156.3)	0.042	(0.001)
2	2	85.8	(4.4)	36.8	(0.1)	21.5	(16.3)	0.045	(0.003)
3	2	52.5	(1.8)	147.5	(0.8)	69.5	(78.5)	0.067	(0.002)
4	5	81.7	(5.3)	149.5	(3.2)	194	(230.2)	0.047	(0.004)
5	8	37.9	(1.7)	174.9	(6.4)	47.8	(47.4)	0.075	(0.001)
6	2	73.1	(5.7)	199.6	(12.3)	12.5	(3.5)	0.052	(0.004)
7	2	94.4	(3.6)	247.4	(1.9)	302	(369.1)	0.041	0.000
8	4	40.2	(4.3)	296.3	(1.6)	23.2	(10.1)	0.074	(0.002)
9	10	62	(4.0)	311.3	(0.5)	46.7	(40.9)	0.06	(0.003)
10	8	75.7	(5.8)	312.8	(4.3)	120.9	(182.5)	0.051	(0.004)
PFO (Lat: 33.609 Lon: -116.455, Orogen)									
1	4	46.7	(1.8)	119	(0.8)	109	(100.5)	0.052	(0.021)
2	3	60.5	(5.7)	128	(0.9)	401.7	(330.6)	0.06	(0.006)
3	3	74.7	(3.2)	133.5	(2.3)	296.7	(257.6)	0.051	(0.003)
4	2	53.4	(3.0)	178	(2.0)	9.5	(0.7)	0.067	(0.003)
5	8	79.7	(4.4)	235.3	(2.7)	255.5	(270.8)	0.048	(0.003)
6	2	88.6	(0.3)	245	(0.6)	98.5	(58.7)	0.043	(0.001)
7	3	86.7	(0.8)	251	(2.1)	130.3	(10.2)	0.043	(0.001)
8	2	90.1	(1.0)	257.7	(1.4)	21.5	(16.3)	0.042	(0.001)
9	2	93.6	(1.8)	265.5	(2.4)	111.5	(95.5)	0.041	0.000
10	3	47.7	(1.0)	311.4	(0.2)	33	0.0	0.07	(0.001)
11	5	57.7	(2.9)	317.9	(3.9)	24.8	(8.6)	0.064	(0.003)
12	7	70	(1.1)	310.9	(0.5)	45	(34.0)	0.055	(0.001)
13	19	77	(6.6)	308.3	(3.8)	90.7	(135.3)	0.05	(0.004)
ADK (Lat: 51.884 Lon: -176.684, Volcanic Arc)									
1	5	67.9	(3.0)	89.8	(1.3)	34.6	(17.3)	0.056	(0.002)
2	2	40.6	(5.9)	88.7	(1.4)	14	(5.7)	0.074	(0.002)
3	4	72	(3.7)	178.8	(2.6)	182.5	(247.7)	0.053	(0.003)
4	4	66.7	(2.2)	198.7	(3.5)	54.8	(59.1)	0.057	(0.002)

Table A-1: Observations Summary (Continued)

ID	# Obs	Δ (°)	(±)	Back Az (°)	(±)	Depth (km)	(±)	p (s/km)	(±)
5	3	65.7	0.0	221.3	(0.1)	27.3	(2.5)	0.058	0.000
6	10	71.8	(4.6)	236.7	(3.3)	67.8	(57.9)	0.054	(0.003)
7	3	86.2	(0.3)	247.9	(0.4)	19	(7.5)	0.044	(0.001)
8	3	68.8	(7.0)	249.8	(1.9)	33	0.0	0.056	(0.005)
9	4	32.2	(2.2)	265.1	(6.5)	137.2	(222.9)	0.078	(0.002)
10	4	42.1	(4.4)	255.8	(6.2)	104.5	(164.6)	0.073	(0.002)
11	2	55.3	(2.4)	263.9	(1.4)	14.5	(2.1)	0.065	(0.001)
12	3	87.8	(0.4)	265	(5.4)	35.3	(21.6)	0.043	0.000
ANMO (Lat: 34.946 Lon: -106.457, Orogen)									
1	3	88.9	(4.2)	91.6	(3.2)	12.3	(3.2)	0.043	(0.002)
2	14	71.9	(3.4)	144.7	(3.8)	208.3	(243.9)	0.053	(0.003)
3	12	54.1	(5.6)	139.3	(2.5)	207.5	(245.3)	0.065	(0.005)
4	13	37.6	(4.4)	131	(4.6)	43.5	(57.2)	0.076	(0.002)
5	21	85.7	(3.3)	242.6	(2.1)	247.3	(244.6)	0.044	(0.002)
6	11	95.6	(1.1)	256	(3.5)	73.8	(57.5)	0.041	0.000
7	3	95.1	(2.1)	293.2	(2.3)	223	(323.8)	0.041	(0.001)
8	13	46.7	(5.2)	315.3	(5.5)	45.5	(56.3)	0.071	(0.003)
9	30	74.5	(6.1)	316	(2.1)	65.8	(108.0)	0.052	(0.004)
10	11	90.1	(2.5)	310.9	(3.9)	193.8	(207.6)	0.042	(0.001)
CCM (Lat: 38.056 Lon: -91.245, Continental platform)									
1	4	92	(3.3)	32.1	(2.4)	17.8	(7.5)	0.041	0.000
2	3	81	(1.4)	43.7	(4.2)	38.7	(43.6)	0.048	(0.001)
3	3	77.1	(4.0)	101.2	(3.6)	12.3	(3.2)	0.05	(0.003)
4	2	46.4	(7.1)	102.5	(8.5)	10	0.0	0.071	(0.004)
5	11	34.4	(2.4)	154.2	(5.8)	28.8	(36.2)	0.077	(0.002)
6	8	52.3	(5.0)	157.7	(3.5)	215.8	(248.4)	0.066	(0.004)
7	12	68.1	(3.1)	156.6	(3.3)	273.2	(234.3)	0.055	(0.003)
8	2	64.9	(2.1)	197.8	(7.4)	10.5	(0.7)	0.058	(0.001)
9	12	53.2	(5.9)	316.9	(5.6)	49.1	(57.4)	0.066	(0.004)
10	6	69.1	(4.1)	322.6	(2.6)	34.7	(21.0)	0.055	(0.002)
11	25	84.5	(5.0)	322.7	(2.8)	103.3	(164.3)	0.045	(0.003)
COL (Lat: 64.900 Lon: -147.793, Orogen)									
1	9	81.5	(6.8)	105.2	(3.7)	34.6	(37.9)	0.047	(0.004)
2	5	64.3	(5.6)	115.6	(5.9)	31.8	(27.9)	0.059	(0.004)
3	2	35.8	(0.5)	134.3	(2.0)	9.5	(12.0)	0.076	(0.001)
4	8	86.1	(3.1)	206.8	(2.4)	230.8	(246.6)	0.044	(0.002)
5	11	86.6	(2.9)	223.3	(2.5)	63.9	(67.6)	0.044	(0.002)
6	8	84.1	(1.6)	242.8	(3.9)	59.2	(64.1)	0.045	(0.001)
7	2	67.2	(2.3)	254.7	(0.3)	36.5	(31.8)	0.057	(0.001)
8	3	88	(4.0)	257.4	(2.1)	44.7	(29.3)	0.043	(0.002)
9	34	42.3	(7.0)	272.1	(3.2)	99.9	(133.6)	0.073	(0.005)
10	7	69.5	(5.0)	279.5	(2.1)	68.4	(68.6)	0.055	(0.003)
11	9	86.4	(5.1)	268.4	(2.2)	86.4	(169.1)	0.044	(0.002)
12	3	78.5	(4.2)	302.9	(1.7)	56.3	(58.2)	0.049	(0.003)
13	5	75.3	(1.5)	327.4	(4.2)	136.8	(111.8)	0.051	(0.001)
14	3	73.5	(1.8)	351.8	(2.1)	20	(6.1)	0.052	(0.001)

Table A-1: Observations Summary (Continued)

ID	# Obs	Δ (°)	(±)	Back Az (°)	(±)	Depth (km)	(±)	p (s/km)	(±)
COR (Lat: 44.586 Lon: -123.303, Continental Arc)									
1	7	87.2	(2.9)	131.5	(2.7)	288.6	(263.4)	0.043	(0.002)
2	5	75.8	(1.8)	125.9	(1.6)	508	(213.1)	0.049	(0.001)
3	12	55.9	(5.8)	122	(3.9)	45.2	(46.9)	0.065	(0.005)
4	9	34.3	(3.2)	135.5	(4.5)	51	(45.0)	0.077	(0.002)
5	2	78.1	(6.1)	162.8	(0.5)	10.5	(0.7)	0.049	(0.004)
6	15	82.1	(5.7)	228.5	(2.0)	194.1	(185.5)	0.047	(0.004)
7	14	87.1	(2.0)	244.1	(4.2)	87.6	(64.6)	0.043	(0.001)
8	6	89.1	(0.9)	260.7	(3.0)	72.8	(65.1)	0.043	0.000
9	3	78.6	(0.5)	282.8	(2.3)	252	(305.8)	0.049	(0.001)
10	8	38.7	(5.4)	306.4	(6.6)	25	(9.3)	0.075	(0.003)
11	14	61.9	(3.9)	306	(3.5)	120.1	(183.4)	0.06	(0.003)
12	3	73.4	(0.5)	297.3	(4.0)	216.3	(182.2)	0.052	(0.001)
13	4	89.8	(3.3)	303.3	(1.9)	87	(86.8)	0.042	(0.001)
HKT (Lat: 29.962 Lon: -95.838, Continental platform)									
1	2	36.2	(1.9)	109.9	(3.7)	76	(100.4)	0.076	(0.001)
2	3	33.4	(3.0)	142.5	(5.7)	128	(102.5)	0.077	(0.001)
3	4	61.5	(3.4)	154.6	(2.6)	39	(13.5)	0.06	(0.002)
4	2	60.2	(8.1)	193	(10.1)	10	0.0	0.062	(0.006)
5	4	91.8	(3.5)	247.7	(2.4)	201	(234.7)	0.042	(0.001)
6	3	74.6	(10.1)	319.1	(2.9)	32	(11.5)	0.052	(0.007)
HRV (Lat: 42.506 Lon: -71.558, Paleozoic orogen)									
1	4	91.6	(3.3)	24.9	(6.6)	128.2	(99.8)	0.042	(0.001)
2	2	81.2	(4.5)	43	(0.9)	17.5	(2.1)	0.047	(0.003)
3	3	66.7	(1.0)	54.6	(4.7)	38.7	(43.6)	0.057	(0.001)
4	3	64.3	(3.3)	117.3	(4.6)	12.3	(3.2)	0.059	(0.002)
5	10	68.3	(3.1)	174.8	(2.8)	321.1	(227.7)	0.055	(0.002)
6	4	55.9	(2.3)	177.7	(1.8)	488.5	(240.9)	0.062	(0.001)
7	3	46.8	(1.6)	187.8	(1.0)	49.3	(41.3)	0.07	(0.001)
8	13	36.3	(1.8)	190.8	(8.6)	46.8	(57.2)	0.076	(0.001)
9	9	35	(0.6)	232.5	(4.4)	31.6	(15.2)	0.077	(0.001)
10	8	38.7	(1.4)	282.9	(6.5)	12.9	(6.2)	0.075	(0.001)
11	9	63.8	(4.6)	318.7	(2.6)	22.7	(8.7)	0.059	(0.003)
12	16	83.6	(5.3)	333.2	(3.0)	73.5	(144.0)	0.046	(0.003)
SSPA (Lat: 40.640 Lon: -77.891, Paleozoic orogen)									
1	2	72.1	(1.0)	53.5	(0.8)	13.5	(0.7)	0.054	(0.001)
2	4	61.1	(7.9)	171.9	(4.6)	235.5	(258.9)	0.06	(0.005)
3	7	39.7	(4.2)	177	(2.7)	103.3	(74.7)	0.074	(0.002)
4	3	31.2	(1.7)	229.5	(8.5)	34	(13.5)	0.079	(0.001)
5	4	63.2	(5.8)	317.2	(1.4)	28.8	(8.5)	0.06	(0.004)
6	2	72.5	(0.7)	328.1	(0.4)	33	0.0	0.054	(0.001)
7	7	86.6	(3.9)	330.2	(2.8)	39.4	(14.4)	0.044	(0.002)
TUC (Lat: 32.309 Lon: -110.785, Extended crust)									
1	12	70.9	(2.9)	140.3	(3.3)	171	(208.4)	0.054	(0.002)
2	3	58.1	(3.6)	135.8	(4.2)	256.7	(326.2)	0.062	(0.004)
3	10	45	(2.6)	124.9	(6.6)	40.5	(35.6)	0.072	(0.002)

Table A-1: Observations Summary (Continued)

ID	# Obs	Δ (°)	(±)	Back Az (°)	(±)	Depth (km)	(±)	p (s/km)	(±)
4	15	81.7	(4.0)	240	(3.0)	242.3	(257.3)	0.046	(0.003)
5	12	91.7	(1.3)	252.7	(4.4)	91.7	(64.4)	0.042	(0.001)
6	3	92.8	(1.9)	290.6	(2.4)	223	(323.8)	0.041	0.000
7	7	48.7	(5.1)	317	(7.6)	27	(8.4)	0.07	(0.003)
8	23	76	(7.6)	314.3	(3.5)	76.5	(110.5)	0.051	(0.005)
NETWORK: Terrascope (TS)									
BAR (Lat: 32.680 Lon: -116.672, Calif. Coast ranges)									
1	7	70	(6.3)	132.6	(4.7)	314.9	(288.8)	0.054	(0.004)
2	5	48.8	(2.0)	121.4	(4.5)	53.2	(45.3)	0.069	(0.001)
3	2	49.7	(7.0)	186.7	(14.7)	12.5	(3.5)	0.07	(0.004)
4	4	83.7	(6.4)	231.1	(4.1)	76.2	(36.7)	0.046	(0.004)
5	4	87.8	(0.4)	244.9	(0.8)	102.8	(87.2)	0.043	0.000
6	2	88.3	(2.5)	287.8	(3.3)	327.5	(379.7)	0.042	0.000
7	2	43.6	(5.5)	314.8	(3.6)	31.5	(2.1)	0.073	(0.003)
8	4	66.1	(4.9)	315.8	(3.5)	51	(44.5)	0.057	(0.004)
9	9	82	(5.7)	309.3	(3.7)	115.7	(170.8)	0.047	(0.003)
CALB (Lat: 34.143 Lon: -118.627, Calif. Coast ranges)									
1	2	50.2	(1.5)	115.9	(2.9)	43.5	(36.1)	0.069	(0.001)
2	3	69.6	(6.8)	132.3	(6.7)	228	(349.1)	0.055	(0.005)
3	2	50.9	(7.4)	184.1	(14.0)	12.5	(3.5)	0.068	(0.004)
4	2	75.9	(6.0)	234.3	(3.0)	71	(56.6)	0.051	(0.004)
5	3	87.3	(1.1)	244.1	(3.2)	70	(64.1)	0.043	(0.001)
6	6	71.1	(6.9)	312.4	(4.4)	106.8	(178.8)	0.054	(0.005)
CWC (Lat: 36.439 Lon: -118.080, Orogen)									
1	3	87.4	(1.9)	251	(6.0)	83.3	(56.2)	0.043	(0.001)
2	2	55.6	(16.1)	314.3	(6.8)	33	0.0	0.064	(0.011)
GLA (Lat: 33.052 Lon: -114.827, Extended crust)									
1	2	60.9	(12.3)	92.2	(2.9)	12.5	(3.5)	0.061	(0.009)
2	5	48.8	(2.3)	125	(4.6)	60	(50.5)	0.07	(0.002)
3	2	67.9	(4.3)	132.5	(6.4)	340.5	(410.8)	0.056	(0.001)
4	2	89.1	(0.2)	247.9	(2.3)	88.5	(78.5)	0.043	(0.001)
5	4	94.2	(1.1)	266.7	(1.2)	150.5	(163.3)	0.041	0.000
6	4	45	(5.1)	313.9	(2.9)	23.2	(11.4)	0.072	(0.003)
7	10	72.7	(5.1)	313.3	(3.3)	84.1	(139.0)	0.053	(0.004)
GSC (Lat: 35.303 Lon: -116.808, Orogen)									
1	15	49.6	(4.4)	121.6	(5.7)	39.7	(36.5)	0.064	(0.006)
2	11	76.5	(4.3)	134.3	(3.5)	332	(252.1)	0.049	(0.003)
3	2	50.1	(4.0)	187.6	(12.1)	12	(4.2)	0.069	(0.003)
4	14	79.1	(4.5)	235.6	(3.2)	208.1	(246.9)	0.048	(0.003)
5	7	89	(0.7)	244.5	(1.3)	101.9	(70.4)	0.042	0.000
6	6	87.8	(1.9)	253.9	(3.2)	40.5	(50.4)	0.043	(0.001)
7	5	93.2	(1.1)	265.5	(1.5)	84.2	(68.7)	0.041	0.000
8	3	87	(2.0)	287.3	(2.3)	223	(323.8)	0.043	(0.001)
9	11	44.6	(6.2)	315.7	(7.3)	32.5	(28.3)	0.072	(0.004)
10	20	69.3	(7.4)	311.2	(2.2)	61	(77.4)	0.055	(0.005)
ISA (Lat: 35.663 Lon: -118.473, Orogen)									

Table A-1: Observations Summary (Continued)

ID	# Obs	Δ (°)	(±)	Back Az (°)	(±)	Depth (km)	(±)	p (s/km)	(±)
1	4	66	(8.3)	87.7	(6.3)	11.2	(2.5)	0.058	(0.006)
2	7	48.7	(4.2)	117.5	(2.9)	50.9	(41.8)	0.07	(0.002)
3	6	66.2	(2.9)	129.6	(2.9)	264.8	(268.5)	0.057	(0.002)
4	8	77.7	(3.2)	135.6	(3.0)	175.9	(249.6)	0.049	(0.003)
5	3	52.7	(5.2)	181.8	(10.5)	11.3	(3.2)	0.067	(0.004)
6	15	78.7	(4.4)	234.1	(2.6)	258	(252.2)	0.049	(0.003)
7	2	87.5	(0.3)	243.9	(1.1)	119.5	(122.3)	0.043	(0.001)
8	7	86.3	(1.5)	253	(2.2)	40	(30.2)	0.044	(0.001)
9	6	91.7	(2.5)	264	(3.0)	101	(141.3)	0.042	0.000
10	2	91.4	(4.9)	285.1	(1.0)	34.5	(34.6)	0.042	(0.001)
11	7	37.7	(4.9)	317	(7.7)	43.7	(31.1)	0.075	(0.003)
12	5	56.8	(2.7)	316.3	(4.0)	27.8	(10.8)	0.064	(0.002)
13	9	72.4	(4.7)	309.8	(2.1)	84.9	(147.8)	0.053	(0.003)
MLA (Lat: 37.631 Lon: -118.834, Continental Arc)									
1	3	30.9	(1.5)	129.2	(4.4)	70	(79.4)	0.079	(0.001)
2	6	53	(2.4)	121.2	(5.3)	58	(48.6)	0.067	(0.002)
3	9	76.8	(5.7)	134.3	(3.9)	196	(245.9)	0.05	(0.004)
4	2	54.4	(7.5)	183.6	(13.3)	12.5	(3.5)	0.066	(0.005)
5	3	78.7	(4.6)	233.9	(2.0)	230.7	(279.4)	0.048	(0.003)
6	5	88.5	(1.0)	243.8	(2.3)	88.8	(81.7)	0.043	(0.001)
7	3	86.2	(1.9)	253.1	(1.9)	82.7	(55.1)	0.043	(0.001)
8	4	90.8	(0.4)	263.5	(1.2)	118	(179.0)	0.042	0.000
9	3	84.8	(2.0)	285.9	(2.3)	223	(323.8)	0.044	(0.001)
10	7	39.9	(4.8)	310	(3.3)	27.1	(8.7)	0.075	(0.002)
11	19	68.2	(6.7)	309.4	(3.6)	78.2	(121.5)	0.056	(0.005)
12	3	86.9	(1.9)	305	(1.3)	26.7	(4.5)	0.044	(0.001)
NEE (Lat: 34.823 Lon: -114.596, Extended crust)									
1	6	49.3	(2.4)	124.9	(5.3)	62.5	(44.0)	0.069	(0.001)
2	5	69.2	(5.9)	135.7	(4.5)	194.4	(248.1)	0.055	(0.004)
3	2	52	(6.6)	188.9	(14.4)	12.5	(3.5)	0.068	(0.004)
4	3	80.4	(9.9)	240.3	(2.5)	35	(5.3)	0.049	(0.006)
5	4	72.5	(8.3)	313.1	(2.9)	153	(212.8)	0.053	(0.006)
PAS (Lat: 34.148 Lon: -118.172, Calif. Coast ranges)									
1	2	63.7	(12.3)	90.9	(3.1)	12.5	(3.5)	0.059	(0.008)
2	15	48	(5.7)	120.6	(4.5)	40.9	(39.3)	0.07	(0.003)
3	12	71.6	(6.8)	131.2	(4.1)	324.2	(250.6)	0.053	(0.004)
4	14	78.3	(5.5)	233.7	(3.6)	123.2	(160.5)	0.049	(0.004)
5	11	86.6	(1.2)	247	(3.6)	85.5	(72.9)	0.044	(0.001)
6	7	92.5	(2.2)	264.8	(1.8)	74.7	(58.5)	0.041	(0.001)
7	2	85.2	(0.4)	287.6	(2.3)	305	(411.5)	0.045	(0.001)
8	8	40.8	(4.7)	316.5	(5.6)	49.5	(65.7)	0.074	(0.002)
9	15	69.6	(5.7)	312.2	(3.3)	84.8	(147.7)	0.055	(0.004)
10	7	85.3	(4.0)	304.3	(3.2)	106.4	(147.2)	0.044	(0.002)
RPV (Lat: 33.744 Lon: -118.404, Calif. Coast ranges)									
1	4	49.6	(1.0)	116.6	(2.1)	56	(52.6)	0.069	0.000
2	3	71.9	(3.8)	130.5	(4.5)	299.7	(299.8)	0.053	(0.002)

Table A-1: Observations Summary (Continued)

ID	# Obs	Δ (°)	(±)	Back Az (°)	(±)	Depth (km)	(±)	p (s/km)	(±)
3	2	79	(10.5)	242.1	(7.7)	32	(1.4)	0.049	(0.007)
4	2	86.6	(2.5)	286.8	(3.3)	327.5	(379.7)	0.044	(0.001)
5	3	40.1	(5.5)	315.8	(4.1)	31.3	(1.2)	0.074	(0.003)
6	11	71.3	(5.5)	311	(2.0)	82.1	(132.4)	0.054	(0.004)
SBC (Lat: 34.442 Lon: -119.713, Calif. Coast ranges)									
1	9	49.9	(5.5)	118.9	(4.8)	54	(46.4)	0.069	(0.004)
2	11	73.8	(5.7)	131.4	(4.0)	269.9	(269.1)	0.052	(0.004)
3	2	51.2	(7.6)	182.8	(13.8)	12.5	(3.5)	0.068	(0.004)
4	7	78.4	(5.1)	233.2	(4.1)	206.3	(242.3)	0.049	(0.004)
5	5	85.9	(1.5)	244.5	(3.4)	63.8	(79.9)	0.044	(0.001)
6	4	88.4	(1.2)	258.2	(3.5)	20.5	(9.9)	0.043	(0.001)
7	2	85.4	(2.5)	286	(3.3)	327.5	(379.7)	0.044	(0.001)
8	5	42.3	(4.0)	314	(5.1)	24.6	(9.6)	0.073	(0.002)
9	10	71.2	(4.3)	311	(3.4)	83.1	(139.6)	0.054	(0.003)
SMTC (Lat: 32.949 Lon: -115.720, Extended crust)									
1	3	49.5	(1.6)	125	(4.0)	24	(10.8)	0.069	(0.002)
2	3	73.9	(7.4)	131.8	(3.9)	598.7	(33.6)	0.051	(0.004)
3	3	87.8	(1.5)	248.3	(4.8)	125.3	(90.2)	0.043	(0.001)
4	2	71.3	(1.3)	311	0.0	26	(9.9)	0.054	(0.001)
SNCC (Lat: 33.248 Lon: -119.524, Calif. Coast ranges)									
1	3	50.5	(1.1)	114.8	(2.4)	51.7	(63.6)	0.069	(0.001)
2	2	75	(2.5)	135.7	(3.2)	33.5	(19.1)	0.051	(0.001)
3	4	74.8	(3.6)	233.2	(1.9)	68	(44.6)	0.052	(0.003)
4	2	86.4	(1.5)	243.7	(4.5)	33	0.0	0.044	(0.001)
5	4	89.8	(0.4)	263.3	(1.1)	130	(172.3)	0.042	0.000
6	5	73	(5.0)	312.1	(4.8)	126.2	(193.1)	0.053	(0.004)
SVD (Lat: 34.105 Lon: -117.097, Orogen)									
1	2	49.2	(1.8)	114.9	(3.7)	72.5	(74.2)	0.069	(0.001)
2	6	69.7	(7.1)	133.2	(4.1)	201.8	(201.1)	0.055	(0.005)
3	3	81.6	(3.4)	235	(4.7)	392.7	(311.6)	0.045	(0.002)
4	4	87.9	(0.4)	245.7	(1.8)	102.8	(87.2)	0.043	0.000
5	2	92	(0.2)	264	(0.7)	21	(7.1)	0.041	0.000
6	3	87.2	(1.9)	287.2	(2.4)	223	(323.8)	0.043	(0.001)
7	3	40.2	(5.9)	315.7	(4.0)	30.7	(2.3)	0.074	(0.003)
8	8	72.6	(4.2)	311.9	(3.8)	98.1	(154.0)	0.053	(0.003)
USC (Lat: 34.021 Lon: -118.287, Calif. Coast ranges)									
1	3	51	(4.3)	122.3	(5.7)	48	(48.1)	0.068	(0.003)
2	5	70.7	(7.3)	130	(3.5)	416.4	(272.7)	0.052	(0.005)
3	2	50.8	(7.3)	184.5	(14.1)	12.5	(3.5)	0.068	(0.004)
4	4	79.9	(6.9)	236.5	(3.6)	181.2	(248.6)	0.048	(0.004)
VTV (Lat: 34.567 Lon: -117.333, Orogen)									
1	5	51	(3.2)	122.6	(5.9)	39	(36.5)	0.068	(0.002)
2	6	68.4	(7.5)	131.6	(3.6)	335.7	(301.0)	0.055	(0.006)
3	2	51.4	(7.1)	185.7	(14.1)	12.5	(3.5)	0.068	(0.004)
4	4	77.4	(3.8)	235	(2.0)	180	(249.6)	0.049	(0.003)
5	4	87.7	(0.7)	246.5	(2.6)	82	(60.1)	0.043	0.000

Table A-1: Observations Summary (Continued)

ID	# Obs	Δ (°)	(±)	Back Az (°)	(±)	Depth (km)	(±)	p (s/km)	(±)
6	3	90.9	(1.7)	261.3	(4.4)	31	(14.1)	0.042	(0.001)
7	4	44.7	(4.6)	312.1	(2.6)	28	(8.1)	0.072	(0.002)
8	8	68.4	(6.4)	313.2	(3.4)	101.8	(152.2)	0.055	(0.005)
9	2	87	(5.4)	304.6	(0.6)	189	(229.1)	0.044	(0.003)
NETWORK: U.S. National Seismic Network (USNSN)									
AAM (Lat: 42.300 Lon: -83.656, Continental platform)									
1	3	47.8	(9.3)	169.5	(1.9)	129.7	(99.6)	0.049	(0.026)
2	3	29	(1.5)	217.5	(11.1)	45.3	(21.4)	0.08	0.000
3	4	65.3	(4.0)	320.1	(5.9)	33	0.0	0.058	(0.003)
BINY (Lat: 42.199 Lon: -75.986, Paleozoic orogen)									
1	3	44.9	(6.1)	179.4	(1.6)	173.3	(54.6)	0.071	(0.003)
2	3	59.6	(5.6)	175.1	(4.2)	223	(314.5)	0.061	(0.004)
3	2	77.9	(7.3)	211	(7.3)	10	0.0	0.049	(0.005)
4	3	32.9	(2.1)	229.6	(9.6)	45.3	(21.4)	0.078	(0.002)
5	3	67.2	(3.7)	321.4	(6.5)	33	0.0	0.056	(0.003)
BLA (Lat: 37.211 Lon: -80.421, Paleozoic orogen)									
1	4	38.5	(6.0)	172.2	(1.4)	167.5	(46.1)	0.075	(0.003)
2	3	55	(5.4)	169.5	(4.4)	221	(316.1)	0.064	(0.004)
3	2	72.7	(6.5)	173.3	(2.9)	40	(9.9)	0.053	(0.004)
4	3	27.1	(2.3)	229.4	(11.2)	45.3	(21.4)	0.082	(0.002)
5	3	69.5	(3.8)	321.2	(5.8)	33	0.0	0.055	(0.003)
BMN (Lat: 40.431 Lon: -117.222, Extended crust)									
1	2	64.5	(10.1)	97.7	(9.0)	7.5	(3.5)	0.058	(0.006)
2	2	29.9	(6.2)	137.8	(8.3)	65.5	(6.4)	0.081	(0.005)
3	2	62.7	(6.6)	133	(4.2)	78.5	(64.3)	0.059	(0.004)
4	2	69.8	(10.5)	171.9	(5.8)	10	0.0	0.054	(0.007)
5	2	92.4	(0.5)	229	(0.2)	220.5	(159.1)	0.041	0.000
6	5	80.3	(4.2)	235.6	(2.1)	251	(270.3)	0.047	(0.004)
7	3	89.6	(2.2)	251.2	(6.3)	54.3	(20.1)	0.042	(0.001)
8	3	47.1	(5.9)	308.7	(4.3)	33	0.0	0.07	(0.003)
9	3	82.4	(3.0)	303.9	(5.8)	26.7	(20.4)	0.046	(0.003)
BW06 (Lat: 42.778 Lon: -109.556, Wyoming)									
1	3	69.4	(5.3)	140.9	(3.9)	221	(316.1)	0.035	(0.024)
2	3	86.3	(3.8)	241.8	(1.6)	367.7	(306.3)	0.043	(0.003)
3	2	94.9	(2.3)	259.9	(2.2)	53	(28.3)	0.041	(0.001)
4	2	90.3	(2.0)	291.7	(1.5)	125	(33.9)	0.042	(0.001)
5	3	49.9	(5.0)	309.3	(5.6)	33	0.0	0.069	(0.003)
6	4	76.5	(5.6)	309	(5.7)	86.2	(96.3)	0.051	(0.003)
CBKS (Lat: 38.814 Lon: -99.737, Continental platform)									
1	3	43.4	(4.0)	144	(3.7)	168.7	(56.4)	0.072	(0.002)
2	4	63.5	(5.5)	149.5	(3.5)	178.2	(271.9)	0.058	(0.003)
3	2	68.3	(9.0)	190.7	(5.2)	10	0.0	0.057	(0.006)
4	2	94	(2.1)	244.3	(0.9)	106.5	(6.4)	0.041	(0.001)
5	4	57	(4.5)	313.4	(4.7)	33	0.0	0.064	(0.003)
6	2	89.1	(2.8)	311.2	(4.8)	32	(32.5)	0.042	(0.001)
CEH (Lat: 35.891 Lon: -79.093, Paleozoic orogen)									

Table A-1: Observations Summary (Continued)

ID	# Obs	Δ (°)	(±)	Back Az (°)	(±)	Depth (km)	(±)	p (s/km)	(±)
1	2	36	(5.7)	174.9	(1.8)	137	(18.4)	0.076	(0.003)
2	3	56.6	(5.7)	169.2	(2.0)	226.7	(311.2)	0.063	(0.002)
3	3	27.1	(2.6)	233.5	(10.9)	45.3	(21.4)	0.082	(0.002)
4	2	68.1	(0.7)	318.3	(0.3)	33	0.0	0.056	(0.001)
5	3	80.7	(8.2)	328.3	(0.3)	40	(12.1)	0.048	(0.005)
DAC (Lat: 36.277 Lon: -117.590, Extended crust)									
1	3	65.9	(9.6)	130.1	(4.4)	251.3	(292.6)	0.057	(0.007)
2	2	89.4	(0.5)	228.8	(0.2)	220.5	(159.1)	0.042	0.000
3	3	77.7	(3.8)	236.4	(2.4)	239.7	(270.1)	0.049	(0.003)
4	2	88.2	(1.3)	246.5	(3.7)	90	(46.7)	0.043	(0.001)
5	3	52.8	(6.2)	313.9	(3.9)	33	0.0	0.066	(0.004)
DUG (Lat: 40.195 Lon: -112.813, Extended crust)									
1	4	69.3	(7.3)	136.7	(3.6)	211	(256.0)	0.055	(0.004)
2	2	68.9	(9.7)	178.4	(3.2)	10	0.0	0.056	(0.007)
3	2	94.8	(0.5)	231.7	(0.2)	220.5	(159.1)	0.041	(0.001)
4	5	83.8	(3.0)	238.5	(2.0)	279.6	(245.9)	0.045	(0.002)
5	4	51.1	(5.9)	311.4	(4.8)	33	0.0	0.066	(0.004)
6	3	82.5	(4.1)	305.5	(5.2)	28.7	(23.7)	0.047	(0.003)
ELK (Lat: 40.745 Lon: -115.239, Extended crust)									
1	2	63.1	(10.0)	99.3	(9.2)	7.5	(3.5)	0.06	(0.007)
2	3	56.6	(5.3)	130	(4.0)	173.3	(54.6)	0.063	(0.003)
3	3	70.7	(5.3)	135.5	(4.0)	221	(316.1)	0.054	(0.003)
4	3	85.3	(8.4)	234.8	(3.8)	308	(255.4)	0.045	(0.004)
5	4	46.7	(5.0)	308.5	(4.4)	33	0.0	0.069	(0.003)
6	5	80	(5.3)	306.6	(5.3)	72.4	(88.5)	0.048	(0.004)
EYMN (Lat: 47.946 Lon: -91.495, Shield)									
1	2	59.8	(10.1)	313.7	(7.4)	33	0.0	0	0.000
GOGA (Lat: 33.411 Lon: -83.467, Paleozoic orogen)									
1	2	37.1	(9.6)	121.4	(14.6)	7.5	(3.5)	0.076	(0.004)
2	3	32.9	(4.5)	166	(2.5)	168.7	(56.4)	0.077	(0.002)
3	4	53.5	(5.5)	165.4	(3.7)	178.2	(271.9)	0.066	(0.003)
4	2	69.3	(6.3)	170.5	(3.3)	40	(9.9)	0.055	(0.004)
5	3	68	(0.9)	317.7	(0.3)	33	0.0	0.056	(0.001)
6	2	85.1	(13.3)	328.8	(2.2)	130	(137.2)	0.046	(0.006)
GWDE (Lat: 38.826 Lon: -75.617, Paleozoic orogen)									
1	2	50.2	(4.8)	179.1	(1.4)	98.5	(92.6)	0.035	(0.047)
2	2	70.7	(11.4)	176.7	(3.4)	41.5	(12.0)	0.055	(0.008)
HWUT (Lat: 41.700 Lon: -111.200, Orogen)									
1	2	52.6	(4.4)	133	(4.6)	178	(76.4)	0.067	(0.003)
2	3	74.7	(6.8)	140.2	(5.6)	225.7	(312.1)	0.051	(0.004)
3	3	88.9	(4.1)	244.3	(7.8)	276	(228.8)	0.042	(0.002)
4	3	52.8	(5.2)	312.3	(5.0)	33	0.0	0.064	(0.004)
ISCO (Lat: 39.800 Lon: -105.613, Orogen)									
1	4	49.2	(5.4)	138.4	(3.7)	167.5	(46.1)	0.069	(0.003)
2	3	65.2	(5.4)	143.7	(4.0)	221	(316.1)	0.057	(0.004)
3	2	89.7	(1.0)	244	(3.4)	352.5	(263.8)	0.042	0.000

Table A-1: Observations Summary (Continued)

ID	# Obs	Δ (°)	(±)	Back Az (°)	(±)	Depth (km)	(±)	p (s/km)	(±)
4	4	57.7	(4.6)	315.6	(4.4)	33	0.0	0.062	(0.003)
5	3	85.7	(6.3)	312.1	(7.1)	95	(116.1)	0.045	(0.004)
JFWS (Lat: 42.915 Lon: -90.249, Continental platform)									
1	2	44.8	(5.4)	159.7	(2.9)	178	(76.4)	0.071	(0.003)
2	3	67.9	(8.2)	162.3	(1.7)	43.3	(9.1)	0.056	(0.005)
3	2	76.9	(17.1)	321.6	(1.5)	44	(15.6)	0.05	(0.011)
KNB (Lat: 37.017 Lon: -112.822, Orogen)									
1	2	60.6	(10.5)	99	(8.7)	7.5	(3.5)	0.061	(0.007)
2	5	66.1	(6.5)	136.4	(3.7)	175.4	(235.6)	0.057	(0.004)
3	2	92.8	(0.5)	231.6	(0.2)	220.5	(159.1)	0.041	(0.001)
4	4	80.2	(3.8)	239.9	(1.3)	286	(298.7)	0.047	(0.003)
5	2	92.1	(1.4)	255.4	(4.9)	78	(63.6)	0.041	(0.001)
6	2	86.1	(3.6)	295.5	(6.6)	79	(99.0)	0.044	(0.003)
7	2	47.6	(0.8)	309.5	0.0	33	0.0	0.07	(0.001)
8	2	58.5	(0.4)	316.9	(0.7)	33	0.0	0.063	0.000
9	5	81.4	(7.6)	310.6	(2.6)	81.4	(82.5)	0.047	(0.004)
LBNH (Lat: 44.240 Lon: -71.926, Paleozoic Orogen)									
1	2	38.2	(5.4)	147	(19.2)	7.5	(3.5)	0.076	(0.003)
2	3	47	(6.1)	185	(1.9)	173.3	(54.6)	0.07	(0.004)
3	2	58.3	(1.1)	180.3	(5.6)	309.5	(391.0)	0.061	(0.002)
4	3	73.2	(9.5)	179.4	(2.3)	42.3	(8.6)	0.053	(0.007)
5	3	69.4	(3.8)	326.4	(6.8)	33	0.0	0.055	(0.002)
LDS (Lat: 37.243 Lon: -113.350, Orogen)									
1	3	64.1	(9.8)	134.1	(4.0)	251.3	(292.6)	0.058	(0.007)
2	3	89.7	(5.1)	233.1	(3.2)	202.3	(116.8)	0.042	(0.002)
3	3	54.6	(6.0)	314.2	(4.3)	33	0.0	0.065	(0.004)
LSCT (Lat: 41.678 Lon: -73.224, Paleozoic orogen)									
1	2	41.8	(5.7)	184.4	(0.4)	178	(76.4)	0.073	(0.003)
2	4	64.3	(7.0)	176.5	(1.4)	181.8	(269.5)	0.058	(0.004)
3	2	82.6	(1.2)	205.8	(3.0)	10	0.0	0.046	(0.001)
4	2	70.1	(3.9)	324.8	(7.8)	33	0.0	0.055	(0.003)
MCWV (Lat: 39.658 Lon: -79.846, Paleozoic orogen)									
1	3	46.1	(9.4)	173.5	(1.4)	143	(101.1)	0.049	(0.027)
2	2	67.2	(4.7)	171	(1.3)	48.5	(2.1)	0.057	(0.003)
3	2	68.2	(5.4)	322.2	(7.8)	33	0.0	0.056	(0.003)
MIAR (Lat: 34.546 Lon: -93.573, Paleozoic orogen)									
1	3	42.9	(8.7)	153.2	(5.2)	129.7	(99.6)	0.05	(0.028)
2	3	68.9	(7.3)	159.9	(5.0)	41.3	(7.4)	0.056	(0.004)
3	2	65.4	(8.4)	197	(6.4)	10	0.0	0.058	(0.006)
4	4	94.7	(3.1)	250.3	(2.5)	212	(223.9)	0.041	(0.001)
5	3	64.2	(5.1)	317.6	(5.2)	33	0.0	0.057	(0.003)
6	2	91.3	(3.3)	321.4	(4.4)	141	(121.6)	0.041	(0.001)
MNV (Lat: 38.433 Lon: -118.153, Extended crust)									
1	2	65	(10.4)	96.2	(8.5)	7.5	(3.5)	0.058	(0.007)
2	2	31.6	(2.8)	130.7	(3.3)	47	(19.8)	0.079	(0.002)
3	3	60.9	(8.8)	125.9	(4.3)	327.3	(226.6)	0.06	(0.007)

Table A-1: Observations Summary (Continued)

ID	# Obs	Δ (°)	(±)	Back Az (°)	(±)	Depth (km)	(±)	p (s/km)	(±)
4	2	67.9	(10.6)	171	(5.7)	10	0.0	0.056	(0.007)
5	2	90.5	(0.5)	228.4	(0.2)	220.5	(159.1)	0.042	(0.001)
6	5	77.9	(3.5)	235.4	(1.8)	249.2	(271.5)	0.049	(0.003)
7	3	88.8	(1.1)	249.3	(6.1)	71	(46.6)	0.042	(0.001)
8	3	50.7	(5.8)	312.9	(4.5)	33	0.0	0.068	(0.004)
9	2	84.8	(0.1)	306.8	0.0	35.5	(19.1)	0.045	0.000
MYNC (Lat: 35.074 Lon: -84.128, Paleozoic orogen)									
1	3	53.6	(5.4)	164.9	(4.5)	221	(316.1)	0.043	(0.028)
2	2	71.1	(6.3)	170.1	(3.3)	40	(9.9)	0.054	(0.004)
3	2	68	(6.7)	203	(10.6)	10	0.0	0.056	(0.004)
4	3	75.4	(9.7)	322.7	(5.0)	33	0.0	0.052	(0.006)
NEW (Lat: 48.263 Lon: -117.120, Orogen)									
1	2	65.7	(8.8)	101.4	(10.5)	7.5	(3.5)	0.058	(0.006)
2	2	31.2	(1.3)	156.5	(7.0)	51.5	(26.2)	0.079	(0.001)
3	2	62.2	(7.8)	130.6	(3.8)	198	(48.1)	0.06	(0.006)
4	3	77.1	(5.5)	135.6	(3.8)	223	(314.5)	0.05	(0.004)
5	6	87	(6.5)	234	(2.7)	264.7	(244.1)	0.044	(0.003)
6	3	91.2	(1.5)	253	(3.6)	76.3	(45.1)	0.042	(0.001)
7	2	83.5	(2.1)	286.1	(1.3)	125	(33.9)	0.046	(0.001)
8	2	59.8	(16.6)	306.4	(5.2)	44	(15.6)	0.061	(0.011)
OXF (Lat: 34.512 Lon: -89.409, Continental platform)									
1	3	35.5	(4.3)	156.3	(3.3)	168.7	(56.4)	0.076	(0.002)
2	3	59.8	(7.8)	158.8	(4.4)	225.7	(312.1)	0.061	(0.004)
3	3	69.5	(4.2)	321.8	(5.1)	33	0.0	0.055	(0.003)
TPH (Lat: 38.075 Lon: -117.223, Extended crust)									
1	2	62.5	(8.4)	128.7	(0.3)	355	(326.7)	0.059	(0.007)
2	2	74.5	(0.6)	170	(3.3)	10	0.0	0.052	0.000
3	2	90.8	(0.5)	229	(0.2)	220.5	(159.1)	0.042	0.000
4	2	77.4	(3.9)	237.5	(1.9)	276.5	(371.2)	0.049	(0.004)
5	2	89.2	(1.4)	246.7	(3.7)	90	(46.7)	0.042	0.000
6	2	45.1	(0.5)	308.1	0.0	33	0.0	0.071	(0.001)
7	3	55	(0.5)	315.5	(0.6)	33	0.0	0.065	(0.001)
TPNV (Lat: 36.929 Lon: -116.224, Extended crust)									
1	3	56.3	(7.4)	128.9	(7.0)	129.7	(99.6)	0.044	(0.024)
2	2	90.7	(0.5)	229.6	(0.2)	220.5	(159.1)	0.042	0.000
3	2	78.2	(5.2)	236.8	(0.2)	295.5	(359.9)	0.049	(0.005)
4	3	89.7	(1.1)	250.5	(6.1)	71	(46.6)	0.042	0.000
5	3	53.1	(6.1)	313.8	(4.1)	33	0.0	0.066	(0.004)
6	2	70.8	(6.0)	311.3	(2.4)	130	(137.2)	0.054	(0.004)
7	2	84.1	(4.1)	303.1	(6.9)	29	(28.3)	0.045	(0.002)
WCI (Lat: 39.100 Lon: -86.500, Continental platform)									
1	3	38.1	(4.5)	162.9	(2.4)	168.7	(56.4)	0.075	(0.002)
2	3	70.8	(7.8)	166.6	(3.9)	41.3	(7.4)	0.054	(0.005)
3	2	70.3	(9.3)	319.6	(5.6)	33	0.0	0.055	(0.005)
WMOK (Lat: 34.738 Lon: -98.781, Continental platform)									
1	2	67.2	(4.3)	152.6	(3.1)	45.5	(2.1)	0.057	(0.003)

Table A-1: Observations Summary (Continued)

ID	# Obs	Δ (°)	(±)	Back Az (°)	(±)	Depth (km)	(±)	p (s/km)	(±)
2	2	88.9	(3.7)	247	(2.3)	71.5	(43.1)	0.043	(0.002)
3	2	57.7	(0.8)	313.2	(0.1)	33	0.0	0.063	0.000
WVOR (Lat: 42.434 Lon: -118.637, Orogen)									
1	2	65.8	(9.8)	97.6	(9.3)	7.5	(3.5)	0.058	(0.007)
2	3	59.6	(5.3)	127.6	(3.9)	173.3	(54.6)	0.061	(0.003)
3	2	70.7	(1.8)	131.9	(4.8)	309.5	(391.0)	0.054	(0.001)
4	3	81.4	(3.0)	137.2	(2.7)	47	(3.0)	0.047	(0.002)
5	2	71.9	(10.6)	170.7	(5.6)	10	0.0	0.054	(0.007)
6	6	80.8	(3.8)	233.9	(2.1)	226.2	(249.3)	0.047	(0.003)
7	4	89.1	(1.9)	249.7	(5.2)	71.5	(38.1)	0.042	(0.001)
8	2	41.7	(0.5)	304.2	(0.1)	33	0.0	0.074	0.000
9	2	51.5	(0.5)	312.7	(0.8)	33	0.0	0.067	0.000
10	4	72.6	(7.4)	306.7	(3.0)	96.2	(87.2)	0.053	(0.005)
11	2	79.8	(4.0)	291.4	(6.5)	79	(99.0)	0.048	(0.003)
WVT (Lat: 36.130 Lon: -87.830, Continental platform)									
1	2	37.8	(5.4)	160.5	(3.6)	137	(18.4)	0.076	(0.003)
2	2	57.1	(6.5)	158.8	(3.4)	315	(383.3)	0.062	(0.003)
3	2	72.7	(6.1)	167	(3.6)	40	(9.9)	0.053	(0.004)
4	2	71.9	(0.6)	324.9	(0.5)	33	0.0	0.054	(0.001)
YSNY (Lat: 42.476 Lon: -78.537, Paleozoic orogen)									
1	3	47.5	(9.4)	176.5	(0.9)	129.7	(99.6)	0.049	(0.026)
2	2	32.3	(2.2)	230.8	(6.0)	51.5	(26.2)	0.079	(0.002)
3	3	65.8	(3.8)	320.3	(6.5)	33	0.0	0.057	(0.002)

ID: Identification number for the cluster.

Obs: Number of events in the cluster.

Δ: Mean epicentral distance in degrees.

Back Az: Mean back azimuth (clockwise angle (in degrees) from station's north to epicenter direction).

p represents horizontal slowness, or ray parameter

± : Standard Deviation

B POISSON'S RATIO MEASUREMENTS

Table B-1 on page 202 lists the estimated arrival times of the Ps and PpPmS phases used to estimate Poisson's Ratio. A value is given for each station and each azimuth-distance cluster. Uncertainties are estimated using a range of V_P values in the equations.

Table B-1: Poisson's Ratio Measurements By Station Cluster

Station - Network	Cluster	Back Az (°)	t_{Ps}	t_{PpP}	p (s/km)	Vp/Vs	Thickness (km)	PR	Mean Vp/Vs	Mean Thickness (km)	Mean PR
Shield											
fcc-cnsn	1	158.7	4.608	9.930	0.044	1.871	33.23	0.300	1.862 (0.024)	34.088 (2.178)	0.297 (0.007)
	2	157.1	4.383	9.439	0.056	1.835	32.47	0.289			
	3	313.9	5.288	10.283	0.067	1.881	36.56	0.303			
frb-cnsn	2	178.9	4.716	7.632	0.043	2.167	25.49	0.365	1.849 (0.206)	39.617 (5.600)	0.281 (0.055)
	3	184.2	4.954	7.427	0.050	2.234	25.17	0.375			
	4	187.9	5.151	12.258	0.063	1.731	43.02	0.250			
	5	218.0	4.919	12.793	0.068	1.650	45.64	0.210			
	6	254.8	5.954	11.798	0.074	1.831	43.04	0.287			
	7	306.3	5.293	12.270	0.071	1.720	44.25	0.244			
	8	327.8	5.335	12.221	0.062	1.764	42.76	0.263			
	9	333.7	5.335	12.473	0.054	1.775	42.69	0.267			
	10	350.0	5.461	13.393	0.040	1.773	44.48	0.267			
gac-cnsn	1	181.8	4.574	10.509	0.071	1.726	37.90	0.247	1.786 (0.049)	37.966 (1.234)	0.271 (0.018)
	2	180.7	4.764	10.331	0.062	1.808	36.15	0.280			
	3	220.5	4.956	10.647	0.077	1.750	39.32	0.257			
	4	225.6	4.805	11.535	0.052	1.760	39.28	0.262			
	5	315.0	5.097	10.807	0.064	1.819	38.05	0.283			
	6	328.4	5.112	10.840	0.054	1.855	37.10	0.295			
schq-cnsn	1	63.0	5.859	9.997	0.054	2.067	34.21	0.347	1.898 (0.147)	40.039 (7.872)	0.302 (0.044)
	2	181.9	4.907	9.664	0.048	1.942	32.61	0.320			
	4	192.9	6.335	12.616	0.065	1.869	44.56	0.299			
	5	224.1	5.811	13.473	0.072	1.715	48.77	0.242			

Table B-1: Poisson's Ratio Measurements By Station Cluster (Continued)

Station - Network	Cluster	Back Az (°)	t_{Ps}	t_{PpP}	p (s/km)	Vp/Vs	Thickness (km)	PR	Mean Vp/Vs	Mean Thickness (km)	Mean PR
ykw-cnsn	1	27.0	4.431	10.283	0.047	1.800	34.62	0.277	1.781 (0.154)	34.755 (3.500)	0.259 (0.055)
	2	139.1	5.621	9.378	0.041	2.137	31.20	0.360			
	3	138.5	5.097	10.092	0.046	1.943	33.91	0.320			
	4	135.5	4.098	8.474	0.058	1.863	29.31	0.298			
	5	157.0	4.240	10.664	0.070	1.665	38.32	0.218			
	6	238.2	4.145	9.236	0.041	1.849	30.73	0.293			
	7	264.8	4.145	9.093	0.041	1.863	30.26	0.298			
	8	298.5	4.050	10.616	0.074	1.622	38.73	0.194			
	9	298.9	4.002	10.616	0.066	1.644	37.62	0.206			
	10	302.4	4.050	10.854	0.060	1.657	37.75	0.214			
	11	305.0	4.145	10.902	0.050	1.698	36.95	0.234			
	12	309.0	4.288	10.140	0.040	1.802	33.68	0.278			
	13	354.0	3.717	11.663	0.040	1.603	38.74	0.182			
Continental Platform											
aam-usnsn	1	169.5	5.995	11.042	0.049	2.005	37.34	0.334	1.831 (0.164)	43.027 (4.976)	0.280 (0.054)
	2	217.5	6.347	12.452	0.080	1.807	46.58	0.279			
	3	320.1	4.996	13.056	0.058	1.680	45.16	0.226			
cbks-usnsn	1	144.0	5.478	13.220	0.072	1.686	47.86	0.229	1.811 (0.090)	44.102 (2.639)	0.278 (0.031)
	2	149.5	5.690	12.935	0.058	1.784	44.74	0.271			
	3	190.7	5.833	12.556	0.057	1.832	43.31	0.288			
	4	244.3	6.090	11.968	0.041	1.964	39.82	0.325			
	5	313.4	5.735	12.409	0.064	1.802	43.69	0.277			
	6	311.2	5.739	13.559	0.042	1.798	45.20	0.276			
ccm-iu	1	32.1	5.383	13.949	0.041	1.729	46.41	0.249	1.865 (0.161)	41.768 (5.650)	0.290 (0.046)
	2	43.7	5.443	13.544	0.048	1.743	45.70	0.255			

Table B-1: Poisson's Ratio Measurements By Station Cluster (Continued)

Station - Network	Cluster	Back Az (°)	t_{Ps}	t_{PpP}	p (s/km)	Vp/Vs	Thickness (km)	PR	Mean Vp/Vs	Mean Thickness (km)	Mean PR
	3	101.2	5.399	10.105	0.050	1.985	34.25	0.330			
	4	102.5	5.603	11.872	0.071	1.789	42.82	0.273			
	6	157.7	5.646	14.304	0.066	1.675	50.69	0.223			
	7	156.6	5.499	12.452	0.055	1.797	42.72	0.276			
	9	316.9	6.002	10.521	0.066	1.985	37.28	0.330			
	10	322.6	6.387	10.037	0.050	2.176	34.02	0.366			
	11	322.7	5.998	12.650	0.040	1.900	42.02	0.309			
edm-cnsn	1	141.1	5.307	10.440	0.046	1.949	35.08	0.321	1.844 (0.123)	38.392 (6.206)	0.287 (0.042)
	2	239.4	4.787	10.383	0.041	1.873	34.55	0.301			
	3	260.0	5.138	13.690	0.041	1.709	45.55	0.240			
ffc-ii	1	10.3	4.478	13.828	0.042	1.609	46.10	0.186	1.703 (0.090)	38.991 (4.561)	0.232 (0.042)
	2	36.8	4.182	12.898	0.045	1.604	43.25	0.182			
	4	149.5	3.802	11.198	0.047	1.629	37.70	0.198			
	5	174.9	4.240	8.331	0.075	1.833	30.51	0.288			
	6	199.6	4.193	11.617	0.052	1.657	39.56	0.214			
	7	247.4	4.748	11.744	0.041	1.765	39.08	0.263			
	8	296.3	4.972	10.228	0.074	1.799	37.31	0.277			
	9	311.3	4.574	11.045	0.060	1.731	38.42	0.249			
jfws-usnsn	1	159.7	5.493	9.465	0.071	1.976	34.14	0.328	1.988 (0.024)	33.338 (0.725)	0.331 (0.005)
	2	162.3	5.352	9.511	0.056	2.016	32.72	0.337			
	3	321.6	5.157	9.784	0.050	1.972	33.16	0.327			
lmq-cnsn	1	181.5	5.186	10.337	0.048	1.931	34.88	0.317	1.879 (0.073)	37.805 (4.138)	0.301 (0.022)
	3	219.0	5.621	11.121	0.075	1.827	40.73	0.286			
oxf-usnsn	1	156.3	5.536	11.898	0.076	1.754	43.75	0.259	1.786 (0.045)	42.462 (1.828)	0.271 (0.017)

Table B-1: Poisson's Ratio Measurements By Station Cluster (Continued)

Station - Network	Cluster	Back Az (°)	t_{Ps}	t_{PpP}	p (s/km)	Vp/Vs	Thickness (km)	PR	Mean Vp/Vs	Mean Thickness (km)	Mean PR
	2	158.8	5.483	11.801	0.061	1.818	41.17	0.283			
res-cnsn	3	301.4	3.050	7.236	0.074	1.690	26.40	0.231	1.739 (0.090)	35.317 (15.502)	0.249 (0.038)
	4	307.1	3.098	6.617	0.066	1.804	23.45	0.278			
	5	309.7	3.145	6.570	0.058	1.854	22.72	0.295			
	6	319.0	5.669	16.234	0.054	1.630	55.56	0.198			
	7	325.9	5.573	14.329	0.049	1.717	48.46	0.243			
sado-cnsn	1	172.8	4.574	11.140	0.052	1.749	37.94	0.257	1.821 (0.163)	35.882 (5.659)	0.277 (0.051)
	2	172.9	4.716	11.235	0.069	1.708	40.23	0.239			
	3	207.5	4.954	7.950	0.078	2.008	29.48	0.335			
ulm-cnsn	1	176.7	4.002	9.236	0.038	1.827	30.57	0.286	1.793 (0.030)	32.128 (1.515)	0.274 (0.011)
	2	154.2	4.145	8.855	0.065	1.808	31.28	0.280			
	3	158.5	4.145	10.092	0.047	1.763	33.98	0.263			
	4	317.3	4.145	9.283	0.064	1.774	32.68	0.267			
wmok-usnsn	1	152.6	6.452	13.953	0.057	1.828	48.13	0.287	1.900 (0.063)	44.170 (3.750)	0.308 (0.018)
	2	247.0	6.447	13.089	0.043	1.928	43.71	0.316			
	3	313.2	6.260	11.587	0.063	1.945	40.67	0.320			
Paleozoic Orogen											
biny-usnsn	1	179.4	5.530	13.128	0.071	1.703	47.07	0.237	1.742 (0.100)	46.201 (3.928)	0.250 (0.038)
	2	175.1	5.245	14.300	0.061	1.643	49.61	0.206			
	3	211.0	5.541	13.674	0.049	1.748	46.00	0.257			
	4	229.6	6.045	10.755	0.078	1.908	39.64	0.311			
	5	321.4	5.622	14.230	0.056	1.709	48.69	0.240			

Table B-1: Poisson's Ratio Measurements By Station Cluster (Continued)

Station - Network	Cluster	Back Az (°)	t_{Ps}	t_{PpP}	p (s/km)	Vp/Vs	Thickness (km)	PR	Mean Vp/Vs	Mean Thickness (km)	Mean PR
ALE - II	1	18.8	2.860	8.617	0.054	1.599	29.33	0.179	1.685 (0.080)	29.724 (2.176)	0.224 (0.042)
	2	41.6	3.198	8.307	0.060	1.679	28.74	0.225			
	3	64.4	2.941	7.702	0.065	1.657	27.05	0.214			
	5	187.4	3.759	9.462	0.040	1.754	31.27	0.259			
	6	195.3	4.040	9.366	0.044	1.810	31.18	0.280			
	11	295.1	3.195	7.063	0.070	1.761	25.23	0.262			
	12	322.3	3.462	8.395	0.070	1.692	29.99	0.232			
	13	331.0	3.448	8.837	0.060	1.688	30.57	0.230			
	14	339.0	2.955	9.589	0.060	1.541	33.17	0.136			
	15	332.9	3.145	9.331	0.040	1.639	30.84	0.203			
	16	354.3	3.144	9.273	0.050	1.622	31.27	0.193			
	17	355.3	3.493	8.486	0.040	1.781	28.04	0.270			
bla-usnsn	1	172.2	6.801	12.440	0.075	1.899	45.29	0.308	1.831 (0.071)	45.724 (3.364)	0.286 (0.026)
	2	169.5	6.359	13.285	0.064	1.832	46.51	0.288			
	3	173.3	6.383	13.616	0.053	1.854	46.24	0.295			
	4	229.4	6.074	13.322	0.082	1.711	49.97	0.240			
	5	321.2	5.653	11.900	0.055	1.859	40.61	0.296			
ceh-usnsn	1	174.9	4.283	10.580	0.076	1.655	38.67	0.212	1.752 (0.066)	36.157 (2.007)	0.256 (0.028)
	2	169.2	4.288	9.997	0.063	1.748	34.89	0.257			
	3	233.5	5.077	10.025	0.082	1.793	37.61	0.274			
	4	318.3	4.545	9.849	0.056	1.831	33.70	0.287			
	5	328.3	4.247	10.700	0.048	1.735	35.92	0.251			
drln-cnsn	1	190.9	3.906	8.518	0.051	1.842	28.79	0.291	1.795 (0.038)	31.355 (1.976)	0.275 (0.013)
	2	197.0	4.098	8.998	0.059	1.810	31.04	0.280			
	4	239.7	4.240	9.331	0.071	1.761	33.45	0.262			

Table B-1: Poisson's Ratio Measurements By Station Cluster (Continued)

Station - Network	Cluster	Back Az (°)	t_{Ps}	t_{PpP}	p (s/km)	Vp/Vs	Thickness (km)	PR	Mean Vp/Vs	Mean Thickness (km)	Mean PR
	5	339.3	3.982	9.554	0.049	1.769	32.14	0.265			
goga-usnsn	1	121.4	4.431	10.741	0.076	1.668	39.26	0.219	1.795 (0.144)	37.522 (4.856)	0.267 (0.051)
	2	166.0	5.038	8.710	0.077	1.941	31.97	0.319			
	3	165.4	5.037	8.738	0.066	1.997	30.79	0.333			
	4	170.5	4.996	11.999	0.055	1.751	40.95	0.258			
	5	317.7	5.048	11.749	0.056	1.773	40.20	0.267			
	6	328.8	4.336	12.556	0.046	1.642	41.97	0.205			
hrv-iu	1	24.9	3.098	9.616	0.042	1.607	31.89	0.184	1.683 (0.067)	30.841 (1.302)	0.224 (0.036)
	2	43.0	3.352	8.834	0.047	1.704	29.59	0.238			
	3	54.6	3.611	9.939	0.057	1.649	34.10	0.209			
	4	117.3	3.707	8.825	0.059	1.746	30.44	0.256			
	5	174.8	3.383	8.902	0.055	1.685	30.38	0.228			
	6	177.7	3.805	8.647	0.062	1.771	30.09	0.266			
	7	187.8	3.703	8.307	0.070	1.750	29.68	0.258			
	8	190.8	3.684	8.449	0.076	1.707	30.88	0.239			
	9	232.5	3.431	8.712	0.077	1.632	31.97	0.200			
	10	282.9	3.720	8.281	0.070	1.756	29.58	0.260			
	11	318.7	3.118	9.026	0.050	1.634	30.43	0.200			
	12	333.2	2.777	9.397	0.040	1.559	31.05	0.151			
lmn-cnsn	1	185.8	4.431	12.044	0.051	1.673	40.70	0.222	1.683 (0.014)	44.417 (5.253)	0.227 (0.007)
	2	194.6	5.573	13.425	0.071	1.693	48.13	0.232			
lsct-usnsn	1	184.4	3.747	8.213	0.073	1.755	29.67	0.260	1.728 (0.089)	30.188 (3.307)	0.244 (0.040)
	2	176.5	3.498	7.496	0.058	1.833	25.79	0.288			
	3	205.8	3.599	9.552	0.046	1.702	31.93	0.236			
	4	324.8	3.384	9.778	0.055	1.623	33.37	0.194			

Table B-1: Poisson's Ratio Measurements By Station Cluster (Continued)

Station - Network	Cluster	Back Az (°)	t_{Ps}	t_{PpP}	p (s/km)	Vp/Vs	Thickness (km)	PR	Mean Vp/Vs	Mean Thickness (km)	Mean PR
mbc-cnsn	3	135.6	3.226	9.440	0.050	1.627	31.83	0.196	1.748 (0.087)	29.777 (2.161)	0.252 (0.039)
	5	181.7	3.386	9.109	0.075	1.603	33.16	0.182			
	6	263.0	3.873	8.508	0.041	1.862	28.17	0.297			
	7	280.3	3.745	8.569	0.049	1.807	28.83	0.279			
	8	279.5	3.546	7.871	0.075	1.736	28.65	0.252			
	9	286.9	3.669	8.560	0.069	1.724	30.47	0.247			
	10	296.3	3.707	9.722	0.050	1.701	32.78	0.236			
	11	303.4	3.669	7.934	0.050	1.852	26.75	0.294			
	12	297.3	3.621	8.606	0.040	1.799	28.44	0.276			
	13	297.9	3.516	8.682	0.040	1.768	28.69	0.265			
mcwv-usnsn	1	173.5	5.846	11.102	0.049	1.975	37.35	0.328	1.965 (0.116)	38.534 (5.625)	0.323 (0.029)
	2	171.0	6.124	13.017	0.057	1.844	44.66	0.292			
	3	322.2	5.839	9.819	0.056	2.075	33.60	0.349			
miar-usnsn	1	153.2	6.906	12.949	0.050	1.984	43.66	0.330	1.959 (0.026)	41.176 (2.259)	0.324 (0.006)
	4	250.3	6.002	11.854	0.041	1.960	39.24	0.324			
	5	317.6	6.144	11.841	0.057	1.932	40.62	0.317			
mync-usnsn	1	164.9	6.284	14.428	0.043	1.820	47.94	0.284	1.792 (0.039)	48.877 (1.322)	0.274 (0.014)
	2	170.1	6.174	14.633	0.054	1.765	49.81	0.263			
sspa-iu	1	53.5	6.125	12.369	0.054	1.900	42.11	0.308	1.880 (0.200)	40.376 (9.075)	0.290 (0.063)
	2	171.9	5.255	7.960	0.060	2.177	27.54	0.366			
	3	177.0	5.954	11.288	0.074	1.871	40.93	0.300			
	4	229.5	5.716	14.302	0.079	1.633	52.93	0.200			

Table B-1: Poisson's Ratio Measurements By Station Cluster (Continued)

Station - Network	Cluster	Back Az (°)	t_{Ps}	t_{PpP}	p (s/km)	Vp/Vs	Thickness (km)	PR	Mean Vp/Vs	Mean Thickness (km)	Mean PR
	5	317.2	5.192	13.254	0.060	1.691	45.85	0.231			
	6	328.1	5.335	9.664	0.054	2.005	32.90	0.334			
Mesozoic – Tertiary Orogen											
anmo-iu	1	91.6	3.995	12.249	0.043	1.612	40.70	0.187	1.664 (0.053)	40.127 (1.922)	0.216 (0.026)
	2	144.7	4.311	11.785	0.053	1.664	40.02	0.217			
	3	139.3	4.241	11.014	0.065	1.663	38.68	0.217			
	4	131.0	4.378	10.563	0.076	1.671	38.61	0.221			
	5	242.6	4.587	11.074	0.044	1.777	36.87	0.268			
	6	256.0	4.458	11.639	0.041	1.724	38.53	0.247			
	7	293.2	4.296	12.445	0.041	1.652	41.20	0.211			
	8	315.3	4.413	11.750	0.071	1.625	42.13	0.195			
	9	316.0	4.193	12.689	0.052	1.601	42.98	0.180			
	10	310.9	4.336	12.573	0.040	1.653	41.55	0.212			
cmb-bk	6	243.9	4.880	11.405	0.044	1.803	37.97	0.278	1.744 (0.110)	46.000 (8.297)	0.249 (0.044)
	8	285.0	5.335	11.045	0.045	1.905	36.84	0.310			
	10	312.4	5.526	13.711	0.060	1.712	47.43	0.241			
	11	308.7	5.621	16.186	0.050	1.637	54.57	0.202			
	12	306.1	5.621	16.091	0.040	1.662	53.18	0.216			
col-iu	1	105.2	3.402	8.913	0.047	1.709	29.86	0.239	1.713 (0.108)	30.045 (3.556)	0.234 (0.052)
	2	115.6	3.695	8.429	0.059	1.779	29.08	0.269			
	3	134.3	3.972	7.600	0.076	1.853	27.78	0.294			
	5	223.3	3.093	9.812	0.044	1.590	32.67	0.173			
	6	242.8	3.250	9.959	0.045	1.609	33.22	0.185			
	9	272.1	3.336	9.661	0.073	1.566	34.90	0.156			

Table B-1: Poisson's Ratio Measurements By Station Cluster (Continued)

Station - Network	Cluster	Back Az (°)	t_{Ps}	t_{PpP}	p (s/km)	Vp/Vs	Thickness (km)	PR	Mean Vp/Vs	Mean Thickness (km)	Mean PR
	12	302.9	3.336	7.760	0.040	1.816	25.65	0.282			
	13	327.4	3.251	7.321	0.050	1.817	24.68	0.283			
	14	351.8	3.574	9.664	0.050	1.679	32.58	0.225			
cwc-ts	1	251.0	4.149	8.898	0.043	1.878	29.57	0.302	1.826 (0.074)	31.913 (3.318)	0.284 (0.025)
	2	314.3	4.357	9.785	0.064	1.773	34.26	0.267			
dawy-cnsn	2	215.9	4.709	10.350	0.042	1.859	34.33	0.297	1.791 (0.090)	33.999 (1.608)	0.270 (0.036)
	3	238.0	4.248	9.706	0.043	1.824	32.25	0.285			
	4	279.8	4.145	9.569	0.079	1.688	35.42	0.230			
dlbc-cnsn	1	128.4	4.405	8.995	0.064	1.852	31.49	0.294	1.784 (0.090)	35.703 (4.398)	0.268 (0.036)
	2	223.2	4.319	12.109	0.042	1.672	40.16	0.222			
	3	246.4	4.653	11.668	0.043	1.750	38.77	0.258			
	4	294.1	4.681	8.861	0.076	1.862	32.39	0.297			
gsc-ts	1	121.6	3.546	6.978	0.064	1.885	24.43	0.304	1.890 (0.106)	25.875 (3.109)	0.302 (0.030)
	2	134.3	3.525	7.274	0.049	1.896	24.47	0.307			
	4	235.6	3.617	6.968	0.048	1.964	23.39	0.325			
	5	244.5	3.697	6.787	0.042	2.031	22.51	0.340			
	6	253.9	3.693	6.607	0.043	2.055	21.95	0.345			
	7	265.5	3.694	8.889	0.041	1.786	29.43	0.272			
	8	287.3	3.756	8.843	0.043	1.799	29.38	0.277			
	9	315.7	3.701	7.996	0.072	1.771	28.77	0.266			
	10	311.2	3.795	8.463	0.050	1.826	28.53	0.286			
hwut-usnsn	1	133.0	3.840	8.969	0.067	1.731	31.71	0.250	1.788 (0.080)	30.895 (1.151)	0.271 (0.030)
	2	140.2	4.098	8.901	0.051	1.845	30.08	0.292			
isco-usnsn	1	138.4	6.205	13.234	0.069	1.794	47.11	0.275	1.726 (0.128)	45.346 (6.091)	0.238 (0.068)

Table B-1: Poisson's Ratio Measurements By Station Cluster (Continued)

Station - Network	Cluster	Back Az (°)	t_{Ps}	t_{PpP}	p (s/km)	Vp/Vs	Thickness (km)	PR	Mean Vp/Vs	Mean Thickness (km)	Mean PR
	2	143.7	5.048	10.488	0.057	1.864	35.98	0.298			
	3	244.0	5.211	13.001	0.042	1.756	43.12	0.260			
	4	315.6	5.533	14.020	0.062	1.690	48.79	0.231			
	5	312.1	4.386	15.508	0.045	1.527	51.73	0.124			
isa-ts	1	87.7	4.494	13.959	0.058	1.571	48.02	0.160	1.684 (0.098)	44.830 (5.205)	0.221 (0.050)
	2	117.5	5.145	10.476	0.070	1.828	37.42	0.287			
	3	129.6	4.716	15.006	0.057	1.560	51.48	0.151			
	4	135.6	4.793	15.415	0.049	1.572	51.86	0.160			
	5	181.8	4.647	12.761	0.067	1.620	45.12	0.192			
	6	234.1	4.954	11.412	0.049	1.802	38.39	0.277			
	7	243.9	5.157	12.107	0.043	1.802	40.23	0.277			
	8	253.0	5.056	12.002	0.044	1.790	39.96	0.273			
	9	264.0	4.692	12.851	0.042	1.688	42.62	0.230			
	10	285.1	4.993	13.195	0.040	1.718	43.61	0.244			
	11	317.0	5.143	13.443	0.070	1.641	48.02	0.205			
	12	316.3	5.143	15.225	0.060	1.594	52.67	0.176			
	13	309.8	4.916	12.868	0.050	1.702	43.39	0.236			
Ink-cnsn	3	138.9	4.050	10.569	0.065	1.660	37.12	0.215	1.802 (0.141)	28.784 (6.374)	0.270 (0.050)
	4	220.5	3.812	11.187	0.041	1.644	37.04	0.206			
	7	279.3	3.764	8.521	0.072	1.734	30.66	0.251			
	8	282.9	3.526	5.951	0.066	2.026	20.97	0.339			
	9	286.8	3.621	6.903	0.058	1.939	23.75	0.319			
	10	291.5	3.383	7.569	0.050	1.823	25.52	0.285			
	11	284.4	3.336	7.998	0.040	1.792	26.43	0.274			
knb-usnsn	1	99.0	6.742	10.048	0.061	2.192	34.86	0.369	1.984 (0.324)	34.361 (3.396)	0.305 (0.096)
	2	136.4	5.406	11.356	0.057	1.854	38.96	0.295			
	3	231.6	6.646	9.711	0.041	2.301	32.15	0.384			

Table B-1: Poisson's Ratio Measurements By Station Cluster (Continued)

Station - Network	Cluster	Back Az (°)	t_{Ps}	t_{PpP}	p (s/km)	Vp/Vs	Thickness (km)	PR	Mean Vp/Vs	Mean Thickness (km)	Mean PR
	9	310.6	2.997	9.397	0.047	1.591	31.48	0.173			
lds-usnsn	1	134.1	5.199	10.213	0.058	1.911	35.13	0.311	1.957 (0.101)	31.790 (6.212)	0.322 (0.024)
	2	233.1	4.211	7.424	0.042	2.074	24.62	0.348			
	3	314.2	5.192	10.140	0.065	1.887	35.61	0.305			
kcc-bk	1	133.9	4.812	13.044	0.054	1.667	44.40	0.219	1.918 (0.210)	36.627 (4.815)	0.301 (0.064)
	3	257.2	5.716	10.759	0.044	1.999	35.82	0.333			
	4	313.0	4.431	10.807	0.061	1.721	37.49	0.245			
	5	307.6	5.811	9.521	0.054	2.113	32.41	0.356			
	6	291.8	5.764	9.854	0.047	2.091	33.01	0.352			
min-bk	4	233.0	4.716	11.508	0.049	1.756	38.71	0.260	1.705 (0.058)	40.038 (1.720)	0.236 (0.029)
	5	246.2	4.666	11.729	0.044	1.746	39.05	0.256			
	6	263.5	4.574	11.736	0.042	1.735	38.92	0.251			
	7	307.3	4.409	11.495	0.076	1.619	42.01	0.192			
	8	284.3	4.580	11.729	0.044	1.732	39.05	0.250			
	9	309.0	4.495	12.243	0.061	1.644	42.48	0.206			
new-usnsn	1	101.4	3.956	10.797	0.058	1.652	37.14	0.211	1.711 (0.1030	34.192 (4.342)	0.234 (0.050)
	2	156.5	4.246	8.407	0.079	1.807	31.12	0.279			
	3	130.6	3.638	7.811	0.060	1.825	27.02	0.285			
	4	135.6	3.955	9.354	0.050	1.778	31.54	0.269			
	5	234.0	3.483	11.133	0.044	1.585	37.07	0.170			
	6	253.0	3.414	10.995	0.042	1.584	36.47	0.169			
	8	306.4	4.752	11.239	0.061	1.744	38.99	0.255			
orv-bk	1	130.1	4.669	11.616	0.078	1.641	42.81	0.205	1.761 (0.077)	36.242 (4.005)	0.259 (0.033)

Table B-1: Poisson's Ratio Measurements By Station Cluster (Continued)

Station - Network	Cluster	Back Az (°)	t_{Ps}	t_{PpP}	p (s/km)	Vp/Vs	Thickness (km)	PR	Mean Vp/Vs	Mean Thickness (km)	Mean PR
	2	116.2	4.526	10.243	0.066	1.759	36.09	0.261			
	3	125.7	4.478	9.997	0.063	1.782	34.89	0.270			
	4	131.4	4.431	9.331	0.056	1.855	31.93	0.295			
	5	133.9	4.366	10.616	0.046	1.767	35.49	0.264			
pfo-ii	5	235.3	3.288	8.807	0.048	1.691	29.56	0.231	1.683 (0.037)	30.187 (0.743)	0.226 (0.018)
	6	245.0	3.150	9.145	0.043	1.647	30.39	0.208			
	7	251.0	3.211	9.170	0.043	1.658	30.47	0.214			
	8	257.7	3.171	9.034	0.042	1.661	29.96	0.216			
	9	265.5	3.078	8.924	0.041	1.652	29.54	0.211			
	10	311.4	3.625	8.834	0.070	1.689	31.56	0.230			
	11	317.9	3.639	8.504	0.060	1.756	29.42	0.260			
	12	310.9	3.479	8.814	0.050	1.725	29.72	0.247			
	13	308.3	3.354	9.211	0.050	1.669	31.06	0.220			
svd-ts	1	114.9	4.595	9.490	0.069	1.821	33.78	0.284	1.802 (0.068)	36.400 (3.227)	0.276 (0.023)
	2	133.2	4.646	9.509	0.055	1.884	32.45	0.304			
	3	235.0	4.599	10.929	0.045	1.787	36.46	0.272			
	4	245.7	4.449	10.880	0.043	1.769	36.15	0.265			
	5	264.0	4.787	12.361	0.041	1.732	40.92	0.250			
	6	287.2	4.812	9.872	0.043	1.919	32.80	0.314			
	7	315.7	4.901	10.848	0.074	1.743	39.33	0.255			
	8	311.9	4.836	11.573	0.053	1.760	39.30	0.262			
vtv-ts	1	122.6	3.798	10.115	0.068	1.636	35.88	0.202	1.782 (0.138)	30.985 (4.323)	0.262 (0.048)
	2	131.6	3.777	9.981	0.055	1.682	34.06	0.227			
	3	185.7	3.901	8.694	0.068	1.763	30.84	0.263			
	4	235.0	3.846	10.814	0.049	1.655	36.38	0.213			
	5	246.5	3.793	7.669	0.043	1.932	25.48	0.317			
	6	261.3	4.250	7.686	0.042	2.046	25.49	0.343			

Table B-1: Poisson's Ratio Measurements By Station Cluster (Continued)

Station - Network	Cluster	Back Az (°)	t_{Ps}	t_{PpP}	p (s/km)	Vp/Vs	Thickness (km)	PR	Mean Vp/Vs	Mean Thickness (km)	Mean PR
	7	312.1	3.807	8.408	0.072	1.753	30.26	0.259			
	8	313.2	3.717	7.826	0.055	1.859	26.71	0.296			
	9	304.6	3.859	10.140	0.044	1.713	33.76	0.242			
wdc-bk	1	116.8	7.240	12.568	0.066	1.996	44.29	0.333	1.871 (0.096)	29.008 (10.193)	0.298 (0.029)
	10	311.3	3.326	6.913	0.060	1.852	23.91	0.294			
	11	306.5	3.288	6.950	0.050	1.872	23.43	0.300			
	12	308.8	3.003	7.236	0.050	1.763	24.40	0.263			
why-cnsn	2	118.2	4.193	10.569	0.053	1.721	35.89	0.245	1.673 (0.080)	39.789 (4.951)	0.217 (0.048)
	3	219.3	4.098	12.378	0.043	1.622	41.13	0.193			
	4	239.8	4.288	12.044	0.044	1.667	40.10	0.219			
	5	253.3	4.240	15.377	0.043	1.517	51.10	0.116			
	6	268.3	4.431	10.997	0.042	1.760	36.47	0.262			
	9	289.2	4.145	11.521	0.057	1.642	39.52	0.205			
	10	291.7	4.383	11.045	0.040	1.753	36.50	0.259			
	11	282.8	4.193	11.378	0.040	1.699	37.60	0.235			
wvor-usnsn	1	97.6	4.478	9.759	0.058	1.819	33.57	0.284	1.819 (0.192)	29.470 (3.642)	0.271 (0.059)
	2	127.6	4.210	9.541	0.061	1.777	33.10	0.268			
	3	131.9	6.074	8.969	0.054	2.237	30.53	0.375			
	6	233.9	2.756	7.203	0.047	1.710	24.13	0.240			
	7	249.7	2.431	7.800	0.042	1.587	25.87	0.170			
	8	304.2	4.002	8.749	0.074	1.752	31.72	0.258			
	9	312.7	3.888	8.758	0.067	1.759	30.96	0.261			
	10	306.7	3.802	7.674	0.050	1.913	25.87	0.312			
Extended Crust											

Table B-1: Poisson's Ratio Measurements By Station Cluster (Continued)

Station - Network	Cluster	Back Az (°)	t_{Ps}	t_{PpP}	p (s/km)	Vp/Vs	Thickness (km)	PR	Mean Vp/Vs	Mean Thickness (km)	Mean PR
dac-usnsn	1	130.1	3.602	9.746	0.057	1.665	32.36	0.218	1.839 (0.124)	31.504 (1.070)	0.284 (0.044)
	2	228.8	4.896	9.447	0.042	1.983	30.38	0.330			
	3	236.4	4.244	10.071	0.049	1.782	32.83	0.270			
	4	246.5	4.646	9.496	0.043	1.925	30.60	0.315			
	5	313.9	4.442	9.212	0.066	1.838	31.36	0.290			
bmn-usnsn	1	97.7	3.141	9.219	0.058	1.609	30.68	0.186	1.690 (0.062)	29.120 (1.157)	0.228 (0.029)
	2	137.8	3.747	7.413	0.081	1.809	26.63	0.280			
	3	133.0	3.263	8.974	0.059	1.648	29.95	0.209			
	4	171.9	3.597	8.556	0.054	1.766	28.20	0.264			
	5	229.0	3.142	9.154	0.041	1.651	29.39	0.210			
	6	235.6	3.383	9.017	0.047	1.699	29.27	0.235			
	7	251.2	3.315	9.143	0.042	1.686	29.41	0.229			
	8	308.7	3.358	8.605	0.070	1.661	29.67	0.216			
	9	303.9	3.232	8.913	0.046	1.678	28.88	0.225			
dug-usnsn	1	136.7	3.443	9.447	0.055	1.660	31.21	0.215	1.753 (0.063)	27.855 (2.239)	0.257 (0.028)
	3	231.7	3.479	8.283	0.041	1.798	26.60	0.276			
	4	238.5	3.465	8.283	0.045	1.785	26.79	0.271			
	5	311.4	3.497	7.881	0.066	1.770	26.83	0.265			
elk-usnsn	1	99.3	3.749	9.530	0.060	1.699	31.89	0.235	1.740 (0.070)	30.685 (1.176)	0.251 (0.032)
	2	130.0	3.852	9.107	0.063	1.743	30.73	0.255			
	3	135.5	3.944	9.017	0.054	1.798	29.72	0.276			
	4	234.8	3.320	9.925	0.045	1.627	32.10	0.196			
	5	308.5	3.898	8.901	0.069	1.748	30.59	0.257			
	6	306.6	3.952	8.944	0.048	1.823	29.09	0.285			
gla-ts	1	92.2	2.696	8.785	0.061	1.541	29.47	0.136	1.630 (0.063)	27.634 (1.545)	0.195 (0.037)
	2	125.0	3.150	8.519	0.070	1.626	29.37	0.196			

Table B-1: Poisson's Ratio Measurements By Station Cluster (Continued)

Station - Network	Cluster	Back Az (°)	t_{Ps}	t_{PpP}	p (s/km)	Vp/Vs	Thickness (km)	PR	Mean Vp/Vs	Mean Thickness (km)	Mean PR
	3	132.5	2.998	8.558	0.056	1.632	28.34	0.199			
	4	247.9	2.648	8.387	0.043	1.595	27.02	0.176			
	5	266.7	2.702	8.631	0.041	1.593	27.71	0.175			
	6	313.9	3.104	7.440	0.072	1.701	25.83	0.236			
	7	313.3	3.081	7.813	0.053	1.721	25.69	0.245			
mnv-usnsn	1	96.2	4.598	10.329	0.058	1.800	34.38	0.277	1.758 (0.053)	34.858 (1.249)	0.259 (0.022)
	2	130.7	4.478	9.310	0.079	1.779	33.17	0.269			
	3	125.9	4.503	10.211	0.060	1.786	34.17	0.272			
	4	171.0	4.153	10.752	0.056	1.698	35.61	0.234			
	5	228.4	4.345	11.060	0.042	1.744	35.57	0.255			
	6	235.4	4.403	10.956	0.049	1.745	35.71	0.255			
	7	249.3	4.594	10.410	0.042	1.836	33.48	0.289			
	8	312.9	4.232	10.736	0.068	1.675	36.78	0.223			
nee-ts	1	124.9	3.654	7.233	0.069	1.866	24.86	0.299	1.850 (0.059)	26.018 (2.138)	0.292 (0.020)
	2	135.7	3.724	7.523	0.055	1.901	24.85	0.309			
	3	188.9	3.597	7.067	0.068	1.877	24.21	0.302			
	4	240.3	3.652	9.036	0.049	1.749	29.45	0.257			
	5	313.1	3.793	8.126	0.053	1.855	26.72	0.295			
tph-usnsn	1	128.7	4.341	10.056	0.059	1.772	33.56	0.266	1.727 (0.074)	34.953 (1.125)	0.245 (0.034)
	2	170.0	4.302	10.507	0.052	1.751	34.47	0.258			
	3	229.0	3.829	11.405	0.042	1.635	36.68	0.201			
	4	237.5	3.943	11.011	0.049	1.663	35.89	0.217			
	5	246.7	3.842	11.073	0.042	1.656	35.61	0.213			
	6	308.1	4.698	9.846	0.071	1.809	34.06	0.280			
	7	315.5	4.681	10.134	0.065	1.806	34.39	0.279			

Table B-1: Poisson's Ratio Measurements By Station Cluster (Continued)

Station - Network	Cluster	Back Az (°)	t_{Ps}	t_{PpP}	p (s/km)	Vp/Vs	Thickness (km)	PR	Mean Vp/Vs	Mean Thickness (km)	Mean PR
tpnv-usnsn	2	229.6	5.345	10.709	0.042	1.947	34.44	0.321	2.014 (0.079)	33.099 (1.095)	0.335 (0.017)
	3	236.8	5.192	10.549	0.049	1.915	34.39	0.312			
	4	250.5	5.288	10.322	0.042	1.972	33.20	0.327			
	5	313.8	5.771	9.463	0.066	2.066	32.21	0.347			
	6	311.3	5.812	9.804	0.054	2.086	32.31	0.351			
	7	303.1	5.787	9.908	0.045	2.100	32.04	0.353			
tuc-iu	1	140.3	3.510	9.918	0.054	1.643	32.69	0.206	1.703 (0.073)	30.734 (1.710)	0.234 (0.032)
	2	135.8	3.589	9.718	0.062	1.650	32.69	0.210			
	3	124.9	3.744	9.446	0.072	1.665	32.79	0.218			
	4	240.0	3.288	9.272	0.046	1.663	30.04	0.217			
	5	252.7	3.245	9.371	0.042	1.655	30.14	0.212			
	6	290.6	3.526	9.236	0.041	1.724	29.66	0.247			
	7	317.0	4.050	8.331	0.070	1.829	28.72	0.287			
	8	314.3	3.859	8.902	0.051	1.799	29.14	0.276			
California Coast ranges											
bar-ts	1	132.6	5.097	10.156	0.054	1.912	34.57	0.312	1.836 (0.163)	36.450 (6.968)	0.277 (0.066)
	2	121.4	5.103	10.807	0.069	1.800	38.47	0.277			
	3	186.7	4.462	13.584	0.070	1.548	48.53	0.142			
	4	231.1	4.815	8.636	0.046	2.043	28.87	0.342			
	5	244.9	4.526	8.760	0.043	1.974	29.11	0.327			
	6	287.8	4.716	11.330	0.042	1.786	37.58	0.271			
	7	314.8	4.855	12.715	0.073	1.628	45.93	0.197			
	8	315.8	4.812	9.236	0.057	1.936	31.69	0.318			
	9	309.3	4.792	9.946	0.047	1.897	33.32	0.308			
bks-bk	1	126.5	3.145	7.046	0.079	1.710	26.08	0.240	1.743 (0.057)	32.141 (4.196)	0.253 (0.023)

Table B-1: Poisson's Ratio Measurements By Station Cluster (Continued)

Station - Network	Cluster	Back Az (°)	t_{Ps}	t_{PpP}	p (s/km)	Vp/Vs	Thickness (km)	PR	Mean Vp/Vs	Mean Thickness (km)	Mean PR
	11	284.3	4.288	9.854	0.040	1.826	32.57	0.286			
	14	307.4	4.145	10.378	0.050	1.734	34.99	0.251			
	15	304.8	3.907	10.569	0.040	1.701	34.93	0.236			
hops-bk	4	225.4	3.596	9.737	0.044	1.692	32.42	0.232	1.631 (0.059)	33.537 (1.176)	0.196 (0.036)
	6	239.6	3.510	9.870	0.044	1.666	32.86	0.218			
	8	290.0	3.288	10.045	0.049	1.602	33.79	0.181			
	10	310.2	3.241	10.140	0.060	1.562	35.08	0.153			
calb-ts	2	132.3	4.056	8.305	0.055	1.884	28.34	0.304	1.869 (0.077)	27.867 (0.929)	0.298 (0.024)
	3	184.1	3.664	8.098	0.068	1.770	28.73	0.266			
	4	234.3	3.812	7.807	0.051	1.897	26.38	0.308			
	5	244.1	3.717	8.521	0.043	1.821	28.31	0.284			
	6	312.4	4.329	8.099	0.054	1.972	27.57	0.327			
jrsc-bk	4	133.1	3.050	9.474	0.050	1.590	31.94	0.173	1.617 (0.031)	31.700 (0.497)	0.190 (0.019)
	10	308.3	3.382	8.714	0.070	1.650	31.13	0.210			
	11	307.4	3.168	9.499	0.050	1.612	32.03	0.187			
mhc-bk	11	284.5	3.241	6.284	0.040	1.981	20.77	0.329	1.847 (0.090)	22.745 (1.489)	0.290 (0.031)
	13	309.3	2.955	7.093	0.070	1.700	25.34	0.235			
	14	312.2	3.098	6.617	0.060	1.829	22.89	0.287			
	15	308.9	3.168	6.785	0.050	1.860	22.88	0.297			
	16	302.9	3.082	6.728	0.040	1.870	22.23	0.300			
	17	303.6	2.997	6.766	0.040	1.841	22.36	0.291			
pas-ts	2	120.6	3.907	6.300	0.070	2.053	22.51	0.344	1.884 (0.170)	25.857 (2.948)	0.296 (0.042)
	3	131.2	4.148	6.045	0.053	2.258	20.53	0.378			
	4	233.7	3.431	7.219	0.049	1.879	24.29	0.302			
	5	247.0	3.479	7.492	0.044	1.872	24.94	0.300			

Table B-1: Poisson's Ratio Measurements By Station Cluster (Continued)

Station - Network	Cluster	Back Az (°)	t_{Ps}	t_{PpP}	p (s/km)	Vp/Vs	Thickness (km)	PR	Mean Vp/Vs	Mean Thickness (km)	Mean PR
	6	264.8	3.514	8.328	0.041	1.799	27.57	0.276			
	7	287.6	3.607	8.210	0.045	1.822	27.39	0.285			
	8	316.5	3.506	7.980	0.074	1.722	28.94	0.245			
	9	312.2	3.548	8.344	0.055	1.768	28.48	0.265			
	10	304.3	3.498	8.497	0.040	1.781	28.08	0.270			
rpv-ts	1	116.6	2.439	4.814	0.069	1.860	17.14	0.297	1.887 (0.044)	21.433 (4.465)	0.304 (0.012)
	2	130.5	2.431	4.981	0.053	1.890	16.91	0.306			
	3	242.1	3.813	7.337	0.049	1.962	24.68	0.325			
	4	286.8	3.686	8.091	0.044	1.855	26.94	0.295			
	6	311.0	3.019	6.315	0.054	1.868	21.50	0.299			
sao-bk	3	114.7	4.336	6.998	0.067	2.068	24.74	0.347	1.794 (0.181)	28.041 (2.024)	0.261 (0.068)
	4	124.7	4.098	8.379	0.063	1.855	29.25	0.295			
	5	124.7	3.596	8.928	0.053	1.732	30.32	0.250			
	6	131.7	3.853	8.005	0.048	1.893	26.87	0.306			
	7	225.4	2.812	8.379	0.042	1.632	27.79	0.199			
	8	233.8	2.765	8.664	0.051	1.583	29.28	0.168			
sbc-ts	5	244.5	4.344	10.020	0.044	1.814	33.36	0.282	1.869 (0.058)	30.027 (3.345)	0.298 (0.017)
	6	258.2	4.287	9.836	0.043	1.821	32.68	0.284			
	7	286.0	4.205	8.844	0.044	1.893	29.44	0.307			
	8	314.0	3.951	6.897	0.073	1.954	24.91	0.323			
	9	311.0	4.146	8.735	0.054	1.862	29.73	0.297			
stan-bk	1	125.7	4.752	10.819	0.079	1.698	40.04	0.235	1.786 (0.124)	36.573 (4.908)	0.268 (0.047)
	5	309.9	4.716	9.569	0.060	1.874	33.10	0.301			
Volcanic Arc											

Table B-1: Poisson's Ratio Measurements By Station Cluster (Continued)

Station - Network	Cluster	Back Az (°)	t_{Ps}	t_{PpP}	p (s/km)	Vp/Vs	Thickness (km)	PR	Mean Vp/Vs	Mean Thickness (km)	Mean PR
bbb-cnsn	1	226.2	3.247	7.918	0.044	1.768	26.59	0.265	1.783 (0.056)	25.928 (0.777)	0.269 (0.024)
	2	248.3	3.053	7.797	0.043	1.736	26.13	0.252			
	3	302.0	3.516	6.845	0.074	1.845	25.07	0.292			
adk-iu	1	89.8	4.669	8.331	0.056	2.011	28.76	0.336	1.952 (0.096)	31.509 (2.129)	0.320 (0.022)
	2	88.7	4.582	8.275	0.074	1.913	30.31	0.312			
	8	249.8	5.042	9.296	0.056	1.978	32.09	0.328			
	9	265.1	4.898	8.953	0.078	1.879	33.34	0.302			
	10	255.8	4.848	9.009	0.070	1.907	32.50	0.310			
	11	263.9	4.714	9.844	0.060	1.847	34.37	0.293			
	12	265.0	5.192	8.760	0.040	2.127	29.19	0.358			
cor-iu	1	131.5	6.280	13.446	0.043	1.879	45.06	0.302	1.978 (0.086)	40.174 (4.050)	0.327 (0.019)
	2	125.9	6.493	13.077	0.049	1.917	44.38	0.313			
	3	122.0	6.828	13.049	0.065	1.905	46.27	0.310			
	4	135.5	7.001	11.526	0.077	1.986	42.74	0.330			
	5	162.8	6.273	11.884	0.049	1.976	40.33	0.328			
	6	228.5	6.004	10.757	0.047	2.040	36.34	0.342			
	7	244.1	6.045	10.435	0.043	2.093	34.97	0.352			
	8	260.7	6.155	10.284	0.043	2.129	34.46	0.358			
	9	282.8	6.239	12.140	0.049	1.950	41.20	0.322			
	10	306.4	6.192	9.553	0.070	2.099	34.46	0.353			
	11	306.0	5.984	11.917	0.060	1.889	41.60	0.305			
	12	297.3	5.899	11.576	0.050	1.939	39.37	0.319			
	13	303.3	5.907	12.330	0.040	1.910	41.09	0.311			
mobc-cnsn	1	221.7	4.669	6.474	0.044	2.359	21.74	0.391	2.071 (0.407)	24.241 (3.542)	0.331 (0.085)
	2	299.4	3.479	7.331	0.073	1.783	26.75	0.271			
pgc-cnsn	2	233.8	5.335	9.569	0.044	2.048	32.13	0.343	2.048 (0.000)	32.129 (0.000)	0.343 (0.000)

Table B-1: Poisson's Ratio Measurements By Station Cluster (Continued)

Station - Network	Cluster	Back Az (°)	t_{Ps}	t_{PpP}	p (s/km)	Vp/Vs	Thickness (km)	PR	Mean Vp/Vs	Mean Thickness (km)	Mean PR
pmb-cnsn	3	230.3	4.193	11.378	0.044	1.690	38.20	0.231	1.688 (0.003)	37.900 (0.428)	0.230 (0.061)
	4	304.3	4.240	10.569	0.066	1.686	37.60	0.229			
unm-g	1	138.7	6.544	10.895	0.072	2.005	39.60	0.334	1.781 (0.142)	49.329 (7.069)	0.262 (0.053)
	2	249.1	5.954	14.812	0.044	1.753	49.73	0.259			
	3	322.3	6.150	15.990	0.078	1.610	59.55	0.186			
	4	327.2	6.049	13.656	0.066	1.759	48.58	0.261			
	5	321.5	6.091	14.621	0.045	1.778	49.19	0.269			

Cluster: Cluster identification number (see Appendix 2).

BackAz: Back azimuth from station to Cluster center.

t_{Ps}: Time pick of Ps phase.

t_{PpPms}: Time pick of PpPms phase.

* Average.

C RECEIVER FUNCTION VELOCITY STRUCTURES

Using the observed radial receiver-functions stacks at each station, a preliminary velocity structure was estimated using the method described in Ammon et al. (1990). *These structures are neither intended, nor suitable for geologic interpretation!* Our goal was to construct models that provide a correction for variations in the upper crust when we measured the MCT thickness. Non-uniqueness problems with receiver function inversion are well documented (Ammon et al., 1990). Although the velocity-contrast travel and travel times above the contrast are well represented in the structures, these are not the only structures that fit the stacked receiver functions. Structures more consistent with geological variations undoubtedly exist, but were not sought since they were not needed for this work.

The results are grouped by tectonic setting (see label in lower-right corner of each station panel) following the same classification of Appendix 1. Each station's panel contains the observed receiver function stack (dashed curve) and the synthetic receiver function (solid curve) calculated using the inverted velocity model shown to the right. During the inversion, a high-pass filter (0.03 Hz corner frequency, two-passes) was used to equalize the bandwidth between the observed signals (which often lack long periods) and the predicted receiver functions (and partial derivatives).

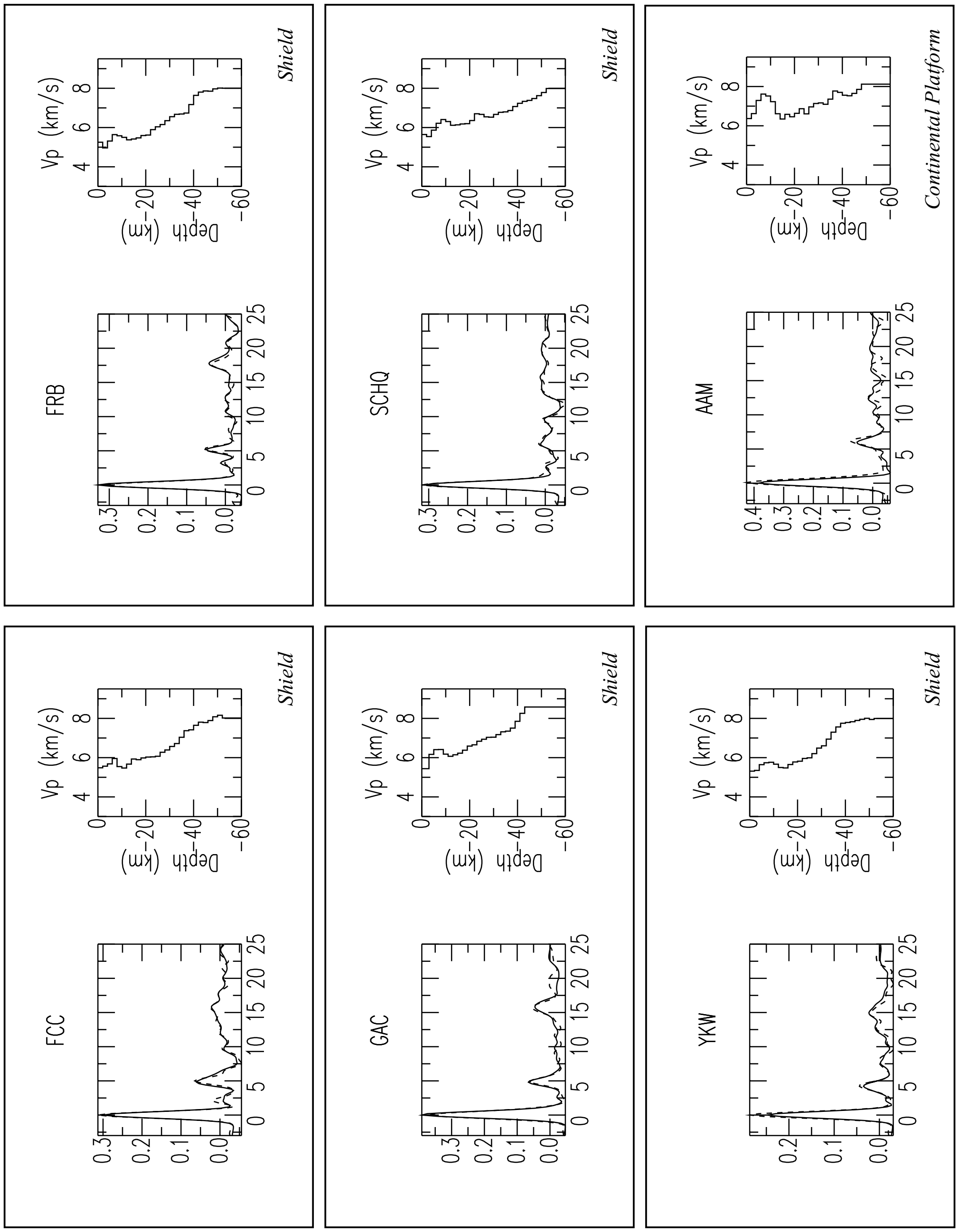

FCC
Shield
GAC
Shield
YKW
Shield
FRB
Shield
SCHQ
Shield
AAM
Continental Platform
Vp (km/s)
Depth (km)

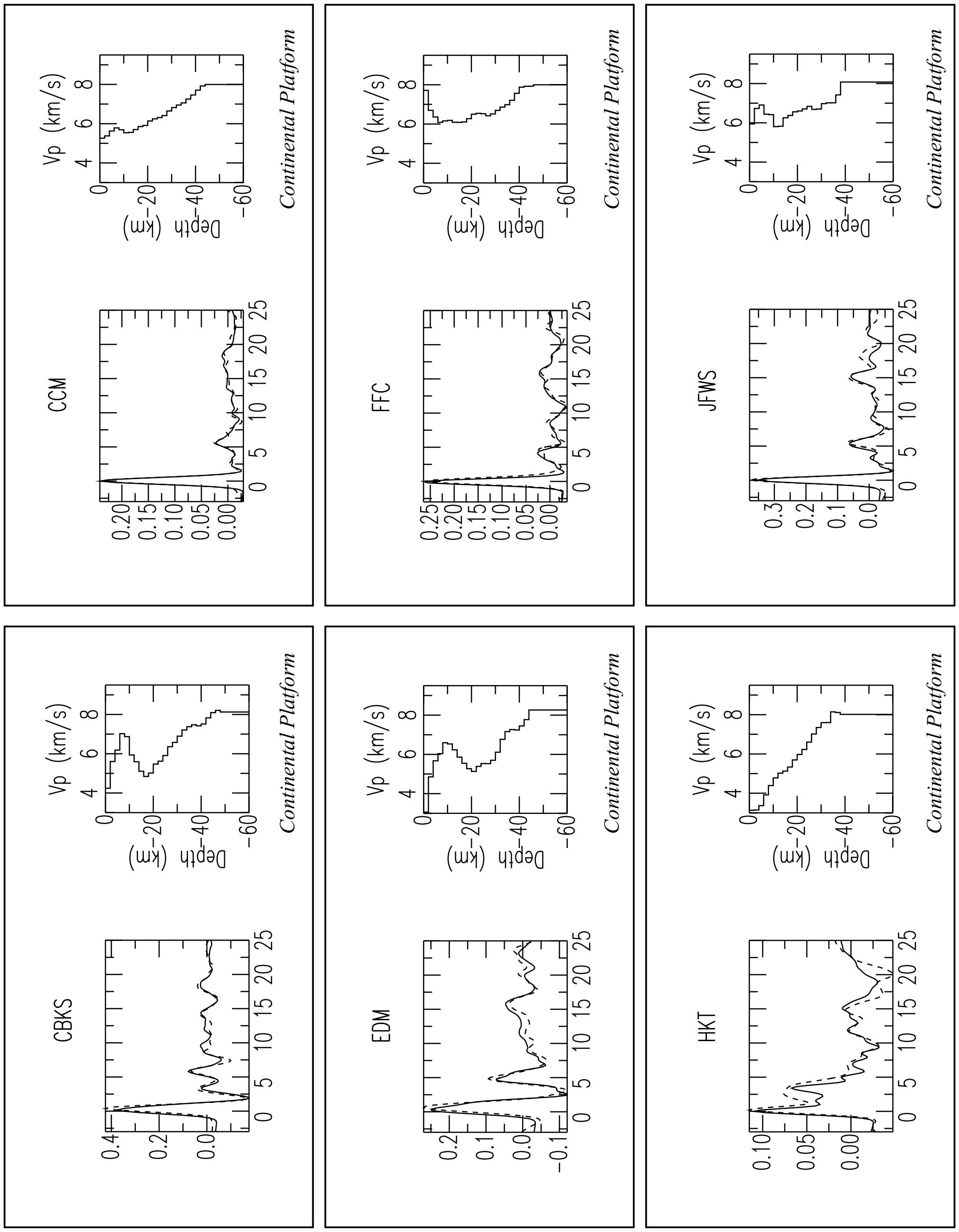
CCM
FFC
JFWS
CBKS
EDM
HKT
Vp (km/s)
Depth (km)
Continental Platform

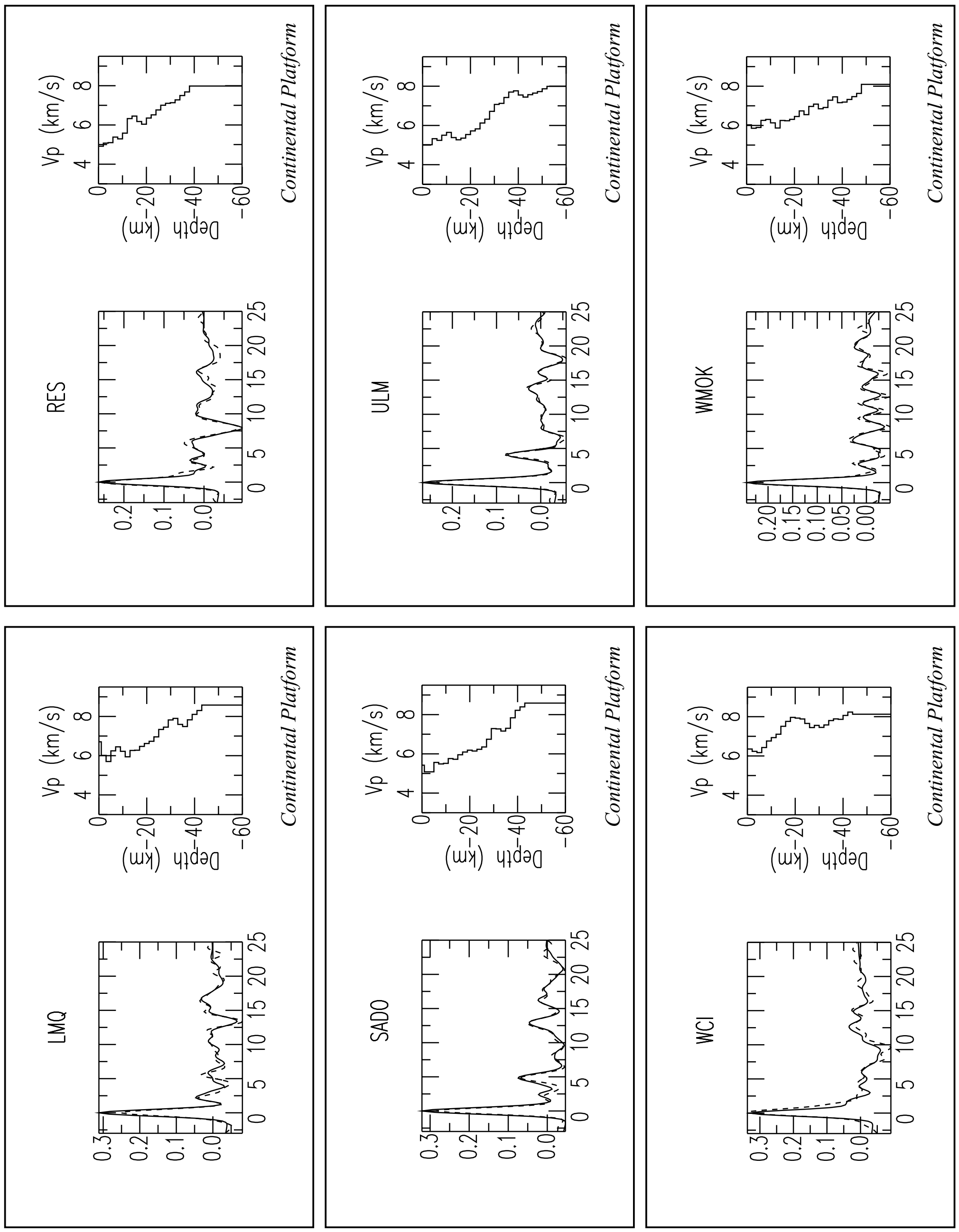
RES
Continental Platform
ULM
Continental Platform
WMOK
Continental Platform
LMQ
Continental Platform
SADO
Continental Platform
WCI
Continental Platform
Vp (km/s)
Depth (km)

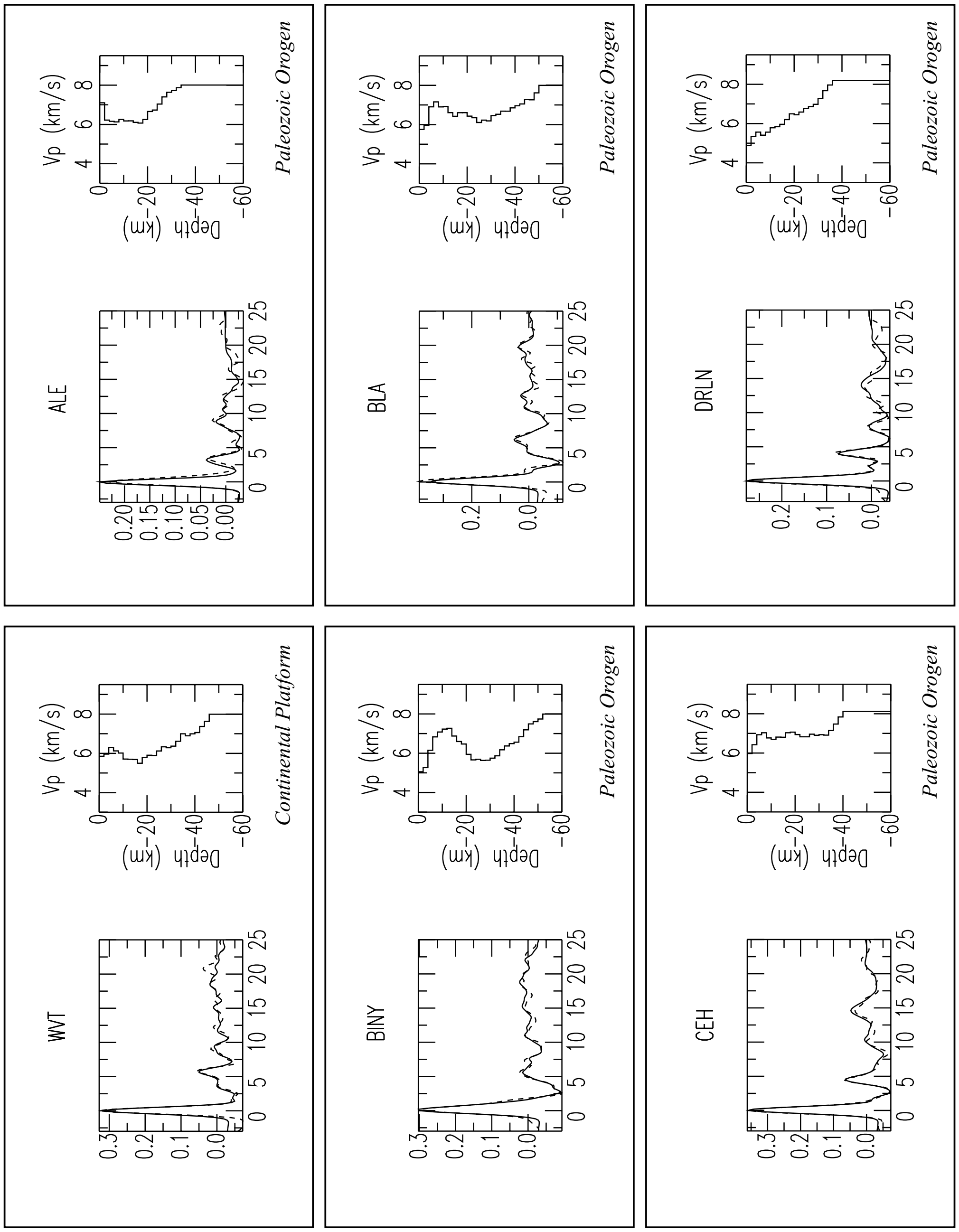

ALE
Paleozoic Orogen
BLA
Paleozoic Orogen
DRLN
Paleozoic Orogen
WVT
Continental Platform
BINY
Paleozoic Orogen
CEH
Paleozoic Orogen
Vp (km/s)
Depth (km)

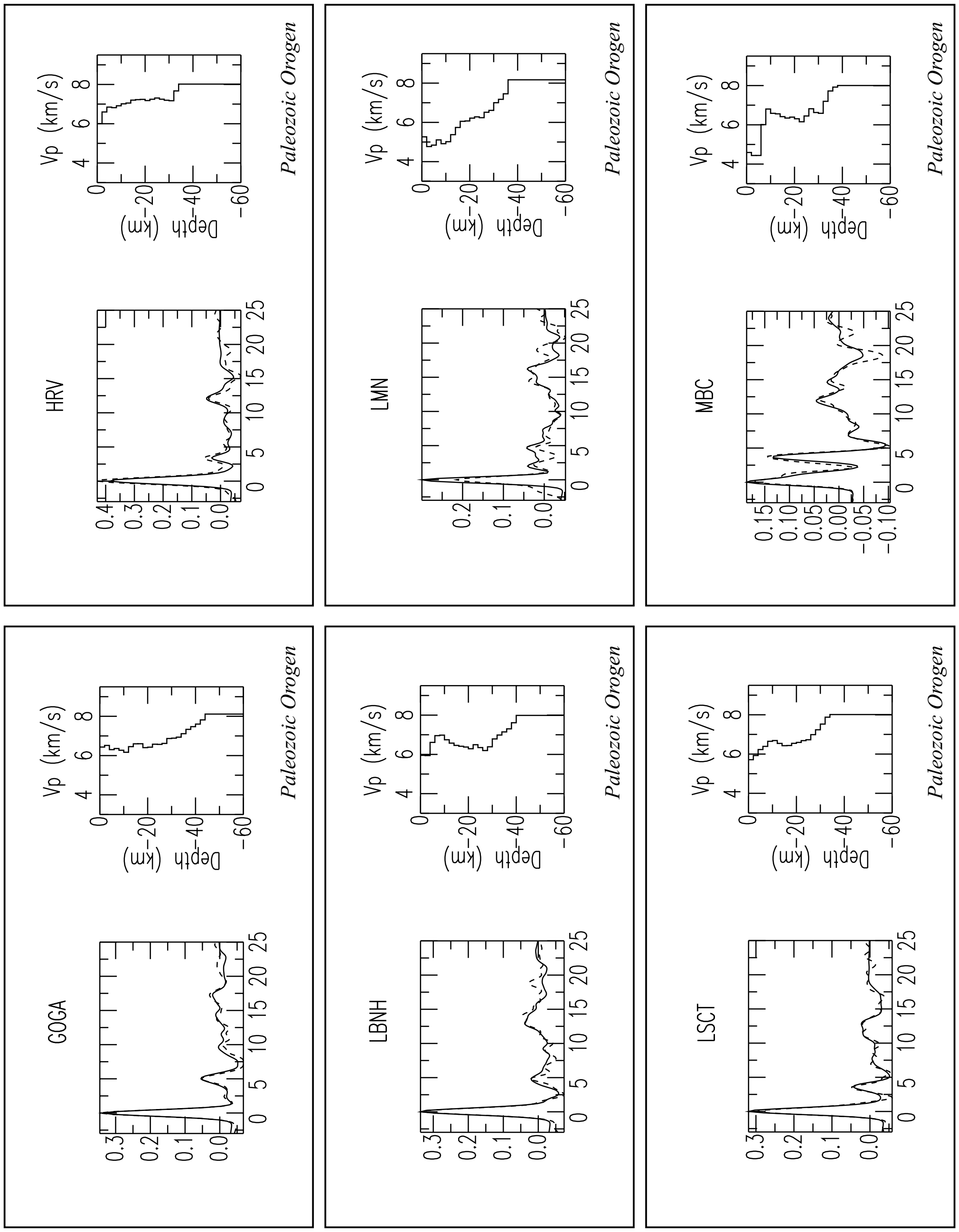

HRV
Vp (km/s)
Depth (km)
Paleozoic Orogen
LMN
Vp (km/s)
Depth (km)
Paleozoic Orogen
MBC
Vp (km/s)
Depth (km)
Paleozoic Orogen
GOGA
Vp (km/s)
Depth (km)
Paleozoic Orogen
LBNH
Vp (km/s)
Depth (km)
Paleozoic Orogen
LSCT
Vp (km/s)
Depth (km)
Paleozoic Orogen

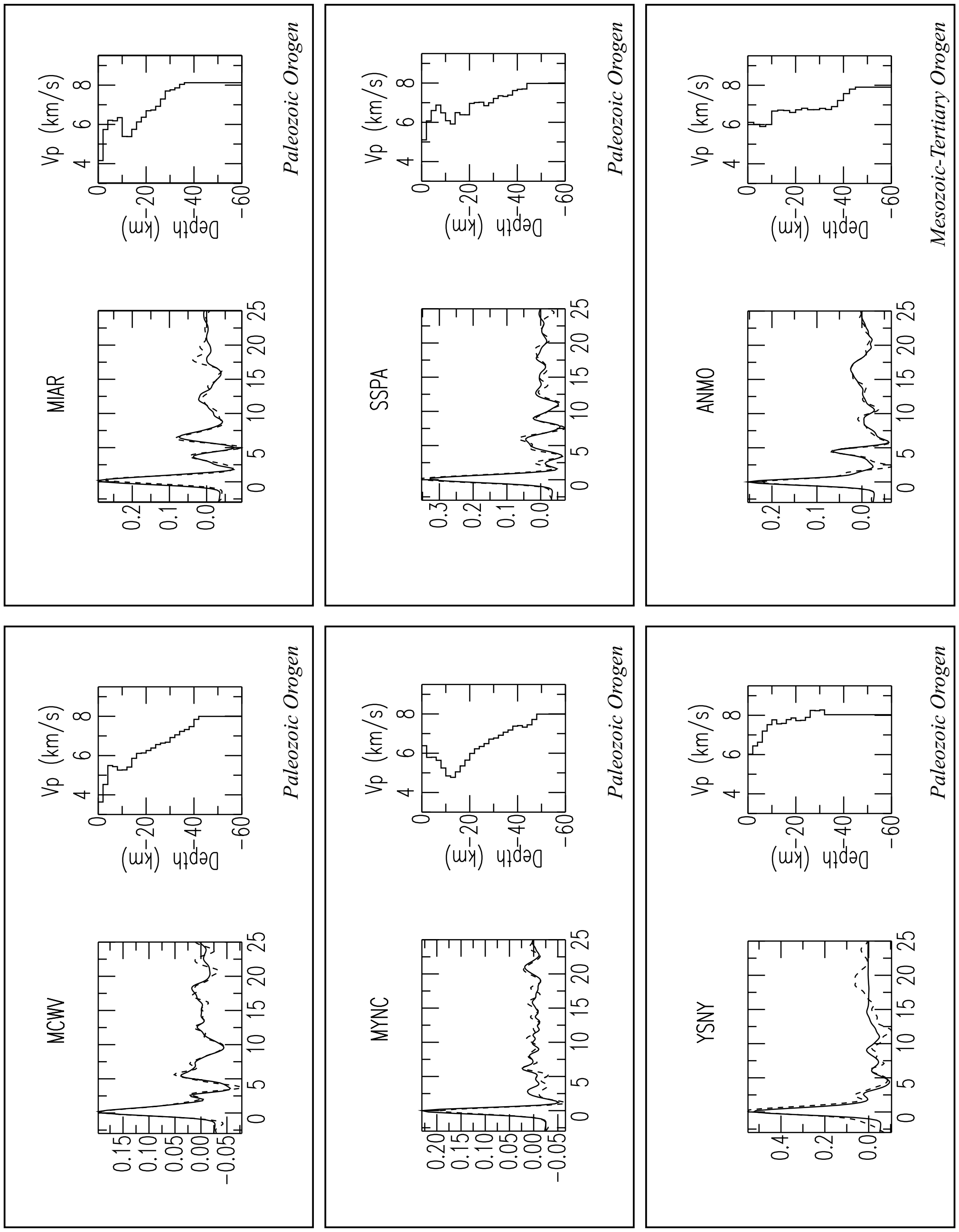

MCWV
Paleozoic Orogen
MYNC
Paleozoic Orogen
YSNY
Paleozoic Orogen
MIAR
Paleozoic Orogen
SSPA
Paleozoic Orogen
ANMO
Mesozoic-Tertiary Orogen
Vp (km/s)
Depth (km)

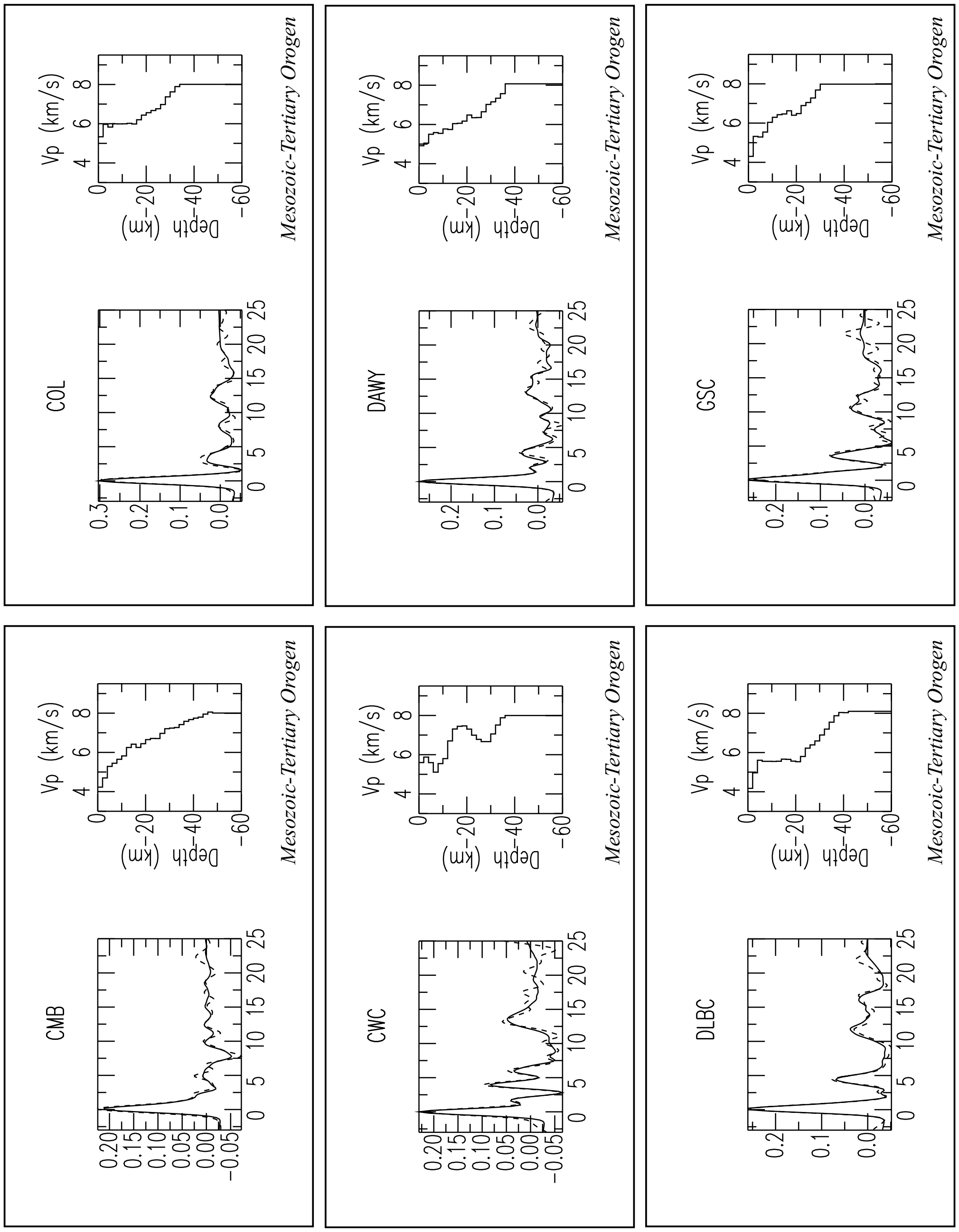

COL
Vp (km/s)
Depth (km)
Mesozoic-Tertiary Orogen
DAWY
Vp (km/s)
Depth (km)
Mesozoic-Tertiary Orogen
GSC
Vp (km/s)
Depth (km)
Mesozoic-Tertiary Orogen
CMB
Vp (km/s)
Depth (km)
Mesozoic-Tertiary Orogen
CWC
Vp (km/s)
Depth (km)
Mesozoic-Tertiary Orogen
DLBC
Vp (km/s)
Depth (km)
Mesozoic-Tertiary Orogen

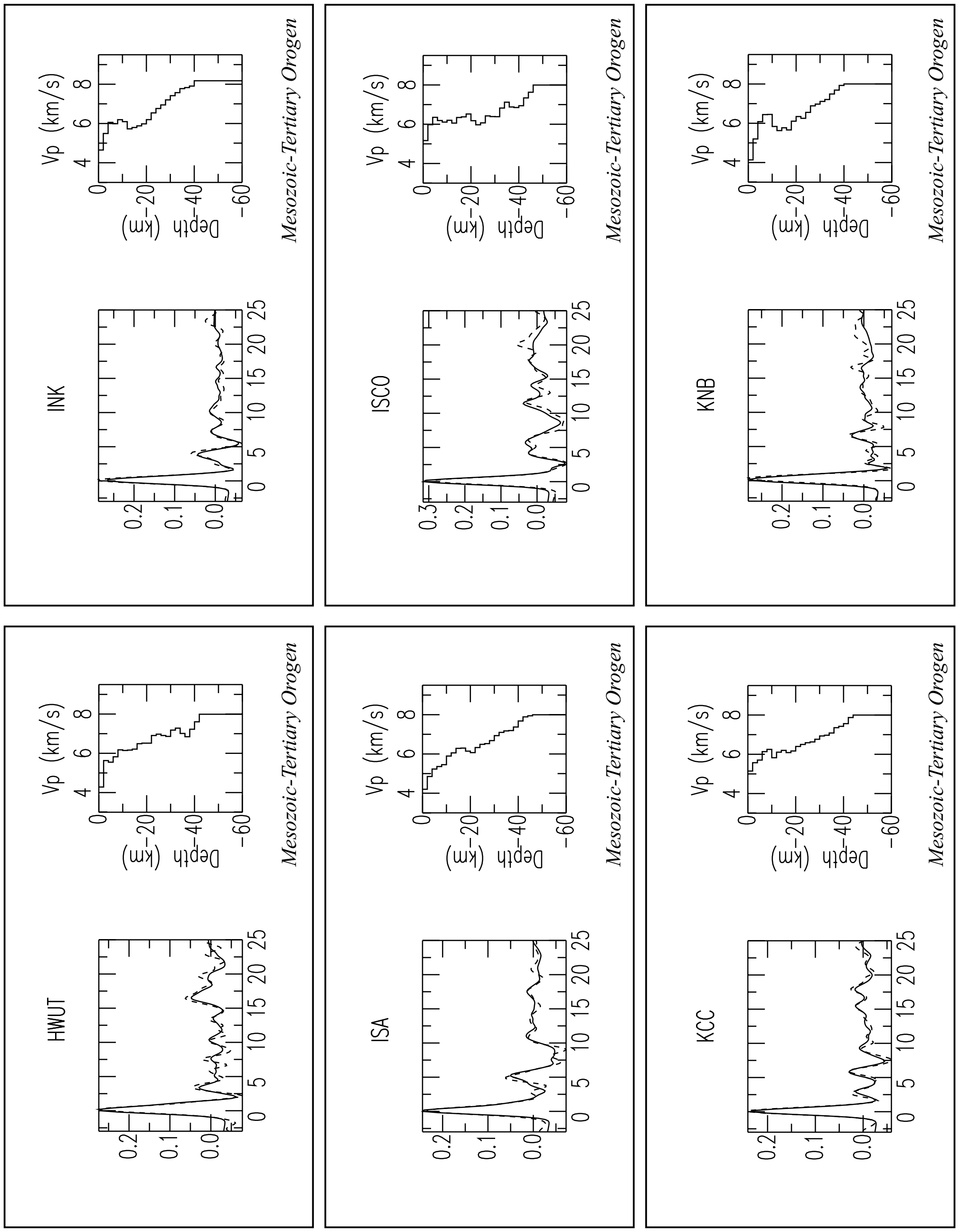
HWUT
INK
ISA
ISCO
KCC
KNB
Vp (km/s)
Depth (km)
Mesozoic-Tertiary Orogen

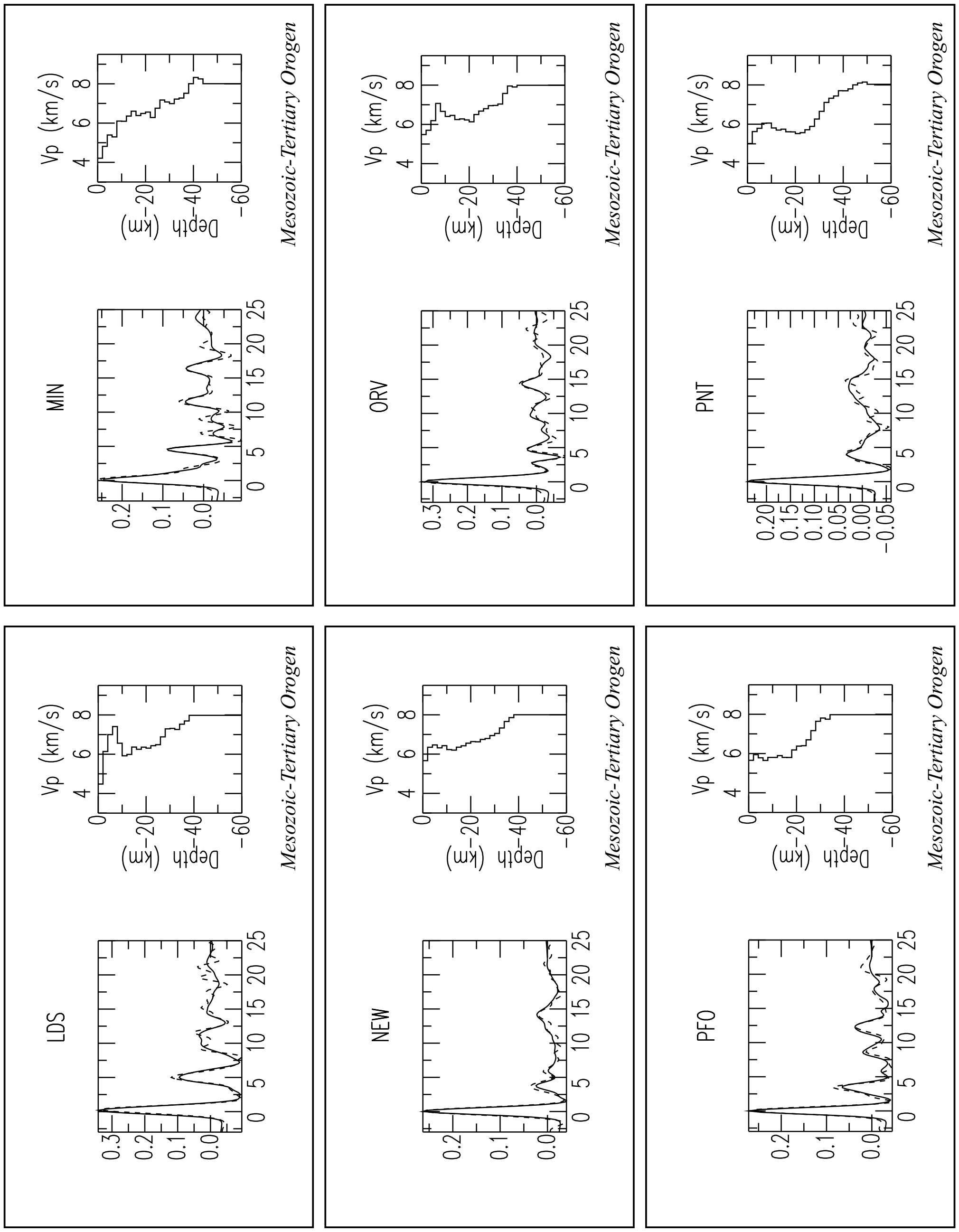

LDS
Vp (km/s)
Depth (km)
Mesozoic-Tertiary Orogen
NEW
Vp (km/s)
Depth (km)
Mesozoic-Tertiary Orogen
PFO
Vp (km/s)
Depth (km)
Mesozoic-Tertiary Orogen
MIN
Vp (km/s)
Depth (km)
Mesozoic-Tertiary Orogen
ORV
Vp (km/s)
Depth (km)
Mesozoic-Tertiary Orogen
PNT
Vp (km/s)
Depth (km)
Mesozoic-Tertiary Orogen

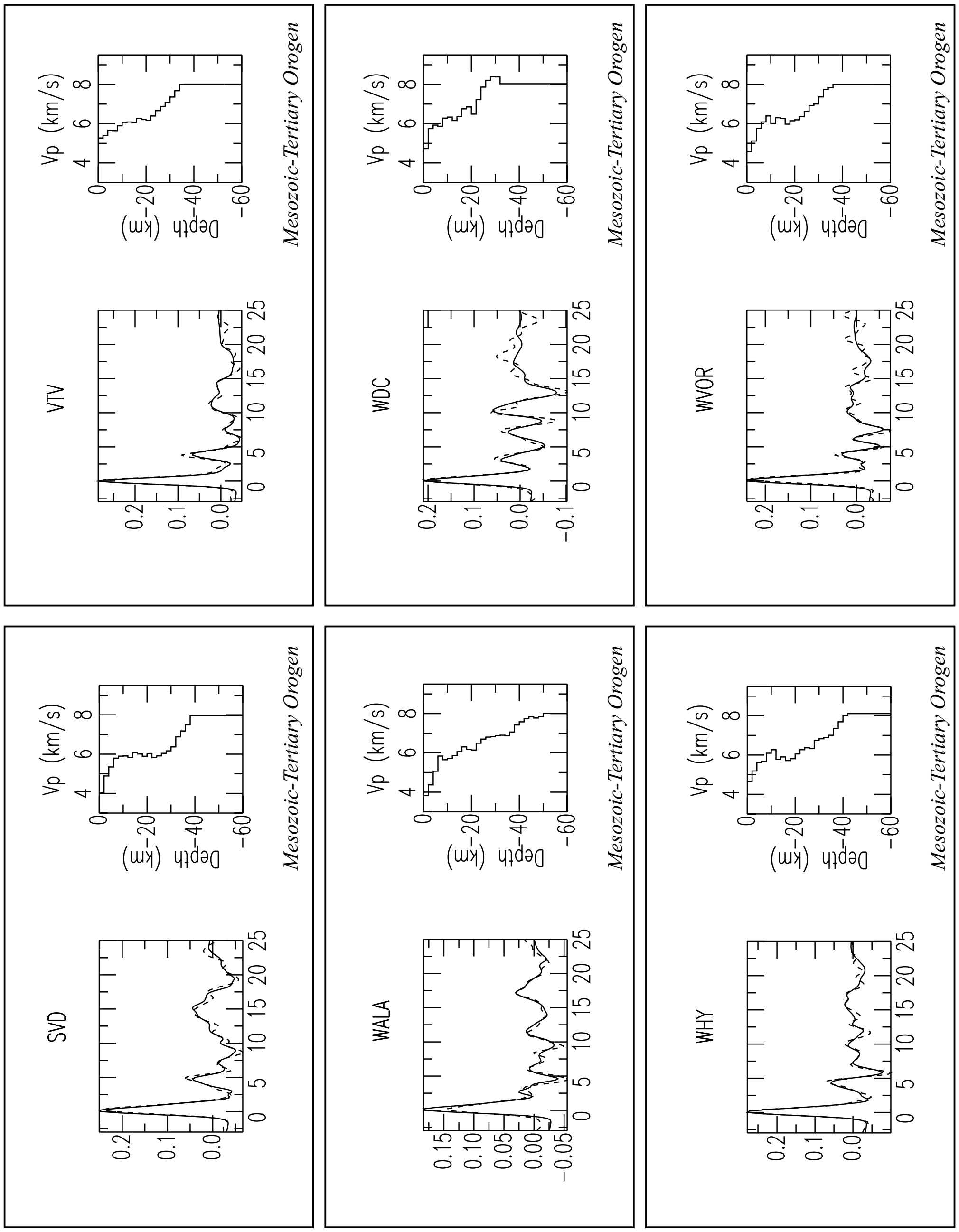
SVD
WALA
WHY
VTV
WDC
WWOR
Vp (km/s)
Depth (km)
Mesozoic-Tertiary Orogen

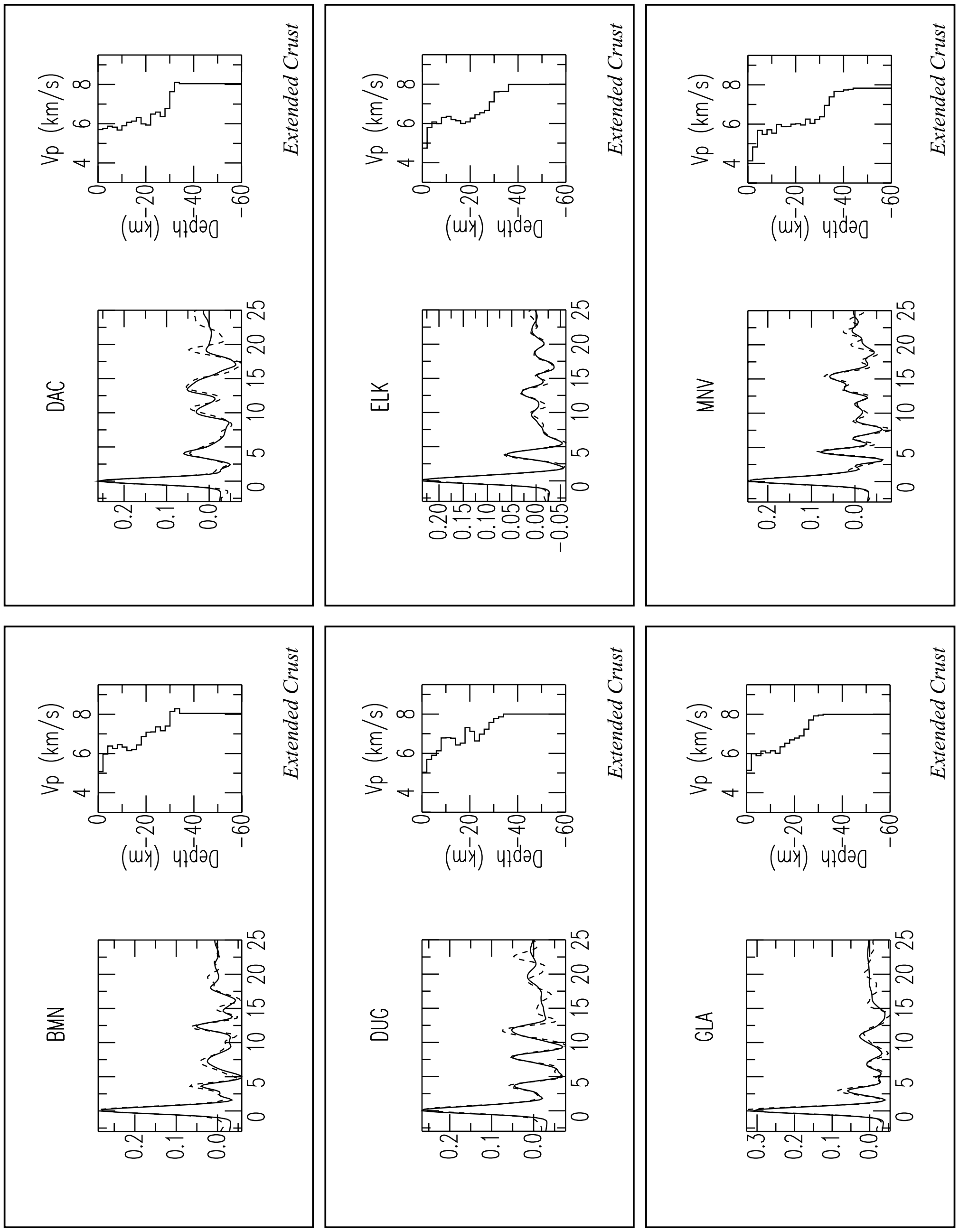
BMN
DUG
GLA
DAC
ELK
MNV
Vp (km/s)
Depth (km)
Extended Crust

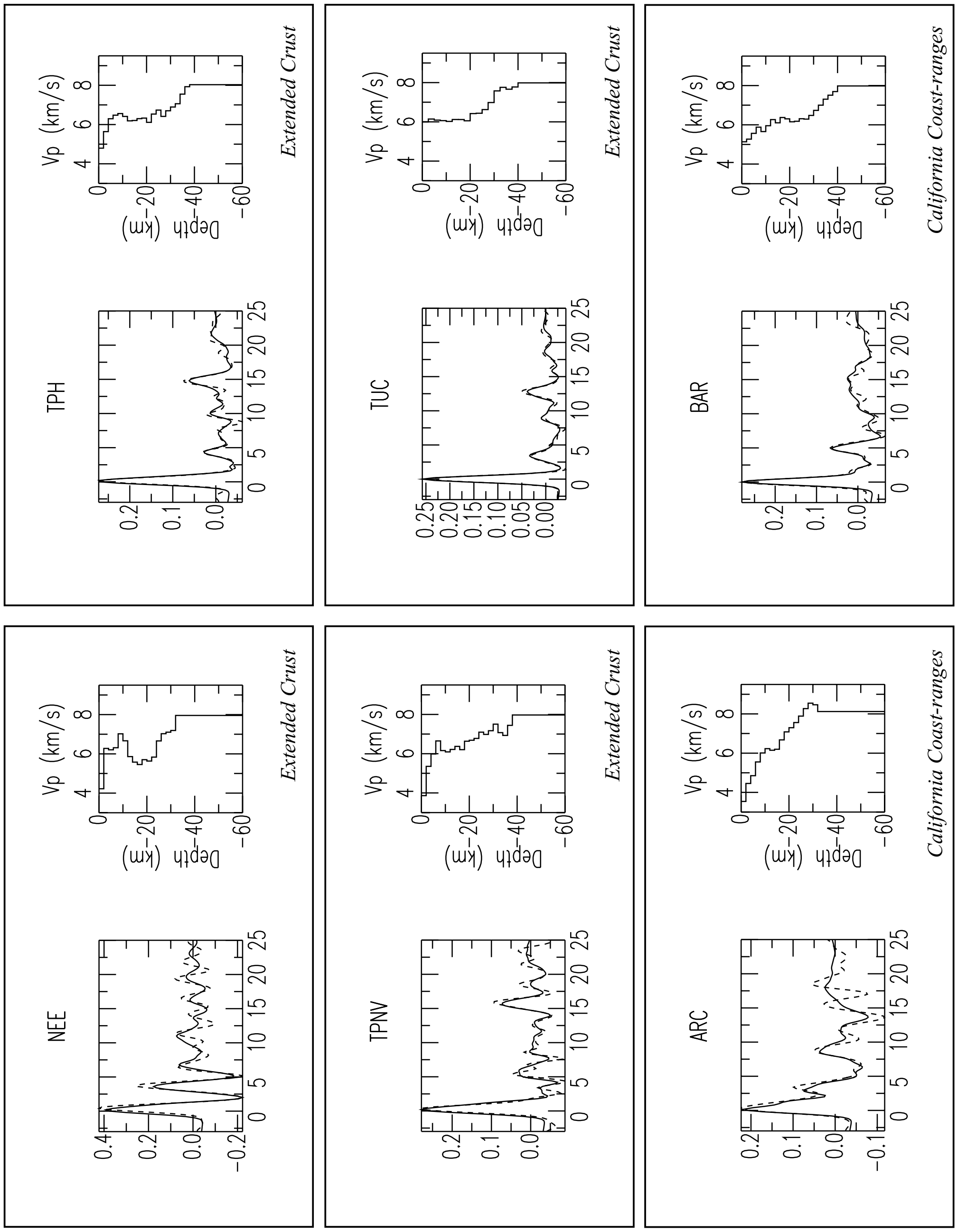
NEE
Vp (km/s)
Depth (km)
Extended Crust
TPNV
Vp (km/s)
Depth (km)
Extended Crust
ARC
Vp (km/s)
Depth (km)
California Coast-ranges
TPH
Vp (km/s)
Depth (km)
Extended Crust
TUC
Vp (km/s)
Depth (km)
Extended Crust
BAR
Vp (km/s)
Depth (km)
California Coast-ranges

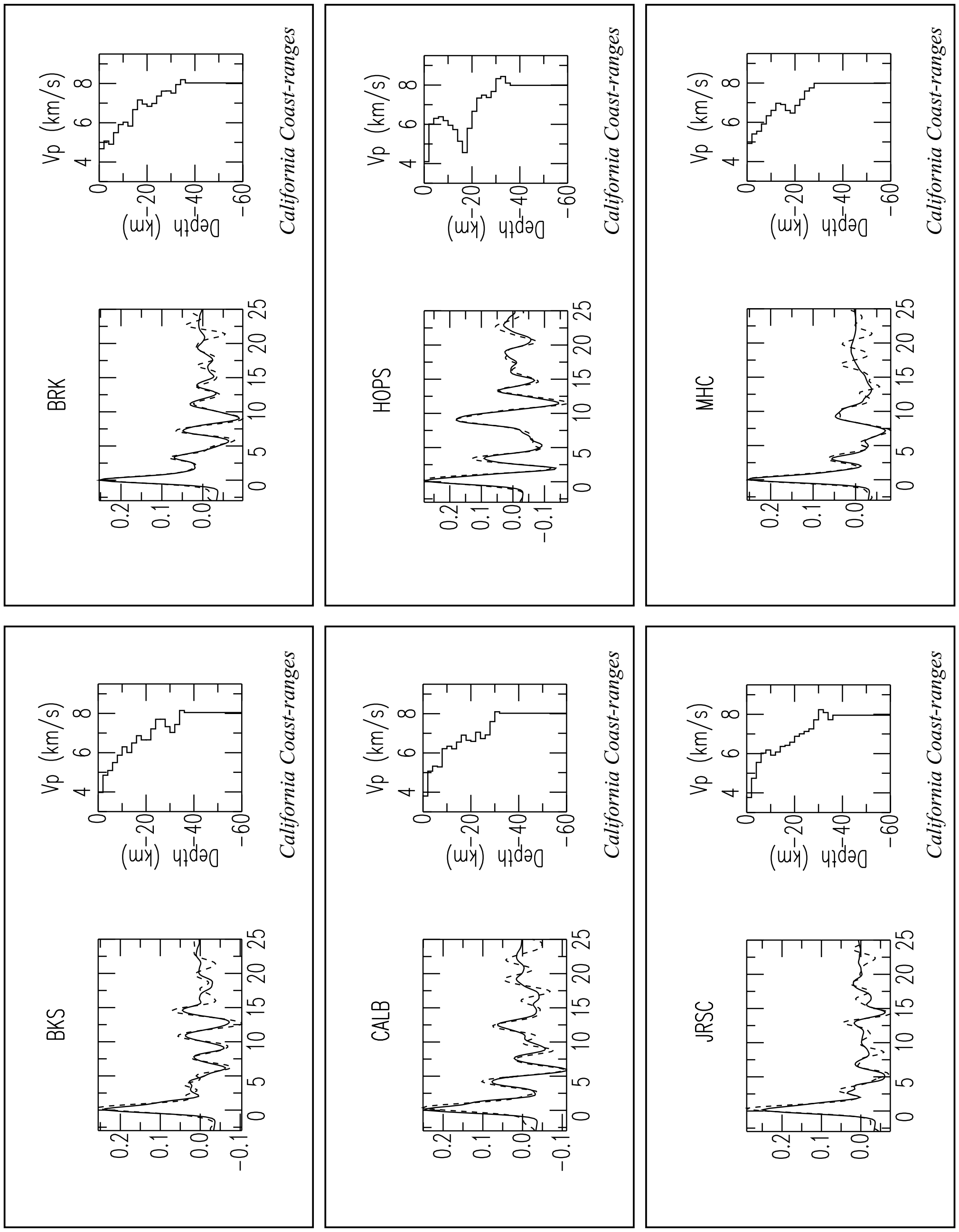
BRK
HOPS
MHC
BKS
CALB
JRSC
Vp (km/s)
Depth (km)
California Coast-ranges

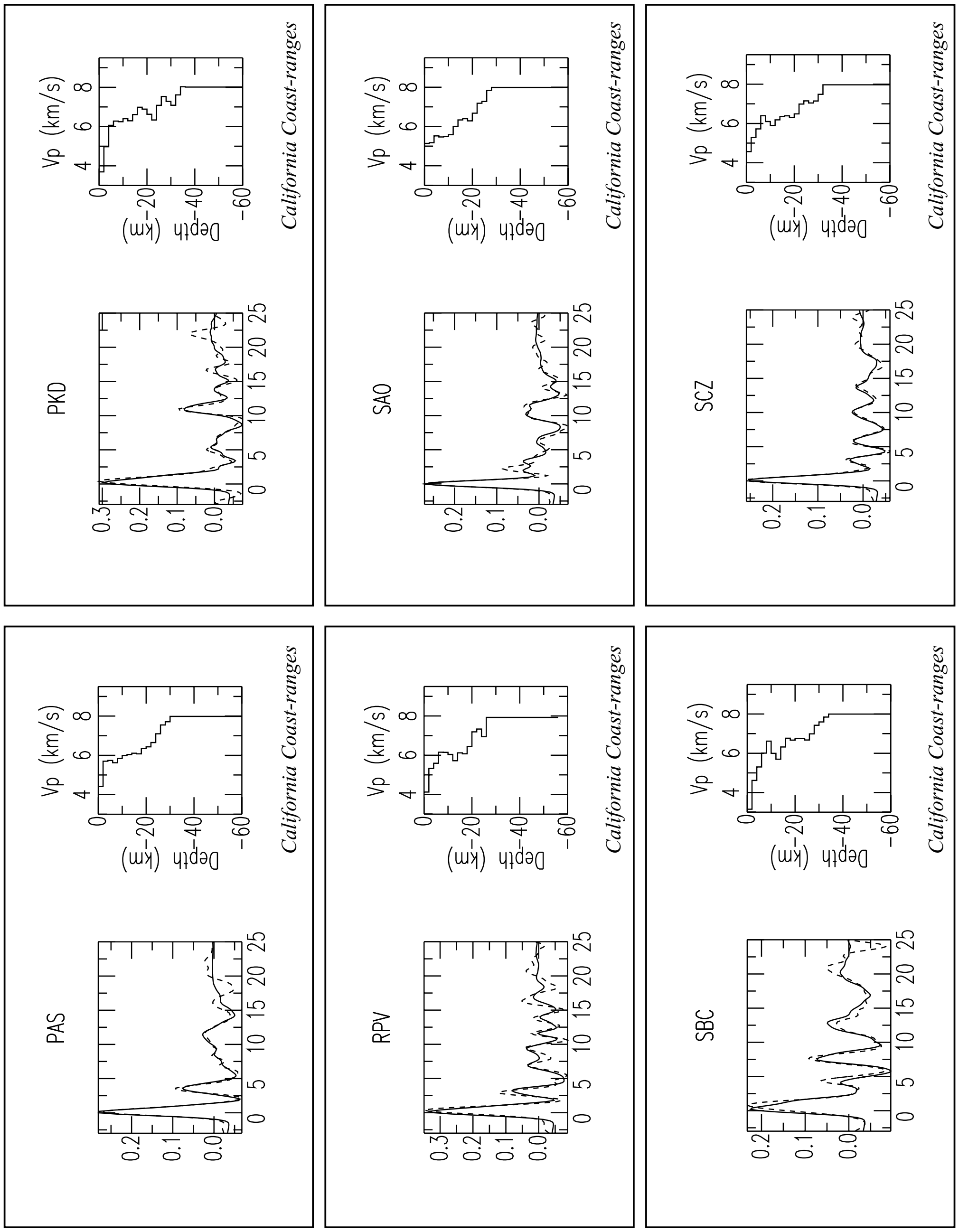

PAS
RPV
SBC
PKD
SAO
SCZ
Vp (km/s)
Depth (km)
California Coast-ranges

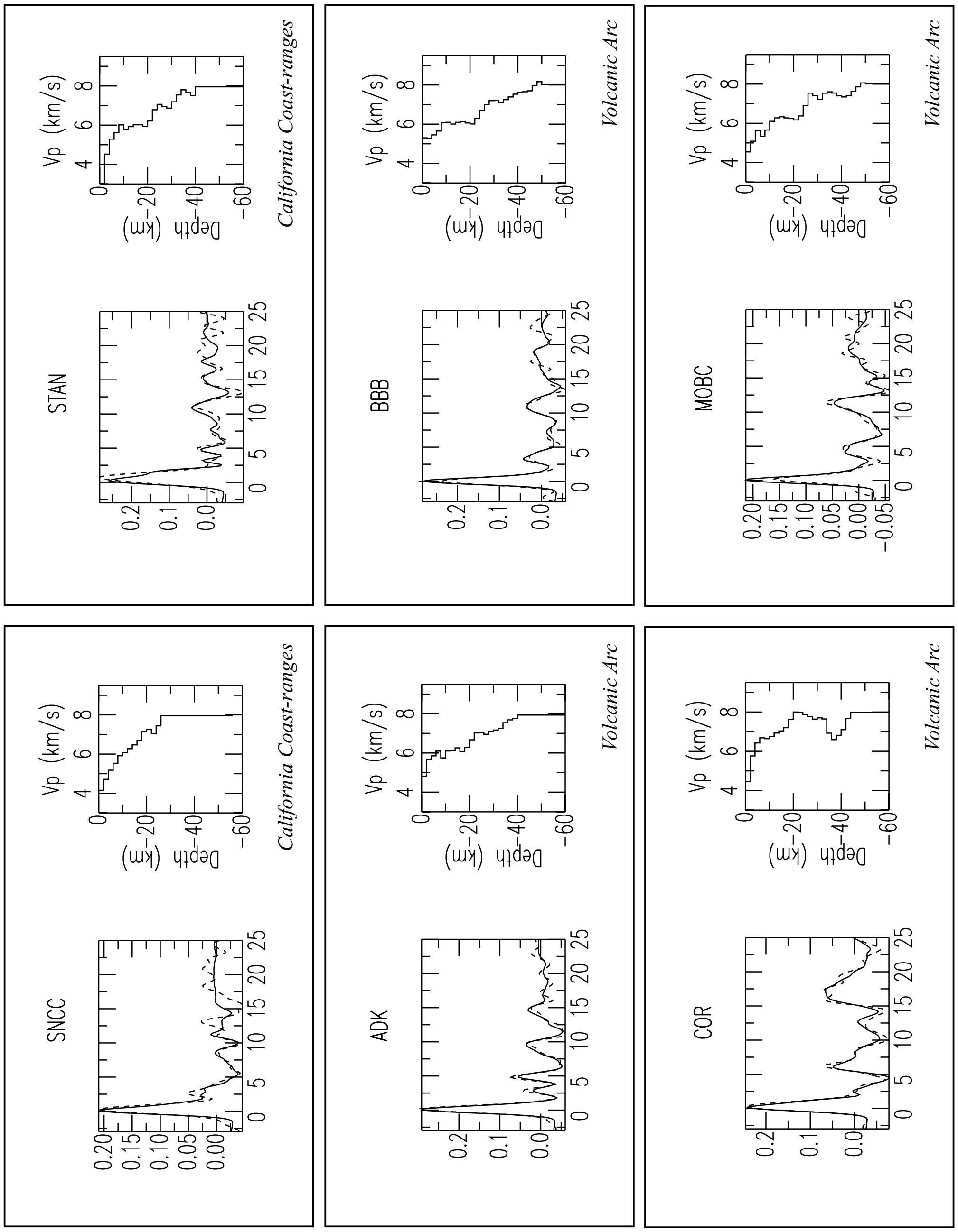
STAN
Vp (km/s)
Depth (km)
California Coast-ranges
BBB
Volcanic Arc
MOBC
Volcanic Arc
SNCC
California Coast-ranges
ADK
Volcanic Arc
COR
Volcanic Arc

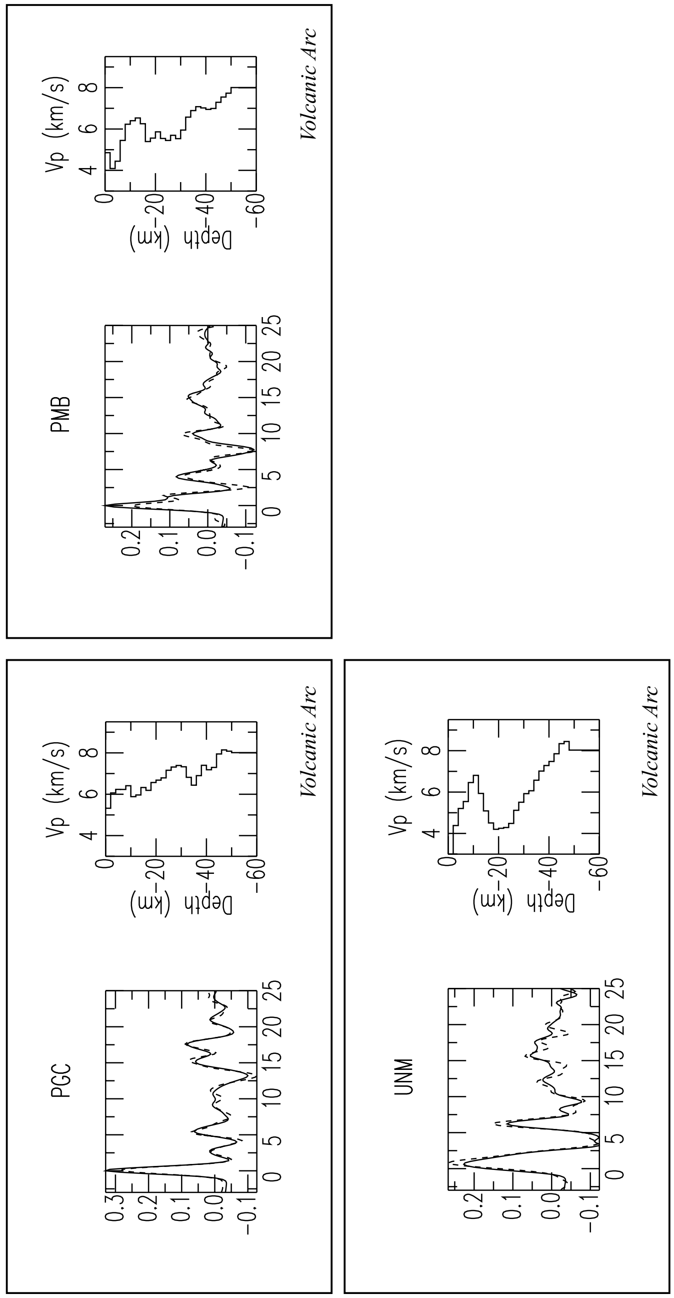
PMB
Vp (km/s)
Depth (km)
Volcanic Arc
PGC
Vp (km/s)
Depth (km)
Volcanic Arc
UNM
Vp (km/s)
Depth (km)
Volcanic Arc

D MCT THICKNESS ESTIMATES

Table D-1: MCT Thickness Estimates

Station	ID	BackAz (°)	p (s/km)	MCT (km)	±	ID	Back Az (°)	p (s/km)	MCT (km)	±	Mean	SD
Shield												
FCC	1	158.7	0.04	4.0	1.0	2	157.1	0.06	7.0	1.0	5.83	1.61
	3	313.9	0.07	6.5	1.5							
FRB	1	64.8	0.06	6.0	1.0	2	178.9	0.04	5.5	1.5	5.95	1.36
	3	184.2	0.05	6.5	1.5	4	187.9	0.06	5.5	0.5		
	5	218.0	0.07	4.5	1.0	6	254.8	0.07	7.5	0.5		
	7	306.3	0.07	8.5	0.5	8	327.8	0.06	6.5	1.0		
	9	333.7	0.05	5.0	1.0	10	350.0	0.04	4.0	1.0		
GAC	1	181.8	0.07	4.0	0.5	2	180.7	0.06	8.0	1.0	4.08	2.01
	3	220.5	0.08	3.0	1.0	4	225.6	0.05	2.5	0.5		
	5	315.0	0.06	3.0	1.0	6	328.4	0.05	4.0	1.0		
SCHQ	1	63.0	0.05	3.0	1.0	2	181.9	0.05	3.5	1.5	5.30	2.39
	4	192.9	0.07	6.0	1.0	5	224.1	0.07	5.0	1.0		
	6	331.9	0.06	9.0	2.0							
YKW	1	27.0	0.05	4.0	2.0	2	139.1	0.04	3.5	1.0	3.81	2.62
	3	138.5	0.05	9.0	2.0	4	135.5	0.06	9.0	2.0		
	5	157.0	0.07	6.0	1.0	6	238.2	0.04	4.0	1.0		
	7	264.8	0.04	2.0	1.0	8	298.5	0.07	2.0	1.0		
	9	298.9	0.07	2.0	1.0	10	302.4	0.06	1.5	0.5		
	11	305.0	0.05	2.0	1.0	12	309.0	0.04	2.0	1.0		
	13	354.0	0.04	2.5	1.0							
Continental Platform												
AAM	1	169.5	0.05	6.0	1.0	2	217.5	0.08	7.0	1.5	6.67	0.58
	3	320.1	0.06	7.0	1.5							
CBKS	1	144.0	0.07	3.0	1.0	2	149.5	0.06	5.0	1.0	3.50	1.05
	3	190.7	0.06	2.0	1.0	4	244.3	0.04	4.0	2.0		
	5	313.4	0.06	4.0	2.0	6	311.2	0.04	3.0	1.0		
CCM	1	32.1	0.04	4.0	1.0	2	43.7	0.05	3.0	1.0	6.45	2.11
	3	101.2	0.05	4.0	2.0	4	102.5	0.07	9.0	2.0		
	5	154.2	0.08	9.0	2.0	6	157.7	0.07	8.0	2.0		

Table D-1: MCT Thickness Estimates (Continued)

Station	ID	BackAz (°)	p (s/km)	MCT (km)	±	ID	Back Az (°)	p (s/km)	MCT (km)	±	Mean	SD
	7	156.6	0.06	7.0	1.0	8	197.8	0.06	5.0	2.0		
	9	316.9	0.07	7.0	2.0	10	322.6	0.05	7.0	2.0		
	11	322.7	0.04	8.0	2.0							
EDM	2	239.4	0.04	3.0	2.0	3	260.0	0.04	6.0	2.0	4.00	1.73
	4	307.6	0.07	3.0	1.5							
FFC	1	10.3	0.04	2.0	1.0	2	36.8	0.05	3.0	1.0	3.95	1.42
	3	147.5	0.07	3.0	1.5	4	149.5	0.05	5.5	1.0		
	5	174.9	0.08	3.0	1.0	6	199.6	0.05	2.5	1.0		
	7	247.4	0.04	4.5	1.5	8	296.3	0.07	4.5	1.5		
	9	311.3	0.06	6.0	1.0	10	312.8	0.05	5.5	1.0		
HKT	1	109.9	0.08	3.0	1.0	2	142.5	0.08	5.0	2.0	5.80	2.28
	3	154.6	0.06	5.0	1.5	4	193.0	0.06	9.0	2.0		
	6	319.1	0.05	7.0	2.0							
JFWS	1	159.7	0.07	2.0	1.0	2	162.3	0.06	2.5	1.0	3.83	2.75
	3	321.6	0.05	7.0	2.0							
LMQ	1	181.5	0.05	7.0	2.0	2	186.2	0.07	2.0	1.0	4.50	3.54
RES	1	161.5	0.05	6.0	1.0	2	185.4	0.06	5.0	1.0	4.81	1.73
	3	301.4	0.07	7.0	2.0	4	307.1	0.07	3.0	1.0		
	5	309.7	0.06	3.0	1.0	6	319.0	0.05	3.0	2.0		
	7	325.9	0.05	7.0	1.5	8	323.5	0.04	4.5	1.5		
SADO	1	172.8	0.05	2.0	1.0	2	172.9	0.07	3.0	1.0	2.33	0.58
	3	207.5	0.08	2.0	1.0							
ULM	1	176.7	0.04	3.0	1.0	3	158.5	0.05	2.5	1.0	2.83	0.29
	4	317.3	0.06	3.0	1.0							
WCI	1	162.9	0.08	3.0	1.0	2	166.6	0.05	3.5	1.5	3.17	0.29
	3	319.6	0.06	3.0	1.0							
WMOK	1	152.6	0.06	5.0	2.0	2	247.0	0.04	8.0	2.0	6.50	1.50
	3	313.2	0.06	6.5	1.5							
WVT	1	160.5	0.08	4.5	2.0	2	158.8	0.06	6.0	2.5	5.38	1.38
	3	167.0	0.05	4.0	1.0	4	324.9	0.05	7.0	1.5		
Paleozoic Orogen												
ALE	1	18.8	0.05	4.0	1.0	2	41.6	0.06	4.0	1.0	3.97	1.14
	3	64.4	0.07	3.5	1.0	4	84.1	0.06	2.5	1.0		

Table D-1: MCT Thickness Estimates (Continued)

Station	ID	BackAz (°)	p (s/km)	MCT (km)	±	ID	Back Az (°)	p (s/km)	MCT (km)	±	Mean	SD
	5	187.4	0.04	3.0	1.0	6	195.3	0.04	3.5	2.0		
	7	193.6	0.05	3.0	1.0	8	202.3	0.05	3.0	1.0		
	9	218.1	0.06	4.0	1.0	10	246.8	0.07	2.5	1.0		
	11	295.1	0.07	4.0	1.0	12	322.3	0.07	4.5	1.0		
	13	331.0	0.06	4.0	1.0	14	339.0	0.06	5.5	1.5		
	15	332.9	0.04	6.5	1.5	16	354.3	0.05	6.0	1.0		
	17	355.3	0.04	4.0	2.0							
BINY	1	179.4	0.07	5.0	1.0	2	175.1	0.06	3.0	1.5	4.40	1.67
	3	211.0	0.05	4.0	1.0	4	229.6	0.08	3.0	1.0		
	5	321.4	0.06	7.0	1.5							
BLA	1	172.2	0.08	6.0	1.0	2	169.5	0.06	7.0	1.0	6.60	1.67
	3	173.3	0.05	4.0	1.0	4	229.4	0.08	8.0	2.0		
	5	321.2	0.06	8.0	1.5							
CEH	1	174.9	0.08	5.5	1.5	2	169.2	0.06	3.0	1.0	4.60	2.22
	3	233.5	0.08	8.0	2.0	4	318.3	0.06	4.0	1.0		
	5	328.3	0.05	2.5	1.0							
DRLN	1	190.9	0.05	4.5	1.5	2	197.0	0.06	7.0	1.0	6.20	2.02
	3	205.0	0.07	4.0	2.0	4	239.7	0.07	9.0	2.0		
	5	339.3	0.05	6.5	1.0							
GOGA	1	121.4	0.08	7.5	1.5	2	166.0	0.08	3.0	1.0	4.58	1.91
	3	165.4	0.07	3.0	1.0	4	170.5	0.06	3.0	1.5		
	5	317.7	0.06	6.0	1.0	6	328.8	0.05	5.0	1.5		
HRV	1	24.9	0.04	5.0	1.0	2	43.0	0.05	5.0	1.0	4.21	1.21
	3	54.6	0.06	3.5	2.0	4	117.3	0.06	4.0	1.5		
	5	174.8	0.06	4.0	1.0	6	177.7	0.06	4.0	1.5		
	7	187.8	0.07	4.0	1.0	8	190.8	0.08	6.5	1.5		
	9	232.5	0.08	6.0	1.0	10	282.9	0.07	2.5	1.0		
	11	318.7	0.05	3.0	1.0	12	333.2	0.04	3.0	1.0		
LBNH	1	147.0	0.08	9.0	2.0	2	185.0	0.07	9.0	2.0	9.10	0.22
	3	180.3	0.06	9.0	2.0	4	179.4	0.05	9.5	1.5		
	5	326.4	0.06	9.0	1.0							
LMN	1	185.8	0.05	5.0	1.5	2	194.6	0.07	6.0	2.0	5.50	0.71
LSCT	1	184.4	0.07	3.0	1.0	2	176.5	0.06	8.0	2.0	4.88	2.59
	3	205.8	0.05	2.5	1.0	4	324.8	0.06	6.0	1.0		
MBC	1	2.1	0.05	3.0	1.0	2	134.0	0.04	4.0	1.0	3.00	0.98
	3	135.6	0.05	2.0	1.0	5	181.7	0.08	2.0	1.0		

Table D-1: MCT Thickness Estimates (Continued)

Station	ID	BackAz (°)	p (s/km)	MCT (km)	±	ID	Back Az (°)	p (s/km)	MCT (km)	±	Mean	SD
	6	263.0	0.04	2.0	1.0	7	280.3	0.05	3.0	1.0		
	8	279.5	0.08	2.0	1.0	9	286.9	0.07	4.0	1.0		
	10	296.3	0.05	4.5	1.0	11	303.4	0.05	3.0	1.0		
	12	297.3	0.04	4.0	1.0	13	297.9	0.04	4.0	1.0		
	14	325.9	0.05	1.5	1.0	15	350.0	0.06	3.0	2.0		
MCWV	1	173.5	0.05	5.0	1.5	2	171.0	0.06	5.5	1.5	6.50	2.18
	3	322.2	0.06	9.0	2.0							
MIAR	1	153.2	0.05	5.0	1.0	2	159.9	0.06	3.0	1.0	7.00	2.83
	3	197.0	0.06	9.0	1.0	4	250.3	0.04	9.0	1.0		
	5	317.6	0.06	9.0	1.0							
MYNC	1	164.9	0.04	7.0	1.0	2	170.1	0.05	6.0	1.0	5.67	1.53
	3	203.0	0.06	4.0	1.0							
SSPA	1	53.5	0.05	3.0	1.0	2	171.9	0.06	4.0	1.0	4.64	1.31
	3	177.0	0.07	4.0	1.0	4	229.5	0.08	5.0	1.0		
	5	317.2	0.06	4.0	1.5	6	328.1	0.05	5.5	2.0		
	7	330.2	0.04	7.0	2.0							
YSNY	1	176.5	0.05	9.0	2.0	2	230.8	0.08	8.0	1.0	8.33	0.58
	3	320.3	0.06	8.0	1.5							
Mesozoic-Tertiary Orogen												
ANMO	1	91.6	0.04	4.0	1.5	2	144.7	0.05	3.0	1.0	4.25	1.60
	3	139.3	0.07	3.5	1.5	4	131.0	0.08	4.0	1.0		
	5	242.6	0.04	7.0	1.0	6	256.0	0.04	7.0	1.0		
	7	293.2	0.04	2.0	1.0	8	315.3	0.07	4.5	1.0		
	9	316.0	0.05	3.5	1.0	10	310.9	0.04	4.0	1.0		
CMB	1	128.6	0.08	2.5	1.0	2	120.9	0.07	4.0	1.5	6.42	2.75
	3	128.1	0.05	8.0	2.0	4	133.6	0.05	8.0	2.0		
	5	233.2	0.05	2.5	1.5	6	243.9	0.04	5.5	1.0		
	7	263.1	0.04	9.0	2.0	8	285.0	0.05	8.0	2.0		
	9	310.1	0.08	3.0	1.0	10	312.4	0.06	10.0	2.0		
	11	308.7	0.05	8.5	2.0	12	306.1	0.04	8.0	2.0		
COL	1	105.2	0.05	1.5	1.0	2	115.6	0.06	3.0	1.0	4.23	2.92
	3	134.3	0.08	2.5	1.0	4	206.8	0.04	1.5	1.0		
	5	223.3	0.04	2.5	1.0	6	242.8	0.05	1.5	1.0		
	7	254.7	0.06	3.0	1.0	9	272.1	0.07	6.5	1.0		
	10	279.5	0.06	8.5	1.0	11	268.4	0.04	9.0	2.0		
	12	302.9	0.04	7.0	1.5							

Table D-1: MCT Thickness Estimates (Continued)

Station	ID	BackAz (°)	p (s/km)	MCT (km)	±	ID	Back Az (°)	p (s/km)	MCT (km)	±	Mean	SD
CWC	1	251.0	0.04	2.0	1.0	2	314.3	0.06	4.0	1.5	3.00	1.41

Station	ID	BackAz (°)	p (s/km)	MCT (km)	±	ID	Back Az (°)	p (s/km)	MCT (km)	±	Mean	SD
DAWY	2	215.9	0.04	1.0	0.5	3	238.0	0.04	2.0	1.0	1.33	0.58
	4	279.8	0.08	1.0	0.5							

Station	ID	BackAz (°)	p (s/km)	MCT (km)	±	ID	Back Az (°)	p (s/km)	MCT (km)	±	Mean	SD
DLBC	1	128.4	0.06	2.0	1.0	2	223.2	0.04	2.0	1.0	1.83	0.29
	4	294.1	0.08	1.5	1.0							

Station	ID	BackAz (°)	p (s/km)	MCT (km)	±	ID	Back Az (°)	p (s/km)	MCT (km)	±	Mean	SD
GSC	1	121.6	0.06	1.5	1.0	2	134.3	0.05	2.5	1.0	2.95	1.04
	3	187.6	0.07	3.0	1.0	4	235.6	0.05	3.0	1.0		
	5	244.5	0.04	4.0	1.5	6	253.9	0.04	4.0	1.0		
	7	265.5	0.04	3.5	1.5	8	287.3	0.04	1.0	0.5		
	9	315.7	0.07	4.0	1.5	10	311.2	0.05	3.0	1.0		

Station	ID	BackAz (°)	p (s/km)	MCT (km)	±	ID	Back Az (°)	p (s/km)	MCT (km)	±	Mean	SD
HWUT	1	133.0	0.07	5.5	2.0	2	140.2	0.05	4.0	1.5	4.75	1.19
	3	244.3	0.04	3.5	1.5	4	312.3	0.06	6.0	1.0		

Station	ID	BackAz (°)	p (s/km)	MCT (km)	±	ID	Back Az (°)	p (s/km)	MCT (km)	±	Mean	SD
ISA	1	87.7	0.06	5.0	1.5	2	117.5	0.07	4.0	1.0	4.25	1.48
	3	129.6	0.06	4.0	1.5	4	135.6	0.05	5.0	1.0		
	5	181.8	0.07	7.0	1.5	7	243.9	0.04	6.0	1.0		
	8	253.0	0.04	3.0	1.5	9	264.0	0.04	5.0	1.5		
	10	285.1	0.04	2.0	1.0	11	317.0	0.07	2.0	1.0		
	12	316.3	0.06	4.0	1.0	13	309.8	0.05	4.0	1.0		

Station	ID	BackAz (°)	p (s/km)	MCT (km)	±	ID	Back Az (°)	p (s/km)	MCT (km)	±	Mean	SD
INK	1	11.2	0.05	2.5	1.0	2	121.3	0.05	4.0	1.5	5.68	2.44
	3	138.9	0.07	3.0	1.0	4	220.5	0.04	2.5	1.0		
	5	242.1	0.04	5.5	1.0	6	277.3	0.08	8.5	1.0		
	7	279.3	0.07	7.5	1.0	8	282.9	0.07	8.5	1.5		
	9	286.8	0.06	8.5	1.5	10	291.5	0.05	7.0	1.5		
	11	284.4	0.04	5.0	1.5							

Station	ID	BackAz (°)	p (s/km)	MCT (km)	±	ID	Back Az (°)	p (s/km)	MCT (km)	±	Mean	SD
ISCO	1	138.4	0.07	9.0	2.0	2	143.7	0.06	7.0	2.0	7.00	2.45
	3	244.0	0.04	9.0	2.0	4	315.6	0.06	7.0	1.5		
	5	312.1	0.05	3.0	1.5							

Station	ID	BackAz (°)	p (s/km)	MCT (km)	±	ID	Back Az (°)	p (s/km)	MCT (km)	±	Mean	SD
KNB	1	99.0	0.06	1.5	1.0	2	136.4	0.06	5.0	1.5	3.44	1.40
	3	231.6	0.04	6.0	1.5	4	239.9	0.05	3.0	1.0		
	5	255.4	0.04	3.0	1.5	6	295.5	0.04	3.0	1.0		
	7	309.5	0.07	3.0	1.0	8	316.9	0.06	3.0	1.0		

Station	ID	BackAz (°)	p (s/km)	MCT (km)	±	ID	Back Az (°)	p (s/km)	MCT (km)	±	Mean	SD
KCC	1	133.9	0.05	9.0	2.0	2	233.1	0.05	5.0	1.5	4.86	2.69
	3	257.2	0.04	4.0	1.0	4	313.0	0.06	2.0	1.0		
	5	307.6	0.05	8.0	1.0	6	291.8	0.05	2.5	1.5		
	7	306.0	0.05	3.5	1.5							

Station	ID	BackAz (°)	p (s/km)	MCT (km)	±	ID	Back Az (°)	p (s/km)	MCT (km)	±	Mean	SD
LDS	1	134.1	0.06	3.0	1.0	2	233.1	0.04	3.0	1.0	4.33	2.31

Table D-1: MCT Thickness Estimates (Continued)

Station	ID	BackAz (°)	p (s/km)	MCT (km)	±	ID	Back Az (°)	p (s/km)	MCT (km)	±	Mean	SD
	3	314.2	0.07	7.0	1.5							
MIN	1	133.1	0.08	4.0	1.0	2	119.5	0.06	2.0	1.0	3.50	0.75
	3	130.1	0.05	3.0	1.0	4	233.0	0.05	4.0	1.5		
	5	246.2	0.04	4.0	1.5	6	263.5	0.04	3.0	1.0		
	7	307.3	0.08	4.5	1.5	8	284.3	0.04	3.0	1.5		
	9	309.0	0.06	4.0	1.5	10	305.3	0.05	3.5	1.0		
NEW	1	101.4	0.06	2.0	1.0	2	156.5	0.08	2.0	1.0	3.19	1.25
	3	130.6	0.06	5.0	1.5	4	135.6	0.05	3.0	1.0		
	5	234.0	0.04	3.5	1.5	6	253.0	0.04	3.0	1.5		
	7	286.1	0.05	5.0	1.0	8	306.4	0.06	2.0	1.0		
ORV	1	130.1	0.08	7.0	2.0	2	116.2	0.07	7.5	2.0	4.38	1.68
	3	125.7	0.06	4.5	1.5	4	131.4	0.06	6.5	1.0		
	5	133.9	0.05	3.5	2.0	6	232.2	0.05	6.0	1.5		
	7	245.8	0.04	2.0	1.0	8	263.0	0.04	2.5	1.0		
	9	284.1	0.05	4.0	1.0	10	311.1	0.08	4.0	1.0		
	11	305.9	0.07	2.0	1.0	12	311.3	0.07	4.0	1.0		
	13	307.0	0.06	3.0	1.0	14	314.5	0.05	4.5	1.5		
	15	303.4	0.05	4.0	1.5	16	303.3	0.05	5.0	1.5		
PFO	1	119.0	0.05	5.5	1.5	2	128.0	0.06	5.0	1.5	3.81	1.79
	3	133.5	0.05	3.0	1.0	4	178.0	0.07	2.5	1.0		
	5	235.3	0.05	2.5	1.0	6	245.0	0.04	5.0	1.5		
	7	251.0	0.04	1.5	1.0	8	257.7	0.04	3.0	1.0		
	9	265.5	0.04	7.0	1.5	10	311.4	0.07	6.5	1.0		
	11	317.9	0.06	3.5	1.0	12	310.9	0.05	2.5	1.5		
	13	308.3	0.05	2.0	1.0							
PNT	1	139.4	0.04	4.0	1.0	3	136.9	0.04	6.0	2.0	4.20	1.04
	4	233.1	0.04	3.5	1.5	5	254.9	0.04	3.5	1.0		
	6	307.8	0.07	4.0	1.0							
SVD	1	114.9	0.07	1.5	1.0	2	133.2	0.06	1.5	1.0	2.38	1.19
	3	235.0	0.05	2.5	1.0	4	245.7	0.04	3.0	1.0		
	5	264.0	0.04	2.0	1.0	6	287.2	0.04	2.0	1.0		
	7	315.7	0.07	1.5	1.0	8	311.9	0.05	5.0	1.5		
VTV	1	122.6	0.07	4.0	1.5	2	131.6	0.06	4.5	1.5	3.72	1.00
	3	185.7	0.07	4.5	1.0	4	235.0	0.05	4.0	1.0		
	5	246.5	0.04	5.0	1.0	6	261.3	0.04	4.0	1.0		
	7	312.1	0.07	2.0	1.0	8	313.2	0.06	2.5	1.0		
	9	304.6	0.04	3.0	1.0							
WDC	1	116.8	0.07	4.5	1.0	2	128.2	0.05	4.5	1.0	3.00	1.43

Table D-1: MCT Thickness Estimates (Continued)

Station	ID	BackAz (°)	p (s/km)	MCT (km)	±	ID	Back Az (°)	p (s/km)	MCT (km)	±	Mean	SD
	4	165.8	0.05	3.5	1.0	5	225.9	0.04	1.5	1.0		
	6	231.7	0.05	2.5	1.0	7	240.6	0.04	1.0	0.5		
	8	247.9	0.05	2.0	1.0	9	306.0	0.08	2.5	1.0		
	10	311.3	0.06	5.0	1.5	11	306.5	0.05	2.0	1.0		
	12	308.8	0.05	2.0	1.0	14	301.8	0.05	5.0	3.0		
WALA	3	147.5	0.04	2.0	1.0	4	237.5	0.04	2.0	1.0	2.33	0.58
	6	310.2	0.07	3.0	1.0							
WHY	1	132.5	0.07	2.0	1.0	2	118.2	0.05	5.0	1.5	5.00	2.28
	3	219.3	0.04	4.0	1.0	4	239.8	0.04	2.5	1.0		
	5	253.3	0.04	2.0	1.0	6	268.3	0.04	5.5	1.5		
	7	285.7	0.07	6.0	1.5	8	287.2	0.07	5.5	1.0		
	9	289.2	0.06	8.0	1.5	10	291.7	0.04	5.5	1.0		
	11	282.8	0.04	9.0	2.0							
WVOR	1	97.6	0.06	2.5	1.0	2	127.6	0.06	5.5	1.0	3.95	0.96
	3	131.9	0.05	3.0	1.0	4	137.2	0.05	3.5	1.0		
	6	233.9	0.05	5.0	1.5	7	249.7	0.04	4.0	1.0		
	8	304.2	0.07	5.0	2.0	9	312.7	0.07	3.5	1.0		
	10	306.7	0.05	3.5	1.5	11	291.4	0.05	4.0	1.0		
Extended Crust												
BMN	1	97.7	0.06	6.0	1.5	2	137.8	0.08	4.0	1.0	3.63	1.60
	3	133.0	0.06	6.0	1.5	4	171.9	0.05	3.0	1.0		
	5	229.0	0.04	3.0	1.0	6	235.6	0.05	3.0	1.0		
	7	251.2	0.04	2.0	1.0	8	308.7	0.07	2.0	1.0		
DAC	1	130.1	0.06	4.0	1.0	2	228.8	0.04	2.0	1.0	3.40	1.14
	3	236.4	0.05	5.0	1.0	4	246.5	0.04	3.0	1.0		
	5	313.9	0.07	3.0	1.0							
DUG	1	136.7	0.06	2.0	1.0	2	178.4	0.06	2.0	1.0	2.17	0.41
	3	231.7	0.04	2.0	1.0	4	238.5	0.05	2.0	1.0		
	5	311.4	0.07	3.0	1.0	6	305.5	0.05	2.0	1.0		
ELK	1	99.3	0.06	3.0	1.0	2	130.0	0.06	6.0	1.5	3.80	1.30
	4	234.8	0.05	3.0	1.0	5	308.5	0.07	4.0	1.5		
	6	306.6	0.05	3.0	1.0							
GLA	1	92.2	0.06	2.0	1.0	2	125.0	0.07	7.0	2.0	5.43	2.76
	3	132.5	0.06	4.0	1.0	4	247.9	0.04	2.0	1.0		
	5	266.7	0.04	9.0	2.0	6	313.9	0.07	7.0	2.0		
	7	313.3	0.05	7.0	1.0							

Table D-1: MCT Thickness Estimates (Continued)

Station	ID	BackAz (°)	p (s/km)	MCT (km)	±	ID	Back Az (°)	p (s/km)	MCT (km)	±	Mean	SD
MNV	1	96.2	0.06	9.0	2.0	2	130.7	0.08	8.0	2.0	6.00	2.88
	3	125.9	0.06	9.0	2.0	4	171.0	0.06	7.0	2.0		
	5	228.4	0.04	2.0	1.0	6	235.4	0.05	3.0	1.0		
	7	249.3	0.04	3.0	1.0	8	312.9	0.07	7.0	2.0		
NEE	1	124.9	0.07	2.0	1.0	2	135.7	0.06	2.0	1.0	2.50	0.58
	3	188.9	0.07	3.0	1.5	4	240.3	0.05	3.0	1.0		
TPH	1	128.7	0.06	4.0	1.0	2	170.0	0.05	4.0	1.0	3.36	0.63
	3	229.0	0.04	3.0	1.0	4	237.5	0.05	3.0	1.0		
	5	246.7	0.04	2.5	1.0	6	308.1	0.07	4.0	1.0		
	7	315.5	0.07	3.0	1.0							
TPNV	2	229.6	0.04	2.0	1.0	3	236.8	0.05	2.5	1.0	2.83	0.93
	4	250.5	0.04	4.0	1.0	5	313.8	0.07	4.0	1.0		
	6	311.3	0.05	2.0	1.0	7	303.1	0.05	2.5	1.0		
TUC	1	140.3	0.05	5.0	1.0	2	135.8	0.06	3.0	1.0	3.88	1.62
	3	124.9	0.07	7.0	1.5	4	240.0	0.05	4.0	1.0		
	5	252.7	0.04	2.0	1.0	6	290.6	0.04	2.5	1.0		
	7	317.0	0.07	4.5	1.0	8	314.3	0.05	3.0	1.0		
California Coast-ranges												
ARC	1	127.6	0.05	2.0	1.0	2	124.1	0.06	4.0	1.0	3.00	0.89
	3	114.1	0.06	4.0	1.0	4	127.0	0.08	3.0	1.0		
	5	307.2	0.07	2.0	1.0	6	305.7	0.06	3.0	1.5		
BAR	1	132.6	0.05	3.0	1.0	2	121.4	0.07	2.5	1.0	3.50	1.39
	3	186.7	0.07	7.0	1.0	4	231.1	0.05	3.0	1.0		
	5	244.9	0.04	2.5	1.0	6	287.8	0.04	3.5	1.5		
	7	314.8	0.07	3.0	1.0	8	315.8	0.06	3.0	1.0		
	9	309.3	0.05	4.0	1.0							
BKS	1	126.5	0.08	6.0	2.0	2	116.1	0.07	3.0	2.0	3.33	1.75
	3	124.1	0.06	3.0	2.0	4	127.4	0.05	4.0	2.0		
	5	134.6	0.05	4.5	2.0	6	179.6	0.07	4.5	2.0		
	9	250.3	0.05	3.0	2.0	10	262.3	0.04	6.0	2.0		
	11	284.3	0.04	6.0	2.0	12	310.0	0.08	2.0	1.5		
	13	312.1	0.07	1.0	0.5	14	307.4	0.05	2.0	1.5		
	15	304.8	0.04	1.0	0.5	16	303.3	0.04	2.0	1.5		
BRK	1	298.7	0.05	2.0	1.0						2.00	0.00
CALB	1	115.9	0.07	2.0	1.0	2	132.3	0.06	2.0	1.0	4.42	2.69
	3	184.1	0.07	9.0	2.0	4	234.3	0.05	5.0	1.5		
	5	244.1	0.04	3.0	1.0	6	312.4	0.05	5.5	1.5		

Table D-1: MCT Thickness Estimates (Continued)

Station	ID	BackAz (°)	p (s/km)	MCT (km)	±	ID	Back Az (°)	p (s/km)	MCT (km)	±	Mean	SD
HOPS	1	125.6	0.08	2.0	1.0	2	122.0	0.06	2.0	1.0	1.91	0.83
	3	128.9	0.05	1.0	0.5	4	225.4	0.04	2.0	1.0		
	5	229.9	0.05	2.0	1.0	6	239.6	0.04	1.0	0.5		
	7	260.6	0.04	1.0	0.5	8	290.0	0.05	3.0	1.0		
	9	306.8	0.07	3.0	1.0	10	310.2	0.06	1.0	0.5		
	11	303.5	0.05	3.0	1.0							
JRSC	1	125.9	0.08	3.0	1.0	2	115.1	0.07	2.5	1.0	2.50	0.50
	3	124.0	0.06	2.5	1.0	4	133.1	0.05	2.0	1.0		
	5	230.2	0.05	2.0	1.0	6	241.8	0.04	3.0	1.0		
	7	251.7	0.05	2.0	1.0	8	261.6	0.04	2.5	1.0		
	9	290.8	0.05	2.5	1.0	10	308.3	0.07	2.0	1.0		
	11	307.4	0.05	3.5	1.0							
MHC	2	116.2	0.07	2.5	1.5	3	124.5	0.06	3.0	1.5	2.58	1.12
	4	126.3	0.05	1.5	1.0	6	225.0	0.04	2.5	1.0		
	7	232.8	0.05	2.0	1.0	8	243.3	0.04	2.0	1.0		
	10	262.4	0.04	1.0	0.5	11	284.5	0.04	2.0	1.0		
	13	309.3	0.07	4.5	1.5	14	312.2	0.06	2.0	1.0		
	15	308.9	0.05	2.0	1.0	16	302.9	0.04	4.5	1.0		
	17	303.6	0.04	4.0	1.0							
PAS	1	90.9	0.06	2.5	1.0	2	120.6	0.07	2.0	1.0	3.61	1.82
	3	131.2	0.05	4.0	1.0	4	233.7	0.05	3.5	1.0		
	5	247.0	0.04	3.5	1.5	6	264.8	0.04	4.0	1.0		
	7	287.6	0.05	2.0	1.0	8	316.5	0.07	8.0	2.0		
	9	312.2	0.06	3.0	1.0							
PKD	1	120.6	0.07	2.5	1.0	2	128.2	0.05	2.0	1.0	2.31	0.84
	3	131.2	0.05	3.0	1.0	5	244.1	0.04	2.0	1.0		
	6	253.5	0.05	4.0	1.5	8	307.9	0.06	2.0	1.0		
	9	304.1	0.04	1.5	1.0	10	315.9	0.05	1.5	1.0		
RPV	1	116.6	0.07	3.0	1.0	2	130.5	0.05	2.0	1.0	2.83	1.47
	3	242.1	0.05	2.0	1.0	4	286.8	0.04	1.0	0.5		
	5	315.8	0.07	4.0	1.5	6	311.0	0.05	5.0	1.5		
SAO	1	121.2	0.08	6.0	2.0	2	95.9	0.06	2.5	1.5	3.34	1.61
	3	114.7	0.07	5.5	1.5	4	124.7	0.06	5.5	1.5		
	5	124.7	0.05	4.0	2.0	6	131.7	0.05	5.0	1.5		
	8	233.8	0.05	2.0	1.0	9	243.3	0.04	3.0	1.0		
	10	253.4	0.04	4.5	1.0	11	262.9	0.04	4.0	1.0		
	12	284.9	0.05	2.5	1.0	13	321.3	0.08	2.0	1.0		
	14	308.5	0.07	1.5	1.0	15	313.3	0.07	3.0	1.0		
	16	307.8	0.06	1.5	1.0	17	303.1	0.05	1.0	0.5		

Table D-1: MCT Thickness Estimates (Continued)

Station	ID	BackAz (°)	p (s/km)	MCT (km)	±	ID	Back Az (°)	p (s/km)	MCT (km)	±	Mean	SD
SBC	1	118.9	0.07	2.0	1.0	3	182.8	0.07	1.5	1.0	1.94	0.18
	4	233.2	0.05	2.0	1.0	5	244.5	0.04	2.0	1.0		
	6	258.2	0.04	2.0	1.0	7	286.0	0.04	2.0	1.0		
	8	314.0	0.07	2.0	1.0	9	311.0	0.05	2.0	1.0		
SCZ	1	119.7	0.07	7.0	2.0	2	233.0	0.05	3.5	1.0	4.25	1.67
	3	252.4	0.05	4.5	1.0	4	264.6	0.04	6.0	1.5		
	5	283.3	0.05	2.0	1.0	6	313.7	0.08	4.5	1.5		
	7	312.7	0.06	4.0	1.5	8	306.8	0.05	2.5	1.0		
SNCC	1	114.8	0.07	1.5	1.0	2	135.7	0.05	2.0	1.0	2.75	1.25
	3	233.2	0.05	3.0	1.0	4	243.7	0.04	2.0	1.0		
	5	263.3	0.04	3.0	1.5	6	312.1	0.05	5.0	1.5		
STAN	1	125.7	0.08	1.5	1.0	2	115.7	0.07	2.5	1.0	2.25	0.50
	3	129.8	0.05	2.5	1.0	5	309.9	0.06	2.5	1.0		
Volcanic Arc												
ADK	1	89.8	0.06	5.5	1.5	3	178.8	0.05	3.0	1.0	3.73	1.31
	4	198.7	0.06	2.5	1.0	5	221.3	0.06	2.5	1.0		
	6	236.7	0.05	5.5	1.0	7	247.9	0.04	2.0	1.0		
	8	249.8	0.06	5.0	1.5	9	265.1	0.08	4.0	1.5		
	10	255.8	0.07	5.0	1.0	11	263.9	0.06	3.0	1.0		
	12	265.0	0.04	3.0	1.0							
BBB	1	226.2	0.04	3.0	1.0	2	248.3	0.04	2.0	1.0	2.33	0.58
	3	302.0	0.07	2.0	1.0							
COR	1	131.5	0.04	7.0	1.5	2	125.9	0.05	2.0	1.0	4.27	1.88
	3	122.0	0.07	2.5	1.0	4	135.5	0.08	8.0	2.0		
	5	162.8	0.05	3.0	1.5	6	228.5	0.05	3.0	1.0		
	7	244.1	0.04	3.0	1.0	8	260.7	0.04	3.0	1.0		
	9	282.8	0.05	6.0	1.5	10	306.4	0.07	5.0	1.5		
	11	306.0	0.06	5.0	1.5	12	297.3	0.05	5.0	1.5		
	13	303.3	0.04	3.0	1.0							
MOBC	1	221.7	0.04	2.5	1.0	2	299.4	0.07	8.0	2.5	5.25	3.89
PGC	2	233.8	0.04	2.0	1.5						2.00	0.00
PMB	2	132.8	0.04	3.0	1.0	3	230.3	0.04	2.0	1.0	2.50	0.50
	4	304.3	0.07	2.5	1.5							
UNM	1	138.7	0.07	3.0	1.5	2	249.1	0.04	2.0	1.5	2.70	0.45

Table D-1: MCT Thickness Estimates (Continued)

Station	ID	Back Az (°)	p (s/km)	MCT (km)	±	ID	Back Az (°)	p (s/km)	MCT (km)	±	Mean	SD
	3	322.3	0.08	2.5	1.5	4	327.2	0.07	3.0	1.5		
	5	321.5	0.05	3.0	1.5							

Station: Station Code

ID: Cluster Identification number (see appendix 1).

Back Az.: Back Azimuth from station to Cluster center.

p: Horizontal slowness or ray parameter.

MCT Thickness, ±, Average and Standard Deviation (SD): Values in km.

BIBLIOGRAPHY

Abbott, D., and W. Mooney, The structural and geochemical evolution of the continental crust: Support for the oceanic plateau model of continental growth, Rev. of Geophys, supplement, U.S. Natl. Report to IUGG 1991-1994, 231-242, 1995.

Ammon, C. J. (1991). The isolation of receiver effects from teleseismic P wavefronts. Bull. Seism. Soc. Am., 81, 2504-2510.

Ammon, C. J. and G. Zandt (1993). Receiver structure beneath the Southern Mojave block, California. Bull. Seism. Soc. Am., 83, 737-755.

Ammon, C. J., G. E. Randall and G. Zandt (1990). On the Nonuniqueness of Receiver Function Inversions. J. Geophys. Res., 95, 15303-15318.

Anderson, D. L. (1995). Lithosphere, Asthenosphere, and Perisphere. Rev. Geophys., 33, 125-149.

Anderson, D. L. (1989). Theory of the Earth, Blackwell Scientific Publications, Oxford, England, 366 pages.

Arndt, N. T. and S. L. Goldstein (1989). An open boundary between lower continental crust and mantle: its role in crust formation and crustal recycling. Tectonophysics, 161, 201 - 212.

Bally, A. W. (1989). Phanerozoic basins of North America. In: Bally, A.W., and A. R. Palmer, eds. The Geology of North America-An overview. Boulder, Co. Geological Society of America, The Geology of North America, v. A.

Bally, A. W. and A. R. Palmer, eds. (1989). The Geology of North America-An overview. Boulder, Co. Geological Society of America, The Geology of North America, v. A.

Bally, A. W., C.R. Scotese and M. I. Ross (1989). North America; Plate-tectonic setting and tectonic elements. In: Bally, A.W., and A. R. Palmer, eds. The

Geology of North America-An overview. Boulder, Co. Geological Society of America, The Geology of North America, v. A.

Bates, R. L. and J. A. Jackson (1983). Dictionary of Geological Terms. Anchor Books.

Benz, H. M. and J. McCarthy (1994). Evidence for an upper mantle low velocity zone beneath the southern Basin and Range-Colorado Plateau transition zone. Geophys. Res. Lett., 21, 509-512.

Benz, H. M., R. B. Smith and W. D. Mooney (1990). Crustal structure of the Northern Basin and Range province from the 1986 Program for Array Seismic Studies of the Continental Lithosphere Seismic Experiment. J. Geophys. Res., 95, 21823-21842.

Braile, L. W., J. Hinze, R. R. B. von Frese and G. R. Keller (1989). Seismic properties of the crust and uppermost mantle of the conterminous United States and adjacent Canada. In: Pakiser, L.C. and W. D. Mooney, eds. Geophysical Framework of the Continental United States. Mem. Geol. Soc. Am., 172, 655-680.

Braile, L. W. and C. S. Chiang (1986), The continental Mohorovicic discontinuity: results from near-vertical and wide-angle seismic reflection studies. In: Barangazi, M. and L. Brown, eds. Reflection Seismology: A global Perspective. Geodyn. Ser. 13. American Geophysical Union. 257-272.

Brown, G. C., and A. E. Mussett (1993), The Innaccessible Earth - An Integrated View of Its Structure and Composition, Chapman & Hall, London, 276 pages.

Burdick, L. J. and C. A. Langston (1977). Modelling crustal structure through the use of converted phases in the teleseismic body waveforms. Bull. Seism. Soc. Am., 67, 677-692.

Cassidy, J. F. (1995). A comparison of the receiver structure beneath stations of the Canadian National Seismograph Network. Can. J. Earth Sci., 32, 938-951.

Cassidy, J. F. (1992). Numerical experiments in broadband receiver function analysis, Bull. Seism. Soc. Am., 82, 1453-1474.

Chapman, D. S. and K. P. Furlong (1992). Thermal state of the continental crust. In: Fountain, D. M., R. Arculus and R. W. Kay, eds., Continental Lower Crust. Elseiver Sci., 179 - 200.

Chernicoff, S. and H. A. Fox (1997). Essentials of Geology. Worth Publishers.

Christensen, N. I. (1995). Poisson's ratio and crustal seismology. J. Geophys. Res., 101, 3139-3156.

Christensen, N. I. and W. D. Mooney (1995). Seismic velocity structure and composition of the continental crust: A global view. J. Geophys. Res., 100, 9761-9788.

Clarke, T. J. and P.G. Silver (1993). Estimation of crustal Poisson's ratio from broadband teleseismic data. Geophys. Res. Lett., 20, 241-244.

Clayton, R. W. and R. A. Wiggins (1976). Source shape estimation and deconvolution of teleseismic body waves. J. R. Astr. Soc., 47, 151-177.

Clowes, R. M. (1993). Variations in continental crustal structure in Canada form LITHOPROBE seismic reflection and other data. Tectonophysics, 219, 1-27.

Condie, K. C. (1993), Plate Tectonics & Crustal Evolution, Third Edition, Pergamon Press, Oxford, 492 pages.

Constable, S. C., R. L. Parker and C. G. Constable, Occam's inversion: A practical algorithm for generating smooth models from electromagnetic sounding data, Geophys., 52, 289-300, 1987.

Davidson, J. P., W. E. Reed and P. M. Davis (1997). Exploring Earth. Prentice Hall.

De Bari, S., S. M. Kay and R. W. Kay (1987). Ultramafic xenoliths from Adagdak volcano, Adak, Aleutian Islands, Alaska: Deformed igneous cumulates from the Moho of an Island arc. J. Geol., 95, 329-341.

Dobrin, M. B. and C. H. Savit (1988). Introduction to Geophysical Prospecting. Fourth edition. McGraw-Hill book Co.

Durrheim, R. J. and W. D. Mooney (1994). Evolution of the Precambrian lithosphere: Seismological and geochemical constraints. J. Geophys. Res., 99, 15359-15374.

Dziewonski, A. M. and D. L. Anderson (1981). Preliminary reference Earth model, Phys. Earth Planet. Int., 25, 297-356.

Fountain, D. M., R. Arculus and R. W. Kay, eds. (1992). Continental Lower Crust. Elseiver Sci.

Fountain, D. M. and N. I. Christensen (1989). Composition of the continental crust and upper mantle; A review. In: Pakiser, L.C. and W. D. Mooney, eds. Geophysical Framework of the Continental United States. Mem. Geol. Soc. Am., 172, 711-742.

Fountain, D. M. and M. H. Salisbury (1981). Exposed cross-sections through the continental crust: implications for crustal structure, petrology, and evolution. Earth. Planet. Sci. Lett., 56, 263 - 277.

Furlong, K. P. and D.M. Fountain (1986). Continental crustal underplating: Thermal considerations and Seismic-Petrologic consequences. J. Geophys. Res., 91, 8285-8294.

Gajewski, D., W. S. Holbrook and C. Prodehl (1987). Combined seismic reflection and refraction profiling in southwest Germany – detailed velocity mapping by the refraction survey. Geophys. J. R. astr. Soc., 89, 333-338.

Griffin, W. L., S. Y. O'Reilly, C. G. Ryan, O. Gaul and D. A. Ionov (1998). Secular variation in the composition of subcontinental lithospheric mantle: Geophysical and geodynamic implications. In: Braum, J. and others, eds., Structure and Evolution of the Australian continent, Geodynamics Series, 26, American Geophysical Union.

Gurrola, H., J. B. Minster and T. J. Owens, The use of velocity spetrum for stacking receiver functions and imaging upper mantle discontinuities, Geopys. J. Int., 117, 427-440, 1994.

Gurrola, H., G. E. Baker and J. B. Minster (1995). Simultaneous time domain deconvolution with application to the computation of receiver functions, Geophys. J. Int., 120, 537-543.

Hale, L. D. and G. A. Thompson (1982). The seismic reflection character of the continental Moho discontinuity. J. Geophys. Res., 87, 4625-4635.

Hambling, W. K. and J. D. Howard (1995). Exercises in Physical Geology. Ninth edition. Prentice Hall.

Hammer, P. T. C., and R. M. Clowes, Moho reflectivity patterns - a comparison of Canadian LITHOPROBE transects, Tectonophys., 269, 179-198, 1997.

Hanna, W.F., R.E. Sweeney, T. G. Hildenbrand, J.G. Tanner, R.K. McConnell and R.H. Godson (1989). The Gravity Anomaly Map of North America. In: Bally, A.W., and A. R. Palmer, eds. The Geology of North America-An overview. Boulder, Co. Geological Society of America, The Geology of North America, v. A.

Hermann, J, O. Müntener, V. Trommsdorff, W. Hansmann and G. B. Piccardo (1997). Fossil crust-to-mantle transition, Val Malenco. J. Geophys. Res., 102, 20123-20132.

Hoffman, P. F. (1989). Precambrian geology and tectonic history of North America. In: Bally, A.W., and A. R. Palmer, eds. The Geology of North America-An overview. Boulder, Co. Geological Society of America, The Geology of North America, v. A.

Holbrook, W.S., W. D. Mooney and N. I. Christensen (1992). The seismic velocity structure of the deep continental crust. In: Fountain, D. M., R. Arculus and R. W. Kay, eds., Continental Lower Crust. Elseiver Sci., 1 - 44.

Hynes, A. and D. B. Snyder (1995). Deep-crustal mineral assemblages and potential for crustal rocks below the Moho in the Scottish Caledonides. Geophys. J. Int. 123, 323-339.

Irwin, W. P. (1990). 3. Geology and Plate-Tectonic development. In: Wallace, R. E., ed. The San Andreas fault system, California. U. S. Geological Survey., Professional Paper 1515.

Jarchow, C. M., G. A. Thompson, R. D. Catchings and W. D. Mooney (1993). Seismic evidence for active magmatic underplating beneath the Basin and Range province, western United States. J. Geophys. Res., 98, 22095 - 22108.

Jarchow, C. M. and G. A. Thompson (1989). The Nature of the Mohorovicic Discontinuity. Ann. Rev. Earth Planet. Sci., 17, 475-506.

Jordan, T. H. (1988). Structure and formation of the continental tectosphere. In: M. A. Menzies and K. G. Cox, eds., Oceanic and Continental lithosphere: similarities and differences. J. Petrol. Special Volume. 11-38.

Jordan, T. H. (1979). Mineralogies, densities and seismic velocities of garnet lherzolites and their geophysical implications. In: Boyd, F. R. and H. O. A. Meyer, eds. The Mantle Sample: Inclusions in Kimberlites and other volcanics. Proceedings of the Second International Kimberlite conference. V. 2. American Geophysical Union.

Kennett, B. L. N. (1983). Seismic Wave Propagation in Stratified Media, Cambridge University Press, Cambridge, England, 342 pages.

Kikuchi, M. and H. Kanamori (1982). Inversion of complex body waves. Bull. Seism. Soc. Am., 72, 491-506.

Lachenbruch, A. H. and P. Morgan (1990). Continental extension, magmatism and elevation; formal relations and rules of thumb. Tectonophysics, 174, 39-62.

Langston, C. A. (1994). An integrated study of crustal structure and regional wave propagation for southeastern Missouri. Bull. Seism. Soc. Am., 84, 105-118.

Langston, C. A. (1989). Scattering of teleseismic body waves under Pasadena, California. J. Geophys. Res., 94, 1935-1951.

Langston, C. A. (1979). Structure under Mount Rainier, Washington, inferred from teleseismic body waves. J. Geophys. Res., 84, 4749-4762.

Langston, C. A. (1977). The effect of planar dipping structure on source and receiver responses for constant ray parameter. Bull. Seism. Soc. Am., 67, 1029-1050.

Larkin, S. P., A. Levander, T. J. Henstock and S. Pullammanappalli (1997). Is the Moho flat? Seismic evidence for a rough crust-mantle interface beneath the northern Basin and Range. Geology, 25, 451-454.

Lay, T. and T. Wallace (1995). Modern Global Seismology. Academic Press.

Levin, J. L. (1994). The Earth Through Time, Suanders College Publishing, Fort Worth, TX, 651 pages pages.

Ligorría, J. P., and C. J. Ammon, Iterative deconvolution of teleseismic seismograms and receiver function estimation, Bull. Seism. Soc. Am., 89, 1395-1400, 1999.

Macdougall, J. D. (1996). A Short History of Planet Earth - Mountains, Mammals, Fire, and Ice, John Wiley & Sons, Inc., New York, NY, 266 pages.

Mangino, S. G., G. Zandt and C. J. Ammon (1993). The receiver structure beneath Mina, Nevada. Bull. Seism. Soc. Am., 83, 542-560.

Markl, G. and K. Bucher (1998). Composition of fluids in the lower crust inferred from metamorphic salt in lower crustal rocks. Nature, 391, 781-783.

McCarthy, T. C. and A. E. Patiño-Douce (1997). Experimental evidence for high-temperature felsic melts formed during basaltic intrusion on the deep crust. Geology, 25, 463-466.

McLennan, S. M. (1992). Continental Crust, int The Encyclopedia of Earth System Science, Academic Press, Inc. 581-592.

McNamara, D. E. and T. J. Owens (1993). Azimuthal shear wave velocity anisotropy in the Basin and Range province using Moho P_s converted phases. J. Geophys. Res., 98v, 12003-12017.

Meissner, R. (1986). The Continental Crust: A Geophysical Approach, Academic Press, New York, 426 pages.

Mengel, K. and H. Kern (1992). Evolution of the petrological and seismic Moho - implications for the continental crust-mantle boundary. Terra Nova, 4, 109-116.

Mohorovicic, A. (1910). Das Beben vom 8. X. 1909. Jahrb. Meteorol. Obs. Zagreb. 9. Teil 4. Abschn. 1. 63.

Mooney, W. D. And R. Meissner (1992). Multi-genetic origin of crustal reflectivity: a review of seismic reflection profiling of the contiental lower crust and

Moho. In: Fountain, D. M., R. Arculus and R. W. Kay, eds., Continental Lower Crust. Elseiver Sci., 45 - 80.

Mooney, W. D. and L. W. Braile (1989). The seismic structure of the continental crust and upper mantle of North America. In: Bally, A.W., and A. R. Palmer, eds. The Geology of North America-An overview. Boulder, Co. Geological Society of America, The Geology of North America, v. A.

Mooney, W. D. and T. M. Brocher (1987). Coincident seismic reflection/refraction studies of the continental lithosphere - a global review. Rev. Geophys., 25, 723-742.

Morgan, P. and C. A. Swanberg (1985). On the Cenozoic uplift and Tectonic stability of the Colorado Plateau. Journal of Geodynamics, 3, 39-63.

Neal, C. R., J. J. Mahoney, L. W. Kroenke, R. A. Duncan and M. G. Petterson (1997). The Ontong Java Plateau, in Large Igneous Provinces, Continental Oceanic, and Planetary Flood Volcanism, J. J. Mahoney and M. F. Coffin Ed., American Geophysical Union, Wahington, D.C., 183-216.

Nelson, K.D. (1991). A unified view of craton evolution motivated by recent deep seismic reflection and refraction results. Geophys. J. Int., 105, 25-35.

O'Reilly, S. Y. (1989). Nature of the East Australian lithosphere. In: R. W. Johnson, ed. Intraplate volcanism in Eastern Australia and New Zealand. 290-212. Cambridge Univ. Press.

O'Reilly, S. Y. and W. L. Griffin (1996). 4-D Lithosphere Mapping: methodology and examples. Tectonophysics, 262, 3-18.

O'Reilly, S. Y. and W. L. Griffin (1994). Moho and petrologic crust-mantle boundary coincide under southern Australia: Comment. Geology, 22, 666-667.

O'Reilly, S. Y., W. L. Griffin and O. Gaul (1997). Paleogeothermal gradients in Australia: key to 4-D lithosphere mapping. AGSO Journal of Australian Geology & Geophysics, 17, 63-72.

Oldenburg, D. W. (1981). A comprehensive solution to the linear deconvolution problem, Geophys. J. R. Astron. Soc., 65, 331-357.

Owens, T. J. (1984). Determination of crustal and upper mantle structure from analysis of broadband teleseismic P-waveforms. PhD thesis. Department of Geology and Geophysics, The University of Utah.

Owens, T. J. and G. Zandt (1985). The response of the continental crust-mantle boundary observed on broadband teleseismic receiver functions. Geophys. Res. Lett., 12, 705-708.

Owens, T. J., S. R. Taylor and G. Zandt (1987). Crustal structure at regional seismic test network stations determined from inversion of broadband teleseismic P waveforms. Bull. Seism. Soc. Am., 77, 631-662.

Owens, T. J., S. R. Taylor, and G. Zandt (1983). Isolation and enhancement of the response of local seismic structure from teleseismic P-waveforms, Rept. UCID-19809, Lawrence Livermore National Laboratory, Livermore, California, 33 pp.

Padovani, E. L., J. Hall and G. Simmons (1982). Constraints on crustal hydration below the Colorado Plateau from V_p measurements on crustal xenoliths. Tectonophysics, 84, 313-328.

Padovani, E. R. and J. L. Carter (1977). Aspects of the deep crustal evolution beneath south-central New Mexico. In: Heacock, J. G., ed. The Earth's crust: Its Nature and Physical Properties. American Geophysical Union, 754.

Peng, X. and E. D. Humphreys (1997). Moho dip and crustal anisotropy in Northwestern Nevada from teleseismic receiver functions. Bull. Seism. Soc. Am., 87, 745-754.

Percival, J. A., D. M. Fountain and M. H. Salsbury (1992). Exposed cross sections as windows of the lower crust. In: Fountain, D. M., R. Arculus and R. W. Kay, eds., Continental Lower Crust. Elseiver Sci., 317-362.

Poirier, J-P. (1991). Introduction to the Physics of the Earth's Interior. Cambridge Topics in Mineral Physics and Chemistry. 3. Cambridge University Press.

Pollack, H. N., S. J. Jurter and J. R. Johnson, Heat flow from the Earth's interior: Analysis of the global data set, Rev. of Geophys., 31, 267-280, 1993.

Raia, F. and F. J. Spera (1997). Simulations of crustal anatexis: Implications for the growth and differentiation of continental crust. J. Geophys. Res., 102, 22629-22648.

Randall, G. E. (1989). Efficient calculation of differential seismograms for lithospheric receiver functions. Geophys. J. Int., 99, 469-481.

Randall, G. E. and T. J. Owens (1994). Array analysis of the large-aperture array of the 1988-89 PASSCAL Basin and Range passive-source seismic experiment. Geophys. J. Int., 116, 618-636.

Rast, N. (1989). The evolution of the Appalachian chain. In: Bally, A.W., and A. R. Palmer, eds. The Geology of North America-An overview. Boulder, Co. Geological Society of America, The Geology of North America, v. A.

Reston, T. J. (1990). Shear in the lower crust during extension: not so pure and simple. Tectonophysics, 173, 175-183.

Rogers, J. J. W. (1993). A History of the Earth, Cambridge University Press, Cambridge, England, 312 pages.

Rudnick, R. L. and D. M. Fountain (1995). Nature and composition of the continental crust: A lower crustal perspective. Rev. Geophys., 33, 267-309.

Rudnick, R. (1990). Growing from below. Nature, 347, 711-712.

Schiano, P. and R. Clocchiatti (1994). Worldwide occurrence of silica-rich melts in sub-continental and sub-oceanic mantle minerals. Nature, 368, 621-624.

Sheehan, A. F., G. A. Abers, C. H. Jones and A. L. Lerner-Lam (1995). Crustal thickness variations across the Colorado Rocky Mountains from teleseismic receiver functions. J. Geophys. Res., 100, 20391-20404.

Simon, R., B. (1981). Earthquake Interpretations, William Kaufmann, Inc., Los Altos, CA, 150 pages.

Tarkov A. P. and V. V. Vavakin (1982). Poisson's ratio behavior in various crystalline rocks: application to the study of the Earth's interior. Phys. Earth Planet. Int., 29, 24-29.

Taylor, S. R. and T. J. Owens (1984). Frequency-Domain inversion of receiver transfer functions for crustal structure. Earthquake Notes, 55, 7-12.

Taylor, S. R. and S. M. McLennan (1995). The geochemical evolution of the continental crust, Rev. of Geophys., 33, 241-265.

Telford, W. M., L. P. Geldart, R. E. Sheriff and D. A. Keys (1985). Applied Geophysics. Cambridge University Press.

Turcotte, D. L., and G. Schubert, Geodynamics, Applications of Continuum Physics to Geological Problems, John Wiley & Sons, New York, NY, 450 pages, 1982.

Voshage, H., A. W. Hofmann, M. Mazzucchelli, G. Rivalenti, S. Sinigoi, I. Raczek and G. Demarchi (1990). Isotopic evidence from the Ivrea zone for a hybrid lower crust formed by magmatic underplating. Nature, 347, 731-736.

Warner, M (1990). Basalts, water, or shear zones in the lower continental crust?. Tectonophysics, 173, 163-174.

Zandt, G. and C. J. Ammon (1995). Continental crust composition constrained by measurements of crustal Poisson's ratio. Nature, 374, 152-154.

Zandt, G., S. C. Myers and T. C. Wallace (1995). Crust and mantle structure across the Basin and Range-Colorado Plateau boundary at 37º N latitude and implications for Cenozoic extensional mechanism. J. Geophys. Res., 100, 10529-10548.

Vita Auctoris

Juan Pablo Ligorría was born in Guatemala City, Guatemala, on August 6, 1964. In 1983, he was granted a scholarship from the Ministry of Energy and Mines of Guatemala to pursue Geophysics Engineering studies at the Instituto Politécnico Nacional of Mexico, a public university funded by the Mexican oil industry. By the time he had to decide the subject of his Bachelor thesis, he had already realized that Petroleum Exploration was not as interesting as scientific research in Geophysics. Thus, he started volunteer work at the Institute of Geophysics of the National Autonomous University of Mexico (UNAM) where he wrote a thesis in Seismology, under the advice of Drs. Lautaro Ponce (QEPD) and Gerardo Suárez.

After graduation in Mexico, Ligorría went back to Guatemala, were he worked for five years at the National Institute of Electricity. By August 1993 he was granted a scholarship from the Swedish Agency for Research and Education Cooperation to conduct graduate level studies at the Institute of Solid Earth Physics of the University of Bergen, Norway, where he received the Master of Science Diploma in June 1995, working under the advice of Professor Jens Havskov.

By graduation day in Bergen, the decision was made to join the Department of Earth and Atmospheric Sciences of St. Louis University, where he started the doctorate program in the Fall semester of 1995.